Numerical Modelling of Liquefaction Under Embankments Subjected To Cyclic Loads By Wind Turbines

by

J. M. Verstijnen

to obtain the degree of Master of Science
in Civil Engineering, Geo-Engineering
at the Delft University of Technology,
to be defended publicly on Tuesday October 20, 2020 at 2:30 PM.

Student number:	4742648	
Thesis committee:	Prof. dr. ir. M. A. Hicks	TU Delft - Geo-Engineering, Chair
	Dr. ir. R. B. J. Brinkgreve	TU Delft - Geo-Engineering
	Dr. ir. T. Schweckendiek	TU Delft - Hydraulic Engineering
	Dr. ir. O. M. Heeres	Arcadis
	Ir. F.S. de Haan	Arcadis

An electronic version of this thesis is available at http://repository.tudelft.nl/.

TU Delft

Preface

In front of you is my master's thesis titled: "Numerical Modelling of Liquefaction Under Embankments Subjected to Cyclic Loads by Wind Turbines". This thesis concludes my master's degree in Civil Engineering at Delft University of Technology. The research has been done in collaboration with Arcadis.

I would not have been able to complete this thesis without the contribution of several people. I would like to thank the members of my graduation committee for their guidance through the process of writing the thesis. Michael Hicks, for your feedback and suggestions during the meetings. Ronald Brinkgreve, for the constructive criticism and feedback on my numerical models. Timo Schweckendiek, for your suggestions during the meetings. Otto Heeres, for introducing me to the interesting topic and many hours of guidance and discussions. Frans de Haan, for your guidance and constructive feedback on my writing. Thanks to my colleagues and fellow graduate students at Arcadis for the many coffee breaks, chats and table tennis matches during the day.

Furthermore, studying at TU Delft wouldn't be as great without all the people I've met during my studies. Many thanks to all of you. Most importantly, I would thank my parents who enabled me to continue studying and their never ending support. And at last, thank you Nienke, for all the support and patience throughout all of my study.

J. M. Verstijnen
Rotterdam, 2020

Abstract

The Netherlands is going through an energy transition towards renewable energy sources. Recent development have caused that the policy regarding the installation of onshore wind turbines on embankments has changed to 'Yes, provided that ...'. (Simplified) approaches are available within professional practice to analyse the risk of liquefaction, but are considered to be conservative. In addition, the amount of conservatism of these methods are not quantified. In this thesis, a methodology is formulated to model the key aspects of liquefaction of a soil layer underneath a dike system subjected to cyclic loading by an onshore wind turbine. The key aspects are defined as: cyclic loading, soil-structure interaction and consolidation behaviour. From the literature study, it is concluded that Seed and Rahman (1978) have developed a method with similar conditions as the current situation (onshore wind turbine on an embankment). In this thesis, the method adapted and implemented so that it can be applied to the current situation with its key aspects.

The applicable modelling conditions (quasi-static or dynamic) are investigated for the current situation. The analysis is performed using analytic and numerical models (Plaxis 2D). Both models conclude that the loads induced by the wind turbine can be modelled as quasi-static as the loads are sufficiently slow to neglect inertia effects. The influence of the cyclic loads by the wind turbine on the liquefiable soil layer is determined by the Cyclic Stress Ratio (CSR). The CSR is the driving force of the liquefaction analysis. The influence due to the soil-structure interaction is determined using a Finite Element Analysis (Plaxis 2D). The Hardening Soil small strain model gives a more accurate prediction of the CSR in the soil, as the soil response is stiffer during un/re-loading. The CSR is determined for a horizontal geometry and a geometry including an embankment. The presence of the embankment results in various modes of shearing in the soil, e.g. triaxial compression, triaxial extension and direct simple shear. The shape and magnitude of the CSR for the two scenarios are very comparable. It is concluded that the presence of static shear stresses (due to the embankment) have little influence on the CSR. This is due to the definition of the CSR. Thus, the effects of static shear stresses should be included in the resisting force of the soil, or Cyclic Resistance Ratio (CRR).

The consolidation behaviour is account for using the model of Seed and Rahman (1978), which applies the consolidation equation with additional generation term. The model is able to account for partial consolidation, which is defined as a state where excess pore pressures can be generated and dissipate at the same time. The generation term is based on empirical data on the development of pore pressures with respect to the number of cycles. The model is implemented using a Finite Difference Method in a cylindrical coordinate system to represent the dissipation behaviour of a permeable soil. The consolidation equation with additional generation term allows to model the consolidation characteristics in radial and vertical direction, a layered soil, the load intensity and the loading frequency. Inclusion of this time-dependent behaviour reduces the maximum pore pressure ratio in the soil. A limitation of the model is its uncoupled nature. Therefore, no strains and only pore pressures are determined. The constitutive behaviour inherent to the liquefaction phenomena, such as plastic deformations, is lacking.

Oostpolderdijk is used as a case study to compare the modified method of Seed and Rahman (1978) to the reference engineering method and the method of Boulanger and Idriss (2014). The comparison with Boulanger and Idriss (2014) suggests that the modified model gives reasonable results. The application of the modified method results in a more favourable result compared to the reference engineering method. However, a sensitivity analysis shows that Oostpolderdijk is at risk as the sensitivity to a variation of the permeability is high. Therefore, liquefaction can not be ruled out for this scenario.

Contents

Preface iii

Abstract v

List of Figures xi

List of Tables xvii

Symbols xix

1 Introduction 1
- 1.1 Research Motivation 1
- 1.2 Problem Statement 2
- 1.3 Research Questions 3
- 1.4 Research approach 3

2 Literature Review 5
- 2.1 Wind Turbines 5
- 2.2 Embankment Design 6
- 2.3 Cyclic Soil Behaviour and Liquefaction 7
  - 2.3.1 Cyclic Soil Behaviour 7
  - 2.3.2 Liquefaction 8
- 2.4 Consolidation 8
- 2.5 Constitutive Soil Models 9
  - 2.5.1 Linear-Elastic Perfectly-Plastic model (Mohr-Coulomb model) 10
  - 2.5.2 Hardening Soil Small Strain 10
  - 2.5.3 Various Models 10
- 2.6 Various Approaches to Liquefaction Modelling 11
  - 2.6.1 Reference Engineering Methodology 11
  - 2.6.2 Offshore Engineering 11
  - 2.6.3 Earthquake Engineering 12

3 Starting Points 13
- 3.1 Soil Profile and Geometry 14
  - 3.1.1 Soil Profile 14
  - 3.1.2 Scenario 1: Geometry with Horizontal Surface 15
  - 3.1.3 Scenario 2: Embankment Geometry 15
- 3.2 Liquefiable Soil Layer Characteristics 16
  - 3.2.1 Wadzand 16
  - 3.2.2 Ottawa Sand 18
- 3.3 Material Parameter Set for Plaxis 2D 19
  - 3.3.1 Linear Elastic 19
  - 3.3.2 Mohr-Coulomb 19
  - 3.3.3 Hardening Soil Small Strain 19
  - 3.3.4 Plate 19
- 3.4 Load signal 19
- 3.5 Natural Frequencies 21
- 3.6 Mesh Calibration 21

4 Soil Structure Interaction and Influence Depth of a Shallow Foundation 25
4.1 Method . . . 25
4.2 Scenario 1: Geometry with Horizontal Surface . . . 26
4.2.1 Mohr-Coulomb . . . 26
4.2.2 Hardening Soil Small Strain . . . 29
4.2.3 Conclusion on applied soil models. . . . 31
4.2.4 3D effect . . . 31
4.3 Scenario 2: Embankment Geometry . . . 32
4.3.1 Sensitivity Analysis . . . 34
4.4 Conclusions and Discussions . . . 36

5 Pore Pressure Response to Cyclic Loading 39
5.1 Method . . . 39
5.2 Model Implementation . . . 42
5.3 Verification . . . 43
5.3.1 Verification case 1: 1D radial consolidation . . . 43
5.3.2 Verification case 2: 2D radial consolidation . . . 44
5.3.3 Verification case 3: 2D radial consolidation . . . 44
5.3.4 Verification case 4: Simulation of CDSS test . . . 45
5.4 Interpretation of the liquefaction output . . . 46
5.5 Sensitivity Analysis . . . 48
5.5.1 Time Step and Element Size . . . 49
5.5.2 Permeability. . . . 50
5.5.3 Soil Heterogeneity . . . 51
5.5.4 Loading Intensity . . . 53
5.5.5 Loading Frequency . . . 54
5.6 Conclusions and Discussions . . . 54

6 Case Study: Oostpolderdijk 57
6.1 Liquefaction analysis using Seed and Rahman (1978) . . . 57
6.1.1 Guidelines for practical applications . . . 57
6.1.2 Results Case Study Oostpolderdijk . . . 60
6.1.3 Conclusion on the application of Seed and Rahman (1978) . . . 64
6.2 Liquefaction triggering procedure by Boulanger and Idriss (2014) . . . 64
6.2.1 Conclusion on the application of Boulanger and Idriss (2014) . . . 65

7 Conclusions and Recommendations 67
7.1 Conclusions and Discussion . . . 67
7.2 Recommendations . . . 71

References 73

Sources 77

A Literature Review 79
A.1 Wind Turbines . . . 79
A.1.1 Loading Situations . . . 80
A.1.2 Foundation . . . 81
A.2 Dike Design . . . 82
A.3 Behaviour of Soils Under Cyclic Loading . . . 83
A.3.1 Volumetric Behaviour . . . 84
A.3.2 Multi-Phase Material . . . 85
A.3.3 Stress Dependent Stiffness . . . 85
A.3.4 Plastic Behaviour . . . 86
A.3.5 Cyclic Loading Scenarios . . . 87
A.4 Liquefaction . . . 88
A.4.1 Flow/Static Liquefaction . . . 88
A.4.2 Cyclic Liquefaction . . . 90

A.5 Constitutive Soil Models . . . 92
A.5.1 Hooke's Law . . . 92
A.5.2 Mohr-Coulomb Model . . . 92
A.5.3 HSsmall Model . . . 92
A.5.4 PM4Sand Model . . . 93
A.5.5 UBC3D-PLM Model . . . 96
A.5.6 Hypoplastic Model . . . 97
A.6 Consolidation . . . 98
A.6.1 Terzaghi's 1D Formulation . . . 98
A.6.2 Biot's Consolidation Formulation . . . 99
A.7 Various Approaches to Liquefaction Modelling . . . 99
A.7.1 Reference Engineering Practice . . . 99
A.7.2 Offshore Engineering . . . 100
A.7.3 Earthquake Engineering . . . 102
A.7.3.1 Cyclic Stress Approach: Boulanger and Idriss (2014) . . . 102
A.7.3.2 Cyclic Strain Approach . . . 104
A.7.3.3 Effective Stress Analysis . . . 104
A.8 Summary on the Literature Review . . . 105

B Starting Points Additional Information 107
B.1 Material Parameter Set for Plaxis 2D . . . 107
B.2 Natural Frequencies . . . 108

C Results Analysis SSI 113
C.1 Results Frequency Analysis . . . 113
C.2 Results Sensitivity Analysis . . . 134

D Verification Python Code 135
D.1 Verification Case 1: 1D Radial Consolidation . . . 135
D.2 Verification Case 2: 2D Radial Consolidation . . . 137
D.3 Verification Case 3: 2D Radial Consolidation . . . 140
D.4 Verification Case 4: Simulation of a CDSS test . . . 143

E Additional Information Case Study Oostpolderdijk 147
E.1 CPT Oostpolderdijk inner berm . . . 149
E.2 Geotechnical Parameters . . . 150
E.3 Construction Phases . . . 153

List of Figures

2.1 Loading scenarios associated with onshore wind turbines, after Seymour (2018). 6
2.2 Failure mechanisms of a dike including a shallow foundation, adapted from Ministerie van Verkeer en Waterstaat (2007) 6
2.3 Pore pressure development due to cyclic shearing, from de Groot et al. (2006) 7
2.4 Effective stress and shear strains due to cyclic shearing, from de Groot et al. (2006) . . 7
2.5 Liquefaction curve of the 'wadzand'-layer and Ottawa sand 8
2.6 Terzaghi's problem representing an oedometer test, after Verruijt (2013) 9

3.1 Location of the Oostpolderdijk case study indicated by the red arrow. 13
3.2 Simplified soil profile. 14
3.3 The horizontal (left) and embankment geometry (right) including the turbine tower height and rotor circumference dimensions to scale. 15
3.4 Geometry with horizontal surface, liquefiable soil layer between -7.5 m and -13 m below surface 15
3.5 Realistic geometry, liquefiable soil layer between -7.5 m and -13 m below NAP 16
3.6 CSR of Wadzand (various σ'_{v0} and e_0, from Tasiopoulou et al. (2019)) and dense Ottawa Sand ($\sigma'_{vc} = 100\ kPa$, from Parra Bastidas (2016)) 17
3.7 Particle Size Distribution of Ottawa Sand (adopted from Parra Bastidas (2016)) and Wadzand (adopted from Tasiopoulou et al. (2019)) 18
3.8 CSR of dense Ottawa Sand ($D_r = 0.67\%$, adopted from Parra Bastidas (2016)) 18
3.9 Loading signal at 0.3 Hz in time domain 20
3.10 Signal in frequency domain 20
3.11 Quasi-static multiplier of the loads on top of the foundation 20
3.12 Influence of the shear wave velocity and damping on the amplification factor of a linear elastic soil layer (Equation B.1) 21
3.13 Medium mesh grid 22
3.14 Fine mesh grid 22
3.15 Locally refined mesh grid 22

4.1 CSR contour plot, Mohr-Coulomb, quasi-static 27
4.2 CSR profile at x = 0m, MC, dynamic 27
4.3 CSR profile at x = 0m, MC, dynamic with 2% Rayleigh Damping 27
4.4 CSR profile at x = 13m, MC, dynamic 28
4.5 CSR profile at x = 13m, MC, dynamic with 2% Rayleigh Damping 28
4.6 CSR profile at x = 18m, MC, dynamic 28
4.7 CSR profile at x = 18m, MC, dynamic with 2% Rayleigh Damping 28
4.8 CSR profile at x = 0m, MC, dynamic with 5% Rayleigh Damping 28
4.9 CSR profile at x = 13m, MC, dynamic with 5% Rayleigh Damping 28
4.10 CSR profile at x = 18m, MC, dynamic with 5% Rayleigh Damping 29
4.11 CSR contour plot, Hardening Soil Small Strain, quasi-static 29
4.12 CSR profile at x = 0m, HSss, dynamic 30
4.13 CSR profile at x = 0m, HSss, dynamic with 2% Rayleigh Damping 30
4.14 CSR profile at x = 13m, HSss, dynamic 30
4.15 CSR profile at x = 13m, HSss, dynamic with 2% Rayleigh Damping 30
4.16 CSR profile at x = 18m, HSss, dynamic 30
4.17 CSR profile at x = 18m, HSss, dynamic with 2% Rayleigh Damping 30
4.18 CSR profile at x = 0m, HSss, dynamic with 5% Rayleigh Damping 31
4.19 CSR profile at x = 13m, HSss, dynamic with 5% Rayleigh Damping 31
4.20 CSR profile at x = 18m, HSss, dynamic with 5% Rayleigh Damping 31

4.21 CSR contour plot, quasi-static, HSss, 3D 32
4.22 CSR profile at x = 0m, HSss, 3D 32
4.23 CSR profile at x = 13m, HSss, 3D 32
4.24 CSR profile at x = 18m, HSss, 3D 32
4.25 Natural frequency for the embankment geometry 33
4.26 CSR contour plot, Hardening Soil Small Strain, quasi-static, embankment geometry 33
4.27 CSR profile at x = 37m, HSss, embankment geometry 34
4.28 CSR profile at x = 50m, HSss, embankment geometry 34
4.29 CSR profile at x = 55.5m, HSss, embankment geometry 34
4.30 Result sensitivity analysis, soil parameters HSss 35
4.31 Result sensitivity analysis, geometric features 35

5.1 Empirical relationship describing pore pressure development at various rates, from Seed and Rahman (1978) 40
5.2 Schematic representation of progressive built-up of excess pore pressure, from Taiebat (1999) 41
5.3 Schematic representation of a cylindrical coordinate system. 42
5.4 FDM grid and boundary conditions 42
5.5 CSR as a result of cyclic loading by a shallow foundation 43
5.6 De Leeuw's problem, from Verruijt (2013) 43
5.7 Result verification case 1: 1D radial consolidation in sand. $c_r = 0.001\ m^2/d$, $E_{oed} = 20.000$ kPa, k_r = $5.0 \cdot 10^{-7}$ m/d 44
5.8 Boundary conditions verification case 2 44
5.9 Result verification case 2: 2D radial consolidation in sand. $c_r, c_v = 0.001\ m^2/d$, $E_{oed} = 20.000$ kPa, k_r, k_v = $5.0 \cdot 10^{-7}$ m/d 44
5.10 Boundary conditions verification case 3 45
5.11 Result verification case 3: 2D radial consolidation in sand. $c_r, c_v = 0.001\ m^2/s$, $E_{oed} = 20.000$ kPa, k_r, k_v = $5.0 \cdot 10^{-7}$ m/d 45
5.12 Grid and boundary conditions CDSS. $L_r = 0.034\ m$ and $L_z = 0.0267\ m$ 45
5.13 CSR curve, determined in an experimental manner and in a numerical manner 46
5.14 Result CDSS test with CSR = 0.095, experimental and numerical 46
5.15 Visualization of the pore pressure development similar to the empirical curve 47
5.16 Visualization of the pore pressure development resembling a hyperbolic curve 47
5.17 Example of the pore pressure distribution through the liquefiable soil layer. t = 1 hour 47
5.18 Loading conditions as calculated in Chapter 4 48
5.19 Baseline grid 48
5.20 Variation in pore pressure development by changing the time step at the points assigned as in Figure 5.19. 49
5.21 Convergence at t = 1.5 h by varying the time step 49
5.22 Convergence at t = 80 h by varying the time step 49
5.23 Variation in pore pressure development by changing the mesh size 50
5.24 Convergence at t = 1.5 h 50
5.25 Convergence at t = 80 h 50
5.26 Variation in pore pressure development by changing the permeability. 51
5.27 Visualization of the harmonic mean 52
5.28 Visualization of the arithmetic mean 52
5.29 Variation in pore pressure development by changing the heterogeneity of the soil properties. 53
5.30 Variation in pore pressure development by changing the CSR. 53
5.31 Variation in pore pressure development by changing the loading frequency. 54

6.1 Overview of the method 58
6.2 Overview of the Plaxis model of the OPD case. The liquefiable soil layers are situated between the red lines 60
6.3 Result frequency analysis 61
6.4 Loading signal at 0.3 Hz in time domain 61

6.5 Signal in frequency domain 61
6.6 Envelope of the maximum CSR as a result of quasi-static loading at the during the final calculation phase. 62
6.7 σ_v' as a result of the quasi-static loading during the final calculation phase. 62
6.8 Result sensitivity analysis of the OPD case. The red line indicates the threshold value of the permeability for liquefaction. The reference parameter set of OPD is indicated by the blue dot. This case is the basis for the variation in soil parameters of a factor $\sqrt{2}$. . . 63
6.9 Result hand calculation of the factor of safety of the OPD case. 63
6.10 Results using Boulanger and Idriss (2014) for case OPD 65

A.1 Examples of old and new wind power: David (4.5 MW wind turbine, at that time (2017) largest in the Netherlands) and Goliath (old wind mill from 1897) at the Eemshaven. . . 79
A.2 Typical cyclic loads on an onshore wind turbine. After Seymour, 2018 80
A.3 Loading scenarios associated with onshore wind turbines. After Seymour (2018) 81
A.4 Shallow Foundations: a. Plain Slab, b. Stub and Pedestal, c. Tapered Slab and Stub. Adapted from Ashlock and Schaefer (2011) 82
A.5 Deep Foundations: a. Pile group with Cap, b. Solid Monopile, c. Hollow Monopile. After Ashlock and Schaefer (2011) 82
A.6 Failure mechanisms of a dike. After Ministerie van Verkeer en Waterstaat (2007) 83
A.7 Failure mechanisms of a dike including a shallow foundation. Adapted from Ministerie van Verkeer en Waterstaat (2007) 83
A.8 Contractive behaviour 84
A.9 Dilative behaviour 84
A.10 Critical state and state parameter concepts from Kramer (1996). Definition of the CSL depends on the author and parameters should be consistent with their corresponding definition. 85
A.11 Shear Modulus Reduction Curve with Strain Thresholds, from Diaz-Rodriguez and Lopez-Molina (2009) 86
A.12 Strain-stress hysteresis loop 86
A.13 Response to cyclic loading 86
A.14 Visualisation of Extended Masing Rules. (a) shows the variation of shear stress with time while (b) shows the corresponding stress-strain response, including the backbone curve. After Kramer(1996) 87
A.15 Cyclic loading scenarios including unbiased loading. After Randolph and Gourvenec (2011) 88
A.16 Flow failure near Kats in Zeeland, the Netherlands in 1966. From https://www.nationaalarchief.nl/ 88
A.17 Response of isotropically consolidated specimen of loose, saturated sand: (a) stress-strain curve; (b) effective stress path; (c) excess pore pressure; (d) effective confining pressure, after Kramer (1996). 89
A.18 Response of 5 isotropically consolidated specimen of loose, saturated sand with different state parameters. Adapted from Kramer (1996) 89
A.19 Flow liquefaction stress path for monotonic (A-B-C) and cyclic (A-D-C), after Kramer (1996). 90
A.20 Rigid body rotation of several residential buildings as a result of liquefaction due the 1964 Niigata Earthquake. 90
A.21 Three different cyclic loading scenario's, after Kramer (1996). 90
A.22 Relative state parameter definition and the effects of varying Q and R 94
A.23 Yield, critical, dilatancy and bounding lines in q-p space. Position of the dilatancy and bounding lines correspond with a dense-of-critical state of stress 94
A.24 Yield, critical, dilatancy and bounding surfaces in $r_{yy} - r_{xy}$ stress ratio plane with the yield surface, normal tensor, dilatancy back-stress ratio and bounding back-stress ratio. 95
A.25 Graphical representation of the modified Rowe's flow rule 96
A.26 Graphical representation of the yield and failure surfaces of UBC3D-PLM, from Winde (2015) 97
A.27 Terzaghi's problem representing an oedometer test, after Verruijt (2013) 98
A.28 Strain accumulation as a function of number of cycles. After Wichtmann et al. (2004) . . 100

A.29 Strain accumulation divided by the amplitude function. After Wichtmann et al. (2004) . . 100
A.30 Graphical method to identify zones of liquefaction. After Kramer (1996) 102

B.1 Influence of the shear wave velocity and damping on the amplification factor of a linear elastic soil layer (Equation B.1) 109
B.2 SDOF representation of a wind turbine, where m is the mass, c the damping ratio, k the stiffness and f(t) is a time dependent external force 109
B.3 2DOF representation of a wind turbine. Additional mass m_2 represents the foundation and the 77.3% of the tower. The foundation is connected to the soil using lumped parameters k and c to describe the stiffness and damping characteristics, respectively. . . 111

C.1 CSR contour plot, MC, quasi-static 113
C.2 CSR contour plot, MC, dynamic, load frequency of 0.3 Hz 113
C.3 CSR contour plot, MC, dynamic with 2% Rayleigh damping, load frequency of 0.3 Hz . 114
C.4 CSR contour plot, MC, dynamic with 5% Rayleigh damping, load frequency of 0.3 Hz . 114
C.5 CSR contour plot, HSss, quasi-static 114
C.6 CSR contour plot, HSss, dynamic, load frequency of 0.3 Hz 115
C.7 CSR contour plot, HSss, dynamic with 2% Rayleigh damping, load frequency of 0.3 Hz 115
C.8 CSR contour plot, HSss, dynamic with 5% Rayleigh damping, load frequency of 0.3 Hz 115
C.9 CSR contour plot, MC, quasi-static 116
C.10 CSR contour plot, MC, dynamic, load frequency of 0.3 Hz 116
C.11 CSR contour plot, MC, dynamic with 2% Rayleigh damping, load frequency of 0.3 Hz . 116
C.12 CSR contour plot, MC, dynamic with 5% Rayleigh damping, load frequency of 0.3 Hz . 117
C.13 CSR contour plot, HSss, quasi-static 117
C.14 CSR contour plot, HSss, dynamic, load frequency of 0.3 Hz 117
C.15 CSR contour plot, HSss, dynamic with 2% Rayleigh damping, load frequency of 0.3 Hz 118
C.16 CSR contour plot, HSss, dynamic with 5% Rayleigh damping, load frequency of 0.3 Hz 118
C.17 CSR contour plot, MC, quasi-static 118
C.18 CSR contour plot, MC, dynamic, load frequency of 0.3 Hz 119
C.19 CSR contour plot, MC, dynamic with 2% Rayleigh damping, load frequency of 0.3 Hz . 119
C.20 CSR contour plot, MC, dynamic with 5% Rayleigh damping, load frequency of 0.3 Hz . 119
C.21 CSR contour plot, HSss, quasi-static 120
C.22 CSR contour plot, HSss, dynamic, load frequency of 0.3 Hz 120
C.23 CSR contour plot, HSss, dynamic with 2% Rayleigh damping, load frequency of 0.3 Hz 120
C.24 CSR contour plot, HSss, dynamic with 5% Rayleigh damping, load frequency of 0.3 Hz 121
C.25 CSR contour plot, MC, dynamic, load frequency of 0.1 Hz 122
C.26 CSR contour plot, MC, dynamic, load frequency of 0.3 Hz 122
C.27 CSR contour plot, MC, dynamic, load frequency of 1.0 Hz 122
C.28 CSR contour plot, MC, dynamic, load frequency of 2.0 Hz 123
C.29 CSR contour plot, MC, dynamic, load frequency of 5.0 Hz 123
C.30 CSR contour plot, HSss, dynamic, load frequency of 0.1 Hz 123
C.31 CSR contour plot, HSss, dynamic, load frequency of 0.3 Hz 124
C.32 CSR contour plot, HSss, dynamic, load frequency of 1.0 Hz 124
C.33 CSR contour plot, HSss, dynamic, load frequency of 2.0 Hz 124
C.34 CSR contour plot, HSss, dynamic, load frequency of 5.0 Hz 125
C.35 CSR contour plot, MC, dynamic with 2% Rayleigh damping, load frequency of 0.1 Hz . 126
C.36 CSR contour plot, MC, dynamic with 2% Rayleigh damping, load frequency of 0.3 Hz . 126
C.37 CSR contour plot, MC, dynamic with 2% Rayleigh damping, load frequency of 1.0 Hz . 126
C.38 CSR contour plot, MC, dynamic with 2% Rayleigh damping, load frequency of 2.0 Hz . 127
C.39 CSR contour plot, MC, dynamic with 2% Rayleigh damping, load frequency of 5.0 Hz . 127
C.40 CSR contour plot, HSss, dynamic with 2% Rayleigh damping, load frequency of 0.1 Hz 127
C.41 CSR contour plot, HSss, dynamic with 2% Rayleigh damping, load frequency of 0.3 Hz 128
C.42 CSR contour plot, HSss, dynamic with 2% Rayleigh damping, load frequency of 1.0 Hz 128
C.43 CSR contour plot, HSss, dynamic with 2% Rayleigh damping, load frequency of 2.0 Hz 128
C.44 CSR contour plot, HSss, dynamic with 2% Rayleigh damping, load frequency of 5.0 Hz 129
C.45 CSR contour plot, MC, dynamic with 5% Rayleigh damping, load frequency of 0.1 Hz . 130

C.46 CSR contour plot, MC, dynamic with 5% Rayleigh damping, load frequency of 0.3 Hz . 130
C.47 CSR contour plot, MC, dynamic with 5% Rayleigh damping, load frequency of 1.0 Hz . 130
C.48 CSR contour plot, MC, dynamic with 5% Rayleigh damping, load frequency of 2.0 Hz . 131
C.49 CSR contour plot, MC, dynamic with 5% Rayleigh damping, load frequency of 5.0 Hz . 131
C.50 CSR contour plot, HSss, dynamic with 5% Rayleigh damping, load frequency of 0.1 Hz 131
C.51 CSR contour plot, HSss, dynamic with 5% Rayleigh damping, load frequency of 0.3 Hz 132
C.52 CSR contour plot, HSss, dynamic with 5% Rayleigh damping, load frequency of 1.0 Hz 132
C.53 CSR contour plot, HSss, dynamic with 5% Rayleigh damping, load frequency of 2.0 Hz 132
C.54 CSR contour plot, HSss, dynamic with 5% Rayleigh damping, load frequency of 5.0 Hz 133
C.55 CSR profile at x = 37 m, varying G_0 134
C.56 CSR profile at x = 37 m, varying ϕ 134
C.57 CSR profile at x = 50 m, varying G_0 134
C.58 CSR profile at x = 50 m, varying ϕ 134
C.59 CSR profile at x = 55 m, varying G_0 134
C.60 CSR profile at x = 55 m, varying ϕ 134

D.1 De Leeuw's problem, from Verruijt (2013) 135
D.2 Grid and boundary conditions to model De Leeuw's problem using the FDM 136
D.3 Pore pressure development at z = 1/2 of the height of the soil sample, $T_v = c_r t/a^2$ . . . 136
D.4 Pore pressure development at the center of the sample, r = 0. $c_r = 0.001\ m^2/d$, $E_{oed} = 20.000$ kPa, k_r = $5.0 \cdot 10^{-7}$ m/d 136
D.5 Pore pressure development at the center of the sample, r = 0. $c_r = 100\ m^2/d$, $E_{oed} = 20.000$ kPa, k_r = 0.05 m/d 137
D.6 Pore pressure development at the center of the sample, r = 0. $c_r = 2000\ m^2/d$, $E_{oed} = 20.000$ kPa, k_r = 1 m/d 137
D.7 Boundary conditions verification case 2 137
D.8 Pore pressure development at the center of the sample, r = 0 m, z = 4 m. $c_r = c_v = 0.001\ m^2/d$, $E_{oed} = 20.000$ kPa, k_r, k_v = $5.0 \cdot 10^{-7}$ 138
D.9 Contour plot excess pore pressures at t = 0 d 138
D.10 Contour plot excess pore pressures at t = 100 d 138
D.11 Contour plot excess pore pressures at t = 1000 d 138
D.12 Contour plot excess pore pressures at t = 10000 d 138
D.13 Pore pressure development at the center of the sample, r = 0 m, z = 4 m. $c_r = c_v = 100\ m^2/d$, $E_{oed} = 20.000$ kPa, k_r, k_v = 0.05 m/d 139
D.14 Contour plot excess pore pressures at t = 0 d 139
D.15 Contour plot excess pore pressures at t = 0.001 d 139
D.16 Contour plot excess pore pressures at t = 0.01 d 139
D.17 Contour plot excess pore pressures at t = 0.1 d 139
D.18 Pore pressure development at the center of the sample, r = 0 m, z = 4 m. $c_r = c_v = 2000\ m^2/d$, $E_{oed} = 20.000$ kPa, k_r, k_v = 1 m/d 140
D.19 Contour plot excess pore pressures at t = 0 d 140
D.20 Contour plot excess pore pressures at t = 0.00001 d 140
D.21 Contour plot excess pore pressures at t = 0.0001 d 140
D.22 Contour plot excess pore pressures at t = 0.001 d 140
D.23 Boundary conditions verification case 3 141
D.24 Pore pressure development at the center of the sample, r = 0 m, z = 4 m. $c_r = c_v = 0.001\ m^2/d$, $E_{oed} = 20.000$ kPa, k_r, k_v = $5.0 \cdot 10^{-7}$ 141
D.25 Contour plot excess pore pressures at t = 0 d 141
D.26 Contour plot excess pore pressures at t = 100 d 141
D.27 Contour plot excess pore pressures at t = 1000 d 141
D.28 Contour plot excess pore pressures at t = 10000 d 141
D.29 Pore pressure development at the center of the sample, r = 0 m, z = 4 m. $c_r = c_v = 100\ m^2/d$, $E_{oed} = 20.000$ kPa, k_r, k_v = 0.05 m/d 142
D.30 Contour plot excess pore pressures at t = 0 d 142
D.31 Contour plot excess pore pressures at t = 0.001 d 142
D.32 Contour plot excess pore pressures at t = 0.01 d 142

D.33 Contour plot excess pore pressures at t = 0.1 d 142
D.34 Pore pressure development at the center of the sample, r = 0 m, z = 4 m. $c_r = c_v = 2000\ m^2/d$, $E_{oed} = 20.000$ kPa, k_r, k_v = 1 m/d 142
D.35 Contour plot excess pore pressures at t = 0 d 143
D.36 Contour plot excess pore pressures at t = 0.00001 d 143
D.37 Contour plot excess pore pressures at t = 0.0001 d 143
D.38 Contour plot excess pore pressures at t = 0.001 d 143
D.39 Result of CSR curve for experimental and numerical tests 143
D.40 Pore pressure development for experimental and numerical test, CSR = 0.075 144
D.41 Pore pressure development for experimental and numerical test, CSR = 0.08 144
D.42 Pore pressure development for experimental and numerical test, CSR = 0.085 144
D.43 Pore pressure development for experimental and numerical test, CSR = 0.095 144
D.44 Pore pressure development for experimental and numerical test, CSR = 0.105 144
D.45 Pore pressure development for experimental and numerical test, CSR = 0.115 144
D.46 Pore pressure development for experimental and numerical test, CSR = 0.12 144
D.47 Pore pressure development for experimental and numerical test, CSR = 0.125 144
D.48 Pore pressure development for experimental and numerical test, CSR = 0.13 145
D.49 Pore pressure development for experimental and numerical test, CSR = 0.15 145

E.1 CPT at project location 149
E.2 Correlation Benz (2007) 151
E.3 Correlation Brinkgreve et al. (2010) 151
E.4 Correlation CUR162 152
E.5 Correlation Jamiolkowski et al. (2001) 152
E.6 Correlation Lunne and Christoffersen (1983) 152
E.7 Correlation Plaxis (2019b) 153
E.8 Case study phase 1: initial conditions 153
E.9 Case study phase 2: old dike 153
E.10 Case study phase 3: new dike 1977 154
E.11 Case study phase 4: current situation 154
E.12 Case study phase 5: installation turbine 154
E.13 Case study phase 6: consolidation 155
E.14 Case study phase 7: user phase, average forces 155
E.15 Case study phase 8: user phase, largest loads 155
E.16 Case study phase 8: user phase, smallest loads 156

List of Tables

3.1 Wadzand volumetric weight and strength parameters 17
3.2 Static loads induced by the wind turbine at top of the foundation (Arcadis, 2019) 19
3.3 Mohr-Coulomb parameters preliminary analysis 22
3.4 Influence of mesh size 22
3.5 Maximum element height for various loading frequencies 23

5.1 Soil parameters consolidation equation 48
5.2 Numerical and liquefaction parameters consolidation equation 49
5.3 Various permeability and consolidation coefficients 50
5.4 Soil properties weighted means 52
5.5 Heterogeneous soil conditions 52
5.6 Upper and lower limits of the CSR 53
5.7 Upper and lower limits of the CSR 54

6.1 Frequency analysis input parameters wind turbine 61
6.2 Quasi-static loads OPD 61
6.3 Liquefaction and permeability parameters OPD 62
6.4 Local MSF parameter determination 64

B.1 Linear Elastic parameters 107
B.2 Mohr-Coulomb parameters 107
B.3 Hardening Soil Small Strain parameters 108
B.4 Elastic Plate parameters 108
B.5 Input analysis natural frequency 111
B.6 Input analysis natural frequency 111
B.7 Results natural frequencies for a SDOF and 2DOF schematization 112

E.1 Material parameters OPD - 1 150
E.2 Material parameters OPD - 2 150
E.3 Material parameters OPD - 3 151

Symbols

a_{max}	Maximum acceleration [m/s^2]
a	CSR curve fitting parameter [-]
b	CSR curve fitting parameter [-]
c	Cohesion [kN/m^2]
c_{tower}	Damping ratio of the tower [-]
c_r	Correction factor between CTX and CDSS tests [-]
c_v	Consolidation coefficient [m^2/d]
d	Thickness [m]
D	Embedment depth [m]
D_r	Relative density [-]
e	Void ratio [-]
e_c	Critical void ratio [-]
e_{min}	Minimum void ratio [-]
e_{max}	Maximum void ratio [-]
E	Young's modulus [kN/m^2]
E_{50}^{ref}	Secant stiffness at 50% of the maximum stiffness [kN/m^2]
E_{oed}^{ref}	Oedometer stiffness [kN/m^2]
E_{ur}^{ref}	Unload/reload stiffness [kN/m^2]
EA_1	Normal stiffness [kN/m]
EI	Bending stiffness [kNm^2/m]
f	Frequency [Hz]
FS_L	Factor of safety against liquefaction [-]
F_H	Horizontal force [kN]
F_V	Vertical force [kN]
F_W	Amplification factor [-]
g	Gravitational acceleration [m/s^2]
G	Shear modulus [kN/m^2]
G_0	Maximum shear modulus [kN/m^2]
G_s	Specific gravity [kg/m^3]
H	Height soil layer [m]
i, j	Subscript, at location i or j
$i + 1, j + 1$	Subscript, at location i+1 or j+1
I_d	Relative density [-]
k	Equivalent horizontal flexural stiffness of the tower [kN/m]
k_r	Radial hydraulic conductivity [m/d]
k_v	Vertical hydraulic conductivity [m/d]
k_{eq}	Equivalent spring stiffness [kN/m]
k_l	Lateral spring stiffness [kN/m]
k_{rot}	Rotational spring stiffness [kNm/rad]
K_0	At-rest earth pressure coefficient [-]
K_a	Active earth pressure coefficient [-]
K_p	Passive earth pressure coefficient [-]
K_α	Correction factor of the influence of α on CRR [-]
L_r	Radial length [m]
L_{tower}	Length of the tower [m]
L_z	Vertical length [m]
m	Total mass of the wind turbine [ton]
m_{top}	Mass of the nacelle, blades and rotor of the wind turbine [ton]

m_{tower}	Total masss of the wind turbine tower [ton]
m_v	Confined compressibility [m^2/kN]
M	Bending moment [kNm]
N	Number of cycles [-]
N_l	Number of cycles until liquefaction [-]
N_{eq}	Equivalent number of cycles [-]
N_r	Radial number of elements [-]
N_z	Vertical number of elements [-]
n	Superscript, at time step n
$n+1$	Superscript, at time step n+1
p'	Average effective principal stress [kN/m^2]
q	Difference of principal stress [kN/m^2]
Q	Fit parameter for the critical state line [-]
r_d	Reduction factor over the depth [-]
r_{found}	Radius of the foundation [m]
r_{tower}	Inner radius of the tower [m]
r_u	Excess pore pressure ratio [-]
R	Fit parameter for the critical state line [-]
t_{wall}	Wall thickness of the tower [m]
T	Duration of calculation [day]
T_D	Duration of loading [day]
u	Water pressure [kN/m^2]
v_s	Shear wave velocity [m/s]
w	Weight [kN/m/m]
W	Width [m]
xx	Subscript indicating x direction
$x(t)$	Horizontal position [m]
yy	Subscript indicating y direction
zz	Subscript indicating z direction
α	Static shear stress ratio [-]
γ	Shear strain [-]
γ_s	Unit weight of the solid [kN/m^3]
γ_f	Unit weight of the pore fluid [kN/m^3]
γ_{sat}	Saturated unit weight [kN/m^3]
γ_{td}	Shear strain, degradation threshold [-]
γ_{tl}	Shear strain, linear threshold [-]
γ_{tv}	Shear strain, volumetric cyclic threshold [-]
γ_{unsat}	Unsaturated unit weight [kN/m^3]
$\gamma_{0.7}$	70% shear strain [-]
ϵ	Strain [-]
θ	Empirical fitting constant [-]
λ	Wave length [m]
λ_{CSL}	Slope of the critical state line [-]
ν	Poisson's Ratio [-]
ξ	Damping ratio [-]
$\rho_{d,d}$	Dry density, dense [kg/m^3]
$\rho_{d,l}$	Dry density, loose [kg/m^3]
σ	Total stress [kN/m^2]
σ_v	Vertical total stress [kN/m^2]
σ'	Effective stress [kN/m^2]
σ'_d	Effective bulk stress [kN/m^2]
σ'_{v0}	Initial vertical effective stress [kN/m^2]
τ	Shear stress [kN/m^2]
τ_{max}	Maximum induced shear stress [kN/m^2]
τ_s	Static shear stress [kN/m^2]
ϕ	Friction angle [deg]

ψ	State parameter [-]
ψ'	Dilatation angle $[\mathrm{deg}]$
Ψ	Arbitrary pore pressure generation function

1

Introduction

1.1. Research Motivation

The Netherlands are reducing the usage of fossil energy sources and transferring towards renewable energy sources. The National Climate Agreement (Rijksoverheid, 2019) states that the Netherlands is trying to reduce CO2 emissions with 49% by 2030 compared to the emission rate of 1990. The energy sector contributes to this goal by increasing the amount of renewable energy to a desired amount of 84 TeraWatt hour (TWh, $1TW = 10^{12}\ W$). The government has the ambition to produce 35 TWh on land using solar panels and wind turbines. In 2020, 6.000 MW is set to be available, produced by onshore wind turbines. The Energy Agreement (Sociaal-Economische Raad, 2013) includes agreements on the distribution and quantity of production were provinces have agreed to. Many areas surrounding flood defenses are potentially attractive locations for energy production as they often are further away from crowded areas and such locations are often good wind locations. However, the primary function of flood defenses is water safety and potential negative effects of wind turbines on this primary function are to be avoided. Rijkswaterstaat and Water Authorities (Waterschappen) agreed in the so-called “Green Deal Energie” (Union of Water Authorities and Rijkswaterstaat, 2011) to investigate the possibilities and prerequisites of wind turbines on or near flood defenses while maintaining water safety. A few years ago, Rijkswaterstaat changed its policy regarding the installation of wind turbines near flood defenses from ’No installation’ to ’No installation, unless’. Water Authorities are adopting this policy and are even shifting towards ’Yes, provided that’ (STOWA, 2018).

In the spirit of these recent developments, three 2.5 MW wind turbines will be installed on a primary sea dike in Groningen. The identification regarding the influence of the turbine foundations on the dike safety is a major aspect during the design stage. In here, the focus is on the influence of the turbine foundations on the onset of liquefaction of so-called “wadzand” layers, which consist of rather fine alternations of marine sands and clays. Liquefaction of a soil occurs as the effective stress is reduced to 0 kPa by an increase of pore water pressures and can be induced by either static loading (static liquefaction) or cyclic loading (cyclic mobility). This thesis is limited to liquefaction due to cyclic loading by an onshore wind turbine. Onshore wind turbines are slender structures with mass distributed along its height and a concentrated mass at the top and are excited by mainly mechanical and wind loads (seismic loads are not considered in this thesis). These loads result in cyclic loading of the soil supporting the turbine foundation. Cyclic loading might generate excess pore pressures and eventually result in liquefaction of the soil.

The influence of the onshore wind turbine on the liquefaction risk needs to be investigated by geotechnical engineers, to meet the above-mentioned ’Yes, provided that’-criteria. Currently, there are many (simplified) approaches to analyse the risk of liquefaction. One of these so-called “reference engineering methodology” is in line with the theory described by Kramer (1996):

1. Answering the question whether the soil is susceptible to liquefaction.
2. If the soil is susceptible, investigation whether liquefaction will be triggered by looking whether the

shear stress and shear strain mobilization are large enough to initiate static or cyclic liquefaction?

3. If liquefaction is triggered, assessment of damage to the dike and/or wind turbine. What is the residual strength of liquefied soil layers? Will this result in a settlement or stability problem?

Often, suitable laboratory tests to investigate all the required features as stated above are not available. The only investigations that generally are available are the more general geotechnical in-situ and laboratory tests. As a result, in most cases stress paths are not modelled and also consolidation is often not considered. This leads to the need of adopting conservative assumptions such as assuming that 'if pore pressures develop, liquefaction occurs'. In the present thesis, this methodology is referred to as 'reference engineering methodology' . Although this reference engineering methodology approach can be state of the art, it is considered to be conservative. However, the amount of conservatism is often not quantified.

1.2. Problem Statement

Earthquake and offshore engineering are disciplines that are required to account for cyclic loads and the potential of soil liquefaction. Both disciplines use experimental liquefaction curves to quantify the liquefaction resistance characteristics of the soil and are a basis for engineering methods to determine the effect of cyclic loading on the soil. Experimental liquefaction curves quantify the resistance of a soil to liquefaction by determining the number of cycles required to reach liquefaction by a given stress ratio. The curves are determined using various loading frequencies, usually between 0.1 Hz and 1 Hz. A loading frequency $\leq 1\ Hz$ has only minor effect on the cyclic strength during experimental tests ((Lee and Focht, 1975), (Tatsuoka et al.,1986)). The loading frequency of the wind turbine considered in this thesis is between 0.3 Hz and 0.4 Hz, therefore allowing for the use of the experimentally determined liquefaction curves. However, the drainage and loading conditions vary between earthquake engineering, offshore engineering and the current situation (cyclic loads due a onshore wind turbine). Each discipline has its own characteristic within certain 'key aspects' of liquefaction modeling and differs from the current situation. These key aspects can be described as:

- **Cyclic/Dynamic Loading**: Generally, loads are considered dynamic if their frequency of f $\geq$ 5 Hz (Wichtmann and Triantafyllidis, 2012) and are often applied during a short period of time. Earthquake engineering deals with type of loads where inertia forces are present in the soil. However, the loading frequency of the current situation is relatively low ($f \approx 0.3$ Hz) and more in line with loading frequencies in offshore engineering ($f \approx 0.1$ Hz (Randolph and Gourvenec, 2011)).
- **Soil-Structure Interaction** between the turbine foundation and the surrounding soil: Wind forces act on the wind turbine and are transferred through the foundation into the soil. The soil-structure interaction determines how much of the normal and shear stresses are transferred into the soil and result in excess pore pressures. Interaction between stresses induced by the foundation and the existing dike result in irregular modes of shearing in the soil. The stress conditions are due to a local loading phenomena unlike an earthquake load for earthquake engineering. Thereby, the stress conditions are different with respect to an ocean wave for offshore engineering.
- **Consolidation Behaviour**: Loading during undrained conditions results in the generation of excess pore pressures. Hydro-mechanical coupling of the pore water pressure and deformation of the soil is used to describe the process of dissipation of excess pore pressures and consequently the consolidation or deformation of the soil. Where earthquake engineering deals almost exclusively with undrained conditions due to the short loading time, offshore engineering deals with situations where dissipation of pore pressures can occur between loading cycles. Again, the current situation is more in line with the scenarios present in offshore engineering.

Differences in the conditions in which the various methods are applied ensure that the methods cannot be used one-to-one. In addition, the reference engineering methodology makes assumptions leading to conservative estimations. Therefore, the problem statement of this thesis is:

Using the reference engineering methodology, conservative assumptions are made with respect to loading type, soil-structure interaction and consolidation. As a result, the degree of conservatism is unknown.

1.3. Research Questions

The main objective of this research is: to formulate a methodology to model the key aspects of liquefaction of a soil layer underneath a dike system subjected to cyclic loading due to an onshore wind turbine. An underlying objective is the insight on the influence of conservative estimations made in the reference engineering methodology. A better understanding on how to model the key aspects of liquefaction behaviour is required so that limitations of the existing methods can be modified in order to meet the boundary conditions of the current situation. This also reduces the need to make conservative assumptions. The main research question is defined in order to solve the problem statement given in Section 1.2:

What is the best modelling strategy to simulate the key aspects of liquefaction of a soil layer underneath a dike system subjected to cyclic loading induced by an onshore wind turbine on a dike?

Sub-questions are formulated to divide the main research question into more specific questions related to individual components of the situation:
Pertaining to soil-structure interaction(SSI):

1. *How can time dependent shear stresses in the soil induced by an onshore wind turbine be modelled, taking into account the effect of SSI?*
2. *What is the influence of irregular modes of shearing in the soil on the liquefaction behaviour?*

With regard to consolidation behaviour:

3. *What is the influence of accounting for partial drainage response of the soil on the liquefaction behaviour?*

Related to the conservative assumptions of the existing methods:

4. *How do the conventional methods relate to the proposed model with regard to the assumed conservative assumptions?*

1.4. Research approach

The following approach is taken in the research to be able to answer the main and sub-questions. Each step of the research approach is described in one of the chapters.

1. A literature study is conducted covering a theoretic background on the subjects of the foundation, its superstructure and liquefaction phenomena. Various models are reviewed and elaborated from which a method is selected to investigate the main and sub research questions. The literature study is presented in chapter 2.
2. Starting points of the the situations investigated during the theoretical phase of the report are set-up. These situations consists of a situation with a horizontally layered soil and a situation where an embankment geometry is present on top of a horizontally layered soil. The soil, structure and load characteristics are based on a case study but are heavily simplified. The situations contain a liquefiable soil layer located deeper than the surface and is loaded by an onshore wind turbine founded on a shallow foundation. The starting points are presented in chapter 3.
3. An analysis of the time dependent stresses in the soil is performed to answer sub-questions 1 and 2. The statement that low frequency loads can be modeled as quasi-static is verified by performing a frequency analysis. Dynamic and quasi-static analysis are performed using the Mohr-Coulomb and Hardening Soil small strain soil models to investigate the influence of the respective type of load on the soil through soil-structure interaction. From the results of the analysis, the stress state of the soil can be determined which is required for the analysis of Chapter 5. The analysis on the time dependent stresses is presented in chapter 4.
4. The model presented by Seed and Rahman (1978) is implemented and verified using Python. An extension to radial conditions is made whereas the model is originally in 1D. This model is an extension of consolidation theory, allowing for dissipation and generation of excess pore pressures.

The model uses the cyclic stress ratio, as determined in chapter 4, to determine the quantity and location of generated excess pore pressures. A sensitivity analysis is performed to investigate the influence of the main parameters of the model. The results are presented in chapter 5.

5. Finally, the method as described in the previous chapters is applied to a case study situated in Groningen. Comparison is made with existing methods to determine the influence of partial drainage conditions which are included in the model elaborated in this thesis. The existing methods consist of the reference engineering methodology and Boulanger and Idriss (2014) with a modification to account for local loading. The results of the case study are presented in chapter 6.

2

Literature Review

Chapter 2 contains a summary of all relative aspects of the problem considered in this thesis. The main points of the literature study are used as a framework for the thesis. Considered aspects in the thesis are: wind turbines, dike design, liquefaction and consolidation. In addition, the relevant constitutive and numerical models which are used in the thesis are summarized.

2.1. Wind Turbines

Wind turbines are the main loading source which subject the embankment to cyclic loads. An understanding is required on how the time dependent nature of the loads on the wind turbine can be characterized and how they impact the soil. More information on the topic of wind turbines and their foundations are given in appendix A.1.

An onshore wind turbine is mainly loaded by wind and mechanical loads. Wind loads are mainly influenced by the wind speed. Mechanical loads are generated by rotating structural elements of the wind turbine, like the blades and nacelle. These loads can be summarized in three categories, making a distinction between external en internal loads. The loads are dependent on various aspects of the wind spectrum, like wind speed and direction. The loads are generally represented using a frequency band between the lowest and highest revolutions per minute (rpm) rather than a single frequency.

1. External load: an onshore wind turbine is only loaded by wind and its turbulence.
2. 1P loading: first excitation frequency due to revolutions of the rotor system. This load can be induced due to rotor imbalances, wind shear and tower shadow. Modern turbines have a characteristic range within the frequency spectrum where this forcing frequency is located.
3. 3P loading: second excitation frequency due to the passing of the blades, also called 2P when the wind turbine has 2 blades instead of 3. An internal load is generated when the blade passes in front of the tower tower and there is a temporary loss of wind load on the turbine tower (called blade shadowing effect).

Wind turbines are designed in order to avoid loading frequencies as they could result in resonance and instabilities. Figure 2.1 illustrates the source of two different soil-structure interaction situations associated with an onshore wind turbine on a shallow foundation, a fatigue type of problem and a resonance type of problem. Figure 2.1c shows a resonance type of problem where low amplitude vibrations are acting on the structure. The 1P and 3P ranges combined with the stiffness properties of the wind turbine, foundation and soil are important information in order to prevent resonance of the structure. However, large amplitude cyclic loads can lead to a fatigue-type of problem, as illustrated by Figure 2.1b.

Arany et al. (2015) shows that the 1P and 3P loading has little impact (>1%) on the fore-aft (forwards, afterwards) bending moment of an offshore wind turbine, but the low frequency fore-aft bending will result in cyclic shearing of the soil. The loading frequency of the onshore wind turbine from the case study is between 0.3-0.4 Hz. Wichtmann and Triantafyllidis (2012) indicates that dynamic problems can be modelled as quasi-static problem when the loading frequency is low, e.g. $f \leq 5$ Hz. Andresen (2015) states that environmental (wind and wave) loads on offshore wind turbines are around $f = 0.2 - 0.08$ Hz and inertia effects are negligible in the soil domain.

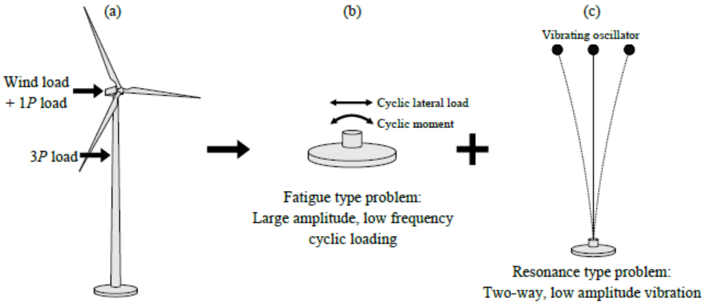
(a)
Wind load
+ 1P load
3P load
(b)
Cyclic lateral load
Cyclic moment
Fatigue type problem:
Large amplitude, low frequency
cyclic loading
(c)
Vibrating oscillator
Resonance type problem:
Two-way, low amplitude vibration

Figure 2.1: Loading scenarios associated with onshore wind turbines, after Seymour (2018).

2.2. Embankment Design

The wind turbine will be constructed on a primary embankment located in Groningen, the Netherlands. This section covers the potential failure mechanisms of an embankment including a shallow foundation. More information is given in appendix A.2.

A dike or an embankment can be defined as a man-made water retaining soil body situated on the border of land and water. The Netherlands has a system which separates the water defence system of dikes into primary and regionally dikes. The maintainer of primary dikes is obligated by law, the Dutch Water act, to report on the general state of the hydrological conditions of the primary flood defences every 12 years (Waterwet 2014). Several guidelines are available to assess the safety of the dikes, like the Voorschrift Toetsen op Veiligheid (VTV2006, (Ministerie van Verkeer en Waterstaat, 2007)) and the WBI 2017 (Rijkswaterstaat, 2017).

In terms of dike safety, wind turbines and their foundations are considered 'non-water retaining' objects (Dutch: 'niet-waterkerend' object). An 'non-water retaining' object is an object present in the flood defense system but does not contribute to the water retaining function of the system which is its primary function (Bizzarri and de Looff, 2000). Ministerie van Verkeer en Waterstaat (2007) categorises the turbine foundation as a type IV construction with respect to the water safety: a construction without any water retaining functions, but object potentially has a negative influence on the flood defense if it fails. The main principle of safety remains that the non-water retaining object is not allowed to influence the dike in any negative way. A detailed analysis on the influence of the non-water retaining object on the embankment is required when the influence zone of a non-water retaining object crosses the influence zone of the embankment. Potential failure mechanisms are given in figure 2.2. These include: excessive settlements, piping, inner and outer slope macro stability, static liquefaction and cyclic liquefaction. Cyclic liquefaction of the soil is of main interest in this thesis.

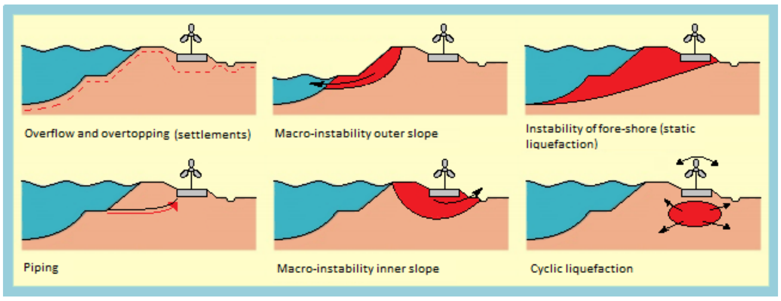
Overflow and overtopping (settlements)
Macro-instability outer slope
Instability of fore-shore (static liquefaction)
Piping
Macro-instability inner slope
Cyclic liquefaction

Figure 2.2: Failure mechanisms of a dike including a shallow foundation, adapted from Ministerie van Verkeer en Waterstaat (2007)

2.3. Cyclic Soil Behaviour and Liquefaction

Cyclic liquefaction is of main interest in this thesis. This section covers the soil mechanical principles which apply to soil subjected to cyclic loading. These include the response of soils to cyclic loading and the principles of liquefaction. More information is given in appendix A.3.

2.3.1. Cyclic Soil Behaviour

Soils are granular materials which can consist of multiple materials. As a result, soils have a distinctive type of material behaviour with respect to other materials, like steel. The soil behavior is dependent on the initial stress state and the incremental stress state due to loading. In addition, soil behaviour is caused by several characteristics. These include: the volumetric behaviour, multi-phase material behaviour, stress-dependent stiffness and plastic behaviour. The following section gives a brief definition of the various characteristics:

1. Volumetric behaviour. The volumetric behaviour of the soil and is dependent on the density of the soil specimen and the different responses during loading. A general distinction between 2 states is made: a loose and dense state. During shearing, the soil response will be contractive (loose state) or dilative (dense state). Negative or positive excess pore pressures develop during undrained loading, respectively.

2. Multi-phase material behaviour. Soils consist of a multi-phase composition of solid particles and water. Soil behaviour is dependent on the drainage response of the pore fluid inside of the soil. The drainage response is defined as drained when the pore fluid is able to move freely along the soil matrix. If the pore fluid is unable to move freely, due to fast loading conditions or low permeability of the soil, the drainage response is defined as undrained. Excess pore pressures dependent on the soil state are generated during an undrained response, as stated in the previous item. As a result, the effective stress changes along with the strength and stiffness of the soil.

3. Stress-dependent behaviour. The soil response is dependent on the stress and strain levels of the soil. A higher stiffness and strength of the soil is expected within the small strain and high stress levels.

4. Plastic behaviour: The soil behaves linearly below a plastic limit threshold and the energy from cyclic loads are dissipated by hysteresis loops. Plastic, or permanent, deformations occur if a soil is loaded beyond the threshold level. From this moment on, the soil structure becomes unstable and the above mentioned soil behaviour becomes dominant. Excess pore pressures are generated as the soil structure is degraded by cyclic loads.

Figures 2.3 and 2.4 illustrate the above mentioned aspects of soil behaviour. Pore pressures develop in the soil sample as a result of cyclic loading. In figure 2.3 it can be observed that the strains are large and increase with increasing pore pressures. At the same time, it is observed that the effective stress decreases towards 0 kPa (figure 2.4).

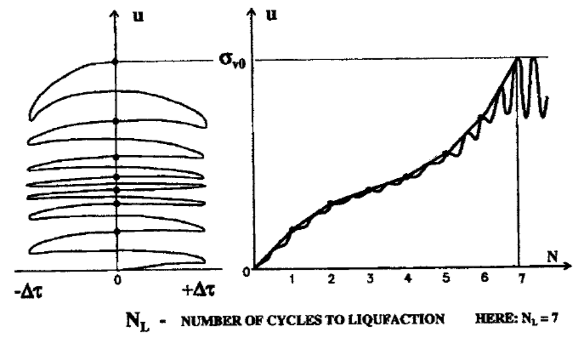

Figure 2.3: Pore pressure development due to cyclic shearing, from de Groot et al. (2006)

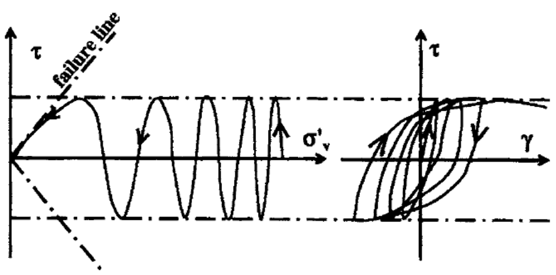

Figure 2.4: Effective stress and shear strains due to cyclic shearing, from de Groot et al. (2006)

2.3.2. Liquefaction

Liquefaction can be defined as ”the transformation of a granular material from a solid to a liquefied state as a consequence of increased pore-water pressure and reduced effective stress” by Youd et al. (October 2001). One can distinguish between static liquefaction and cyclic liquefaction. More information on both subjects is presented in appendix A.4. While static liquefaction can be a serious thread to the construction, it is not the focus of this thesis. The focus of the thesis is on cyclic liquefaction. More information and examples of both failure mechanisms are given in appendix A.4.

Cyclic liquefaction is caused by the repetitive loading of the soil. Essential to the initiation of liquefaction is the change in pore pressures which result in the change of effective stresses in the soil. Cyclic liquefaction is often associated with earthquake loads and their consequences. However, cyclic loads can also consist of traffic, industrial sources or wind and wave loads. The excess pore water pressures are generated as a result of the tendency of granular soils to compact when subjected to cyclic shear deformations but volumetric straining is prevented due to undrained conditions. This phenomena is presented in figure 2.3. As pore pressures rise further, the soil can reach the failure state which allows for the occurrence of large deformations. The latter is termed cyclic mobility. Cyclic mobility occurs after the initiation of liquefaction whereas the thesis is focused on the pore pressure development prior to the initiation of liquefaction. Plastic strains can already accumulate during this initial development of pore pressures.

The resistance of soils to liquefaction is often characterized using cyclic strength curves, or liquefaction curves (figure 2.5). The liquefaction curve relates the density, cyclic shear stress amplitude and number of cycles until cyclic liquefaction. The liquefaction curve is normalized using the initial effective stress (σ'_{v0}) of the soil. This results in the Cyclic Shear Ratio (CSR, equation A.4 (Kramer, 1996), (Randolph and Gourvenec, 2011). A soil loaded by a high CSR requires less cycles until liquefaction compared to a soil loaded by a low CSR. $\Delta\tau_{cyc}$ is the single amplitude of the shear stresses of a full load cycle. It can be determined by calculating the average of the shear stress during the maximum and minimum shear load of a full cycle.

$$CSR = \frac{\Delta\tau_{cyc}}{\sigma'_{v0}} = \frac{(\tau_{max} - \tau_{min})/2}{\sigma'_{v0}} \tag{2.1}$$

The cyclic liquefaction curves can be produced by laboratory tests, such as the cyclic direct simple shear test (CDSS), cyclic triaxial test (CTX) or cyclic torsional test.

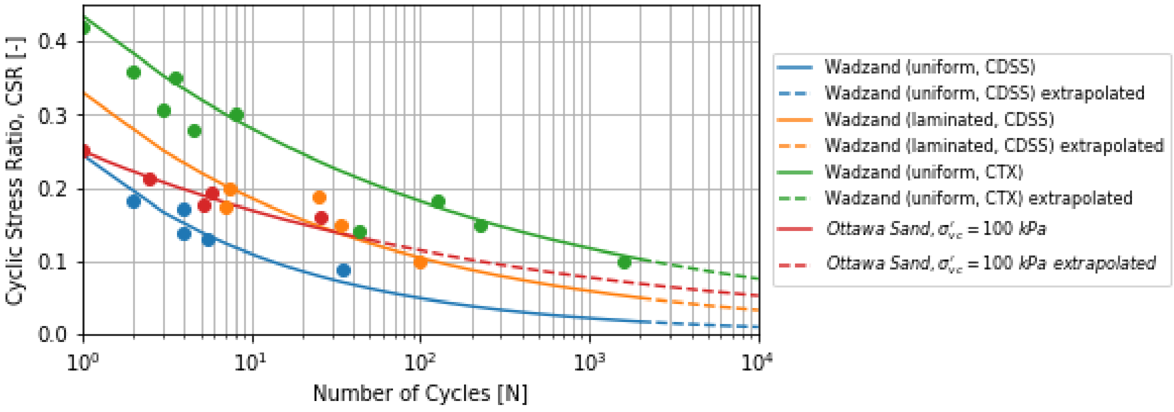

Figure 2.5: Liquefaction curve of the ’wadzand’-layer and Ottawa sand

2.4. Consolidation

The distribution of excess pore pressures can be described using consolidation theory. Consolidation can be described as the coupled response of deformation and groundwater flow of a saturated soil due to a change of stress conditions. A brief summary is presented below, more information is presented in appendix A.6.

The consolidation process is driven by a change of stress conditions in the soil, which influence the effective stresses. Changed stress conditions can occur because of external loading, (re-)distribution of pore pressures, change in geometry, degradation of stiffness or chemical/biological activity. The time required to reach the final steady state pore pressure (fully consolidates situation) is dependent on the characteristics of a geotechnical system, see equation 2.3. Volume changes due to external changes are prevented by the (relatively) incompressible pore water fluid resulting in an undrained soil response and generation of excess pore pressures. The external load is initially fully carried by the pore fluid but gets transferred to the soil skeleton when the excess water pressure dissipates due to consolidation. The flow of water and thus the rate of dissipation of excess pore pressures is, amongst others, controlled by the hydraulic conductivity and the stiffness of the soil.

The simplest consolidation problem is a one-dimensional situation and resembles an oedometer test (figure 2.6). This classic problem was formulated by Terzaghi et al. (1925) and studied and discussed often, like in Verruijt (2013).

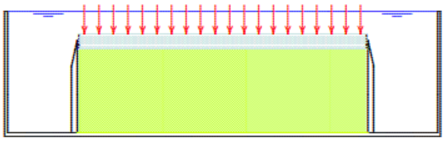

Figure 2.6: Terzaghi's problem representing an oedometer test, after Verruijt (2013)

Terzaghi's classic 1D formulation starts from the mass conservation equation for porous media and assumes a constant load on a homogeneous material:

$$\frac{\partial u}{\partial t} = c_v \frac{\partial^2 u}{\partial z^2} \tag{2.2}$$

with

$$c_v = \frac{k}{\gamma_f m_v} \tag{2.3}$$

where c_v is the consolidation coefficient, k is the hydraulic conductivity, γ_f is the unit weight of the pore fluid and $m_v = 1/E_{oed}$ is the confined compressibility of the soil.

2.5. Constitutive Soil Models

Various methods are available to model the main aspects of soil behaviour, liquefaction and consolidation. An effective stress analysis, used within the various engineering disciplines as described in section 2.6, can be performed using a Finite Element Analysis (FEA). The quality of the FEA is largely dependent on the quality and capabilities of the constitutive models. Constitutive models are mathematical tools to simulate the stress-strain behavior of soils.

Constitutive models can be formulated in terms of total effective stresses and strains, incremental effective stresses, and strains and in terms of infinitesimal increments. Also, material models can be formulated in terms of total stresses and strains instead of effective stresses and strains. Below we consider effective stress type constitutive models and discuss their potential with respect to the potential methods. More information on the considered model that are not included are given in appendix A.5. The following constitutive models are considered:

1. Hooke's Law
2. Linear-Elastic Perfectly-Plastic model (Mohr-Coulomb model)
3. Hardening Soil Small strain
4. PM4Sand

5. UBC3D-PLM
6. Hypoplastic model

2.5.1. Linear-Elastic Perfectly-Plastic model (Mohr-Coulomb model)

The Mohr-Coulomb model (MC) combines the Mohr-Coulomb failure criterion with Hooke's law into a linear elastic perfectly-plastic stress-strain relationship (Plaxis (2019a)). The MC model is straightforward and in many cases it provides a sufficiently good representation of soil behaviour. Also, the failure behavior during drained conditions is good and dilatancy can be included by adapting the dilatancy angle. However, there are several disadvantages of the model: the stiffness is constant, resulting in stress-independency of the stiffness and no distinction between primary and unloading/reloading. In undrained conditions, stress paths are not modelled realistically, and the shear strength can be overestimated. Finally, the MC model is not based on the critical state concept (Brinkgreve, 2019).

The MC model gives a good first estimation of the soil behaviour. Unlike the LE model, the MC model is able to calculate plastic strains in the soil. The loading path is ruled by the cyclic loading which is not accurately incorporated into the model. The model is also not able to calculate the accumulation of strains or pore pressures. However, the model only has a minimum of 4 required parameters and gives a good estimate of the constitutive behaviour of the soil. The model can be used to determine the CSR as a results of cyclic loading and soil-structure interaction, see chapter 4

2.5.2. Hardening Soil Small Strain

The Hardening Soil model with small-strain stiffness (HSsmall) is a modification on the Hardening Soil (Schanz et al. (1999)) model. The HS model is an advanced soil model which is based on the MC model but takes the stress-dependency of the stiffness modulus into account. This results in an increase of stiffness with an increase of effective pressure. Also, the initial conditions of the soil can be taken into account. The HSsmall takes the higher small strain stiffness at small strains into account (degradation curve). The HSsmall model leads to hysteretic material damping during stress reversals. However, HSsmall model does not take softening into account during cyclic loading. Neither are plastic volumetric strain accumulation or pore pressure accumulation incorporated as the HSss only models one hysteresis loop (Brinkgreve, 2019).

The Hardening Soil small strain model gives a more accurate representation of the stresses and strain in the soil compared to the Mohr-Coulomb model. Stress dependency of the model is essential for the considered situation where various stress conditions are present. In addition, the model takes the unloading-reloading behaviour of the soil into better account. A minimum of 6 parameters are required for the model. The model can be used to determine the CSR as a results of cyclic loading and soil-structure interaction, see chapter 4.

2.5.3. Various Models

The other models considered are: Linear-Elastic (LE) model, PM4Sand, UBC3D-PLM and hypo-plasticity. Background information on the models is given in appendix A.5.

The LE model oversimplifies the soil behaviour, as well as the expectation that the soil will deform plastic. Literature indicates that loads applicable in the considered scenario are probably cyclic of nature, thus not dynamic. Chapter 4 will go further into this. Therefore, the LE model will not be used.

The PM4Sand and UBC3D-PLM models are both capable of modelling the accumulation of pore pressures. PM4Sand is a stress-ratio controlled, critical state compatible, bounding surface plasticity model for sand. The model consists of 3 primary parameters an 20 secondary parameters based on default correlations. UBC3D-PLM is an elastoplastic model using isotropic and simplified hardening rules for primary and secondary yield surfaces. The model consists of 10 parameters. Both models require an extensive calibration procedure to calibrate the parameters to element tests. Required laboratory tests include undrained cyclic triaxial and cyclic direct simple shear tests. The required laboratory investigation is not available by which the models can not be used.

Finally, the hypo-plastic model is considered. The model gives a good estimation of the accumulated pore pressures but required additional parameters to do so. These parameters are do not have a clear physical meaning, are difficult to determine and the experimental tests are prone to errors. Therefore, this model will not be used.

2.6. Various Approaches to Liquefaction Modelling

This section describes the various approaches which have been considered to be used for the modelling of liquefaction phenomena surrounding the wind turbine. The following approaches are elaborated:

1. Reference Engineering Methodology
2. Earthquake Engineering
3. Offshore Engineering

2.6.1. Reference Engineering Methodology

The method which is referred to as (see chapter 1) the reference engineering methodology combines several theories on soil mechanics and liquefaction behavior. Further information is given in appendix A.7.1. The approach is developed by Arcadis to give a sound advice on the liquefaction potential using limited available information. This method is the baseline approach containing conservative estimations to which the proposed method of this thesis will be compared.

The method has the following limitations:

- The drainage response of the soil is fully undrained.
- Exceeding the threshold value will lead to full liquefaction. No intermediate stages of pore pressure development are considered.
- The test results, on which the method is based, are obtained by testing an uniform medium sand. A site-specific material is not considered as the desired experimental data is unavailable.

2.6.2. Offshore Engineering

Offshore engineering has many types of calculation approaches for different situations such as instantaneous liquefaction due to wave action, cyclic loaded structures, negative instantaneous liquefaction due to dredging and wave induced residual pore pressures (de Groot et al. (2006)). The method developed by Seed and Rahman (1978) is focused on the analysis of liquefaction due to wave-action.

The model consists of an extension to the consolidation equation (section 2.4). A generation component is added the consolidation equation to account for the pore pressure generation. The derivation of the generation component is presented in appendix A.7.2. The consolidation equation allows for dissipation between loading steps resulting in partial drainage conditions. The pore pressure generation is based on an empiric relationship which relates the rate of pore pressure generation to the cyclic resistance of the soil. The original approach assumes 1D vertical consolidation behaviour of the soil. The cyclic stresses induced by wave-action are derived from linear wave theory.

The loading frequency and duration due to wave-action as described by Seed and Rahman (1978) are similar to the frequency and duration of a storm event as presented in this thesis. In order to be able to apply the method to the current situation several modifications are required to be made. The CSR needs to be determined as a result of cyclic wind turbine loads as well as the modification of the direction of pore pressure dissipation. 2D cylindrical coordinates are implemented as consolidation in all directions is expected. CSR will be determined using the MC and HSss models. The model will be implemented using a finite difference scheme in Python. In addition, the model accounts for various aspects of the problem such as the pore pressure accumulation over time, the liquefaction resistance of the soil and loading characteristic. This is further elaborated in chapter 5.

The method has the following limitations:

- The model simulates the accumulation of residual pore pressures but does not account for the constitutive behaviour of the soil due to cyclic loading. However, residual excess pore pressures are due to plastic deformations of the soil skeleton (de Groot et al. (2006)). Plastic strains are part of the physics of liquefaction, but cannot be determined using this method.
- The liquefaction curves are extrapolated to the desired number of cycles as the available test results do not reach the desired number of cycles. It is assumed that the liquefaction curves are smooth based on experimental curves which reach a high number of cycles.
- The model does not take into account the initial state of the soil. It is assumed that the external loading results in positive excess pore pressures.

2.6.3. Earthquake Engineering

Analysis approaches within earthquake engineering are subdivided into three categories: the cyclic stress method, the cyclic strain method and the effective stress analysis. The most well known approach within the cyclic stress method is presented by Boulanger and Idriss (2014). Further imformation on the method is presented in Appendix A. The method compares the driving and resisting forces in the soil subjected to earthquake loads and determines a factor of safety. Boulanger and Idriss (2014) uses a comprehensive data base to correlate the resistance characteristics of the soil to CPT and SPT results. The cyclic strain approach follows a similar approach, but uses strains rather than stresses to determine the factor of safety. The cyclic strain method is not applied as the method is not widely used and the required data is lacking. Finally, effective stress analysis are preformed to determine the stresses and strains in the soil as a result of earthquake loading. The effective stress analysis is seen as highly potential but, as stated in section 2.5, extensive laboratory investigation is missing to calibrate the required constitutive models.

It is noted that the cyclic stress method by Boulanger and Idriss (2014) is developed for applications where earthquake loads are present. Earthquake loads have a significantly shorter duration (seconds or minutes) and thus lower amount of cycles compared to the current situation. Thereby, the frequency of the loading signal differs greatly. Despite these differences, the cyclic stress method is used for synthesis of the proposed method within the conventional methods since a better matching method are not available. Some adjustments have been implemented to the earthquake approach to make it more applicable to the current situation. The CSR is determined using the MC and HSss soil models in Plaxis 2D. The magnitude scaling factor is determined for a situation with a large number of cycles using the definition of the magnitude scaling factor based on the number of cycles as elaborated in Appendix A of Boulanger and Idriss (2014). This is further elaborated in chapter 6.

The method has the following limitations:

- Only cases which are loaded by an earthquake are collected in the database which forms the backbone of the correlations. These loads are relatively short in duration and contain a high frequency spectrum which is the opposite of the current situation.
- Situations deviating from the collected database require extrapolation which can result in spurious results. The proposed CSR determination does not depend on a (simplified) procedures, but is obtained from constitutive calculations. Therefore, it is assumed that the CSR determination is accurate. However, the modification of the magnitude scaling factor is based on a theoretic concept but has not been validated for the number of cycles to which it is applied.

3

Starting Points

In this chapter, the theoretic scenarios are introduced which are used to perform the calculations on the influence of the soil-structure interaction and the consolidation behaviour (chapter 4 and 5, respectively). The theoretic scenarios are simplified scenarios of the project Oostpolderdijk (hereafter indicated as OPD). Three wind turbines with an individual capacity of 2.5 MW will be installed the OPD in Groningen, see figure 3.1.

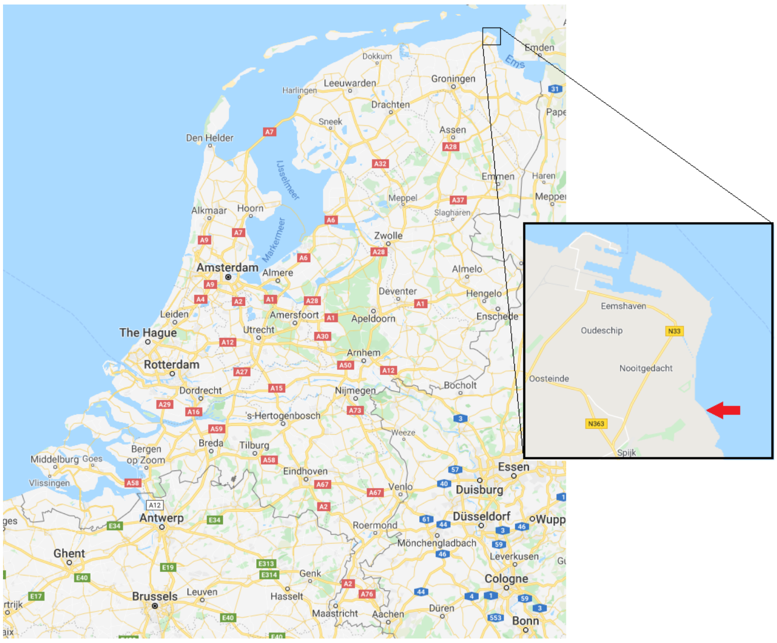
Emden
Dokkum
Groningen
Leeuwarden
Harlingen
Drachten
Sneek
Assen
Den Helder
Emmen
Haren
Meppel
Alkmaar
Hoorn
Zwolle
Amsterdam
Almere
Almelo
Deventer
Hengelo
Leiden
Amersfoort
Apeldoorn
Enschede
The Hague
Utrecht
Arnhem
Rotterdam
Dordrecht
Nijmegen
Bocholt
's-Hertogenbosch
Breda
Tilburg
Bergen op Zoom
Middelburg
Goes
Vlissingen
Eindhoven
Venlo
Essen
Duisburg
Antwerp
Düsseldorf
Roermond
Mönchengladbach
Ghent
Genk
Leverkusen
Brussels
Leuven
Hasselt
Cologne
Maastricht
Aachen
Düren
Bonn
Eemshaven
Oudeschip
Nooitgedacht
Oosteinde
Spijk
N33
N363

Figure 3.1: Location of the Oostpolderdijk case study indicated by the red arrow.

The situation present at OPD has been simplified as much as possible to minimize the influence of complex geometries and different soil layers. For this reason, two simplified geometries have been created: horizontal surface with layered soil profile (scenario 1) and a dike geometry with layered soil (scenario 2). Scenario 1 is introduced in order to perform analysis without the influence of the dike geometry on the stresses in the soil. Scenario 2 is introduced to perform analysis with the influence of the dike geometry on the stresses in the soil but without making the soil profile unnecessary complex. For this thesis, a shallow foundation is considered as it is expected that this foundation type will lead to a maximum impact on the liquefaction risk. A shallow foundation consists of a single element to transfer loads into the soil, whereas a piled foundation can consists of multiple interacting elements. Therefore, it seems logic to first start with this foundation type to understand the underlying principles and their effect on the liquefaction behaviour of the soil.

The following aspects of the theoretic scenarios are presented: the soil profile and geometry, liquefiable soil characteristics, the material parameter set for Plaxis 2D, the load signal, the natural frequencies of the soil and wind turbine and the mesh calibration of the model. Not all information of the Oostpolderdijk can be presented due to project confidentiality.

3.1. Soil Profile and Geometry

This section presents the soil profile of the simplified soil profile which is used for the theoretic scenarios. The geometry with horizontal surface is used to determine the influence of the calculation method (quasi-static/dynamic) and applied soil model on the CSR determination. The situation with the dike geometry is used to give a more representative magnitude of the stress state in the soil due to the presents of the soil body. The profile has been determined using the original model used for the reference engineering methodology and the representative CPT. Thereafter, the geometries of the theoretic scenarios are presented.

3.1.1. Soil Profile

The soil profile of the original analysis in combination with the CPT is used to create a simplified, but representative profile. The soil profile on the right is simplified which preserves several important aspects of the original profile:

- The liquefiable soil layer is not at the surface but located deeper into the soil.
- The liquefiable soil layer is enclosed by clay layers. The low hydraulic conductivity of the clay layers obstruct drainage of pore pressures towards the surface or deeper into the soil.

The material properties of the simplified profile are presented in section 3.3. The simplified profile is used as soil profile for the two theoretic scenarios presented in the following subsections.

The two theoretic scenarios are created to perform the calculations and analysis for the first and second sub question of the thesis. The first theoretic scenario is a situation where the surface is horizontal in order to minimize the effect of the dike geometry at the surface. The soil layers are situated horizontally. The geometry with horizontal surface is used to determine the influence of the calculation method (quasi-static or dynamic) and applied material model of the soil. More information on this situation is presented in subsection 4.2

The second theoretic scenario incorporates a soil body at the surface, representing a dike. The dike profile is generated from data that is publicly available at www.ahn.nl at the location of the reference case, see figure 3.1. The embankment geometry is used to obtain a realistic order of magnitude of the impact of the loads on the liquefiable soil layer. In addition, the influence of the soil body on the stress state in the soil is analysed. More information on this situation is presented in subsection 3.1.3. A 2.5 MW wind turbine has a steel tower with a height of 98m and the rotor diameter is 50m (van der Weijden, 2015). Figure 3.3 shows the dimensions of the wind turbine relative to the horizontal and embankment geometry.

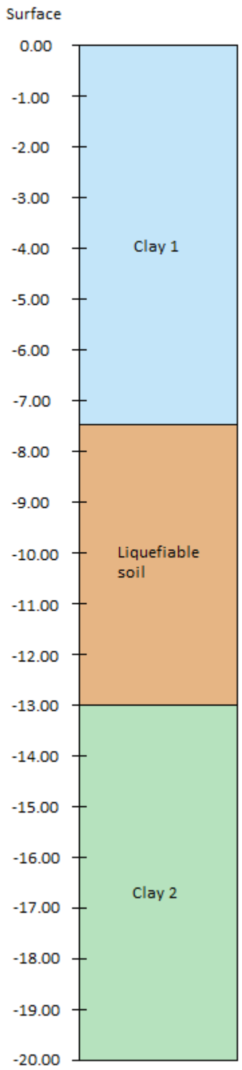

Figure 3.2: Simplified soil profile.

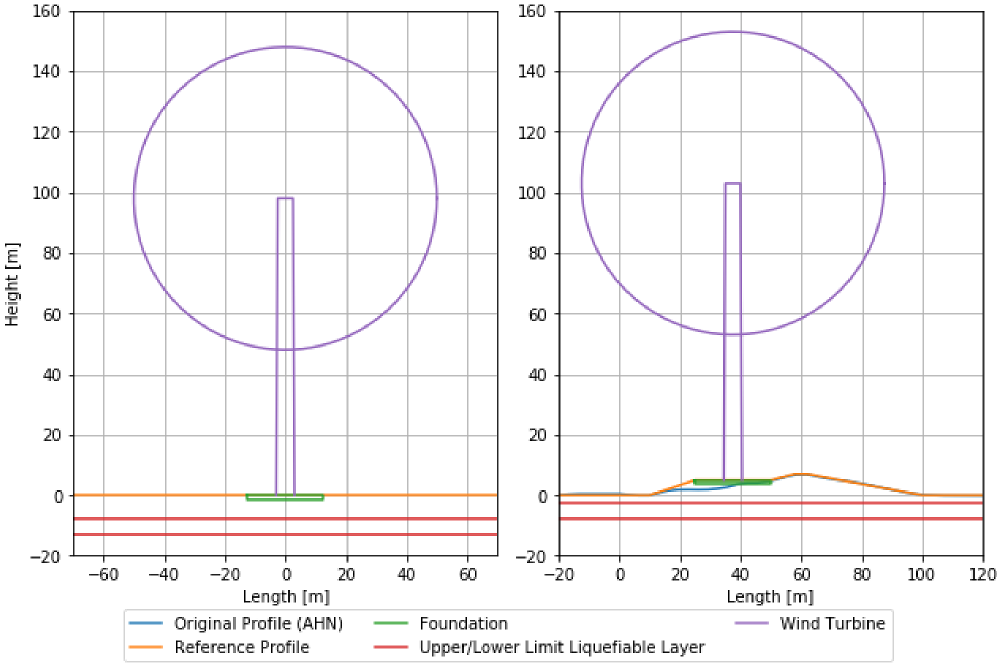

Figure 3.3: The horizontal (left) and embankment geometry (right) including the turbine tower height and rotor circumference dimensions to scale.

3.1.2. Scenario 1: Geometry with Horizontal Surface

The right profile presented in figure 3.2 is used for the theoretic situations. The clay-sand-clay configuration of the soil is similar to the reference case. The liquefiable soil layer is 5.5m thick, which is in agreement with the reference case (Appendix E). The horizontal and vertical boundary conditions are defined at a distance such that the boundaries do not influence the calculation results and thus the CSR reduce to nearly zero. The ground water reaches to the surface, assuming soil assumed to be fully saturated.

The foundation is modelled as a concrete shallow foundation with similar geometric properties to the Groningen case: the rectangular foundation is 25 m wide and 1.5 m deep. The loading induced by the wind turbine acts at the center of the foundation. The point load gets distributed through a very stiff plate in place on top of the foundation to model the effect of the wind turbine tower dimensions. The tower diameter is 6 m wide. More information on the wind turbine is presented in sections 3.4 and 3.5.

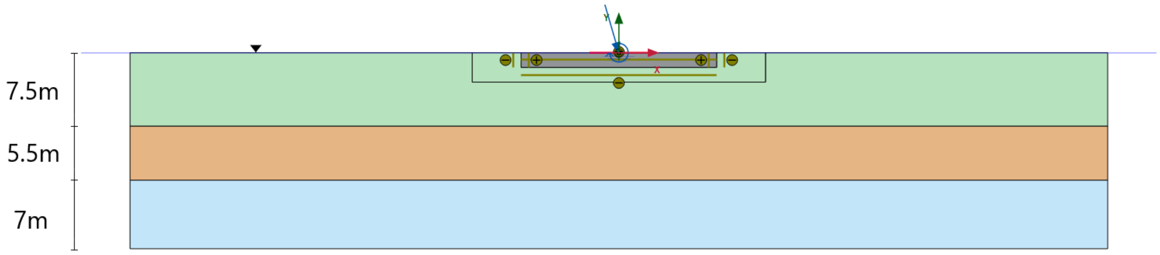

Figure 3.4: Geometry with horizontal surface, liquefiable soil layer between -7.5 m and -13 m below surface

3.1.3. Scenario 2: Embankment Geometry

The realistic geometry consists of the same sequence of materials as used in the case with the geometry with horizontal surface (clay-sand-clay) but the surface geometry resembles a more realistic scenario (see CPT at project location in Appendix E). The soil body of the dike has the same dimensions as the existing dike in Groningen. The geometry is generated using the AHN viewer using the AHN2 topographical data available at www.ahn.nl/ahn-viewer at the reference case project location (figure 3.1).

The liquefiable soil layer and the stress state within the layer as a result of the overlying dike are of main interest for the thesis. The composition of the dike is simplified to one single material to minimize complexity. The shallow foundation consists of concrete and has the same dimensions as in the geometry with horizontal surface and includes a rigid plate on top to distribute the loading forces. The top of the foundation is situated in the inner berm of the dike at a height of +5.0m above NAP. This results in a distance of 7m between the top of the foundation and the top of the liquefiable soil layer, which is comparable with the distance between these elements in the geometry with horizontal surface.

The dike has a maximum height of +7.0m NAP and a width of 90 meters. The outer water level reaches +6.07m above NAP, which in this case is normative (de Bruin et al., 2017) for inward macro stability (in Dutch: binnenwaartse stabiliteit STBI). The water levels are determined according to the Ontwerpinstrumentarium 2014 (OI2014) presented by Rijkswaterstaat (2016). The phreatic line inside the dike results from a linear interpolation between the inner and outer water levels as a conservative estimation. In addition, no variation of the phreatic line is expected as the embankment consists of a single material.

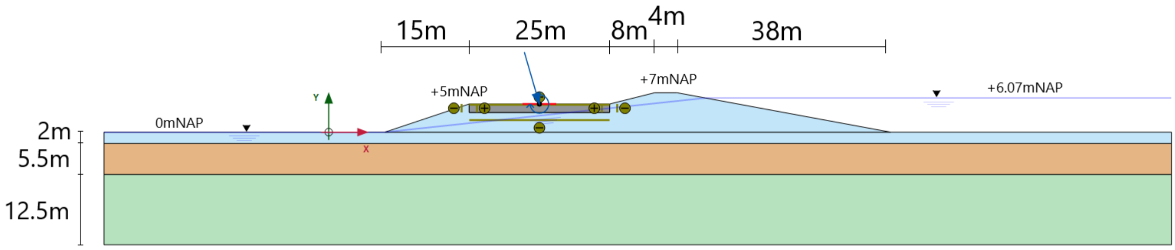

Figure 3.5: Realistic geometry, liquefiable soil layer between -7.5 m and -13 m below NAP

3.2. Liquefiable Soil Layer Characteristics

This section describes the characteristics of the liquefiable soil layer underneath the dike. It is assumed that the soil is susceptible to liquefaction. Only limited data is available for the liquefaction properties of the 'Wadzand'-layer (hereafter wadzand). Available test data of Wadzand contains index characteristics, strength properties, liquefaction resistance available as liquefaction curve and permeability characteristics. Data of the individual element tests is not available.

An alternative material is being introduced, of which more test data is available such as cyclic direct simple shear tests, to analyze the response of a soil to cyclic loading. Ottawa sand is a sand which is often used to physically model liquefaction phenomena in academic research. The Liquefaction Analysis and Experiment Projects (LEAP, Majid et al. (2018)) is an example of such research. The objective of LEAP is to develop a high quality database of centrifuge tests to validate constitutive/numerical models for the analysis of soil liquefaction (Majid et al. (2018)). Ottawa sand is used as the primary material in the LEAP study and, contrary to the Wadzand, it is a material which is investigated extensively both experimentally and numerically.

Ottawa sand is chosen in order to be able to work with a relatively well-known material properties and more certainty regarding the material characteristics. A comparison between the materials is made to check the similarities and differences between the materials.

3.2.1. Wadzand

The Wadzand consists of a Holocene tidal deposit where thin layers of clay and sand alternate (see Appendix E). Tasiopoulou et al. (2019) publish results of experimental and numerical research on the Wadzand. The Wadzand mainly consists of a 'uniform' and a laminated section, as categorised by Tasiopoulou et al. (2019). It should be noted that the uniform samples still contain approximately 20% of fines and all of the samples are not homogeneous. Because of the high content of clay particles, it was not possible to determine a relative density for the samples, but the initial void ratio e_0 is used as an indicative index property. For the uniform sand samples, e_0 varies between 0.65 and 0.69 (Tasiopoulou et al., 2019). For laminated samples, e_0 varies between 0.77 and 1.21 (Tasiopoulou et al., 2019). The Wadzand samples contain a significant amount of fine particles compared to the clean Ottawa sand. The Wadzand has a low hydraulic conductivity as a result of the particle contents, layered structure and limited lateral continuity.

Cyclic Triaxial and Direct Simple Shear devices are used by Tasiopoulou et al. (2019) to determine liquefaction curves for the Wadzand. Only the result of the liquefaction curve is presented, excluding the results of the cyclic tests. The effective vertical stress of the tests range from 80 kPa to 120 kPa. Figure 3.6 shows the liquefaction curves of the Wadzand and Ottawa sand. An extrapolation is performed to determine the cyclic stress ratio required to fail the sample at the equivalent number of cycles associated with a typical storm. From literature (Kramer (1996), Randolph and Gourvenec (2011)) it concluded that liquefaction curve are smooth cruves thus without any discontinuities. The typical storm and corresponding loading frequencies are further elaborated in Section 3.4.

From figure 3.6 it is observed that clay laminations decrease the susceptibility of the sample to liquefy as the CSR curve shifts upwards. While the Ottawa sand and uniform samples of the Wadzand have a similar initial void ratio, the slope of the Ottawa sand is less steep. The curve of the Ottawa sand approaches a higher asymptote compared to the Wadzand. Therefore, the Ottawa sand is less likely to liquefy at a higher number of cycles. The uniform, CDSS samples can be fitted with parameters a and b (see Equation 3.1) equal to 0.245 and 0.35. The laminated, CDSS samples have an a and b parameter of 0.33 ad 25 and the CTX samples have an a and b parameter of 0.435 and 0.19, respectively.

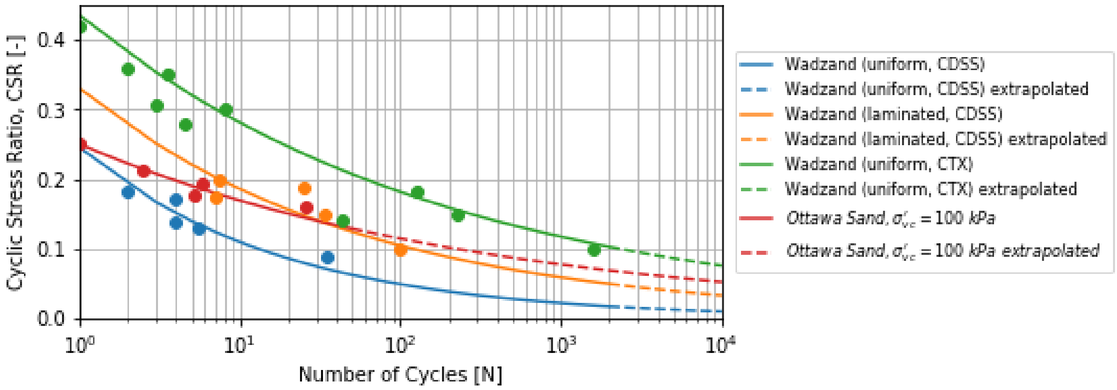

Figure 3.6: CSR of Wadzand (various σ'_{v0} and e_0, from Tasiopoulou et al. (2019)) and dense Ottawa Sand ($\sigma'_{vc} = 100\ kPa$, from Parra Bastidas (2016))

DSS tests are performed on isotropically consolidated soil samples by Tasiopoulou et al. (2019) to determine strength parameters of the Wadzand. Table 3.1 presents the parameters derived from the soil tests. With respect to the volume weight and strength parameters, Ottawa sand has more agreements with the uniform part of the Wadzand than the laminated part. With respect to the liquefaction curve, Ottawa sand is comparable in the lower region of number of cycles (N < 100 cycles) but tends to maintain some resistance towards liquefaction. In comparison, the Wadzad almost always ends up liquefied at a high amount of cycles (10^4).

Table 3.1: Wadzand volumetric weight and strength parameters

Material	γ_{unsat} [kg/m^3]	γ_{sat} [kg/m^3]	ϕ' [°]	c' [kPa]
Wadzand (uniform)	15.0	18.0	23.5	0.0
Wadzand (laminated)	17.1	17.1	14.0	0.6

3.2.2. Ottawa Sand

The Ottawas F-65 sand is used at the centrifuge facility at UC Davis and the LEAP study (Majid et al., 2018). The soil consists of a uniformly graded, round grains with a small fines content (<1%) and high quartz content (>99%). Figure 3.7 depicts the particle size distribution relative to the various sub-layers of the Wadzand. A particle size distribution shows the percentage particle by particle size of a sample. Parra Bastidas (2016) has done extensive research on the properties of the Ottawa sand. The sand has a specific gravity, G_s of 2.65. The dry density for a loose and dense state are ($\rho_{d,l}$ and $\rho_{d,d}$) are 1480 and 1722 kg/m^3. This corresponds with a relative density of about 42% and 67%, respectively. The minimum and maximum void ratios are 0.51 and 0.83, respectively. The hydraulic conductivity is between 0.22 and 0.16 mm/s, for a loose and dense state. A critical state friction angle corresponds to 24.6°. The Young's modulus is 55 MPa. Q=10 and R=1 gives an approximation of the critical state line. The data of the Ottawa F-65 sand is publicly available at https://datacenterhub.org/resources/14288.

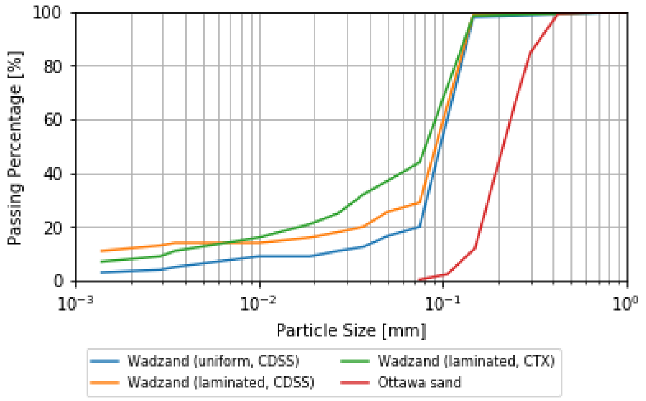

Figure 3.7: Particle Size Distribution of Ottawa Sand (adopted from Parra Bastidas (2016)) and Wadzand (adopted from Tasiopoulou et al. (2019))

Figure 3.8 shows the cyclic liquefaction curve for densely packed samples. The dotted line indicates the extrapolation of the data to the number of cycles of a typical storm. Extrapolation of data is subjected to uncertainties and may result in unreliable results when used. However, this is the best available data and therefore it is used for the analysis. The dense sample has a $D_r = 0.67\%$ which corresponds with an initial void ratio $e_0 = -(D_r(e_{max} - e_{min}) - e_{max}) = 0.61$. The liquefaction curve is constructed by measuring the amount of cycles are required to reach 3% shear strain. The liquefaction curve is generally given by:

$$CSR = aN^{-b} \tag{3.1}$$

where a and b are fitting coefficients and N is the number of cycles until a predetermined amount of shear strain. The liquefaction curve is determined using an effective vertical stress of 50, 100 and 400 kPa resulting in an 'a'-parameter of 0.24, 0.25 and 0.26, respectively. Fitting parameter b is 0.17 for all situations.

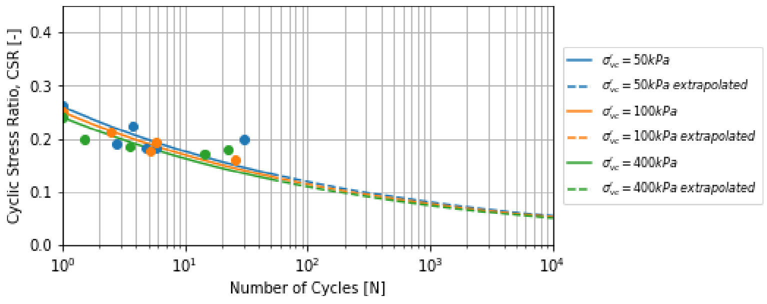

Figure 3.8: CSR of dense Ottawa Sand ($D_r = 0.67\%$, adopted from Parra Bastidas (2016))

3.3. Material Parameter Set for Plaxis 2D

A material parameter set for the various materials is created based on available soil data and common used values for construction materials like concrete. Theoretical correlations and characteristic values from design codes are used where information is missing or incomplete. Appendix B contains the tables with the parameters for the various soil models.

3.3.1. Linear Elastic

The Linear Elastic soil model is used to model the relatively stiff behavior of concrete in comparison with soil. Table B.1 contains the material properties of concrete.

3.3.2. Mohr-Coulomb

The Mohr-Coulomb material is used to generate a first estimate of the soil behavior taking into account plastic behavior of the soil. Table B.2 contains the material properties of the Mohr-Coulomb materials of the soil valid in the engineering strain domain where γ is approximately $\geq 2\%$. The soil parameters of 'Clay' and 'Clay Deep' are originating from the characteristic values of table 2b of Eurocode 7 (ECS, 2016). Table 2b of Eurocode 7 contains general geotechnical parameters not necessarily determined for liquefaction analysis. The strength and porosity properties of the sand layer are based on monotonic tests on the Ottawa Sand material originating from Parra Bastidas (2016).

3.3.3. Hardening Soil Small Strain

The Hardening Soil Small Strain is based on the Mohr-Coulomb model, but takes the stress-dependency of the stiffness parameters into account. Table B.3 contains the adopted Hardening Soil Small Strain parameters. The friction angle, ϕ', is relatively small but it is argued to give a better approximation at the steady state Parra Bastidas (2016). The soil parameters of 'Clay' and 'Clay Deep' are based on table 2b of Eurocode 7 and the properties of the sand layer are based on monotonic tests on the Ottawa Sand material originating from Parra Bastidas (2016). Empirical correlations are used for all the materials to determine the HSsmall parameters and are described in: Plaxis (2019a), Benz (2007), Lunne and Christoffersen (1983), Brinkgreve et al. (2010), Jamiolkowski et al. (2001) and CUR162. The correlations are shown in appendix E.

3.3.4. Plate

The plate on top of the concrete element is modelled as an elastic material. The plate can accommodate bending moments. Furthermore, the degrees of freedom in the plate elements are not only displacements, but also rotations. The point torque load at the foot of the turbine tower is therefore correctly transferred to the concrete plate (consisting of continuum elements). Table B.4 contains the elastic plate parameters. The parameters of the plate have been estimated on the basis of the geometry of the footing and stiffness properties that are used in common professional practice.

3.4. Load signal

Table 3.2 shows the loads induced by the wind turbine at the top of the foundation. Cyclic loads are only induced due to wind and mechanical forces from the wind turbine. Seismic loads are not considered in this thesis. The values of the loads are rounded off due to project confidentiality. The 2.5 MW turbine has a tower with a height of 98m and a rotor diameter of 100m (van der Weijden, 2015). The loads are applied to the foundation through a plate in order to take the effect of the tower width into account and properly distribute the load onto the 25 m wide concrete foundation.

Table 3.2: Static loads induced by the wind turbine at top of the foundation (Arcadis, 2019)

Load	Point Load	Unit	Line Load (=point load/25m)	Unit
F_V	3000	kN	120	kN/m
F_H	1000	kN	40	kN/m
M	70000	kNm	2800	kNm/m

A simplified dynamic signal in the time domain is created by applying a multiplier on the static loads of

Table 3.2. The signal is based on the signal provided by the wind turbine supplier but is not depicted out of confidentiality. Figure 3.9 shows the simplified dynamic multiplier used for dynamic calculations. In figure 3.10 it can be seen that the signal has a distinct peak around 0.3-0.4 Hz in the frequency spectrum. A sine motion is constructed using the dominant frequencies. Higher frequencies, which can be found around the peak presented in the original signal, are ignored in the signal presented in figure 3.9, disregarding frequencies which could potentially cause resonance.

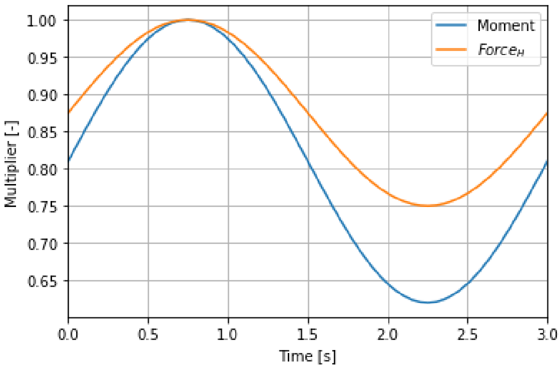

Figure 3.9: Loading signal at 0.3 Hz in time domain

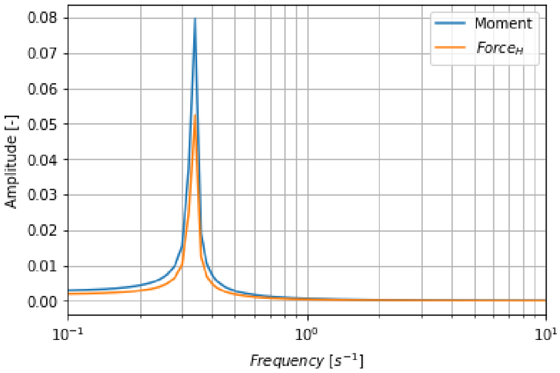

Figure 3.10: Signal in frequency domain

In addition to the simplified dynamic signal, a quasi-static loading sequence is defined to simulate cyclic loading. One full cycle using the quasi-static calculation method is modelled using multiple construction phases in Plaxis 2D. Figure 3.11 shows the multiplier per construction phase to match the dynamic signal as presented in figure 3.9. A total of 5 construction phases are required in order to model one full loading cycle. Relative construction phases 1, 3 and 5 indicate the average value during a cycle and relative construction phases 2 and 4 show the maximum and minimum value during a cycle, respectively. Multiple loading cycles can be modelled by appending the quasi-static multiplier multiple times.

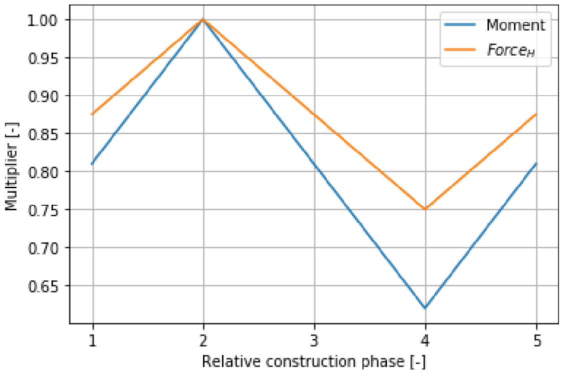

Figure 3.11: Quasi-static multiplier of the loads on top of the foundation

Additional loading signals are defined in order to perform an analysis on the impact of the loading frequency on the inertia forces in the soil. The additional loading signals have the same frequency content and amplitude as the signal presented in figure 3.9 but different frequencies. Slower and faster loading phenomena are simulated varying between 0.1 and 5.0 Hz. This range is used because it contains the frequencies of the following items. The loading frequency of a cyclic test is usually performed between 0.1 and 1 Hz. The natural frequency of a wind turbine can vary between 0.15 and 0.4 Hz as observed in Table B.7 and substantiated in Section 3.5. Wichtmann and Triantafyllidis (2012) indicate that loading signals up to 5 Hz can also be modelled as quasi-static loads.

3.5. Natural Frequencies

This Section contains the analysis of the natural frequencies of the soil and the wind turbine for the purpose of supporting the dynamic analysis in Chapter 4. An estimation of the natural frequency of the soil can be approximated using a linear transfer function. A linear transfer function is a mathematical method to calculate the response of a single-degree-of-freedom system (SDOF) to an excitation. Shearing and damping characteristics can be included when a Kelvin-Voigt type of solid is adopted to model the soil behaviour (Kramer (1996)). Further information on the determination of the linear transfer function can be found in appendix B.

The weighted average of the full profile is used to determine the natural frequency. The weighted average of the shear wave velocity is determined for the Mohr-Coulomb material set (Section 3.3) using shear modulus G and is indicated by MC. The weighted average for the Hardening Soil Small Strain material set (Section 3.3) is determined using the unloading/reloading shear modulus (G_{ur}) and is indicated by HSss.

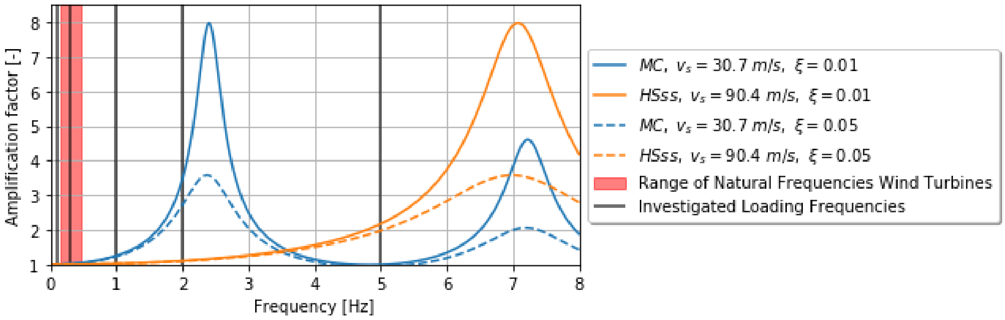

Figure 3.12: Influence of the shear wave velocity and damping on the amplification factor of a linear elastic soil layer (Equation B.1)

The dynamic characteristics of the wind turbine can be modelled using discrete elements like masses and springs. The structure can be represented using either a SDOF system or a multiple-degrees-of-freedom (nDOF) schematization. The applied method is described in appendix B.

The range of frequencies is plotted in figure 3.12 as a red bar to compare the natural frequencies of various wind turbines with respect to the soil. Figure 3.12 also shows the loading frequencies that are defined in Section 3.4 and investigated in the frequency analysis of Chapter 4. The natural frequency of the wind turbine shifts further apart from the natural frequency of the soil as the wind turbines are increasing in size. However, a larger size implies bigger loads induced by the wind turbine onto the soil. In addition, it is observed that the impact of the second mass in the 2DOF schematization has a larger impact on the natural frequency for the heavier turbines compared to the lighter turbines. The addition of the relatively heavy mass on the bottom of the system results in a stiffer response of the system. The distribution of the masses along the length of the turbine gives a more realistic estimation of the natural frequency.

3.6. Mesh Calibration

A preliminary analysis is performed in order to investigate the influence of the mesh size on the bearing capacity of a shallow foundation, because a correct mesh size is important for reliable results (Potts and Zdravković, 2001). A 10 m wide, rigid strip foundation is modelled using a prescribed displacement on a uniform soil. An undrained clay layer is modelled using the Mohr-Coulomb material model with the parameter values given by Table 3.3. This material is introduced in order to be able to demonstrate the effect of local mesh refinement and compare the FEM results with an analytic solution.

Table 3.3: Mohr-Coulomb parameters preliminary analysis

Material	Clay	Unit
Drainage	Undrained (B)	
γ_{unsat}	17	kg/m^3
γ_{sat}	17	kg/m^3
E’	2000	kN/m^2
ν'	0.3	-
$s_{u,ref}$	50.0	kN/m^2
ϕ'	0.0	°
ψ	0.0	°
$e_{initial}$	0.75	-

Prandtl (1920) showed that the bearing capacity for an shallow strip foundation on a undrained, cohesive ($\phi = 0°$) soils equals: $q = 5.14 s_u$. In Table 3.4 it can be seen that mesh refinement as well as local refinement produces results that are closer to the analytic solution. Stress gradients surrounding the edges of the foundation are modelled more accurately by using more elements. Therefore, the result of the FEA converges to the analytic solution with increasing elements. An excessive amount of elements in low stress gradient regions can be prevented by local mesh refinement. In the cyclic stress ratio analysis, a local mesh refinement surrounding the foundation is used to accurately determine the stresses in the soil as a result.

Table 3.4: Influence of mesh size

Type	Nr of elements	Largest element size	Bearing Capacity [kN/m]	Difference [%]
Analytic	-	-	257	-
Medium	442	2.8	258.6	0.62
Very fine	25591	0.25	257.7	0.27
Fine, local	3682	2.8	257.7	0.27

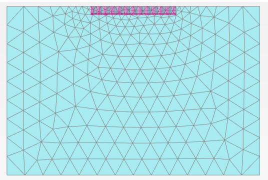

Figure 3.13: Medium mesh grid

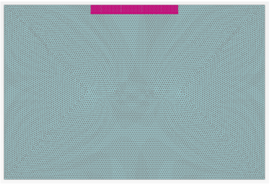

Figure 3.14: Fine mesh grid

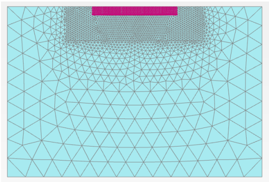

Figure 3.15: Locally refined mesh grid

Proper wave propagation during dynamic FEM calculations is ensured by imposing a maximum element height. The mesh should comply with the equation defined by Kuhlemeyer and Lysmer (1973):

$$h_{element,max} = \frac{\lambda}{8} = \frac{v_{s,min}}{8 f_{max}} \tag{3.2}$$

where λ is the wave length, $v_{s,min}$ is the minimum shear wave velocity and f_{max} is the maximum frequency. The minimum shear wave velocity is dependent on the top clay layer where $v_{s,min} = 21 m/s$. Each frequency used in the dynamic analysis requires a corresponding typical maximum element size. The element sizes used in the analysis are equal or smaller than the calculated maximum element size presented in Table 3.5.

Table 3.5: Maximum element height for various loading frequencies

Frequency [Hz]	Maximum element height [m]
0.1	26.25
0.3	8.75
1.0	2.625
2.0	1.31
5.0	0.525

4

Soil Structure Interaction and Influence Depth of a Shallow Foundation

Chapter 4 investigates the influence of the soil-structure interaction on the stresses in the soil induced by a wind turbine founded on a shallow foundation. The following sub-questions are answered in this chapter:

- ”How can time dependent shear stresses in the soil induced by an onshore wind turbine be modelled, taking into account the effect of SSI?”
- ”What is the influence of irregular modes of shearing in the soil on the liquefaction behaviour?”

The purpose of the first sub-question is to investigate an appropriate method to model the loads induced by the wind turbine foundation. The purpose of the second sub-question is to determine the influence of various shearing modes on the cyclic stress ratio. The various shearing modes are: triaxial compression, triaxial extension and direct simple shear. The induced loads are defined as the cyclic stress ratio, which is the driving force of the method described in this thesis.

The time dependent loads can be modelled as quasi-static or dynamic loads. Wichtmann et al. (2004) suggests that time dependent loads with a frequency $\leq 5\ Hz$ can be modelled as a quasi-static load rather than a dynamic load, disregarding inertia effects. The validity of this claim is investigated by performing a frequency analysis on the the simplified cases of the reference case (Chapter 3). First, the geometry with horizontal surface (section 3.4) is used to get an order of magnitude and location of the Cyclic Stress Ratio (CSR, see section 4.1). This is done using two soil models, e.g. the Mohr-Coulomb and Hardening Soil Small Strain models. Subsequently, an embankment geometry is used to determine the CSR for a realistic scenario resembling a dike geometry with an embedded shallow foundation (Chapter 4.3).

Finally, a sensitivity analysis is performed on the parameters of the soil model to investigate which parameters have the greatest influence on the CSR. The results of the determination of the CSR due to the wind turbine vibrations is used as input for the pore pressure response analysis (Chapter 5).

4.1. Method

The cyclic stress ratio (CSR) is used as a measure to quantify the cyclic loading characteristics of the soil. Boulanger and Idriss (2014) use 65% of the maximum cyclic shear stress or maximum horizontal acceleration as a result of an earthquake to define the CSR as a function of depth. The maximum cyclic shear stress or horizontal acceleration can be determined using a linear or non-linear site response analysis. Seed and Rahman (1978) consider cyclic loading of the soil as a result of cyclic compression stress at the seabed due to waves in the ocean. The shear stresses as a result of ocean waves are evaluated using the theory of elasticity. Both of these “global” loading situations are not similar to the local loading caused by a wind turbine foundation.

Therefore, the CSR over the depth as a result of a cyclic loading by a shallow foundation must be determined. The wind turbine situated on the shallow foundation results in a combination of cyclic horizontal load, cyclic moment load and a static vertical load. Plastic deformations are expected over time as a result of the wind turbine loading. The CSR profile is therefore determined using Plaxis, using the elasto-plastic Mohr-Coulomb model and the Hardening Soil Small Strain model. Important is the compliance of the stiffness parameters of the Mohr-Coulomb with small strain behaviour. The drainage response of the soil is fully undrained as a first estimation to determine the shear stresses in the soil. The cyclic stress ratio is defined in equation 3.1 as:

$$CSR = \frac{\Delta\tau_{cyc}}{\sigma'_{v0}} = \frac{(\tau_{cyc,max} - \tau_{cyc,min})/2}{\sigma'_{v0}} \tag{4.1}$$

Here, the maximum cyclic shear stress $\tau_{cyc,max}$ is the maximum shear stress. The minimum cyclic shear stress $\tau_{cyc,min}$ is the minimum shear stress. Hence, the CSR is determined using the complete shear stress variation over one cycle. The cyclic shear stress is determined after applying the cyclic component of the load. The cyclic load consists of 2 full cycles as indicated by Figure 3.11 multiplied by the loads in Table 3.2 to determine the quasi-static load over time. The dynamic load signal is obtained by multiplying the signal from Figure 3.9 with the loads in Table 3.2. The initial vertical effective stress is determined when the static component of the load is applied to the foundation.

4.2. Scenario 1: Geometry with Horizontal Surface

Literature indicates that cyclic loading induced by wind loads is slow enough to not cause inertia forces in the soil ((Andresen, 2015), (Wichtmann and Triantafyllidis, 2012)). Therefore, it is investigated if the dynamic calculation method in Plaxis results in inertia forces in the soil. The geometry with horizontal surface is used to analyse the effect of the dynamic calculation on the inertia forces in the soil. Different loading frequencies are used to determine the impact of the loading frequency on magnitude of the stresses in the soil. Five frequencies are used, varying from slow to fast. A lower limit of 0.1 Hz is chosen which is similar to the lower limit of cyclic testing and the upper limit of 5 Hz is chosen because Wichtmann and Triantafyllidis (2012) suggest that phenomena slower than 5.0 Hz can be considered to result in quasi-static conditions. Section 3.5 shows that the range of natural frequency of a wind turbine lies between the 0.15 and 0.4 Hz. The following frequencies are used: 0.1 Hz, 0.3 Hz, 1.0 Hz, 2.0 Hz, 5.0 Hz. The corresponding maximum element size for the mesh are presented in Table 3.5.

The response in the soil is calculated using both static and dynamic calculation methods to determine the influence of inertia forces in the dynamic calculation. Additional Rayleigh damping is applied to account for energy dissipation at small strain levels and to prevent spurious oscillations in the frequency domain. Seed et al. (1986) and Vucetic and Dobry (1991) suggests a damping ratio between 0.5% and 5%. The influence of a damping ratio of 2% and 5% is determined compared to the dynamic calculation without additional Rayleigh damping. The CSR development throughout the soil is determined using the Mohr-Coulomb model and Hardening Soil Small Strain model. The two models are used to demonstrate the effect of elasto-plastic behaviour relative with a constant stiffness compared to non-linear plasticity behaviour and stress dependent stiffness.

4.2.1. Mohr-Coulomb

Figure 4.1 shows the CSR as determined by equation 4.1 using the Mohr-Coulomb soil model to simulate the soil behaviour. The applied parameters are presented in table B.2. The liquefiable soil layer is situated between -7.5 m and -13 m below surface level. This is in line with the distance between the foundation and liquefiable soil layer in the OPD reference case. The vertical dashed black lines indicate the locations of the profiles that are created and shown in this Chapter. From the plot it can be seen that the highest CSRs are situated directly next and under the foundation. At the transition between the clay layer and the liquefiable sand layer an increase in CSR is observed. The relatively strong sand attracts shear stresses and results in a relatively high CSR compared to the clay layer directly situated above the sand. Presented in Appendix C are the results of the analysis to determine the influence of the distance between the foundation and liquefiable soil layer. Figures C.1 to C.4, C.9

to C.12 and C.17 to C.20 show that as the depth increases, the influence of the load on the shallow foundation decreases.

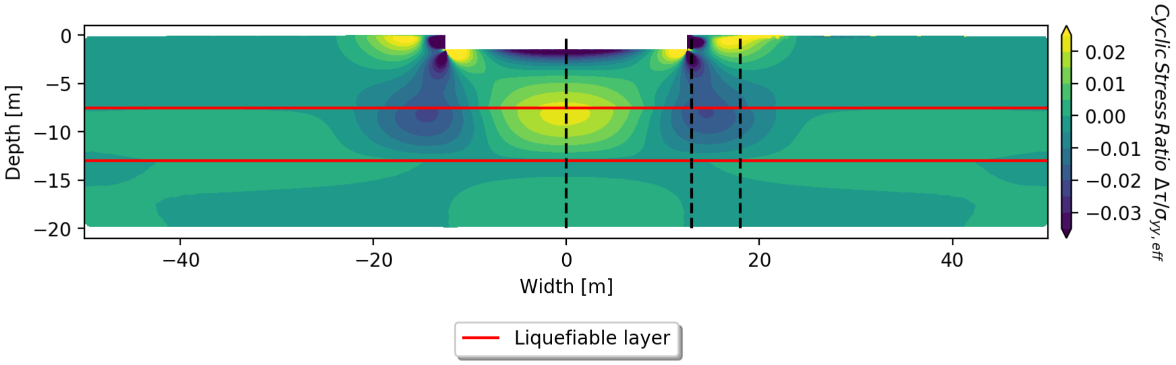

Figure 4.1: CSR contour plot, Mohr-Coulomb, quasi-static

Dynamic calculations were made in order to check whether or not the inertia forces in the soil have an effect on the response in the soil. The cyclic shear stress contour plot is generated from the difference between maximum and minimum shear stresses in one load cycle. The results of the analysis are presented using profiles generated at x = 0 m, x = 13 m and x = 18 m for one calculation method. Contour plots of the individual scenarios are presented in Appendix C. In Figures 4.4 to 4.10 it is observed that a loading frequency of 0.1 and 0.3 Hz gives a good agreement with the quasi-static situation. The dynamic calculation method gives additional stress concentrations throughout the soil for loading frequencies $\geq 1\,Hz$ relative to the quasi-static situation. These additional stresses in the soil are a result of wave propagation at higher loading frequencies. Additional stresses are also present using the slow frequencies ($f < 1\,Hz$), but only in the first 0.5 m of the soil. Additional Rayleigh damping (2% and 5%) suppresses high frequency oscillations and results in smoother stress concentrations in the soil. As a result, the additional stresses at the surface are suppressed for the slow frequencies. Figure B.1 shows that amplification can occur as a result of the cyclic loading at frequencies ≥ 2 Hz which is in agreement with the transfer function plotted in Figure B.1. In Figure B.1 it can be seen that 1 and 2 Hz are within the region where amplification or resonance can be expected. However, 5 Hz is expected to not have a big impact on the soil motion with respect to amplification but does not give results which agree with the quasi-static scenario.

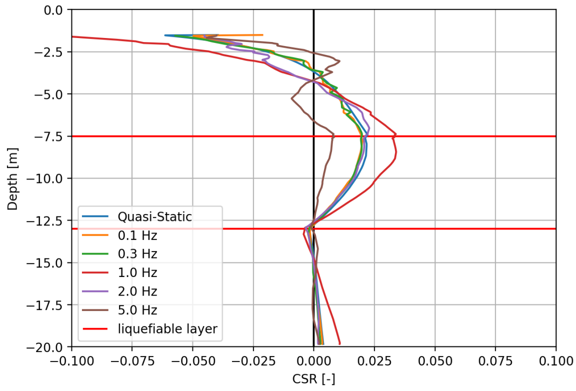

Figure 4.2: CSR profile at x = 0m, MC, dynamic

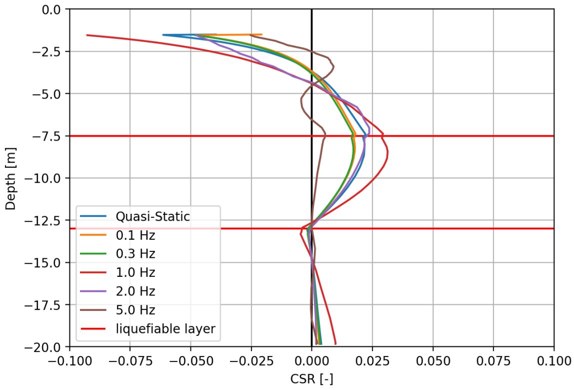

Figure 4.3: CSR profile at x = 0m, MC, dynamic with 2% Rayleigh Damping

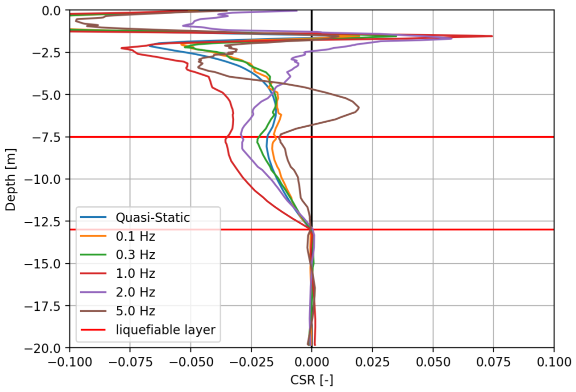

Figure 4.4: CSR profile at x = 13m, MC, dynamic

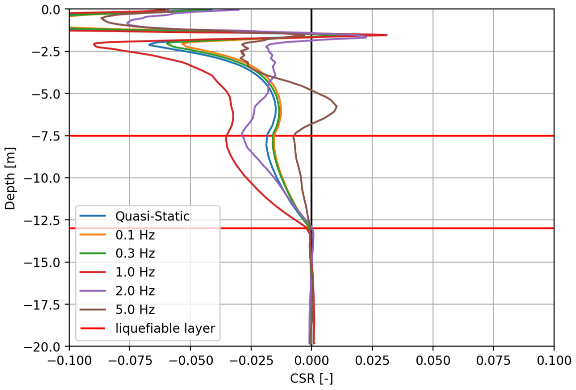

Figure 4.5: CSR profile at x = 13m, MC, dynamic with 2% Rayleigh Damping

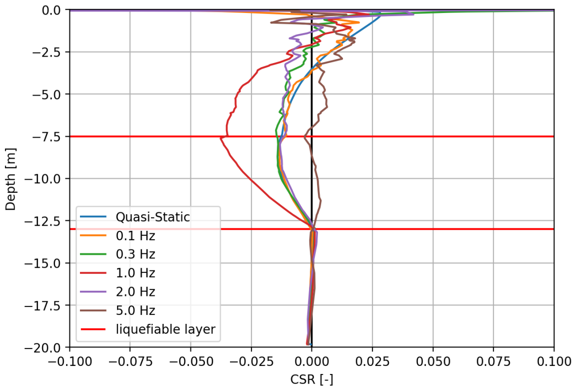

Figure 4.6: CSR profile at x = 18m, MC, dynamic

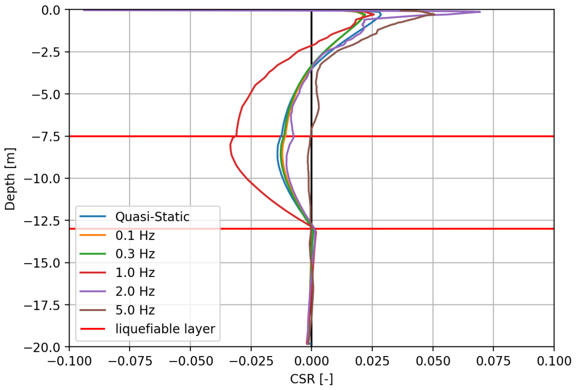

Figure 4.7: CSR profile at x = 18m, MC, dynamic with 2% Rayleigh Damping

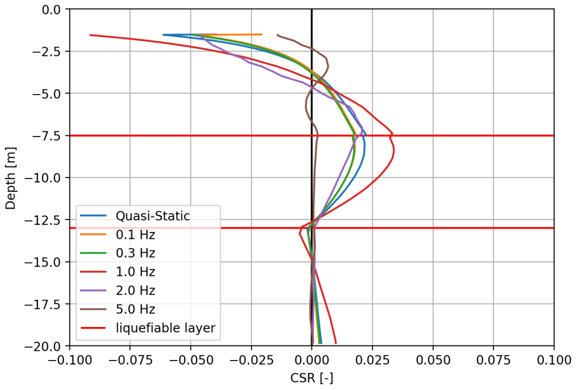

Figure 4.8: CSR profile at x = 0m, MC, dynamic with 5% Rayleigh Damping

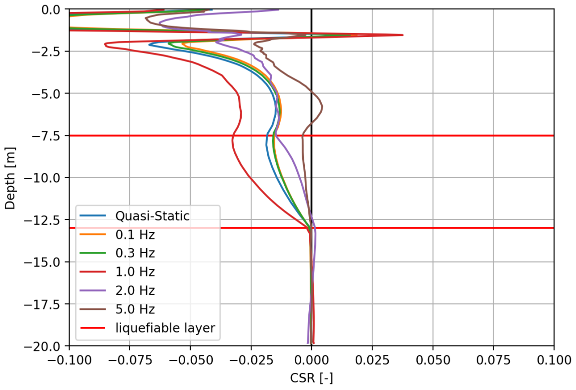

Figure 4.9: CSR profile at x = 13m, MC, dynamic with 5% Rayleigh Damping

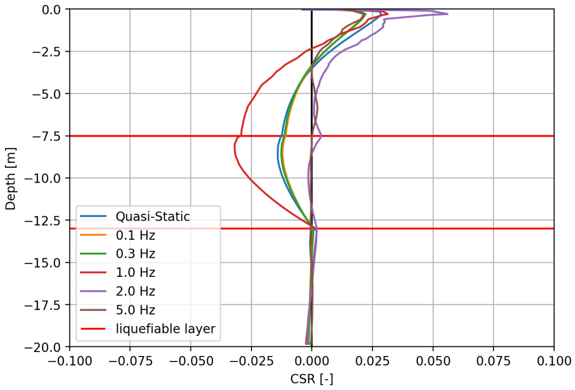

Figure 4.10: CSR profile at x = 18m, MC, dynamic with 5% Rayleigh Damping

4.2.2. Hardening Soil Small Strain

Figure 4.11 shows the CSR as determined by equation 4.1 using the Hardening Soil Small Strain soil model to simulate the soil behaviour. The applied parameters are presented in section 3.3.3. The liquefiable soil layer is situated between -7.5 m and -13 m below surface level. The dashed black lines indicate location of the profiles that are created and shown in this Chapter. From the plot it can be seen that the highest CSRs are situated directly next and under the foundation. At the transition between clay layer and liquefiable sand layer an increase in CSR is observed. It is observed that use of the Hardening Soil Small Strain model results in lower CSRs compared to the use of the Mohr-Coulomb model. This is a result of the use of engineering strain stiffness properties relative to small strain stiffness properties. Presented in Appendix C are the results of the analysis to determine the influence of the distance between the foundation and liquefiable soil layer. Figures C.5 to C.8, C.13 to C.16 and C.21 to C.24 show that as the depth increases, the influence of the load on the shallow foundation decreases.

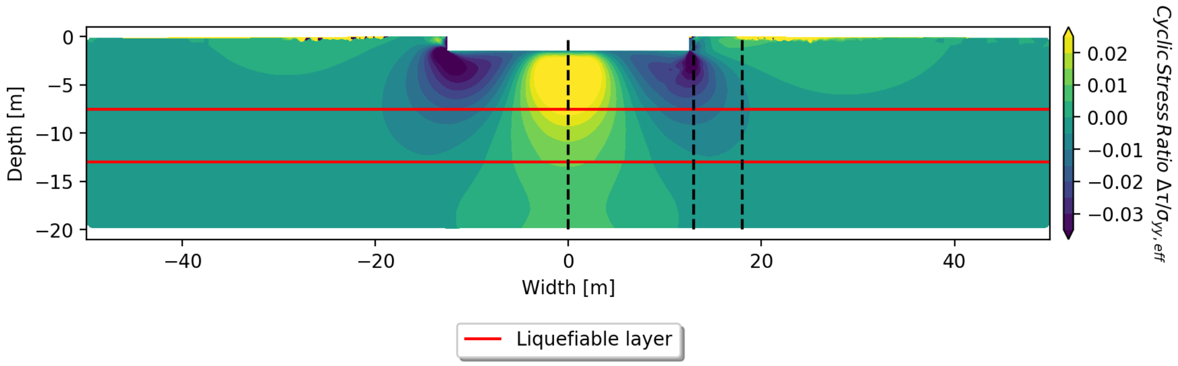

Figure 4.11: CSR contour plot, Hardening Soil Small Strain, quasi-static

Dynamic calculations using the Hardening Soil Small Strain material model are performed to check the influence of different loading frequencies and their effect on inertial forces in the soil. The cyclic shear stress contour plot is generated from the difference between maximum and minimum shear stresses in one load cycle. The results of the analysis are presented using profiles generated at x = 0 m, x = 13 m and x = 18 m for one calculation method. Contour plots of the individual scenarios are presented in Appendix C. In Figures 4.12 to 4.20 it can be seen that the dynamic calculations are comparable with the quasi-static situation at the locations where the profiles are generated, with exception of the scenario using a loading frequency of 5 Hz. At the contour plots generated it is observed that additional stresses are present in the soil when using a loading frequency $\geq 2.0Hz$. Also, the additional stresses throughout the cross-section increases using frequencies $\geq 2\ Hz$ whereas the stresses using a frequency $\leq 1\ Hz$ results comparable to the quasi-static scenario. In Figure B.1 it is observed that the frequencies ≥2 Hz are within the amplification zone. The impact of the 5 Hz loading frequency significant whilst the impact of the loading frequency of 2 Hz is minimum as expected by Figure B.1. Figures 4.14, 4.15 and 4.19 clearly show the effect of Rayleigh damping at frequencies where resonance is expected. Large stresses (as observed in Figure 4.14) are damped and reduced to significantly lower stresses (as observed in 4.19) throughout the soil.

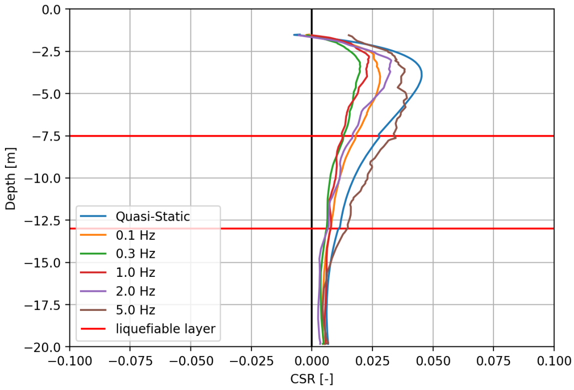

Figure 4.12: CSR profile at x = 0m, HSss, dynamic

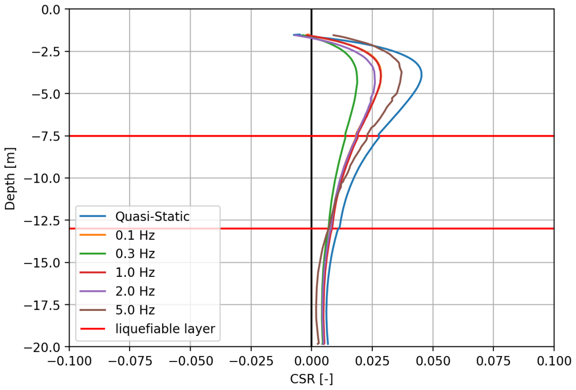

Figure 4.13: CSR profile at x = 0m, HSss, dynamic with 2% Rayleigh Damping

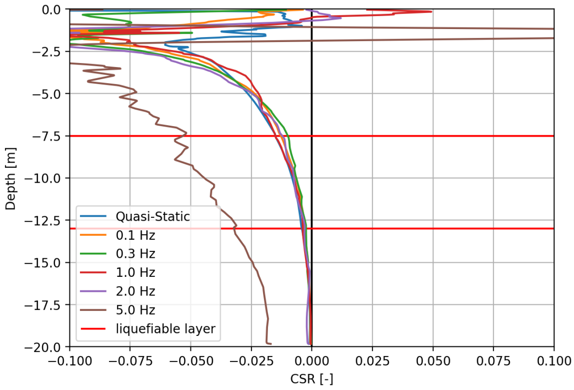

Figure 4.14: CSR profile at x = 13m, HSss, dynamic

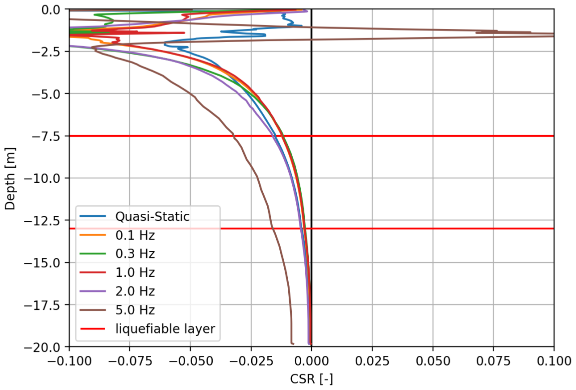

Figure 4.15: CSR profile at x = 13m, HSss, dynamic with 2% Rayleigh Damping

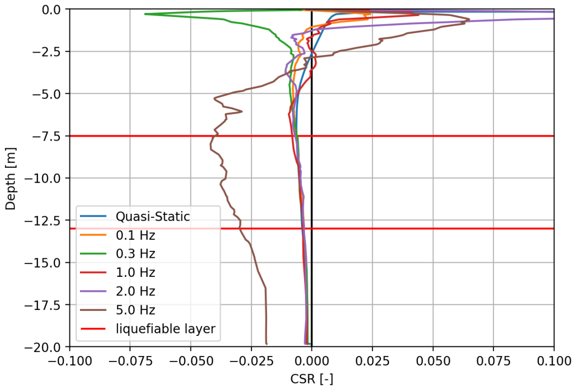

Figure 4.16: CSR profile at x = 18m, HSss, dynamic

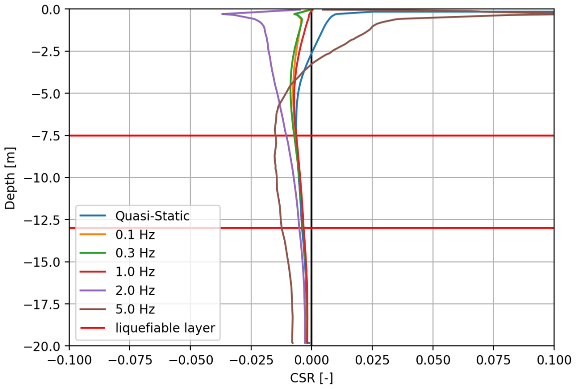

Figure 4.17: CSR profile at x = 18m, HSss, dynamic with 2% Rayleigh Damping

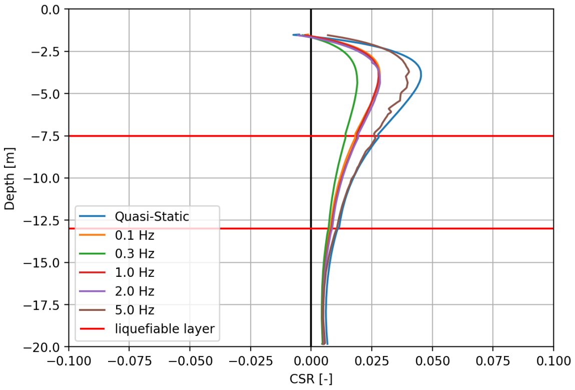

Figure 4.18: CSR profile at x = 0m, HSss, dynamic with 5% Rayleigh Damping

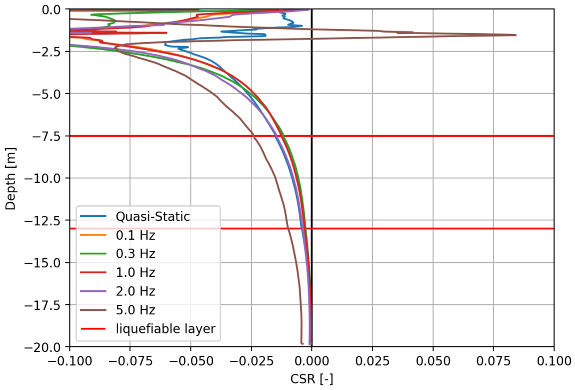

Figure 4.19: CSR profile at x = 13m, HSss, dynamic with 5% Rayleigh Damping

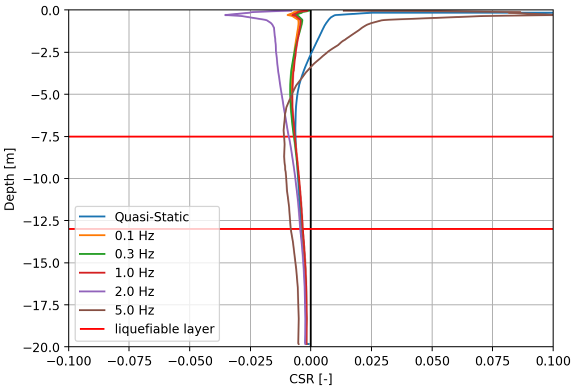

Figure 4.20: CSR profile at x = 18m, HSss, dynamic with 5% Rayleigh Damping

4.2.3. Conclusion on applied soil models

The Mohr-Coulomb and Hardening Soil Small Strains models are used to determine the CSR induced by cyclic loading on a shallow foundation. The calculations using the MC model result in a higher CSR at the location of the liquefiable soil layer with respect to the calculations using the HSss model. This also applies for situations where the liquefiable soil layer is at a different depth, e.g.: -5m or -10m below surface level (Appendix C). It is also observed that the CSR decreased with increasing distance between the foundation and the liquefiable soil layer. The CSR is determined using the maximum and minimum shear stress amplitude after applying the static load first. The MC does not include stress dependency of stiffness parameters and uses the same stiffness properties for both primary loading and unloading/reloading. The HSss model includes both stiffness and strain dependency of stiffness parameters and uses various stiffness parameters for different loading situations. As a result, the soil reacts stiffer during unloading and reloading when using the HSss model compared to the MC model. As the unloading/reloading situation is dominant, it is concluded that the HSss results in a more accurate indication of the CSR even when the result is less conservative compared to the MC model.

4.2.4. 3D effect

The geometry given by Figure 3.4 is extended to a 3D situation using Plaxis 3D. A square shallow foundation of 25m by 25m is modelled in the 3D calculation. The thickness of the shallow foundation is 1.5m. The soil stratification and properties are equivalent to the geometry with horizontal surface. The model boundaries are at $(x_{min}, x_{max}) = (-50, 50)$, $(y_{min}, y_{max}) = (-50, 50)$ and $z = -20$ with 174554 10-noded tetrahedron elements generated. Figure 4.21 shows the CSR contour plot for the 3D situation in xz direction which is the equivalent to the 2D situation.

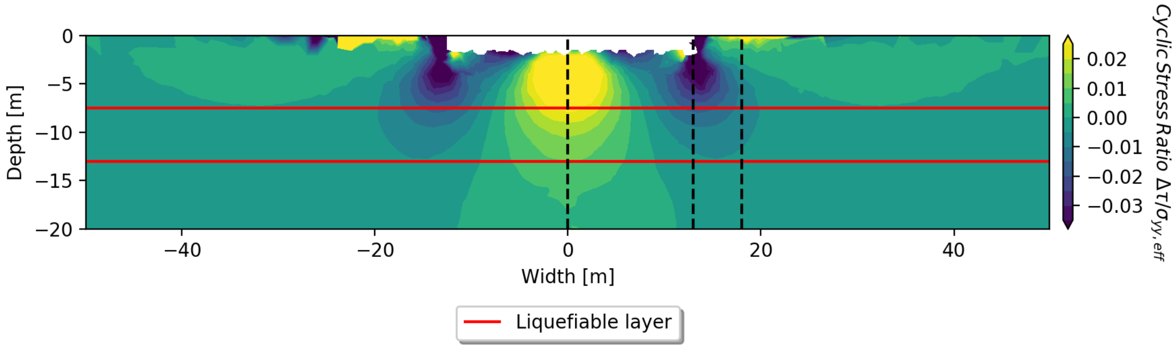

Figure 4.21: CSR contour plot, quasi-static, HSss, 3D

Figures 4.21 and 4.22 indicate a negative effect in 3D of a shallow foundation on the stress state at the liquefiable soil layer. As a result of a square foundation relative to a strip foundation (implied by plain strain conditions in a 2D FEA), an increase of shear stresses is found at the center of the foundation. A strip foundation distributes the stresses into the plane resulting in lower stresses on the soil compared to a square foundation. Using 2D plain-strain calculation models results in non-conservative estimations of the shear stresses and thus the CSR.

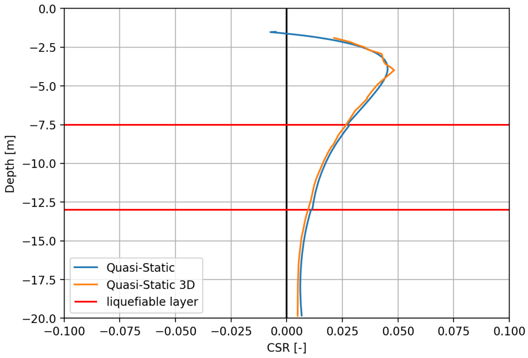

Figure 4.22: CSR profile at x = 0m, HSss, 3D

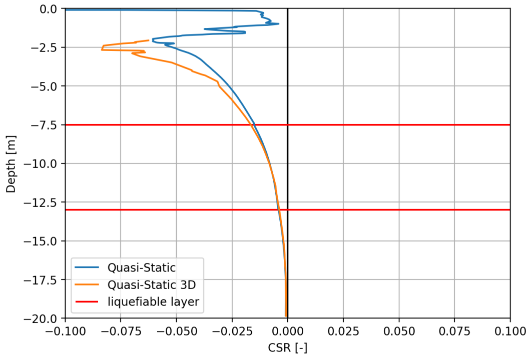

Figure 4.23: CSR profile at x = 13m, HSss, 3D

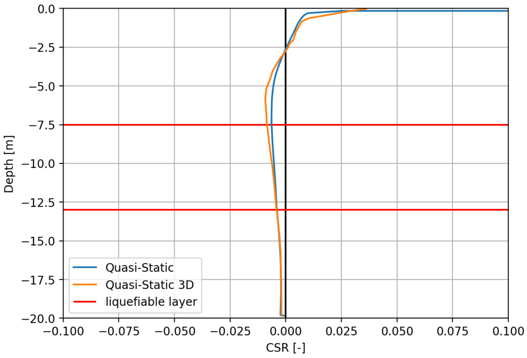

Figure 4.24: CSR profile at x = 18m, HSss, 3D

4.3. Scenario 2: Embankment Geometry

The embankment geometry as defined in Section 3.1 is used to determine the cyclic stress ratio taking into account the presence of a soil body at the surface. The natural frequency of the soil has been determined at the level of the shallow foundation. Again, the weighted average of the shear wave velocity is calculated using the HSss parameter set using the unload/reload shear modulus. Figure

4.25 shows the transfer function of the soil with a height of 25.0 m ($v_s = 88.6\ m/s$, $f_n = 5.57\ Hz$) and the natural frequencies of the wind turbines as determined in Section 3.5. The natural frequencies of the wind turbines do not coincide with the first natural frequency of the soil thus assuming that the quasi-static method is allowed to be used for the cyclic loading.

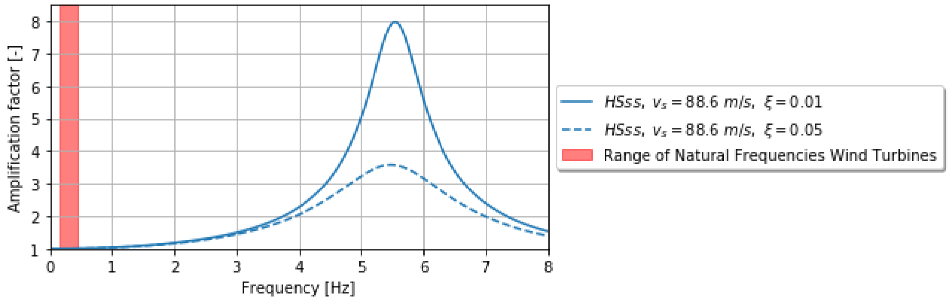

Figure 4.25: Natural frequency for the embankment geometry

The quasi-static load is applied in the same way as explained in Section 3.4. The CSR is determined using the shear stresses during the maximum and minimum of the loading cycle. Figures 4.26 to 4.29 depict the result of the CSR determination using the HSss parameter set. From the figures it can be seen that the highest absolute value of the CSR at the liquefiable soil layer is located at the center of the foundation. The maximum value of the CSR is 0.023. The profile in Figure 4.28 is therefore used as a baseline for a sensitivity analysis to determine which factors are sensitive to variation when determining the CSR. It is also observed that the CSR is reduced to almost 0 at a distance of 18.5 m away from the foundation. The CSR also is reduced to 0 at a depth of -15 m below surface level.

The definition of the CSR as presented by equation 4.1 only accounts for the shear stress amplitude and does not account for the presence of static shear stresses in the soil. The presence of the embankment geometry does not influence the CSR compared to the simplified geometry as a result. This is concluded as the shape and magnitude of the CSR at the same distance of the center line of the foundation are similar. The CSR only accounts for the amplitude of the cyclic loading induced by the wind turbine.

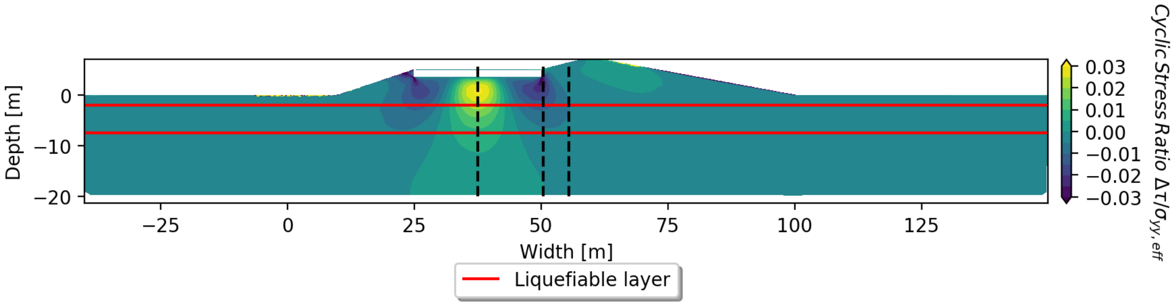

Figure 4.26: CSR contour plot, Hardening Soil Small Strain, quasi-static, embankment geometry

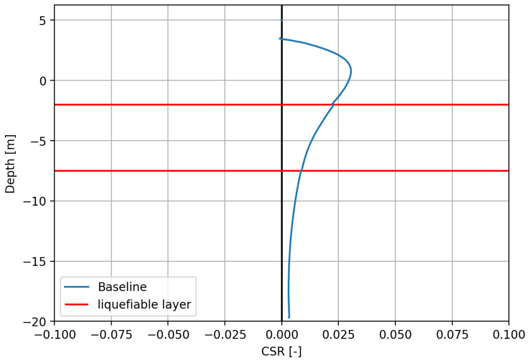

Figure 4.27: CSR profile at x = 37m, HSss, embankment geometry

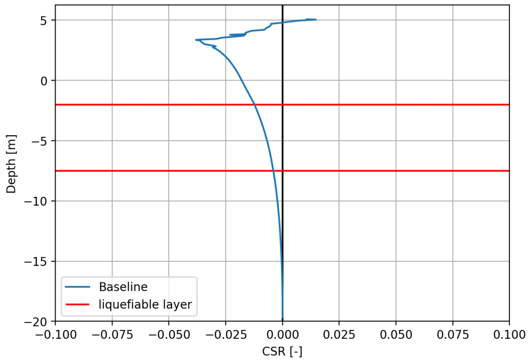

Figure 4.28: CSR profile at x = 50m, HSss, embankment geometry

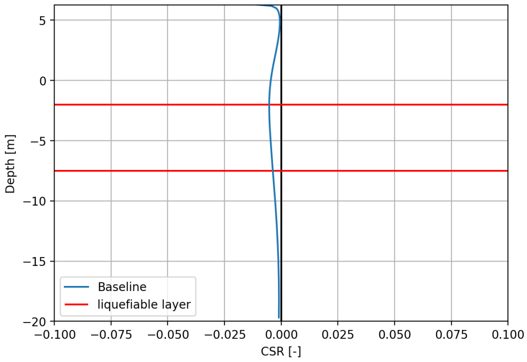

Figure 4.29: CSR profile at x = 55.5m, HSss, embankment geometry

4.3.1. Sensitivity Analysis

The sensitivity analysis is performed on the material properties of the HSss model and two geometric properties of the dike cross-section. The maximum value of the CSR at the liquefiable soil layer is used to determine the sensitivity of the parameters. The maximum value of the CSR is normative for this situation. The following soil parameters of the HSss model are analysed: the initial shear modulus (G_0 $[kN/m^2]$), 70% shear strain level ($\gamma_{0.7}$ $[-]$), friction angle (ϕ [°]), cohesion (c [kPa]), secant elastic modulus (E_{50} $[kN/m^2]$), oedometer stiffness (E_{oed} $[kN/m^2]$), unload/reload elastic modulus (E_{UR} $[kN/m^2]$) and saturated unit weight (γ_{sat} $[kN/m^3]$).

The above mentioned parameters are varied using a factor $\sqrt{2}$ resulting in an upper limit by multiplying by $\sqrt{2}$ and a lower limit by dividing by $\sqrt{2}$. A factor $\sqrt{2}$ is a common factor within engineering practice to account for the uncertainty of soil parameters and denotes the 95% uncertainty interval of a normal distribution. Only one parameter is changed from the baseline situation during each individual calculation. The cohesion is varied between 0 and 5 kPa as the initial value of c = 0 kPa. This is comparable for materials categorized as sand in Table 2b of Eurocode 7 (ECS, 2016).

Only the soil parameters of the liquefiable soil layer are varied for the sensitivity analysis and are applied for all the construction phases in the Plaxis model. Figure 4.30 shows the result of the analysis for the soil parameters. It is observed that the initial shear modulus at small strains (G_0) and the friction angle (ϕ) have the most significant impact on the CSR. The relationship between G_0 and the CSR is directly proportional, resulting in an increase of the CSR with an increase of G_0. A stiffer material attracts more stresses to the material, which sequentially results in a higher CSR. A redistribution of the stresses in the soil can be observed in the profiles generated (appendix C.2). The CSR changes throughout the whole profile.

The relation of ϕ to the CSR is inverse, resulting in a decrease of the CSR with increasing value of ϕ.

An increase of strength of the liquefiable soil layer results in a lower CSR value. It is observed that the remaining parameters are directly proportional to the CSR. The change in CSR is mainly located directly below the center of the foundation (appendix C.2). The redistribution of the stresses does not occur in the rest of the profile, which is expected as the friction angle mainly has influence on the failing of the soil.

The remaining parameters have little or almost no influence on the CSR. It is expected that the remaining stiffness parameters would have a bigger influence on the CSR, especially the unloading-reloading stiffness. The unloading-reloading stiffness was expected to have a larger impact as the CSR is determined in this mode of loading. The model showed very little plastic points, indicating that the soil is still within the elastic region and thus the un/re-loading stiffness does not have a big impact compared to the initial stiffness at small strains.

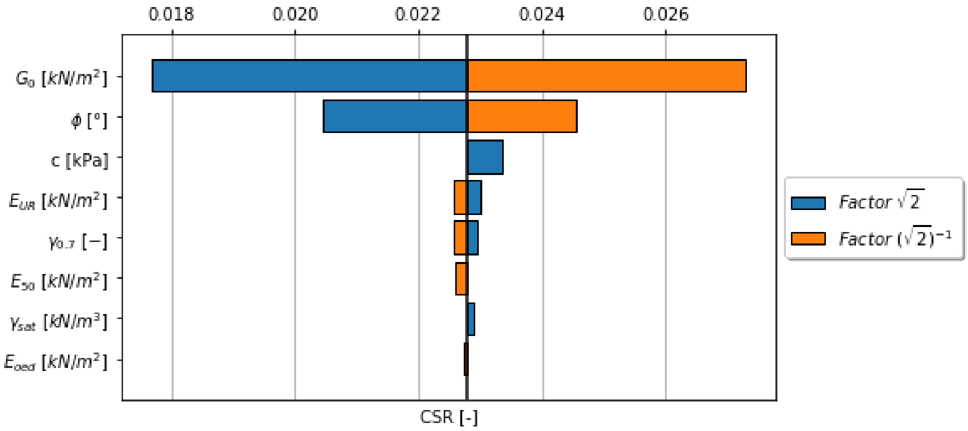

Figure 4.30: Result sensitivity analysis, soil parameters HSss

The variation of the geometric properties of the cross-section are presented separately from the geotechnical soil parameters as their variation is different. The result of the sensitivity analysis is presented in Figure 4.31. The distance to the liquefiable soil layer is varied between 7 m and 15 m, where 7 m is equal to the baseline situation. The outer water level is varied between the crest (+7 m above surface level) and toe (surface level) of the dike. These boundaries are seen as the upper and lower boundaries of the situation. In Figure 4.31 it is observed that these variations have significant impact on the CSR. However, the uncertainty of the variation of the geometric properties are less widely distributed.

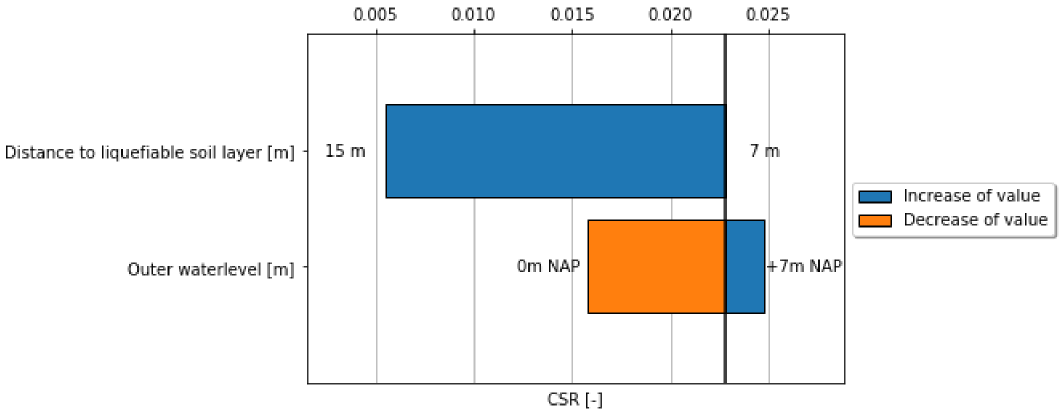

Figure 4.31: Result sensitivity analysis, geometric features

4.4. Conclusions and Discussions

The objective of this chapter is to answer the following sub-questions: ”How can time dependent shear stresses in the soil induced by an onshore wind turbine be modelled, taking into account the effect of SSI?” and ”What is the influence of irregular modes of shearing in the soil on the liquefaction behaviour?”. An analytic frequency analysis is performed to determine the natural frequencies of the wind turbine (including foundation) and the soil profile. The natural frequency of the soil is determined using a linear transfer function using both the MC and HSss parameter set (presented in appendix B). The boundary conditions of the transfer function is a 1D linear-elastic soil on top of a rigid rock layer, which is a simplification of the situation. 1D conditions directly below the foundation are assumed to create a conservative estimation. The natural frequency of the wind turbine is determined using a SDOF and nDOF system (presented in appendix B). The simplification using the mass-damper systems gives a reasonable result of the natural frequency as it has been validated using a signal provided by a wind turbine manufacturer. From the analytic analysis it is concluded that resonance is unlikely to occur as the natural frequencies do not overlap. Therefore, a quasi-static analysis should give the same result as a dynamic calculation for frequencies who do not overlap in the frequency spectrum. This conclusion is validated by performing a numerical frequency analysis.

The numerical frequency analysis consists of a quasi-static calculation and dynamic calculations at various loading frequencies. It is investigated whether or not inertia forces are generated during dynamic calculations for various loading frequencies. The dynamic loads are applied using a range of frequencies varying between 0.1 and 5.0 Hz. In the results it can be seen that the dynamic analysis at high frequency loading leads to accelerations close to the surface (approximately 1.5m deep). The accelerations and additional shear stresses in the soil can be suppressed using Rayleigh damping, but do not disappear. It is found that loading frequencies present within the amplification regions near the natural frequencies of the soil result in greater stresses in the soil. It is also observed that loading frequencies outside the amplification regions result in stresses in the soil similar to the quasi-static calculation method. Therefore, it is concluded that the quasi-static calculation method gives comparable results to the dynamic calculation method as long as the amplification region does not overlap with the loading frequency. This is in agreement with the results of the analytic frequency analysis for both the MC and HSss parameters.

The Mohr-Coulomb and Hardening Soil Small Strains models are used to determine the CSR as a result of cyclic loads induced by wind turbine foundation in sections 4.2.1 and 4.2.2, respectively. The CSR is determined using the maximum and minimum shear stress amplitude after applying the static load first. The calculations with the MC model result in a higher CSR at the location of the liquefiable soil layer with respect to the calculations using the HSss model. This also applies for situations where the liquefiable soil layer is at a different depth, e.g.: -5m or -10m below surface level (Appendix C). It is also observed that the CSR decreased with increasing distance between the foundation and the liquefiable soil layer. The MC does not include stress dependency of stiffness parameters and uses the same stiffness properties for both primary loading and unloading/reloading. The HSss model includes both stiffness and strain dependency of stiffness parameters and uses various stiffness parameters for different loading situations. As a result, the soil reacts stiffer during unloading and reloading when using the HSss model compared to the MC model. As the unloading/reloading situation is dominant, it is concluded that the HSss results in a more accurate indication of the CSR even when the result is less conservative compared to the MC model.

The cyclic stress ratio is determined underneath an embankment geometry using the Hardening Soil Small Strain material model, see section 4.3. The introduction of the embankment geometry has minimum influence on the CSR as the difference between the CSR of the horizontal and embankment geometries is minimum. In addition, the form of the CSR contours in the horizontal geometry are very similar to the contours of the embankment geometry. This might be related to the definition of the CSR, which is determined from the amplitude caused by varying the shear stresses in the soil. The CSR therefore is determined independent of the static shear stress. The influence of the static shear stresses should be accounted for in the resistance forces rather than the driving forces. Seed (1983) introduced the factor K_α to account for static shear stresses which is applied to the CRR rather than the CSR. The influence of the presence of static shear stresses is not accounted for in the liquefaction analysis as the CSR does not account for initial shear stresses and is the input for the liquefaction analysis. Thereby, only one material can be defined in the code in its current form.

A sensitivity analysis is performed to check the sensitivity of the soil parameters of the HSss model, see section 4.3.1. The initial shear modulus, G_0, and the friction angle, ϕ, have the most influence on the CSR. The remaining model parameter have little to no influence on the CSR. The un/re-loading stiffness was expected to have more significant influence as this is the mode where the CSR is determined. The soil is expected to still be within the elastic region (due to little plastic points in the Plaxis calculation) whereas the un/re-loading stiffness lies within the plastic region. This also underlines the influence of the initial shear modulus at small strains. Distance between the liquefiable soil layer and the foundation and outer water level also have a significant influence on the CSR. However, these do not have the same uncertainties as the soil parameters, hence these are not further considered here.

5

Pore Pressure Response to Cyclic Loading

Chapter 5 investigates the impact of partial drainage conditions on the liquefaction behaviour. Therefore, the following sub-question is answered in this Chapter: ”What is the influence of accounting for partial drainage response of the soil on the liquefaction behaviour?”. The purpose of the sub-question is to determine the impact of partially drained conditions with respect to fully undrained conditions on the initiation of liquefaction due to cyclic loading caused by wind turbine vibrations. Conventionally, a drained analysis assumes no generation of pore pressures whereas an undrained analysis assumes pore pressure generation as the pore fluid cannot dissipate. Partially drained conditions are defined as a state where excess pore pressures can be generated and dissipate at the same time. Generation and dissipation can have different rates and accumulation of pore pressures can occur when the rate of generation is larger than dissipation. The impact is defined as the onset and the area of the soil that reaches a state of full liquefaction ($r_u = 1.0$) during loading. Potentially, full liquefaction ($r_u = 1.0$) may not be reached in case dissipation is faster than generation.

The procedure to evaluate the pore pressure development during partially drained conditions is based on the procedure presented by Seed and Rahman (1978). The consolidation equation, or diffusion equation, is used to evaluate the excess pore pressure generation and dissipation using a cylindrical geometry in radial coordinates. The driving force of the pore pressure generation is the CSR that was determined in Chapter 4. In here, the rate of dissipation is dependent on the consolidation coefficient. The 2D consolidation equation is implemented using a finite difference scheme in Python (see section 5.1). The result of the analysis indicates whether pore pressures occur and possibly result in full liquefaction during loading of the soil, depending on the balance between pore pressure generation and dissipation.

A sensitivity analysis is performed to examine the effect of the soil properties and loading characteristics on the onset and spread of liquefaction through the soil.

5.1. Method

Seed and Rahman (1978) have developed a procedure to evaluate the pore pressure development at the seabed level as a result of cyclic wave loading. The procedure utilizes the 1D consolidation equation to account for pore pressure dissipation (also see Section A.7.2). An additional pore pressure generation term is derived based on experimental work by De Alba et al. (1975). Section A.7.2 shows the derivation of the pore pressure generation term. For this research, the effect of radial dissipation is included by converting the 1D (vertical) situation to a 3D situation using an cylindrical coordinate system. Cylindrical coordinates allow for radial and vertical dissipation of excess pore pressures. The consolidation equation then becomes:

$$c_r \left(\frac{\partial^2 u}{\partial r^2} + \frac{1}{r} \frac{\partial u}{\partial r} \right) + c_v \frac{\partial^2 u}{\partial z^2} = \frac{\partial u}{\partial t} - \frac{\partial u_g}{\partial t} \tag{5.1}$$

where u is the excess pore pressure, $\frac{\partial u_g}{\partial t}$ is the rate of generated pore pressure, r is the radial coordinate, z is the vertical coordinate and c_r/c_v are the consolidation coefficients in radial and vertical directions, respectively. The consolidation coefficient is defined as:

$$c_r = \frac{k_r E_{oed}}{\gamma_w} \tag{5.2}$$

where k_r is the hydraulic conductivity, E_{oed} is the compression stiffness and γ_w is the unit weight of water. The vertical consolidation coefficient can be determined using the corresponding hydraulic conductivity. The pore pressure generation rate is determined from the empirical relationship given by Seed and Rahman (1978). Figure 5.1 shows the nondimensionalized pore pressure with respect to the number of cycles required to reach liquefaction.

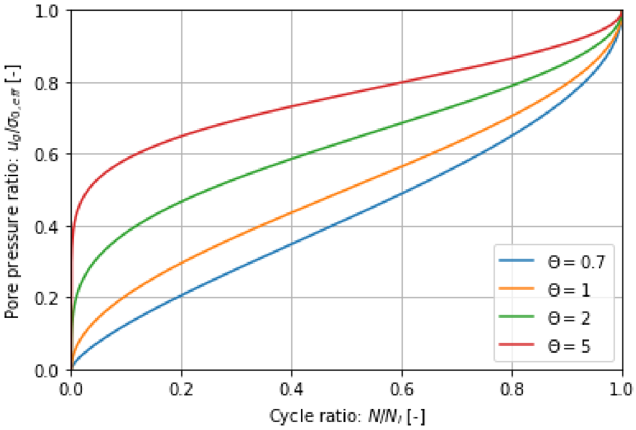

Figure 5.1: Empirical relationship describing pore pressure development at various rates, from Seed and Rahman (1978)

The empirical relationship shown in figure 5.1 is defined as:

$$\frac{u_g}{\sigma'_{v0}} = \frac{2}{\pi}\arcsin\left(\frac{N}{N_l}^{1/2\theta}\right) \tag{5.3}$$

where σ'_{v0} is the initial vertical stress, N_l is the number of cycles required to liquefy the material which is determined by equation 5.5 and Θ is a constant describing the rate of pore pressure generation . θ = 0.7 gives a good fit for general sands according to Seed and Rahman (1978). Equation 5.3 is derived with respect to time to determine the pore pressure generation rate which can be applied in the radial consolidation equation 5.1. The elaborated form of the rate of pore pressure generation term is defined as:

$$\frac{\partial u_g}{\partial t} = \frac{\sigma'_{v0}}{\Theta\pi T_D}\left(\frac{N_{eq}}{N_l}\right)\frac{1}{sin^{2\Theta-1}(\pi/2r_u)cos(\pi/2r_u)} \tag{5.4}$$

where T_D is the duration of the loading, N_{eq} is the number of cycles during the duration of loading and $r_u = u/\sigma'_{v0}$ is the pore pressure ratio. This equation allows to determine the rate of pore pressure generation at time t using the pore pressure ratio r_u at time t-1. The number of cycles required to reach liquefaction is based on the CSR calculation presented in Chapter 4. The variable input parameters of the consolidation equation can be divided into soil and load characteristics:

- Soil characteristics

    1. Consolidation coefficient
    The consolidation coefficient describes the hydro-mechanical conditions of the soil. A hydraulic conductivity of k = 0 m/s is assumed for undrained analysis resulting in $c_r,\ c_v = 0\ m^2/s$. Values of $c_r,\ c_v > 0\ m^2/s$ are applied for a partially drained analysis. The consolidation coefficient can also be unequal for radial and vertical directions to account for heterogeneous conditions in the soil.

2. Cyclic Resistance Ratio
   The CRR determines the resistance of the soil to liquefaction and is generally presented in a liquefaction curve. Cyclic tests are generally used to determine the fitting parameters, see Equation 5.5. A soil with a higher resistance to liquefaction requires a higher CSR to reach liquefaction in the same amount of cycles as a soil with a lower resistance to liquefaction. Effects such as the loading history of the soil and the relative density should be included into the CRR as they influence the resistance of the soil.

- Loading characteristics

  1. Cyclic Stress Ratio
     The CSR determines the pore pressures that are generated during one loading cycle. Seed and Rahman (1978) use linear elastic theory to determine the CSR because of wave action. For the current analysis, the CSR is a result of cyclic loading by a shallow foundation and is determined using FEM as described in Chapter 4.

$$N_l = \left(\frac{a}{CSR}\right)^{1/b} \tag{5.5}$$

  2. Loading duration
     The loading duration has influence on the period where excess pore pressures are able to accumulate in the soil. A longer loading duration results in more excess pore pressures in the soil.
  3. Loading frequency
     The loading frequency describes how many loading cycles occur within the defined loading duration. A high loading frequency results in less time for dissipation of excess pore pressures and results in accumulation of pore pressures.

Equation 5.1 expresses that excess pore pressures can be generated and dissipated simultaneously. A progressive built-up of excess pore pressures is possible when the generated excess pore pressures are larger than the dissipated excess pore pressures. Figure 5.2 illustrates this as a function of time. Liquefaction is initiated at an excess pore pressure ratio of 1.0. A strain criterion is not taken into account as the consolidation equation primarily determines the pore pressures.

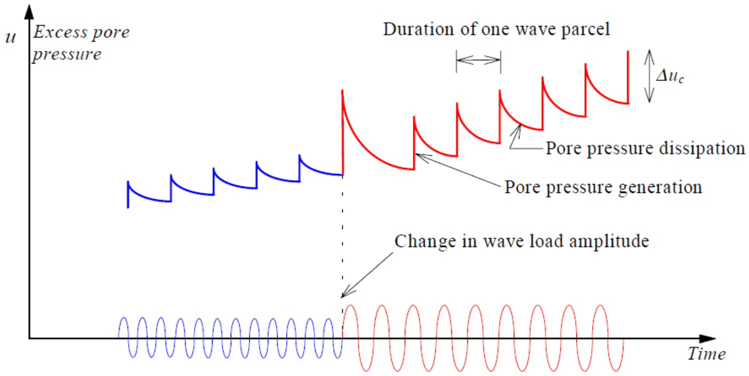
u
Excess pore pressure
Duration of one wave parcel
Δu_c
Pore pressure dissipation
Pore pressure generation
Change in wave load amplitude
Time

Figure 5.2: Schematic representation of progressive built-up of excess pore pressure, from Taiebat (1999)

After verification of the described method above a sensitivity analysis is performed in Section 5.5, to determine the influence of the following parameters on the output:

1. Time step and element size
2. Permeability (variation of k values)
3. Soil heterogeneity (variation of c_r and c_v)
4. Loading intensity (variation of CSR)
5. Loading frequency (variation of N_{eq}/T_D)

5.2. Model Implementation

This section elaborates the space and time discretization of the partial differential equation and algorithm to solve the linear equations of the problem. Equations 5.1 and 5.4 are implemented using the Finite Difference Method (FDM) in Python. A cylindrical coordinate system is adopted to simulate the directions in which the excess pore pressures are able to dissipate. Dissipation in all directions is assumed to be equal resulting in cylindrical conditions. Therefore, there is no influence of the angle which allows for a simplification of the model. Hence, only the plane indicated by r and z in Figure 5.3 is modelled. Figure 5.4 shows the r,z plane with boundary conditions. The space discretization is composed of rectangular or square elements depending on the selected geometry and number of elements. Figure 5.4 shows an arbitrary geometry with a grid of 20 by 20 square elements.

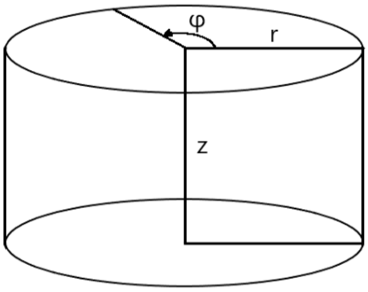

Figure 5.3: Schematic representation of a cylindrical coordinate system.

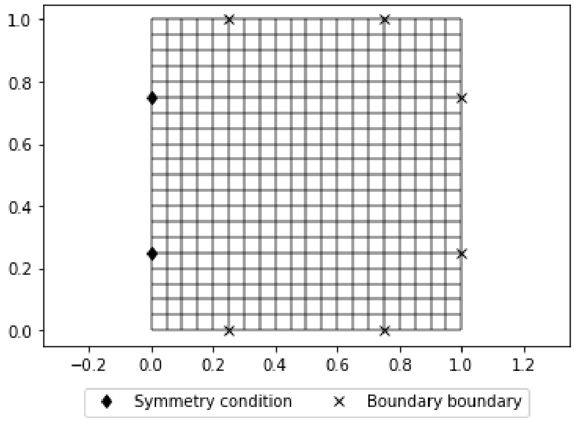

Figure 5.4: FDM grid and boundary conditions

The Θ-rule is used for time discretization and a central difference approximation for space discretization using 2^{nd} order Taylor expansions. The Θ-rule allows for multiple time discretization schemes using one formula. The Crank-Nicolson ($\Theta = 0.5$) is used as standard time discretization in the implementation. Different schemes are possible by using different values for Θ, e.g. $\Theta = 1$ (Backward Euler) and $\Theta = 0$ (Forward Euler). This results in the following discrete equation for equation 5.1 which is implemented in the code:

$$\begin{aligned}\frac{u_{i,j}^{n+1} - u_{i,j}^{n}}{\Delta t} =\\ \Theta\left(c_r \frac{u_{i+1,j}^{n+1} - 2u_{i,j}^{n+1} + u_{i-1,j}^{n+1}}{\Delta r^2} + c_r \frac{1}{r_i} \frac{u_{i+1,j}^{n+1} - u_{i-1,j}^{n+1}}{2\Delta r} + c_v \frac{u_{i,j+1}^{n+1} - 2u_{i,j}^{n+1} + u_{i,j-1}^{n+1}}{\Delta z^2} + u_{g,i,j}^{n+1}\right) +\\ (\Theta - 1)\left(c_r \frac{u_{i+1,j}^{n} - 2u_{i,j}^{n} + u_{i-1,j}^{n}}{\Delta r^2} + c_r \frac{1}{r_i} \frac{u_{i+1,j}^{n} - u_{i-1,j}^{n}}{2\Delta r} + c_v \frac{u_{i,j+1}^{n} - 2u_{i,j}^{n} + u_{i,j-1}^{n}}{\Delta z^2} + u_{g,i,j}^{n+1}\right)\end{aligned} \tag{5.6}$$

Boundary conditions have to be defined at the boundaries of the model as indicated by Figure 5.4 and can consist of Neumann, Dirichlet or Robin conditions. A special boundary condition at r = 0 needs to be implemented due to the symmetric nature of the problem to prevent singularities during the calculation. The symmetry condition is given by Equation 5.7. The initial conditions for the initial-boundary value problem are given by Equation 5.8.

$$\frac{\partial u}{\partial r}(0, z, t) = 0,\ z \in [0, Z],\ t \in [0, T] \tag{5.7}$$

$$u(r, z, 0) = I(r, z),\ (r, z) \in [0, R] \times [0, Z] \tag{5.8}$$

The system of linear equations is solved using predefined tools implemented in Python. The algorithm to set up the coefficient matrix is based on the algorithm presented in Langtangen and Linge (2016) for two dimensional diffusion. The pore pressure generation term is implemented into the algorithm where it uses the pore pressure ratio at time t at a point to determine the rate of pore pressure generation for the next step. The location where pore pressures are generated are dependent on the CSR determined by the Plaxis calculation. A 2D matrix is used to quantify the magnitude of the loading in throughout the profile. An example of the CSR profile is given by figure 5.5. In this figure, the soil layer is loaded by a shallow foundation as presented in Section 4.3.

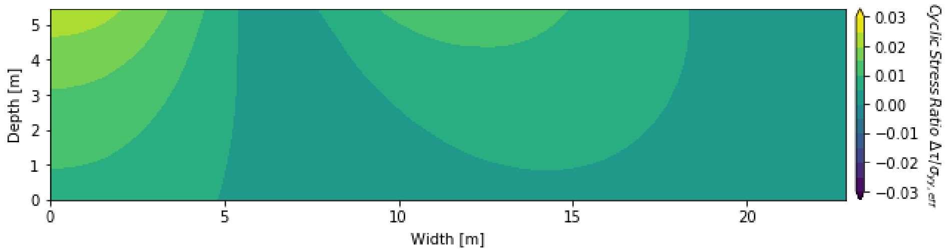

Figure 5.5: CSR as a result of cyclic loading by a shallow foundation

5.3. Verification

The Python code as described in section 5.2 is verified by comparing the results of the code with four verification cases. The first two verification cases are used to verify the applicability of the code for radial consolidation problems without pore pressure generation. 1D, or axisymmetric, and 2D situations are considered. The third verification case is similar to the second, but with different boundary conditions. The fourth verification case is used to verify the applicability of the code for cases where pore pressure generation occurs and is compared with experimental data. The goal is to check whether or not the code gives reliable results for similar situations as the case.

5.3.1. Verification case 1: 1D radial consolidation

The first verification case is used to verify the capability of the model to solve 1D radial consolidation. The results of the code are compared with an analytic solution and a numeric solution determined by Plaxis 2D. The analytic problem is first described by De Leeuw (1965). De Leeuw's problem consists of a cylindrical sample between two stiff and impermeable plates with a diameter of 2a. The sample is loaded by a uniform radial pressure q at the radial boundary. The sample contains a drainage boundary at the radial outside. De Leeuw (1965) gives the analytic solution for this problem and is depicted in Figure 5.6.

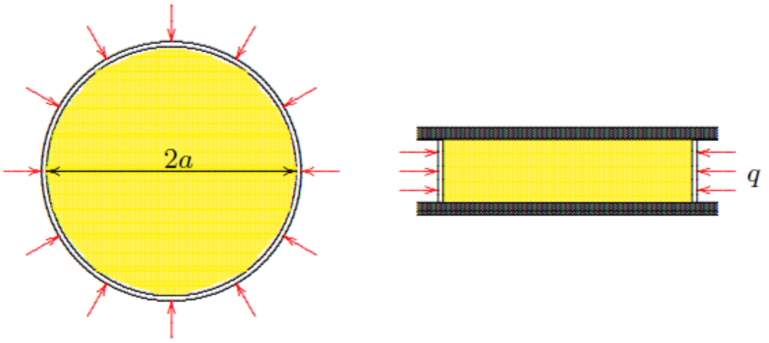

Figure 5.6: De Leeuw's problem, from Verruijt (2013)

Half of the sample is modelled using axisymmetric conditions in the Python code and Plaxis 2D. The top and bottom boundaries are impermeable and the right boundary is set to u = 0 kPa. Figure D.4 shows the result of the analytic solution, the results from Plaxis 2D and the results from the code. A good agreement between the various results are observed. Appendix D contains a more elaborate description of the analytic problem and additional cases.

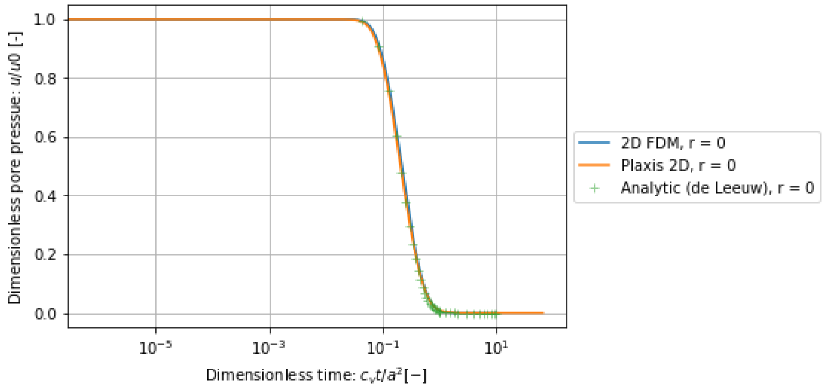

Figure 5.7: Result verification case 1: 1D radial consolidation in sand. $c_r = 0.001\ m^2/d$, $E_{oed} = 20.000$ kPa, $k_r = 5.0 \cdot 10^{-7}$ m/d

5.3.2. Verification case 2: 2D radial consolidation

The second verification case is used to verify the capability of the model to solve 2D radial consolidation. The results of the code are compared with a numeric solution determined by Plaxis 2D as no analytic solution is available for this type of problem. The problem contains a cylindrical layer between impermeable boundaries. Excess pore pressures are applied in the left upper corner of the layer. Consolidation in radial and vertical direction are both affected during the process as the problem is not axisymmetric anymore. Figure D.25 shows the initial conditions of the second verification case. Figure D.8 shows the pore pressure development in the upper left corner of the problem. This is the location where the duration of the consolidation process is the longest. From the figure it is observed that Plaxis 2D and the Python code give a similar result for radial and vertical consolidation. The consolidation process is slightly slower in the implemented Finite Difference Method compared to the results from the Plaxis 2D model. Appendix D shows additional cases and the pore pressure distribution in the layer at several times.

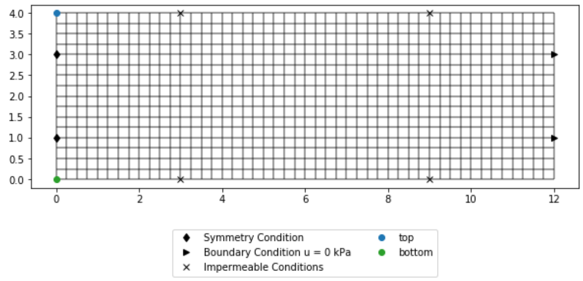

Figure 5.8: Boundary conditions verification case 2

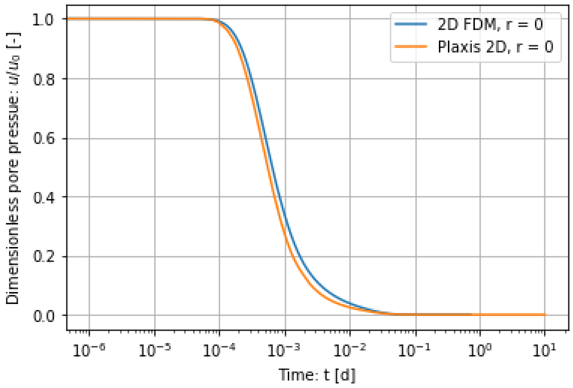

Figure 5.9: Result verification case 2: 2D radial consolidation in sand. $c_r, c_v = 0.001\ m^2/d$, $E_{oed} = 20.000$ kPa, $k_r, k_v = 5.0 \cdot 10^{-7}$ m/d

5.3.3. Verification case 3: 2D radial consolidation

The third verification case is used to verify the capability of the model to solve 2D radial consolidation. The results of the code are compared with a numerical solution determined by Plaxis 2D as no analytical solution is available for this type of problem. The problem contains a cylindrical layer where the top is impermeable and the radial size and bottom are permeable. Excess pore pressures are applied in the left upper corner of the layer. Consolidation in radial and vertical direction are both affected during the process as the problem is not axisymmetric anymore. Figure 5.10 shows the initial conditions of the third verification case. Figure D.24 shows the pore pressure development in the upper left corner of the problem. This is the location where the duration of the consolidation process is the longest. From the figure it is observed that Plaxis 2D and the Python code give quite similar result for radial and vertical consolidation. The consolidation process is slightly slower in the implemented Finite Difference Method compared to the results from the Plaxis 2D model. Differences result from different implementations of the Finite Elements and Finite Differences. Also, different time steps and mesh grids are used for the different calculations. Appendix D shows additional cases and the pore pressure distribution in the layer at several times.

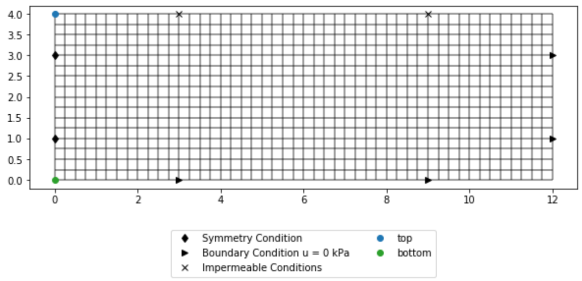

Figure 5.10: Boundary conditions verification case 3

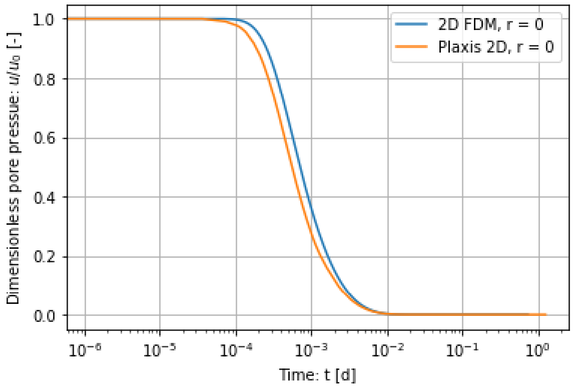

Figure 5.11: Result verification case 3: 2D radial consolidation in sand. $c_r, c_v = 0.001\ m^2/s$, $E_{oed} = 20.000$ kPa, $k_r, k_v = 5.0 \cdot 10^{-7}$ m/d

5.3.4. Verification case 4: Simulation of CDSS test

The fourth verification case is used to verify the capability of the model to generate pore pressures compared to experimental test results. The results of the code are verified using a data set of Cyclic Direct Simple Shear tests compiled by Manzari (2018). The Ottawa Sand used in the tests has an average relative density of 71.5% and is consolidated to a vertical effective stress of 100 kPa. Liquefaction of the sample is initiated at a 7.5% double amplitude shear strain for the applied shear stress ratio. The pore pressure development inside the cylindrical sample is simulated based on the CSR curve of the Ottawa Sand material. Fitting parameters for the CSR curve are a = 0.1734 and b = 0.177. Numerically, the sample is modelled as an cylindrical sample where the pore pressures are generated depending on the CSR ratio within the sample. The symmetry condition is retained, and all the boundaries are closed. Undrained sample conditions are imposed using the impermeable boundaries and a consolidation coefficient ($c_v,\ c_r$) of 1e-10 m^2/s. Figure 5.12 shows the grid and boundary conditions of the model to simulate the CDSS test. The radius of the sample is 0.034 m and the height of the sample is 0.0267 m. The experimental and numerical tests have equal dimensions.

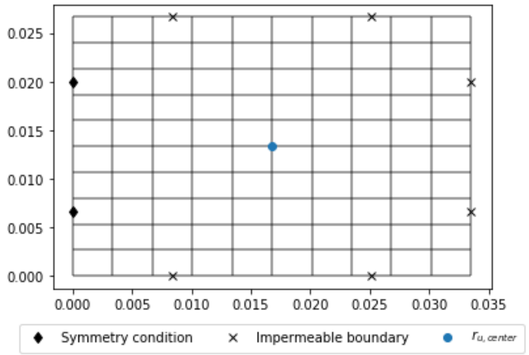

Figure 5.12: Grid and boundary conditions CDSS. $L_r = 0.034\ m$ and $L_z = 0.0267\ m$

Figure 5.13 shows the results of the experimental and numerical tests. The numerical results show a good agreement with the fitted curve from the experimental results. Figure D.43 shows the pore pressure development within the sample as a function of the number of cycles. The shape of the curve is corresponding with the experimental curve for normalized pore pressure development given by De Alba et al. (1975). The pore pressure development stagnates when initial liquefaction is reached ($r_u = 1.0$), but significant straining already occurs prior to the initiation of liquefaction. The model does not utilize a strain criteria for liquefaction like the experimental data, but a stress criteria. It is noted that significant straining can occur at a pore pressure ratio between approximately 0.8 and 1.0 (Wu et al., 2004). An additional calculation shows that variation of the θ-parameter does not affect the number of cycles required to initiate liquefaction but changes the shape of the curve. The θ parameter is a fitting parameter to describe different rates of pore pressure development in the sample. From figure 5.14 it is observed that a $\theta = 2.0$ models the initial pore pressure development most accurate for the CDSS tests performed by Manzari (2018), which is contradictory to the suggestion of $\theta = 0.7$ according to Seed and Rahman (1978). The final stage of the pore pressure development is modelled more accurately using θ = 0.7 but θ = 2.0 gives a conservative approximation of the pore pressures during the final stage. Appendix D gives the individual results of the pore pressure development for all the CDSS tests used to construct the CSR curve in figure 5.13.

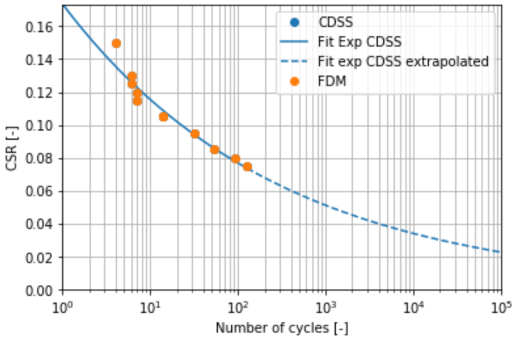

Figure 5.13: CSR curve, determined in an experimental manner and in a numerical manner

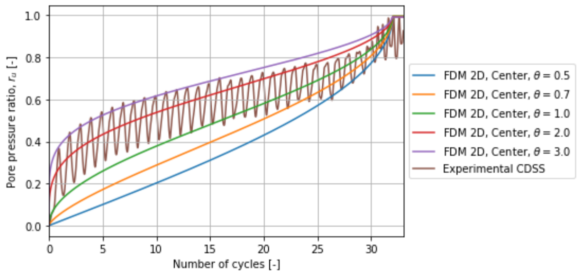

Figure 5.14: Result CDSS test with CSR = 0.095, experimental and numerical

5.4. Interpretation of the liquefaction output

This section elaborates on the interpretation of the results of the liquefaction analysis from section 5.1. The output of the analysis is given in the space domain as presented in figure 5.17 for one time step. Subsequently, the pore pressures at one location can be plotted for multiple time steps in time domain as given in figures 5.15 and 5.16.

The pore pressure development at a specific mesh point can be plotted against the time. Preference of a mesh point is given to the location where the highest CSR is present, as the highest pore pressures are expected here. Figures 5.15 and 5.16 present examples of the two modes of pore pressure development below the foundation. The figures are used for illustrative purposes and generated from the output of the liquefaction analysis of the case study presented in chapter 6. The two modes of pore pressure development are defined as:

1. Pore pressure development presented in figure 5.15, similar to the empirical curve presented in figure 5.1 until initiation of liquefaction (r_u = 1.0). A pore pressure ratio greater than 1.0 is not possible and thus remains at 1.0 until the end of loading.

2. Pore pressure development presented in figure 5.16, resembling a hyperbolic curve towards a state of equilibrium. An equilibrium between the rate of dissipation and generation results in a stagnation of the pore pressure development.

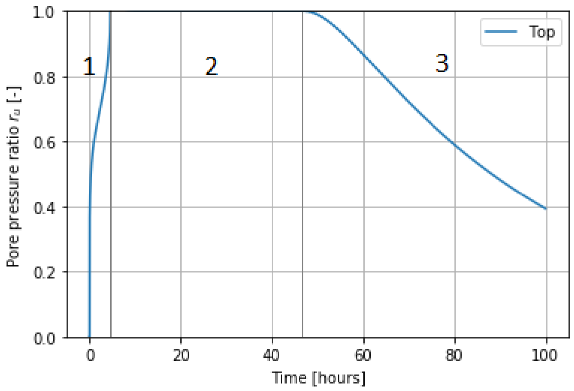

Figure 5.15: Visualization of the pore pressure development similar to the empirical curve

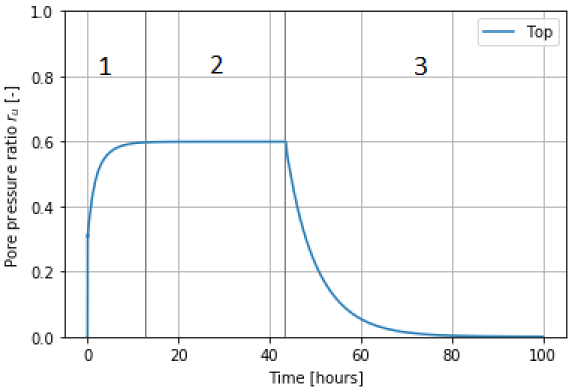

Figure 5.16: Visualization of the pore pressure development resembling a hyperbolic curve

Three generalized phases of pore pressure development are identified within these two modes of pore pressure development. They are indicated in figures 5.15 and 5.16 and defined as:

1. Built-up towards the maximum pore pressure ratio.
2. Maximum pore pressure ratio is reached (and maintained as long as loading occurs).
3. Dissipation of pore pressures.

The first phase of pore pressure development is the most important for the liquefaction analysis. An equilibrium is not yet formed and initiation of liquefaction is still possible. The maximum pore pressure ratio is reached during this first phase of the loading. From the result of the simulation, it can be concluded whether liquefaction is initiated or not. The 2D plot in the space domain (figure 5.17) shows the extent of the pore pressures and their distribution in vertical and radial direction. The combination of the two presented graphs (time and space domain) provide information about the magnitude and area of liquefaction.

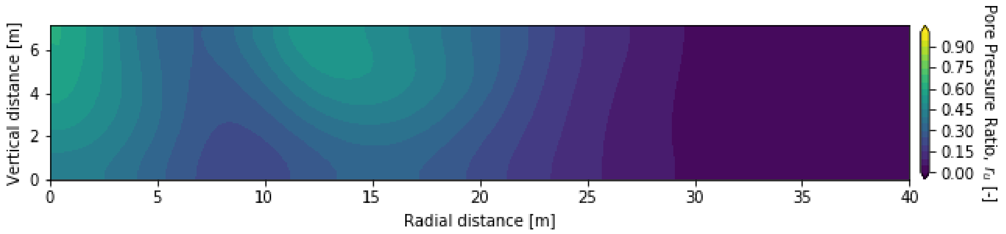

Figure 5.17: Example of the pore pressure distribution through the liquefiable soil layer. t = 1 hour

The second phase is related to the consequences of the maximum pore pressure ratio. An equilibrium of pore pressures is reached as the rate of generation and dissipation are equal. Initiation of full liquefaction results in the total loss of strength of the soil. If the ratio reaches values close to 1.0 it is stated that the soil is at risk of liquefaction, due to natural variability of the soil and the sudden failure mechanism. A smaller pore pressure ratio has less severe consequences but significant straining can occur without the total loss of strength.

The final phase shows the pore pressure development after the loading has stopped. No more pore pressures are generated and the consolidation process reduces the pore pressures to 0 kPa over time.

The influence of the (partial) loss of strength due to sustained excess pore pressures has not been investigated in this thesis. A possibility to investigate the effect of the reduction of effective stresses on the stability and deformations of the embankment would be by performing a FEA (like Plaxis) with reduced strength parameters. It is suggested to reduce the strength of the soil to 8% of the original for the areas which are fully liquefied (Robertson (2010)). A strength reduction relative to the reached maximum pore pressure should be applied at areas where full liquefaction is not initiated.

5.5. Sensitivity Analysis

This section elaborates the sensitivity analysis performed to evaluate the response of the model described in section 5.1 to a parameter variation. The following four parameters are selected as stated in Section 5.1 as well as two numeric parameters:

1. Time step and element size
2. Permeability (variation of k values)
3. Soil heterogeneity (variation of c_r and c_v)
4. Loading intensity (variation of CSR)
5. Loading frequency (variation of N_{eq}/T_D)

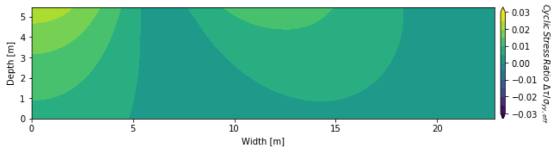

Figure 5.18: Loading conditions as calculated in Chapter 4

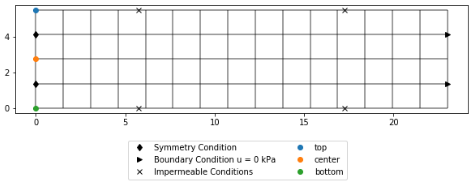

Figure 5.19: Baseline grid

The variation in parameters are chosen to be representative for a wide range of situations, including the Groningen reference case. The baseline situation for the sensitivity analysis consists of the liquefiable soil layer as presented in Chapter 3. The liquefiable soil layer consists of a homogeneous soil layer with equal consolidation coefficients in radial and vertical directions. The soil layer is enclosed by a relatively impermeable material relative to the liquefiable material. Therefore, an impermeable boundary condition is enforced at the top and bottom of the liquefiable soil layer. The symmetry condition is preserved at the center of the geometry. The influence of the loading will have no influence on the pore pressure at r → ∞. Therefore, the final boundary condition consists of u = 0 at r = L_r (Figure 5.19). The initial vertical effective stress is used as the initial condition of the soil layer is determined using a FEA. The vertical effective stress at the top of the layer is 68.5 kPa and increases to 166.1 kPa at the bottom of the layer. The CSR over the depth is the driving force of the pore pressure generation term. The CSR is determined using a FEA as elaborated in Chapter 3. Figure 5.18 indicates the location of the pore pressure generation. The pore pressure generation is only specified at the inter nodes of the grid, because this would otherwise interfere with the specified boundary conditions. This is inherent to the finite difference method, as boundary conditions have to be specified at the boundaries of the problem. Tables 5.1 and 5.2 show the values of the soil and numerical parameters used to calculate the pore pressure development by the code. Parameters are adopted from **Bot2011** (**Bot2011**) and Tasiopoulou et al. (2019).

Table 5.1: Soil parameters consolidation equation

k_r [m/s]	k_z [m/s]	k_r [m/d]	k_z [m/d]	E_{oed} $[kN/m^2]$	c_r $[m^2/s]$	c_v $[m^2/s]$	c_r $[m^2/d]$	c_v $[m^2/d]$
5.8E-7	5.8E-7	0.05	0.05	20.0E3	1.16E-3	1.16E-3	100	100

Table 5.2: Numerical and liquefaction parameters consolidation equation

L_r [m]	L_z [m]	N_r [-]	N_z [-]	T [s]	dt [s]	T_{final} [s]	N_{eq} [-]	a [-]	b [-]
23	5.5	23	6	$3.60 \cdot 10^5$	1	470448	52272	0.245	0.35

Table 5.2 contains the following parameters: L_r = radial length, L_z = vertical length, N_r = radial number of elements, N_z = vertical number of elements, T = total duration calculation, dt = time step, T_{final} = duration of loading, N_{eq} = number of load cycles during duration of loading.

5.5.1. Time Step and Element Size

First, the sensitivity of the code to variations in the time step and element size are investigated. Figure 5.20 shows the pore pressure development for five different time steps. All the calculations show comparable results of the pore pressure development during the loading and when loading has stopped. The implicit implementation of the FDM is unconditionally stable. Therefore, the results do not vary much. However, difference between the various situations is checked for convergence at different moments of the calculation. From figures 5.21 and 5.22 it is observed that a time step dt $\leq$ 10 s gives a converged solution for the pore pressure development. Therefore, a time step of dt = 10 s is used in other calculations.

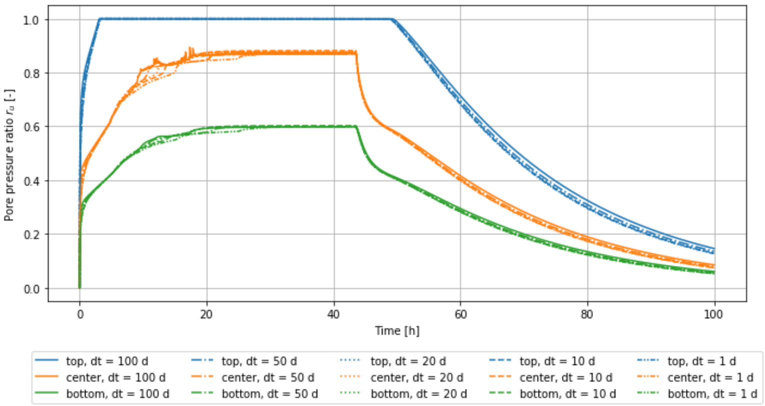

Figure 5.20: Variation in pore pressure development by changing the time step at the points assigned as in Figure 5.19.

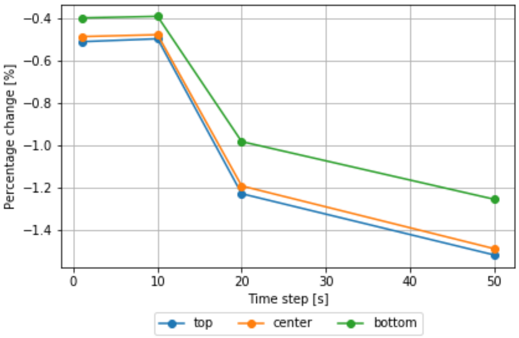

Figure 5.21: Convergence at t = 1.5 h by varying the time step

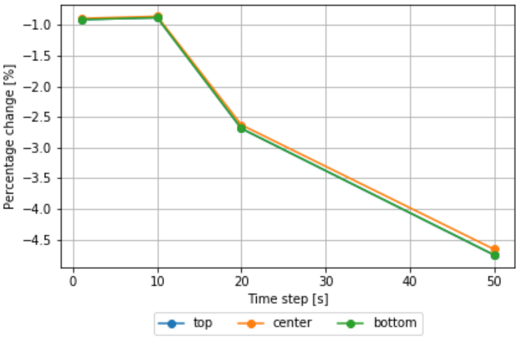

Figure 5.22: Convergence at t = 80 h by varying the time step

Figure 5.23 shows the influence of the mesh size in radial and vertical direction. The pore pressure development is measured at only the top and bottom of the symmetry condition (Figure 5.19) as the location of the middle point can differ for various mesh sizes. All calculations show comparable results. Convergence, or relative error to the last calculation, is checked for the mesh density. From figures

5.24 it is observed that the solution converges during the pore pressure generation phase, whereas in figure 5.25 it is observed that the relative error is approximately 4% at element lengths < 0.2 m. Elements sizes of 0.2 m are used for the other calculations. This corresponds to at least 5 times the length of the considered problem.

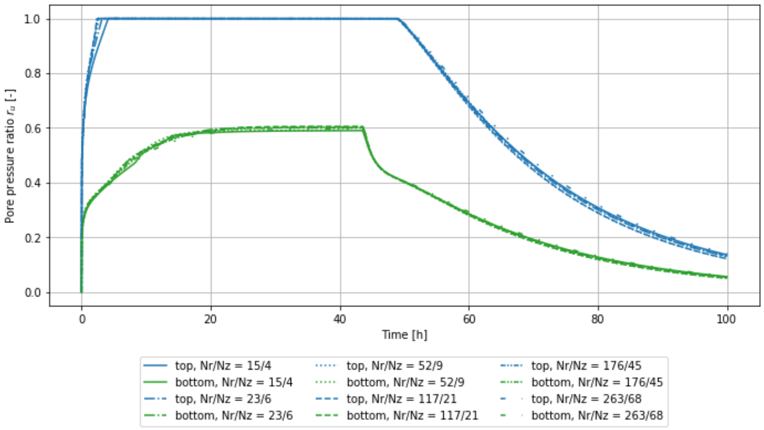

Figure 5.23: Variation in pore pressure development by changing the mesh size

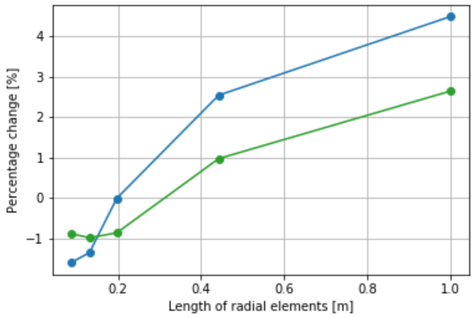

Figure 5.24: Convergence at t = 1.5 h

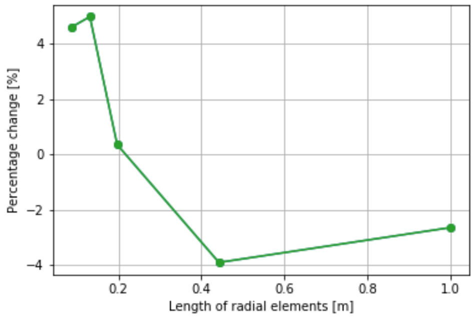

Figure 5.25: Convergence at t = 80 h

5.5.2. Permeability

Variations in permeability are modelled using three additional cases: a fully undrained case (1), a partially drained case (2) with a very porous media (Ottawa sand) and the upper limit of general sands (3). Partially drained conditions are defined as a state where excess pore pressures can be generated and dissipate at the same time. Table 5.3 shows the parameters for the baseline and additional cases.

Table 5.3: Various permeability and consolidation coefficients

Case	k [m/s]	E_{oed} $[kN/m^2]$	c_r [m$^2/s$]	c_v [m$^2/s$]
1	0.0	20.0E3	0.0	0.0
2	1.60E-4	20.0E3	3.20E-1	3.20E-1
3	1.16E-5	20.0E3	2.32E-2	2.32E-2
4	5.80E-7	20.0E3	1.16E-3	1.16E-3

Figure 5.26 shows the result of the fully undrained and partially undrained calculations. For all calculations it is observed that liquefaction is initiated earlier at the top of the soil layer where a lower initial effective stress is present and a higher CSR. For the undrained analysis it is observed that the pore pressure develops according to the experimental curve towards full liquefaction. No pore pressure

dissipation is allowed during the calculation as well as after the last loading cycle. The pore pressure ratio does not decrease and return to 0 kPa as a result of the undrained calculation.

The partially drained calculation of case 2 shows similar pore pressure development curve but requires more time/loading cycles until full liquefaction compared to the undrained analysis. Also, full liquefaction is not reached over the entire depth of the soil layer. Finally, two partially undrained calculations are performed using the properties of a very porous material. Pore pressures dissipate very fast as a result of the high consolidation coefficient, preventing a build-up of excess pore pressures. As a result, the initial pore pressure increase rapidly but an equilibrium is reached where the amount of pore pressure generation and dissipation are equal. Pore pressures drop to 0 kPa very fast at the end of the loading due to the high permeability of the materials.

Figure 5.26 shows a threshold between soils where pore pressures are able to accumulate, whilst there are also situations where an equilibrium between generation and dissipation is reached. Partial drainage therefore has significant influence on the development towards full liquefaction.

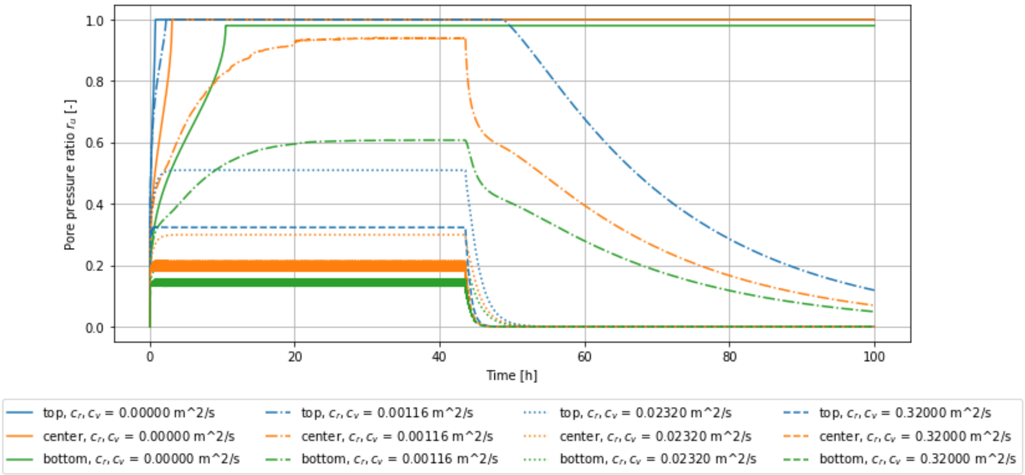

Figure 5.26: Variation in pore pressure development by changing the permeability.

5.5.3. Soil Heterogeneity

The implemented model is capable of modelling the dissipation of excess pore pressures in two directions. The impact of variable consolidation coefficients in both directions is investigated in this section. A high consolidation coefficient indicates a stiff and permeable soil (like sand) whereas a low consolidation coefficient indicates a compressible and impermeable soil (like clay). A variation between consolidation coefficients is applied to simulate the effect of a layered soil of the pore pressure development. Pore pressure dissipation is prevented by impermeable layers. Therefore, a horizontally layered soil will be more impermeable in the vertical direction relative to the radial direction.

The developed code is only capable to model a single material. The layered soil therefore needs to be simplified to a single material. The conversion from a layered material to a single material is performed using the weighted harmonic (Equation 5.9, Figure 5.27) and weighted arithmetic mean (Equation 5.10, Figure 5.28). The weighted harmonic mean is used to determine the consolidation coefficient in vertical direction while the weighted arithmetic mean is used to determine the consolidation coefficient in the radial direction.

$$x_{harmonic} = \frac{\sum d_i}{\sum \frac{d_i}{x_i}} \tag{5.9}$$

$$x_{arithmetic} = \frac{\sum x_i d_i}{\sum d_i} \tag{5.10}$$

where x is the soil parameter, d is the thickness of the layer and subscript i indicates the individual layer.

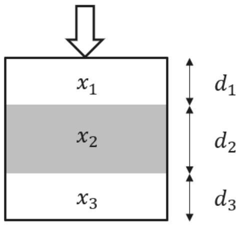

Figure 5.27: Visualization of the harmonic mean

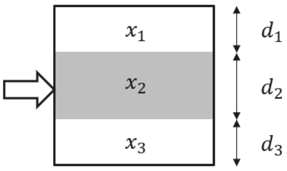

Figure 5.28: Visualization of the arithmetic mean

From the particle size distribution of the 'Wadzand'-layer (Chapter 3) it can be seen that approximately 20% of the sample consists of clay disregarding the spatial distribution of the clay layers. The remaining part of the sample consists of sand. The properties given by Table 5.4 are used to determine the harmonic and arithmetic mean.

Table 5.4: Soil properties weighted means

	k [m/s]	E_{oed} [kN/m^2]	γ_w [kg/m^3]	d [m]
Sand	1.6E-4	25.0E3	10	0.8
Clay	1.0E-9	11.4E3	10	0.2

This results in a radial consolidation coefficient $c_r = 2.85 \cdot 10^{-1}\ m^2/s$ and a vertical consolidation coefficient $c_v = 1.01 \cdot 10^{-5}\ m^2/s$ for the layered soil. This leads to the following two cases where the first simulates homogeneous conditions and the second simulates heterogeneous (layered soil) conditions.

Table 5.5: Heterogeneous soil conditions

Case	c_r [m$^2/s$]	c_v [m$^2/s$]
1	1.16E-3	1.16E-3
2	2.85E-1	1.01E-5

Figure 5.29 shows the results of the various soil conditions. It is observed in the analysis that the heterogeneous situation is less prone to liquefaction compared to the homogeneous situation. The relatively high radial consolidation coefficient allows for easy dissipation in radial direction, while the vertical consolidation coefficient is lower than case 1. The pore pressure development stagnates at a pore pressure ratio of approximately 0.35 at the top of the soil layer. Consideration of layered material can be included by using the appropriate weighted averages for radial and vertical directions. In this analysis, the soil profile is idealized as a perfectly layered system where the sand layers are assumed to be fully permeable and connected. This results in a high consolidation coefficient, while an imperfect layering with disconnections of sand layers results in a lower consolidation coefficient. A higher consolidation coefficient in radial direction allows for easier dissipation in radial direction. As a result, the maximum pore pressure ratio is lower over time which can be observed in figure 5.26.

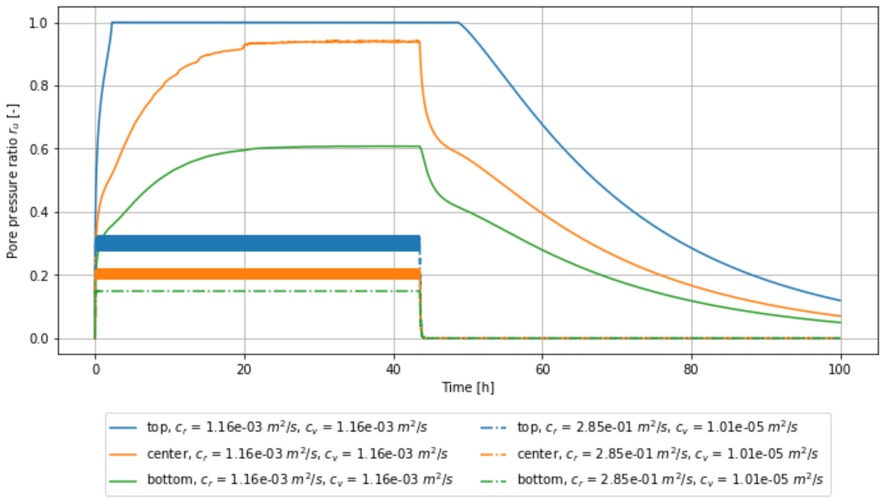

Figure 5.29: Variation in pore pressure development by changing the heterogeneity of the soil properties.

5.5.4. Loading Intensity

The influence of the load intensity is investigated using the upper and lower limits of the CSR profile calculated in Chapter 4. The uncertainties of the geometric properties of the problem are different to the uncertainties of soil parameters. Therefore, only the upper and lower limits of the CSR as a result of variable soil parameters are used.

Table 5.6: Upper and lower limits of the CSR

Case	1	2	3
CSR multiplier [-]	0.776	1.000	1.198

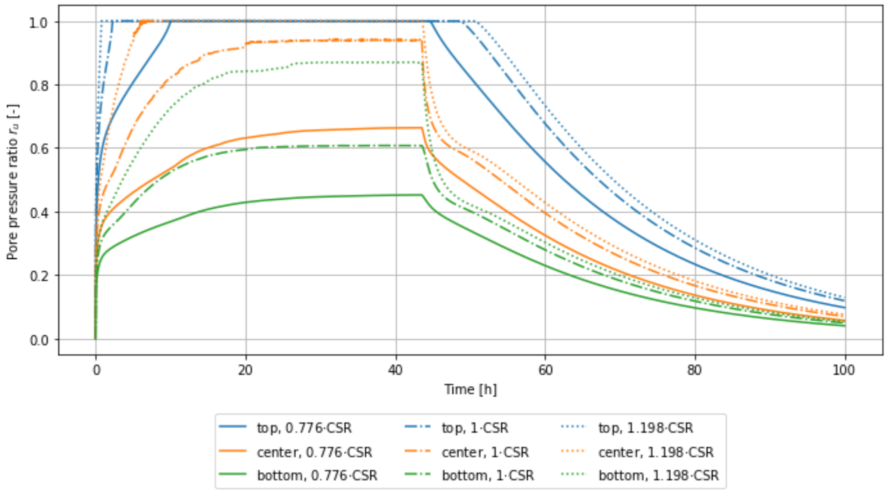

Figure 5.30: Variation in pore pressure development by changing the CSR.

Figure 5.30 shows the result of the various loading intensities. A higher CSR results in earlier onset of liquefaction at the top half of the soil layer. The depth of liquefied material reaches deeper into the soil layer compared to the baseline situation. A lower CSR still results in liquefaction at the top of the soil layer, but the pore pressure ratio at the center of the soil layer is significantly reduced.

5.5.5. Loading Frequency

The influence of the loading frequency is investigated using the upper and lower limits of the scenarios where quasi-static loading conditions apply. The loading frequency is implemented by defining the duration of the loading and the number of cycles that occur during the loading.

Table 5.7: Upper and lower limits of the CSR

Case	1	2	3
Loading frequency [Hz]	0.1	0.33	1.0

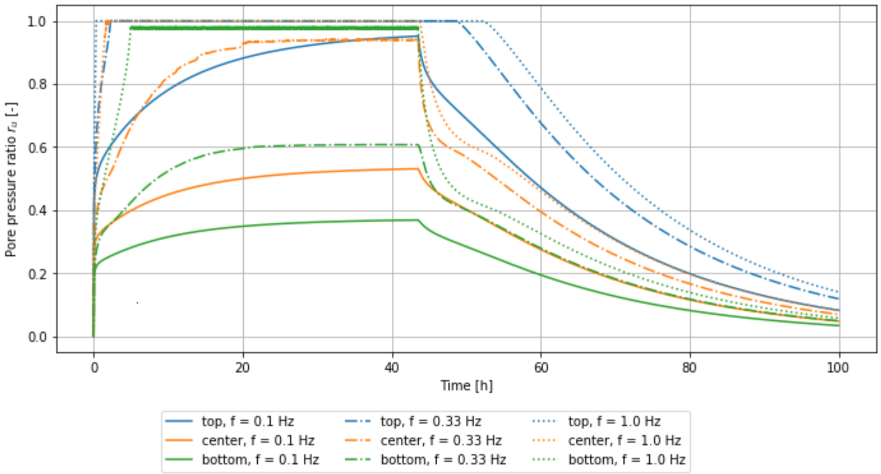

Figure 5.31: Variation in pore pressure development by changing the loading frequency.

From figure 5.31 is is observed that the loading frequency has significant impact on the development of full liquefaction. A higher loading frequency is expected to result in (faster) initiation of liquefaction. This is due to the shorter time between loading cycles which prevents the water pressures from dissipating. A loading frequency of 1.0 Hz results in full liquefaction throughout the whole depth of the soil layer. A loading frequency of 0.33 Hz results only in full liquefaction at the top of the soil layer. Full liquefaction is not observed during a loading frequency of 0.1 Hz.

5.6. Conclusions and Discussions

The objective of this chapter is to answer the sub-question ”What is the influence of accounting for partial drainage response of the soil on the liquefaction behaviour?”. To provide an answer to this question, a finite difference model is created which can account for partial drainage. In this chapter, a modification on the model introduced by Seed and Rahman (1978) is successfully implemented to determine the influence of cyclic loads by onshore wind turbines. The model is implemented in cylindrical coordinates and allows for various boundary conditions. The method is described in section 5.1.

Four verification cases are utilized to verify the model in section 5.3. These demonstrate the usability of the model in various situations and show good agreement with the implemented model. The following situations are verified: axisymmetric (1D) consolidation, radial (2D) consolidation and radial pore pressure generation. The pore pressure generation case is verified by experimental data of CDSS tests as presented by Manzari (2018). A CDSS test is not an axisymmetric test, but the number of cycles required to reach liquefaction and the pore pressure development can be reproduced in an accurate manner as observed in figure 5.14. It is observed that fitting parameter Θ is required to be calibrated on experimental results. The number of cycles required to reach liquefaction remains equal for various values of Θ, but the pore pressure development during loading can be better approximated if Θ is calibrated.

The model has two modes of pore pressure development in time: liquefaction is initiated along a curve similar to the empirical curve (section 5.1) and liquefaction is not initiated and a hyperbolic curve is formed. The two modes are presented in figures 5.15 and 5.16. Three phases are identified within the two modes of pore pressure development: built-up towards maximum pore pressure ratio, maximum pore pressure ratio is maintained and dissipation of pore pressures. The first phase is essential to determine the initiation of liquefaction and is dependent on various factor. The influence of the various factors is described in the following paragraph. The second phase shows the levelling of the pore pressures and an equilibrium is reached. At this point the rate of pore pressure generation and dissipation are equal. Significant straining can occur depending on the value of the maximum pore pressure ratio, even if full liquefaction is not reached. This phenomenon occurs due to the fact that the loading is defined using an equivalent cycle for an entire storm. Loading intensity may vary during a storm and thus is not likely to reach an equilibrium state. Pore pressure ratios close to 1.0 are considered to be at risk due to the natural variability of the soil and the sudden nature of the failure mechanism. The third phase shows the dissipation of pore pressures according to the consolidation theory. The pore pressures reduce to 0 kPa after sufficient time. The influence of the reduction of effective stresses is not considered in this thesis. Suggestions on how to account for (partial) strength loss are given in section 5.4.

The model is dependent on a large variety of parameters. Therefore, a sensitivity study of the various input parameters is performed to determine the influence their influence. The following parameters of the model are included in the analysis: permeability (variation in k values), soil heterogeneity (variation in c_r and c_v), loading intensity (variation in CSR), loading frequency (variation in N_{eq}/T_D). Below, a brief summary of the sensitivity analysis is given:

Permeability (section 5.5.2): the effect of the permeability of the soil can be included in the analysis where undrained or partially drained conditions can be simulated. Partially drained conditions are defined as conditions where excess pore pressures are able to dissipate during the loading. A material with a low permeability is more likely to liquefy compared to a material with a high permeability.

Soil heterogeneity (section 5.5.3): In addition to homogeneous conditions (i.e. permeability equal in all directions) it is possible to define heterogeneous conditions of the soil (i.e. various permeabilities in radial and vertical direction). A perfectly layered soil is modelled using the harmonic and arithmetic means so simulate perpendicular and parallel dissipation, respectively. In reality, a soil is not perfectly layered, resulting in a lower consolidation coefficient in parallel direction. It is concluded that the dissipation is dominated by the lowest resistance, or highest consolidation coefficient. The maximum pore pressure ratio is therefore highly dependent on the highest consolidation coefficient in either direction.

Loading intensity (section 5.5.4): The loading intensity of the model is dependent on the input CSR determined in chapter 4. From the sensitivity analysis it is observed that a higher CSR results faster in liquefaction or a higher maximum pore pressure ratio. This result is in line with the liquefaction curves describing the number of cycles required to reach liquefaction using a certain stress level.

Loading frequency (section 5.5.5): The loading frequency is defined by the duration of the loading/storm and the number of cycles during the storm. A higher frequency results faster in liquefaction or higher maximum pore pressure ratio. This result is as expected as a higher frequency allows for less time to dissipate pore pressures. A low frequency results in more time for the dissipation of pore pressures.

The model has a few limitations that should be considered. The dissipation model is an uncoupled model where only the pore pressures are determined. Plastic strains are connected to liquefaction behaviour, but the model is unable to determine strains. The input of the liquefaction analysis is reduced to the CSR in the soil, and neglecting the stress history of the soil. Static shear stresses do not have the impact as expected from literature. The constitutive behaviour of the soil is oversimplified, with the exception of the definition of liquefaction of the soil. As strains are not considered the applicability of the model is limited to the determination of the ultimate limit state (ULS) of the situation.

Another limitation is the difference of coordinate systems of the model and its input. The CSR input is generated using a 2D plane strain model whereas the dissipation model uses a cylindrical coordinate system. The most unfavorable situation is used as a conservative estimate to determine the CSR, but may overestimate the pore pressure generation in the in/out of plane direction of the 2D situation. Extension to a 3D Cartesian coordinate system requires a lot of effort and significantly increases the computational time and data. In addition, the model is only capable of using an equivalent cycle to define the storm load. A storm load over multiple hours consists of various load intensities whereby an equilibrium with a constant pore pressure ratio does not need to occur. A better definition of the storm may be implemented in a relatively easy manner.

6

Case Study: Oostpolderdijk

This chapter contains the results of the case study using various calculation methods to determine the initiation of liquefaction. The used methods are: the method proposed in this thesis which is an adaption to the model by Seed and Rahman (1978) and the model as described by Boulanger and Idriss (2014).

First, a practical guideline for the application of the method on a real situation is provided. This guideline includes the proposed additional steps that have been implemented in order to be able to apply the method of Seed and Rahman (1978) to the current situation. The modified method is then applied to the case of Oostpolderdijk in Groningen using the guidelines provided in section 6.1.1.

Finally, the method as presented by Boulanger and Idriss (2014) is applied to the case study Oostpolderdijk. As concluded in the literature study, the method is not directly applicable on this case as the boundary conditions vary to the principles of the method. An attempt is made to modify the CSR and magnitude scaling factor such that the method can be applied to a locally loaded soil.

The models are applied to the case of Oostpolderdijk in Groningen. Three wind turbines foundations are built on the inner berm of an embankment. A 'wadzand'-layer, as introduced in chapter 3, is present underneath the embankment. The reference engineering methodology, as explained in section 2.6.1, has been applied to analyse the susceptibility of the soil layer for liquefaction. This method correlates the possibility of densification with the generation of pore pressures. Assumptions in this analysis are the undrained response of the soil where full liquefaction is reached when surpassing the threshold value as well as infinite loading by the shallow foundation. The outcome of the analysis indicates that liquefaction of the 'wadzand'-layer is possible.

6.1. Liquefaction analysis using Seed and Rahman (1978)

This section gives a guideline of the proposed workflow on how apply the method elaborated in the thesis. As stated before, the method is a modification on the method of Seed and Rahman (1978). Thereafter, the method is applied to the case study of Oostpolderdijk and compared with the reference engineering practice.

6.1.1. Guidelines for practical applications

Figure 6.1 shows the general approach used to determine the pore water pressures in the soil. The method is divided into three general parts: the frequency analysis, CSR determination and liquefaction analysis. This corresponds to the numbered list after figure 6.1. The frequency analysis is connected to the CSR determination as the result of this analysis determines the type of calculation used in a later stage. The square boxes indicate a process, the parallelogram indicates input/output, the diamond indicates a decision and the ellipse indicates the final result.

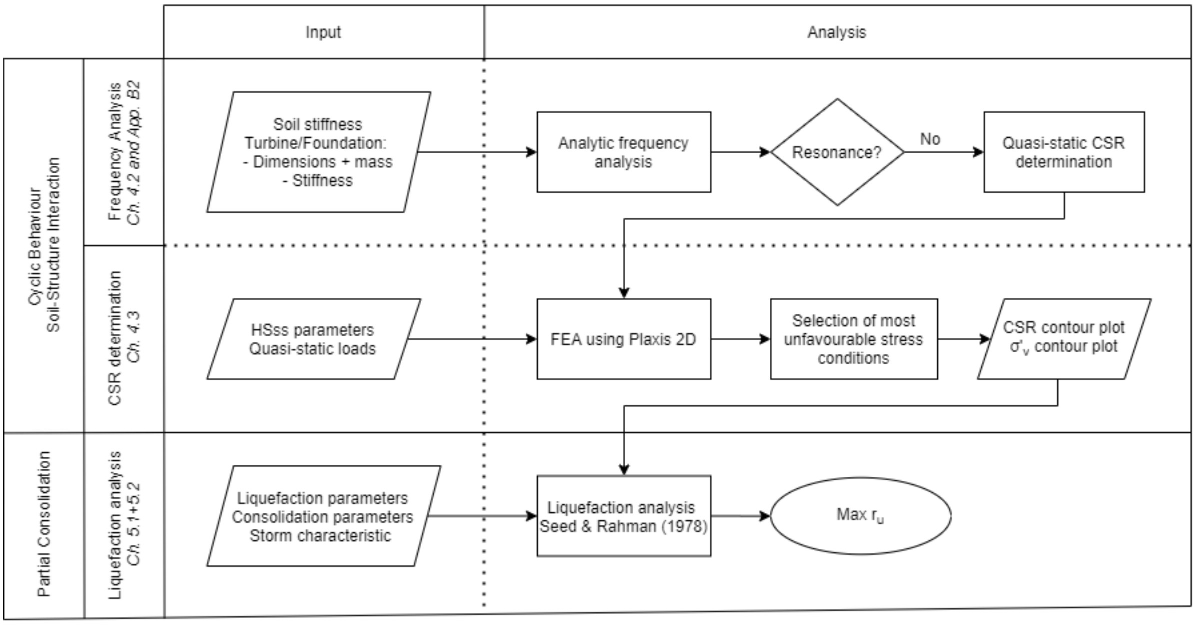
Input
Analysis
Cyclic Behaviour
Soil-Structure Interaction
Frequency Analysis
Ch. 4.2 and App. B2
Soil stiffness
Turbine/Foundation:
- Dimensions + mass
- Stiffness
Analytic frequency analysis
Resonance?
No
Quasi-static CSR determination
CSR determination
Ch. 4.3
HSss parameters
Quasi-static loads
FEA using Plaxis 2D
Selection of most unfavourable stress conditions
CSR contour plot
σ'v contour plot
Partial Consolidation
Liquefaction analysis
Ch. 5.1+5.2
Liquefaction parameters
Consolidation parameters
Storm characteristic
Liquefaction analysis
Seed & Rahman (1978)
Max ru

Figure 6.1: Overview of the method

The following steps are proposed to determine the maximum pore pressure ratio in the soil and the potential initiation of liquefaction:

1. The natural frequency of the soil and wind turbine + foundation are determined for the analytic frequency analysis. The natural frequency of the soil is determined using a linear transfer function (appendix 3.5). The soil profile located below the foundation is used to determine the natural frequency of the soil using a weighted average of the soil properties. The natural frequency of the turbine/foundation is determined using a nDOF system as explained in section 4.2 and appendix 3.5.

   The frequency analysis gives an indication of the potential of resonance. If resonance is unlikely, a quasi-static calculation method to determine the CSR is justified (see section 4.2.2). If resonance is likely to occur, a dynamic calculation method is required to determine the CSR but this method is not considered in this thesis.

   Required input:

   - Soil stiffness.
   - Soil layering.
   - Turbine/foundation dimensions.
   - Turbine/foundation mass.
   - Turbine/foundation stiffness.

2. A 2D finite element analysis (FEA) is performed to determine the CSR due to an onshore wind turbine in Plaxis 2D. Geometry of the embankment is obtained using measurement data or height data sources like www.ahn.nl. Soil stratigraphy is extracted from the geotechnical length profile or individual CPTs and boreholes. A minimum of 3 CPTs/boreholes is required to model the cross section of the embankment. The locations of the tests should be situated at the inner toe, center and outer toe to obtain an accurate image of the development of the soil layers. No boundary influence should be observed in the model. An appropriate depth of the model is approximately -30 mNAP, similar to the case study. The case study and scenario 2 of section 4.3 show that an additional width of 30 m from the inner/outer toe of the embankment is sufficient to prevent boundary influences.

The HSss soil model is used to simulate the constitutive behaviour as this model includes the stress-dependency of the soil stiffness and improved un-/reloading stiffness of the soil. Correlations as presented in section 3.3 can be applied to determine the soil parameters for the HSss model if the required soil tests are missing. From the sensitivity analysis in section 4.3.1 it is concluded that the shear modulus at small strains (G_0) and the friction angle (ϕ) have the largest impact on the CSR.

The foundation is modelled as a linear-elastic element. The forces and bending moments of the wind turbine are applied at the top of the foundation through a very stiff plate. The very stiff plate simulates the diameter of the wind turbine and accommodates bending moments into foundation.

A mesh convergence study should be applied to determine the optimal mesh density. Mesh refinements surrounding the foundation are recommended due to large stress and strain gradients are present at these locations (Potts and Zdravković (2001)). In addition, refinement of the mesh should be applied to the liquefiable soil layer.

Water levels associated with geotechnical failure mechanisms, such as macro-stability, are applied to the model. This is a conservative assumption as the strength and stiffness of the soil are the lowest. The phreatic surface in the soil body of the embankment consists of an interpolation between the outer water level and polder water level behind the embankment. In this situation, no impermeable layers are present in the dike and thus no impoundment of water is expected. If a clay core is situated at the outside of the embankment, the clay core should be fully saturated and afterwards a linear gradient of the water level is modelled towards the polder water level behind the embankment.

The model is constructed using multiple construction phases to get an accurate approximation of the stress paths in the soil. Water levels as explained in the previous paragraph are applied during the loading phases by the foundation. The quasi-static loads are applied during individual construction phases as elaborated in section 3.4. The shear stresses and vertical stresses during these construction phases are used to determine the CSR according to equation 4.1 in section 4.1. Finally, the most unfavourable situation is selected as input for the liquefaction analysis as a conservative assumption.

Required input:

- HSss soil parameters.
- Structural parameters (foundation).
- Construction phases.
- Normative water levels for geotechnical failure
- Load signal to determine the maximum and minimum quasi-static loads.

3. A liquefaction analysis using the modified model based on Seed and Rahman (1978) is performed as explained in sections 5.1 and 5.2. The model is implemented using finite differences in Python. The implemented model uses a cylindrical coordinate system with no variation in polar coordinate (only radial and vertical components are modelled). Critical aspects of this analysis are the definition of the liquefaction curve, the consolidation parameters and the storm definition.

   The liquefaction curve describes the resistance of the soil to cyclic loading. Effects such as the relative density of the soil or loading history of the soil need to be included in the liquefaction curve as they influence the resistance of the soil.

   The consolidation parameters are defined in both radial and vertical direction. This allows to assign a specific consolidation coefficient in either directions and to simulate heterogeneous soils. The permeability of the soil is the hardest to determine, especially in a layered soil, as the value for both directions needs to be determined. An estimate can be obtained by performing in-situ test, such as a dissipation test using a CPTu.

The storm definition defines how the quasi-static loads are characterized in time. Here, the duration of the storm and the number of cycles are required. From this information the loading frequency can be determined. It is only possible to use an equivalent load to describe the storm.

The model determines the pore pressure ratio in the soil during each time step. The development of the pore pressure ratio can be inspected at a single point in the soil over time or at a single time for the full soil profile as explained in section 5.4. Full liquefaction is reached when a pore pressure ratio of 1.0 is present in the soil. Situations where a pore pressure ratio close to 1.0 is present are considered at risk, as uncertainties are present and liquefaction is a sudden failure mechanism. Large straining is also expected when full liquefaction is not initiated.

Required input:

- CSR as explained in point 2 above.
- Initial vertical effective stress, σ'_v.
- Liquefaction parameters for liquefaction curve.
- Consolidation parameters (permeability and E_{oed}).
- Storm characteristics (duration and number of cycles).

6.1.2. Results Case Study Oostpolderdijk

Figure 6.2 shows an overview of the Plaxis model of the Oostpolderdijk (OPD) case study provided by Arcadis. Geotechnical parameters presented in tables E.1 to E.3 in Appendix E are adopted from the accompanying design documents. The applied construction phases are presented in figures E.8 to E.16.

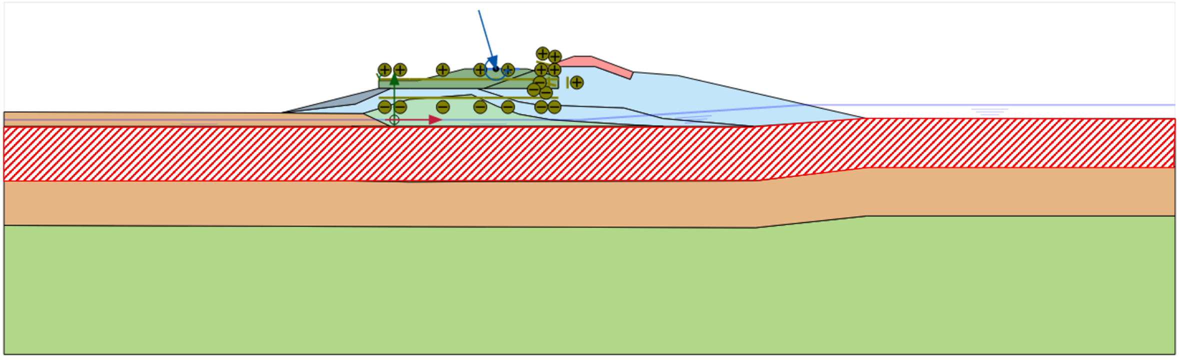

Figure 6.2: Overview of the Plaxis model of the OPD case. The liquefiable soil layers are situated between the red lines

A frequency analysis is performed to check the validity of the application of quasi-static loads, as elaborated in Chapter 4. The weighted average of the shear wave velocity is determined at the location of the shallow foundation, situated at +4 mNAP. Figure 6.3 shows the range of frequencies for the linear transfer function, SDOF system and 2DOF system. The natural frequency of the soil and wind turbine/foundation do not agree, assuming no resonance occurs and thus quasi-static loads are allowed.

Table 6.1: Frequency analysis input parameters wind turbine

r_{tower} [m]	t_{wall} [m]	L_{tower} [m]	m_{top} [ton]	$r_{foundation}$ [m]	$H_{foundation}$ [m]	E'_{tower} $[kN/m^2]$
3	0.125	98	107.35	11.5	1.75	$2.1 \cdot 10^8$

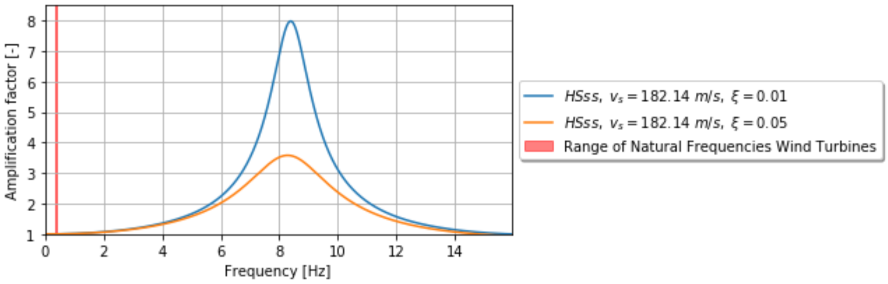

Figure 6.3: Result frequency analysis

Quasi-static loads are derived from the dynamic load signal provided by the wind turbine manufacturer. The dynamic load signal is simplified to a sine wave as presented by figures 6.4 and 6.5. The cycle with the largest double amplitude is used to determine the maximum and minimum forces applied to the foundation. This results in the quasi-static loads as presented in table 6.2. The quasi-static loads are applied in the Plaxis model to determine the CSR in the liquefiable soil layer as a result. The stresses as a result of the soil-structure interaction by loading the shallow foundation as well as the presence of the embankment are given by figures 6.6 and 6.7.

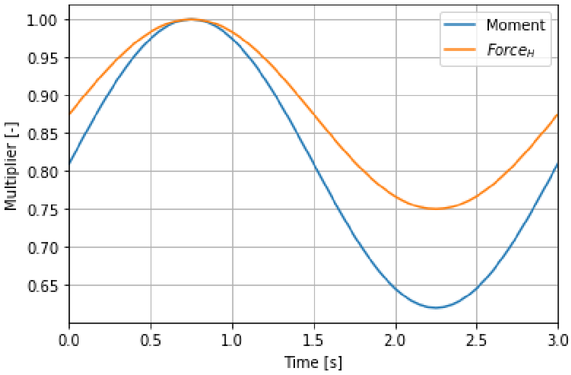

Figure 6.4: Loading signal at 0.3 Hz in time domain

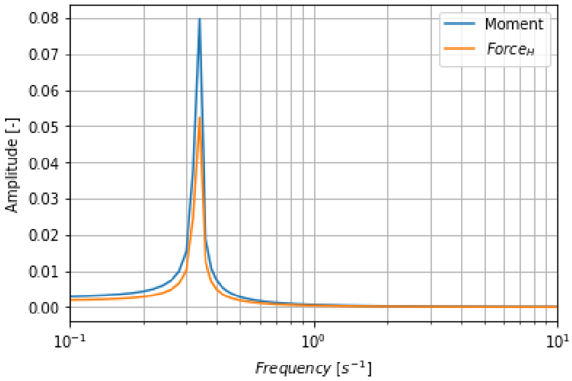

Figure 6.5: Signal in frequency domain

Table 6.2: Quasi-static loads OPD

	F_H [kN/m]	F_V [kN/m]	M [kNm/m]
Max	40.0	-120.0	2800
Min	30.0	-90.0	1736

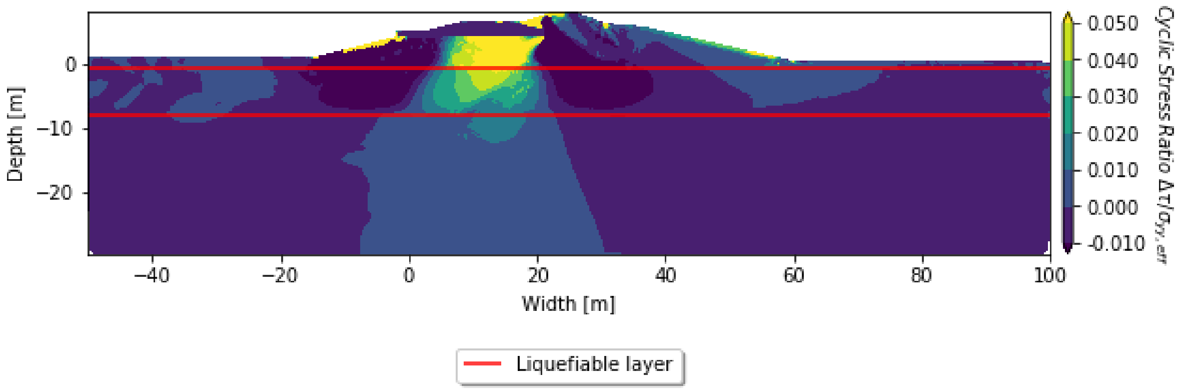

Figure 6.6: Envelope of the maximum CSR as a result of quasi-static loading at the during the final calculation phase.

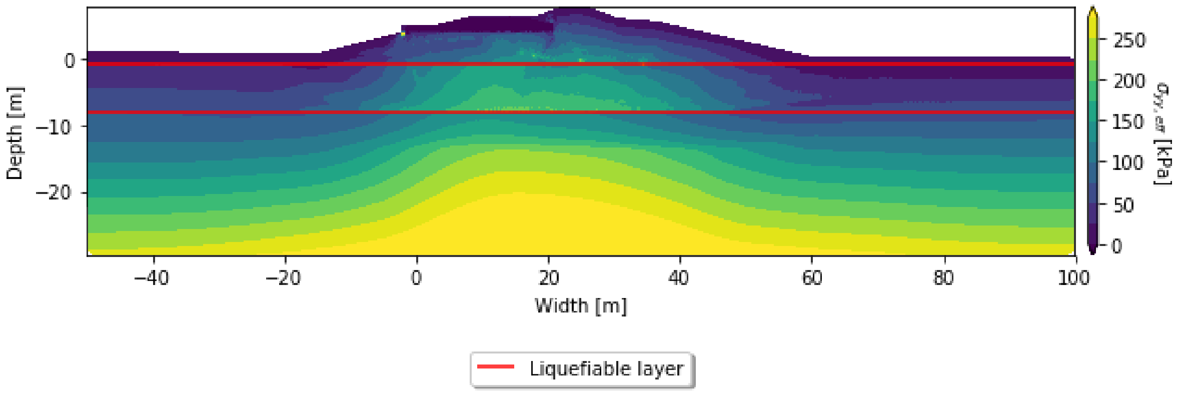

Figure 6.7: σ_v' as a result of the quasi-static loading during the final calculation phase.

The liquefiable soil layer consists of the 'wadzand'-layer and is modelled using the liquefaction curve presented in figure 3.6. This curve is constructed using equation A.4, where a and b are fitting parameters. The consolidation coefficients in radial and vertical directions are determined using the weighted average of the oedometer stiffness and the permeability of the 'wadzand'-layer as presented by equation A.32. Information regarding the determination of the permeability originates from design documents of Arcadis. In these documents, the Kozeny-Carman and Hazen correlations of the soil's permeability related to grains size and fines content are used. Table 6.3 shows the parameters used to determine the liquefaction and consolidation characteristics. The permeability is assumed to be isotropic. For the 'wadzand'-layer, it is assumed that the permeability in both radial and vertical directions are dominated by the layered material and no connection between sand layers is present. This is a conservative assumption where dissipation in radial direction is prevented. A range of permeabilities is used to analyse the potential of liquefaction of the case study as the fines content of a soil varies.

Table 6.3: Liquefaction and permeability parameters OPD

a [-]	b [-]	E_{oed} $[kN/m^2]$	$k_{r/v,min}$ [m/s]	$k_{r/v,max}$ [m/s]	$k_{r/v,min}$ [m/d]	$k_{r/v,max}$ [m/d]	$c_{r/v,min}$ $[m^2/s]$	$c_{r/v,max}$ $[m^2/s]$
0.34	0.25	14283	$9.25 \cdot 10^{-6}$	$7.56 \cdot 10^{-5}$	0.126	6.53	$2.07 \cdot 10^{-3}$	0.11

In order to capture the range of natural variability of the 'wadzand'-layer, a sensitivity of analysis is performed by varying the permeability and CSR. The magnitude of the CSR is varied within the range of 0.75 and 1.2, as determined by chapter 4. Permeability is in radial and vertical direction is assumed the same. This assumption is based on the uncertainty that the 'wadzand'-layer consists of a perfectly layered soil. Figure 6.8 shows the combination of permeability and CSR magnitude with respect to the initiation of liquefaction. Values given in the plot represent the maximum reached r_u, whereas red area indicate initiation of liquefaction in the soil profile. The plot gives the maximum observed value in any of the grid points of the considered situation during the duration of the loading. No distinction between early initiation or at the very last moment is made. From the figure it is observed that liquefaction is a risk for soil with a permeability of $\leq 1.12 \cdot 10^{-5}$ m/s = 0.97 m/d. This is within the range of variation of the geotechnical parameters of the situation and indicated by the black line. Below these values, the situation is at very much at risk for liquefaction as a small change of permeability results in a large change of maximum pore pressure. The results of the cases which are between 0.8 and 1.0 are indicated in shades of orange as full liquefaction is not reached. However, significant straining of the soil is possible as a large part of the strength is lost already. The case study is indicated by the blue dot indicating the value where the 'wadzand'-layer has an approximate value of $9.12 \cdot 10^{-6}$ m/s = 0.79 m/d. This corresponds to a fines content of approximately 20%.

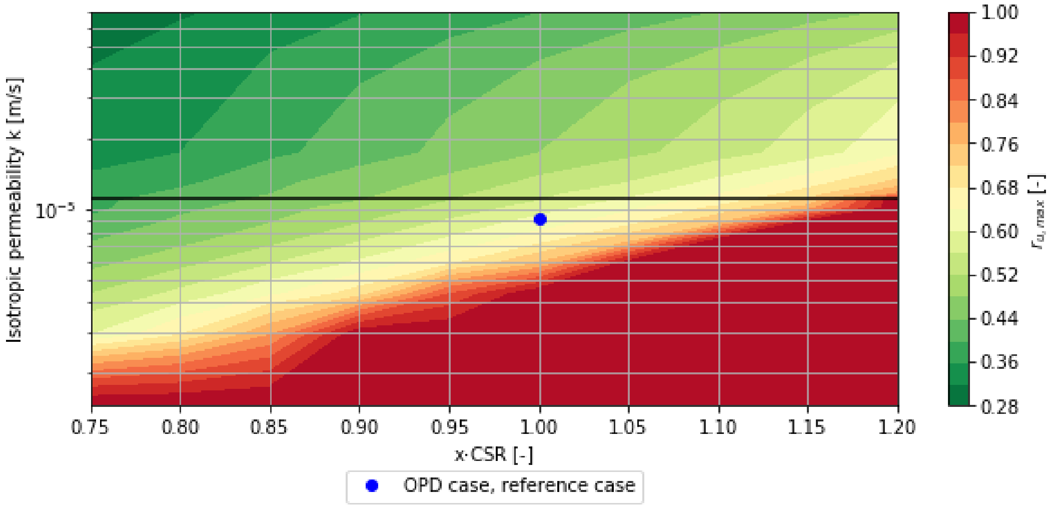

Figure 6.8: Result sensitivity analysis of the OPD case. The red line indicates the threshold value of the permeability for liquefaction. The reference parameter set of OPD is indicated by the blue dot. This case is the basis for the variation in soil parameters of a factor $\sqrt{2}$.

A simple hand calculation is performed using the cyclic stress method to illustrate the significance of the method of Seed and Rahman (1978) to the cyclic stress method. This method is described in section A.7.3 and is analogous to the method presented by Boulanger and Idriss (2014). The analysis is performed using the CRR characteristics of the soil as determined by equation A.4. An important distinction with the method of Seed and Rahman (1978) is the application of the boundary conditions used to determine the CRR which are undrained. The factor of safety which is determined therefore applies to undrained conditions during the full duration of loading. The CSR originates from the Plaxis 2D calculations by applying the cyclic loads induced by a wind turbine founded on a shallow foundation. Figure 6.9 shows the factor of safety for the most favourable method as described above, e.i. $0.7 \cdot CSR$. The figure indicates that soil layer liquefies at multiple locations while not taking into account various aspects of the situation which are included by Seed and Rahman (1978).

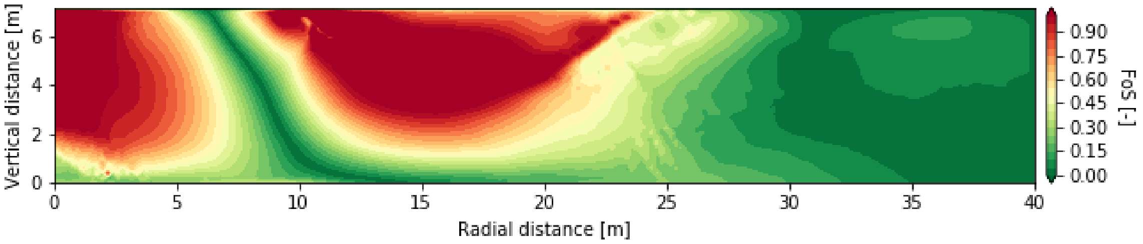

Figure 6.9: Result hand calculation of the factor of safety of the OPD case.

6.1.3. Conclusion on the application of Seed and Rahman (1978)

The reference engineering methodology assesses the instant onset of liquefaction by the exceedance of a threshold value and the hand calculation assesses the initiation of liquefaction by comparing the driving and resisting forces in the soil. These methods simplify the soil behaviour by assuming undrained conditions and an infinite number of cycles through time. The implemented model shows a gradual built-up of excess pore pressures with time in contrast to the other methods. This due the underlying empirical correlation which relates the rate of pore pressure generation based on the value of various variables, including CSR, σ_v', fitting parameters of the liquefaction curve and the previous r_u. Figure 6.8 demonstrates the effect of the permeability of the soil layer on the initiation of liquefaction with respect to the possible variation of CSR values. The time component of the model allows for partial dissipation of excess pore pressures during the loading. Including the effects of soil properties like permeability has a positive influence on the liquefaction potential. The model accounts better for the material properties of the liquefiable soil layer as well as the time factor of the loading. Therefore, giving better insight to the problem.

In the OPD case study, liquefaction is still a possibility despite that the inclusion of before mentioned properties. Liquefaction is not reached for permeabilities ≥ 0.97 m/d. However, for permeabilities ≤ 0.97 m/d, liquefaction is reached within the variation of soil. Therefore, liquefaction can not be ruled out and is still a possibility for the OPD case in its current configuration.

6.2. Liquefaction triggering procedure by Boulanger and Idriss (2014)

Section A.7.3 contains the elaboration of the principles of the widely used method created by Boulanger and Idriss (2014). This method is developed to apply liquefaction correlations to the CPT and SPT site characterization. The relationships to determine the CSR and CRR focused on earthquake applications. In order to make the method compatible with locally loaded soils, such as soils being loaded by a shallow foundation, the CSR and magnitude scaling factor (MSF) have to be modified. The CSR over the depth is determined using the method described in Chapter 4. The MSF for a locally loaded soil can be determined using the method described by appendix A of Boulanger and Idriss (2014). A weighting scheme for converting irregular loads to an equivalent number of uniform loading, which is similar to the Palmgren-Miner cumulative damage hypothesis for high-cycle fatigue of metals. This hypothesis states that a cyclic load with a low CSR but a high number of cycles should have the same effect as a cyclic load with a high CSR but with a low number of cycles. The MSF is a factor which normalizes the CSR load to the equivalent CSR load at a magnitude 7.5 event by:

$$MSF = \frac{CSR_M}{CSR_{M=7.5}} = \left(\frac{N_{M=7.5}}{N_M}\right)^b \tag{6.1}$$

where $N_{M=7.5}$ is the number of cycles for M = 7.5, N_M is the number of cycles for a given magnitude and b is the fitting parameter of the slope of the liquefaction curve. In order to determine the MSF for a locally loaded soil, the number of cycles during the loading by a storm needs to be known, the number of cycles for a M = 7.5 event and the material characteristics of the soil. Idris (1999) determined that a good estimation the number of equivalent loading cycles to liquefaction for an event where M = 7.5 which is $N_{M=7.5}$ = 15 cycles. The MSF can now be determined using the number of cycles and soil characteristics and the fact that a M = 7.5 event can be described by a specified number of loading cycles. The MSF_{max}, maximum MSF, can be determined using the number of cycles required for a M = 5.25 event which is $N_{M=5.25}$ = 2.7. Table 6.4 shows the additional parameters used to determine the local MSF. N_{local} describes the number of cycles for a loading event (storm) and b is a fitting parameter of the liquefaction curve of the ’wadzand’-layer.

Table 6.4: Local MSF parameter determination

$N_{M=7.5}$ [-]	N_{local} [-]	b [-]
15	52272	0.25

The method of Boulanger and Idriss (2014) including the modifications as described in the previous paragraphs is applied to the case study. The result is shown in figure 6.10. The CPT is performed at the inner berm of the embankment located in the center of the foundation. The most unfavourable CSR is used in the analysis. Liquefaction is triggered where the CSR is larger than the CRR. From figure 6.10 it is observed that virtually the whole layer liquefies during the load event.

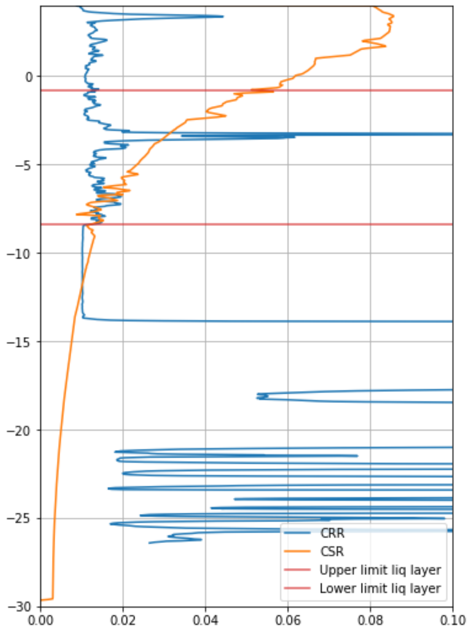

Figure 6.10: Results using Boulanger and Idriss (2014) for case OPD

6.2.1. Conclusion on the application of Boulanger and Idriss (2014)

The results of the analysis using Boulanger and Idriss (2014) are in line with the results of the reference engineering methodology as well as the method of Seed and Rahman (1978). Liquefaction of the 'wadzand'-layer is initiated for virtually the whole layer, but is more obvious at the top part of the soil layer.

The underlying database of the method is focused on cases where earthquakes have occurred rather than locally cyclic loads. The database therefore only includes cases with strong ground motions and high frequencies on which the correlations for the CRR are based. The MSF accounts for the duration/number of cycles during the loading event, but does not scale intensity and frequency of the loads. In addition, the MSF is only verified for the number of cycles related to earthquake loads. A large number of cycles is not verified and the correctness cannot be checked. The CSR can be determined reasonably but the determination of the CSR has the same limitations as discussed in chapters 4 and 5 with respect to the presence of static shear stresses. The trigger procedure is considered conservative as a result.

For the OPD case, liquefaction is triggered according to the analysis. As stated above, the loading characteristics do not comply completely but are modified so that the method can be extrapolated as accurately as possible. The method by Boulanger and Idriss (2014) is a conventional method which is applied often and a more accurate method with regard to cyclic loads is not available. The results of the method are in line with the results of the reference engineering practice and the modified method of Seed and Rahman (1978) and therefore considered to give a reasonable approximation considering the deviating boundary conditions.

7

Conclusions and Recommendations

This chapter contains the final conclusions of the thesis as well as recommendations into further research. The main objective of this thesis is to acquire more insight on how to model the key aspects of liquefaction behaviour of a soil layer cyclically loaded by onshore wind turbines on a dike. A main research question with sub-questions focused on the key aspects is formulated in order to achieve this objective.

7.1. Conclusions and Discussion

The sub-question are formulated to further specify the main question. The sub-questions are related to the individual components of the model and structured in the same manner. The main conclusions on the sub-questions are:
Pertaining the soil-structure interaction (SSI) as discussed in chapter 4:

- *How can time dependent shear stresses in the soil induced by an onshore wind turbine be modelled, taking into account the effect of SSI?*

    1. An analytic frequency analysis is performed (appendix B) to assess the occurrence of resonance. The analysis is performed by comparing the natural frequencies of the soil and the wind turbine (including the foundation). The natural frequency of the wind turbine is determined using a SDOF and 2DOF analysis. The application of the SDOF and 2DOF analyses is validated using a loading signal supplied by the wind turbine manufacturer. The calculated natural frequency corresponds with the frequency of the supplied signal, whereby it can be assumed that the calculation method and material properties are credible. Subsequently, the variety of the natural frequencies for various wind turbines was calculated, varying from small to large wind turbines.

        The natural frequency of the soil is determined using a linear transfer function for an uniform, damped soil on rigid bedrock. In reality, a rigid layer is present at great depth far beyond the boundaries of conventional engineering practice (+- 30m below surface). Due to the rigid boundary, radiation damping does not occur thereby creating conservative conditions.

        From the analytic analysis, it is concluded that resonance is unlikely as the natural frequencies of the wind turbine and soil do not overlap in the frequency spectrum. No additional stresses due to resonance are introduced into the soil resulting in the same result from a quasi-static analysis compared to a dynamic analysis. Therefore, it is stated that a quasi-static analysis gives the same result as a dynamic analysis when applying a low frequency load. This conclusion is confirmed using a numerical frequency analysis which is further elaborated at point 2. The analytical frequency analysis is computationally much less expensive compared to the numerical frequency analysis but still gives a good indication of the preferred calculation method (quasi-static or dynamic). Therefore, the analytic methodology can be applied using the frequency analysis.

2. A numerical frequency analysis is performed to validate the conclusion that a quasi-static calculation gives the same result as a dynamic calculation for a time dependent load using Plaxis 2D. The numerical frequency analysis is performed using the Mohr-Coulomb and Hardening Soil small strain model to determine the cyclic stress ratio (CSR, see section 4.1) in the soil. The Mohr-Coulomb (MC) model is applied to provide a first estimation of the soil behaviour whilst accounting for plastic behaviour. Large strain parameters are applied to the MC model as these are available in literature. However, the CSR is determined during unloading/reloading of the soil which corresponds with the small strain region of the soil. The Hardening Soil small strain (HSss) model gives a better estimation of the small strain region of the soil, includes both stiffness and strain dependency of stiffness parameters and uses various stiffness parameters for different loading situations. As a result, the soil reacts stiffer during unloading and reloading when using the HSss model compared to the MC model. The HSss therefore provides a more realistic result of the soil response in the numerical analysis.

   The results of the numerical frequency analysis show similar results compared with the analytic frequency analysis. The CRS determined in a dynamic analysis loaded by lower frequencies (depending on the used soil material) are in agreement with the CSR determined by a quasi-static analysis. The CSR determined in a dynamic analysis loaded by higher frequencies results in resonance including additional stresses and therefore do not agree with the result of the quasi-static analysis. This is in line with the predictions of the analytic frequency analysis.

3. An embankment geometry is investigated to give a more accurate approximation of the stress state in the soil. It is concluded that a quasi-static calculation can be applied for the embankment geometry from the frequency analysis. For the embankment geometry only an analytic frequency analysis is performed as the results for the simplified geometry showed good agreement. The natural frequency of the embankment geometry is determined by assuming 1D conditions. This is a conservative result as the conditions of the embankment geometry are 2D.

4. The CSR due to the embankment geometry is input for the liquefaction analysis as elaborated in section 5.1. The CSR is determined using the quasi-static method with the HSss model in Plaxis 2D. A sensitivity analysis is performed on the soil parameters of the HSss model. The parameters are individually varied using a factor $\sqrt{2}$ which corresponds to the 95% confidence interval of a normal distribution.

   The initial shear modulus at small strains, G_0, and the friction angle, ϕ, have the most influence on the CSR, see figure 4.31. The CSR varies between 78% and 120% relative to the baseline situation. A higher stiffness, G_0, results in a higher CSR as a stiffer material attracts more stresses to the material (directly proportional). A higher shear strength, ϕ, results in a lower CSR (inversely proportional). The remaining model parameters have little to no influence on the CSR as illustrated in figure 4.31. More influence of parameters such as the unloading-reloading stiffness, E_{UR}, was expected as this is the mode of loading used during the determination of the CSR. The results of the Plaxis calculations show that little/no plastic points are present in the soil and thus the soil is within the small strain region. This explains the large influence of the G_0 compared to the small influence of E_{UR}.

- *What is the influence of irregular modes of shearing in the soil on the liquefaction behaviour?*

5. The introduction of the embankment geometry on top of the horizontal soil does not affect the CSR (see figure 4.11 and 4.26) and therefore not the liquefaction behaviour. This is concluded from the almost equal graphs of the CSR between the horizontal and embankment geometries at the location of the maximum CSR. This might be related to the determination of the CSR, which is the based on the amplitude of cyclic stresses and does not take into account the static shear stress which is already present. As a result, the CSR is not influenced by the static (shear) stresses directly below the foundation and therefore no impact

is observed on the generation of pore pressures in the developed model.

The various modes of shearing (e.g. triaxial compression, triaxial extension or direct simple shear) should be accounted for in the CRR of the soil. A factor such as K_α as introduced by Seed (1983) accounts for the various modes of shearing. The CRR of only one material can be assigned to the liquefiable soil layer in the model in its current configuration. The developed method in this thesis using the CSR as a direct input, is therefore unable to account for the constitutive behaviour of the soil in various modes of shearing. The constitutive model therefore can not be modelled properly. This will be discussed in point 2 of the recommendations.

With regard to consolidation behaviour as discussed in chapter 5:

- *What is the influence of accounting for partial drainage response of the soil on the liquefaction behaviour?*

6. Seed and Rahman (1978) developed a liquefaction model for offshore applications. A modification of this model was successfully implemented to determine the influence of cyclic loads by onshore wind turbines. The developed model is implemented in cylindrical coordinates using the finite difference method where the CSR is used as input. The output of the model is verified using existing generation and dissipation models (1D/2D dissipation and 2D generation). The model results show good agreement with the verification cases, which are used to verify the pore pressure dissipation and generation separately. It is noticed that a CDSS is not an axisymmetric test, but the number of cycles required to reach liquefaction and the pore pressure development in the sample can be modelled accurately as observed in figures 5.13 and 5.14.

   During verification it is noticed that the recommended value of the fitting parameter Θ leads to an underestimation of the pore pressures during the early stages of loading. The fitting parameter should be calibrated using test data (see figure 5.14).
7. The model has two modes in which the pore pressures develop: development until liquefaction similar to the empirical curve presented in section 5.1 and a hyperbolic curve where an equilibrium of the pore pressure ratio is reached. The state of equilibrium is reached when the rate of dissipation and generation are equal and no further increase of pore pressures is observed. Three types of pore pressure development are identified within the two modes (and further elaborated in section 5.4): built-up towards maximum pore pressure ratio, maximum pore pressure reached, dissipation of pore pressures. The identification of these types are important for the consequences that the cyclic loading has on the soil. Initiation of liquefaction (r_u = 1.0) results in total loss of strength, whereas lower pore pressure ratios result in significant straining without reaching full liquefaction. Pore pressure ratios close to 1.0 are considered to be at risk due to the variability of the soil and sudden failure mechanism of liquefaction.
8. The model is dependent on a large variety of parameters. A sensitivity analysis is performed on the following parameters: the permeability, soil heterogeneity, loading intensity and the loading frequency. The analysis shows that the parameters are quite sensitive to the input parameters, requiring an accurate determination.
   (a) The permeability is varied between impermeable/undrained to very permeable/drained conditions. An undrained calculation results in full liquefaction throughout the whole profile, whereas the introduction of partially drained conditions reduces maximum pore pressure ratio, $r_{u,max}$. An equilibrium state of the pore pressures is reached for the cases where the permeability is higher as explained in section 5.4.
   (b) A layered soil is modelled by applying different consolidation coefficients in two directions. The harmonic and arithmetic mean are implemented to simulate the effect of parallel or perpendicular dissipation with respect to the layering of the soil. The harmonic and arithmetic mean allow to include the significance of the different layers based on their thickness. The pore pressure development is dominated by the material with the

highest consolidation coefficient. This approach allows to model an idealized layered soil body. It must be taken into consideration that a realistic soil is not perfectly layered. The consolidation coefficient in parallel direction to the layering will be lower in reality.

(c) The loading intensity is varied based on the results of the CSR sensitivity analysis. A higher CSR results in earlier initiation or initiation where it was previously absent. This is analogous with the liquefaction curve where a higher CSR requires less cycles to result in liquefaction.

(d) The loading frequency is varied within the region where the quasi-static calculation method can be applied. A higher frequency results in earlier initiation or initiation where it was previously absent. A higher frequency reduces the time between load cycles with the result that less pore pressures can dissipate. A lower frequency has the opposite effect.

9. The model allows to account for time dependent behaviour, such as the partial drainage response and loading characteristics, during cyclic loading events. The inclusion of these aspects reduces the maximum pore pressure in the soil profile. The determination of the CSR is generalized by a FEA, so that a larger spectrum of loading conditions can be investigated. However, experimental evidence is lacking to support the theoretical claims with respect to the pore pressure generation by the current loading conditions. Measurement data of the pore pressures must be collected in order to be able to validate the model and to determine it accuracy.
10. A limitation of the model is its uncoupled nature where only pore pressures are determined. Plastic deformations are a part of liquefaction behaviour, but within the current method are only considered in the determination of the CSR but not in the pore pressure development. The constitutive behaviour of the soil and pore water is neglected with exception of the definition of liquefaction of the soil. The model is only applicable for ULS situations as strains are not considered.
11. The CSR is determined using a plane strain model whereas the dissipation model uses cylindrical coordinates. This leads to an overestimation of pore pressure generation in the in/out-of-plane direction of the 2D situation. The dissipation model can be implemented in 2D plane strain, but then will underestimate the dissipation in in/out-of-plane direction.

Related to the conservative assumptions of the existing methods as discussed in chapter 6:

- *How do the conventional methods relate to the proposed model with regard to the assumed conservative assumptions?*

12. The reference engineering methodology assesses the initiation of liquefaction by exceedance of a shear strain threshold value by applying an infinite number of cycles for undrained conditions. This estimation is made less conservative by including a time component which allow for partial drainage. In addition, the soil and loading characteristics are defined more specific. These features are incorporated in the model of Seed and Rahman (1978). The limitations of the implemented model are found in the previous conclusions.

    The analysis for the reference situation of the Oostpolderdijk case where the wind turbine is only founded on a shallow foundation (no piles or cutter soil mixing panels) results in the absence of initiation of liquefaction. However, analysis shows that liquefaction can occur within the variation of soil characteristics of Oostpolderdijk as presented in figure 6.8. Thereby, the possibility of liquefaction can not be excluded for Oostpolderdijk. For this reason, additional measures (such as piles or cutter soil mixing panels) must be introduced to completely rule out liquefaction. This situation has not been analyzed as it is not part of this thesis.
13. The method described by Boulanger and Idriss (2014) is applied to the case study by modifying the CSR and magnitude scaling factor (MSF). The database from which the correlations of Boulanger and Idriss (2014) are determined consist of earthquake loads with strong motions, number of cycles and high frequencies. The loading scenario of the case study consists of an opposite type of loading used in the method. The modification of the MSF allows only to modify the duration/number of cycles of the loading. The effect of strong motion

and high frequencies can not be changed. Finally, the CSR, as determined in chapter 4, is used for the analysis.

The analysis indicates that the liquefiable soil layer in the case study will liquefy as the factor of safety is smaller than 1.0. Reservations on the application of this method are expressed as it is generally not applied to this type of situation. The modified MSF accounts for the large number of cycles, but is not verified. The same conclusion with respect determination of the CSR and the presents of static (shear) stresses apply for this method (conclusion 5).

However, the method is widely used and a more suitable method accounting for cyclic effects is unavailable. Both the method (minding the limitations of Boulanger and Idriss (2014)) indicate that liquefaction is likely to occur, whereby it can be assumed that the method described in the thesis gives a reasonable indication of the development of pore pressures.

Finally, the main research question is answered:

What is the best modelling strategy to simulate the key aspects of liquefaction of a soil layer underneath a dike system subjected to cyclic loading induced by an onshore wind turbine on the dike?

The key aspects related to the liquefaction of a soil are defined as cyclic loading, soil-structure interaction and the consolidation behaviour. They can be modelled using an uncoupled method where the stress-strain response of the cyclic loading and soil-structure interaction is determined using a finite element method (like Plaxis 2D) and the consolidation behaviour is determined using the model described by Seed and Rahman (1978). The model is able to determine the pore pressure development in the soil due to cyclic loads induced by an onshore wind turbine. It should be noted that the method consists of an uncoupled method where the constitutive behaviour during the consolidation calculation is ignored.

7.2. Recommendations

An uncoupled method is developed in this thesis where the pore pressures in a soil layer are determined based on the independently calculated CSR. Recommendations for further research on the topic are:

1. Validation of numerical results using real-life test data
   Multiple sensitivity analysis are performed on the numerical model to obtain an order of magnitude of the possible results. However, real-life field data is required to scientifically support the numerical results of the model. The pore pressures are the main variable of interest which can be measured at different locations in the soil layer with respect to zones where pore pressure development is expected. Daily pore pressure measurements could be sufficient as a storm has a duration of multiple days. However, hourly measurements will give a better overview on how pore pressures develop through time as storm intensity may vary within one storm.

2. Coupled effective stress analysis
   As stated in the conclusions, the constitutive behaviour of the problem is ignored with exception of the definition of liquefaction. Important is the absence of plastic deformation which is inherent to liquefaction behaviour. A coupled effective stress analysis may be used to better include the stress-strain behaviour of the soil. There is a possibility to include the effect of different shearing modes on the pore pressure development in an effective stress analysis. Constitutive models like PM4Sand and UBC-SAND have the potential to include these effects but require extensive calibration of the model parameters. Plaxis 2D has an advanced calculation option ”dynamic with consolidation” where the accumulation and dissipation of excess pore pressures during loading are determined. These results need to be validated using field measurements.

3. Assessment of stability and deformations
   The influence of (partial) strength loss is not determined in this thesis. It is suggested to determine the effect of (partial) strength loss on the stability and deformations of the embankment by reducing the strength of the soil in a FEA (like Plaxis). The model presented in this thesis is an

uncoupled model as discussed in earlier paragraphs, but the output of the model can be applied in a follow-up analysis. A reduction to 8% of the original strength is suggested when full liquefaction is initiated. A reduction relative to the reached maximum pore pressure is suggested for areas where full liquefaction is not reached (see section 5.4).

4. Various definitions of storm loading
   An equivalent load cycle is used to describe the storm load which is the driving force of the cyclic loading. This assumes that a irregular load can be described as an equivalent uniform load and results in the same pore pressure development. This is a conservative assumption. The hyperbolic curve describing the pore pressure development is a result of the equivalent load cycle which does not vary over time. In reality, the intensity of a storm varies with time resulting in a variable load on the soil. A more representative schematization of the storm intensity in- and decrease over time could lead to a more accurate result. The phases as described in section 5.4 can be better indicated.

5. Expansion of scenarios to piled foundations
   This thesis focuses on shallow foundations while wind turbines on piled foundations are not uncommon. Application of the method on deep foundations needs to be assessed.

References

API. (1993). *Planning, Designing and Constructing Fixed Offshore Platforms - Load and Resistance Factor Design* (RP 2A-LRFD) [Section G: Foundation Design]. American Petroleum Institute. Section G: Foundation Design.

Arany, L., Bhattacharya, S., Macdonald, J., & Hogan, S. (2015). Simplified Critical Mudline Bending Moment Spectra of Offshore Wind Turbine Support Structures. *Wind Energy*, *18*(12), 2171–2197.

Benz, T. (2007). *Small-strain stiffness of soils and its numerical consequences* (Doctoral dissertation). Institut für Geotechnik der Universität Stuttgart.

Biot, M. (1956). General Solutions of the Equations of Elasticity and Consolidation for a Porous Material. *Journal of Applied Mechanics*, 91–96.

Bizzarri, A., & de Looff, A. (2000). *Windmolens en Waterkeringen* (Technische eisen voor het plaatsen van windmolens op en nabij waterkeringen). Dienst Weg- en Waterbouwkunde.

Boulanger, R., & Idriss, I. (2014). *CPT and SPT Based Liquefaction Triggering Procedures* (UCD/CGM-14/01). Center for Geotechnical Modeling, University of California, Davis.

Boulanger, R., & Ziotopoulou, K. (2017). *MP4Sand (version 3.1): A sand plasticity model for earthquake engineering applications* (Report No. UCD/CGM-17/01). Center for Geotechnical Modeling, Departement of Civil and Environmental Engineering, University of Califorina, Davis, CA.

Brinkgreve, R., Engin, E., & Engin, H. (2010). Validation of empirical formulas to derive model parameters for sands, In *Numerical methods in geotechnical engineering (eds t. benz and s. nordal)*, Rotterdam, the Netherlands: CRC Press/Balkema.

Clough, R., & Penzien, J. (2003). *Dynamics of Structures*. Berkeley, CA, USA: Computers Structures, Inc.

Conte, E., & Troncone, A. (2006). One-Dimensional Consolidation Under General Time-Dependent Loading. *Canadian Geotechnical Journal*, *43*(11), 1107–1116.

CROW. (2004). *Handboek Zandboek*. CROW. Ede: CROW.

De Alba, P., Chan, C., & Seed, H. (1975). *Determination of Soil Liquefaction Characteristics by Large-Scale Laboratory Tests* (Report No. EERC 75-14). Earthquake Engineering Research Center, University of California. Seattle: Shannon & Wilson.

De Leeuw, E. (1965). The Theory of Three-dimensional Consolidation Applied to Cylindrical Bodies. *Proceedings. 6th International Conference Soil Mechanics and Foundation Engineering*, *1*, 287–290.

de Groot, M., Bolton, M., Foray, P., Meijers, P., Palmer, A., R., S., Sawicki, A., & Teh, T. (2006). Physics of Liquefaction Phenomena Around Marine Structures. *Journal of Waterway, Port, Coastal, and Ocean Engineering*, *132*(4), 227–243.

Diaz-Rodriguez, J., & Lopez-Molina, J. (2009). Strain Thresholds in Soil Dynamics.

DNV/Risø. (2002). *Guidelines for Design of Wind Turbines* [Denmark: Jydsk Centraltrykkeri]. Det Norske Veritas and Risø National Laboratory. Denmark: Jydsk Centraltrykkeri. Copenhagen.

ECS. (2016). *EN 1997-1 Eurocode 7: Geotechnical design - General rules*. European Committee for Standardization.

Elsacker, W. v. (2016). *Evaluation of Seismic Induced Liquefaction and Related Effects on Dynamic Behavior of Anchored Quay Walls* (Master's thesis). TU Delft. Delft, the Netherlands.

Harland, L., & Vugts, J. (1996). *Analytic Expression for the First Natural Period of a Stepped Tower, Using Rayleigh's Approach* (LAH - JHV 18-10-96. Project Opti-OWECS). Workgroup Offshore Technology, Delft University of Technology.

Idris, I. (1999). Lecture Notes: An update to the Seed-Idriss simplified procedure for evaluating liquefaction potential. *Proceedings, TRB Workshop on New Approaces to Liquefaction*, (FHWA-RD-99-165).

Jamiolkowski, M., Lo Presti, D., & Manassero, M. (2001). Evaluation of Relative Density and Shear Strength of Sands from CPT and DMT. *ASCE Geotechnical Special Publication*, (119).

Jefferies, M., & Been, K. (2006). *Soil Liquefaction, A Critical State Approach*. London; New York: Taylor & Francis.

Kramer, S. (1996). *Geotechnical Earthquake Engineering*. Prentice Hall, Englewood Cliffs, N.J.

Kuhlemeyer, R., & Lysmer, J. (1973). Finite Element Method Accuracy for Wave Propagation Problems. *Journal of the Soil Mechanics and Foundations Division*, *99*(5), 421–427.

Kusumawardani, R., Nugroho, U., & Tri, C., H. Lashari. (2015). Cyclic shear strain threshold on clean sand due to cyclic loading. *International Journal of Innovative Research in Science Engineering and Technology*, *4*(9), 8401–8407.

Lee, K., & Focht, J. (1975). Liquefaction Potential of Ekofisk Tank in North Sea. *Journal of the Geotechnical Engineering Division, ASCE*, *100*(GT1).

Lunne, T., & Christoffersen, H. (1983). Interpretation of cone penetrometer data for offshore sands. *Offshore Technol. Conf.; (United States)*, *1*.

Majid, T., El Ghoraiby, M., Kutter, B. L., Zeghal, M., Abdoun, T., Arduino, P., R.J., A., Beaty, M., Carey, T., Chen, Y., Ghofrani, A., Gutierrez, D., Goswami, N., Haigh, S., Hung, W., Iai, S., Kokkali, P., Lee, C., Madabhushi, S., … Ziotopoulou, K. (2018). Liquefaction experiment and analysis projects (LEAP): Summary of observations from the planning phase. *Soil Dynamics and Earthquake Engineering*, *113*, 714–743. https://doi.org/https://doi.org/10.1016/j.soildyn.2017.05.015

Makra, A. (2013). *Evaluation of the UBC3D-PLM Constitutive Model for Prediction of Earthquake Induced Liquefaction on Embankment Dams* (Master's thesis). TU Delft. Delft, the Netherlands.

Manzari, M. (2018). LEAP-2018 - Stress-strain response of Ottawa F65 sand in Cyclic Simple Shear [Dataset].

Ministerie van Verkeer en Waterstaat. (2007). *Voorschrift Toetsen op Veiligheid Primaire Waterkeringen*. Ministerie van Verkeer en Waterstaat.

Parra Bastidas, A. (2016). *Ottawa f-65 sand characterization* (Doctoral dissertation). University of California, Davis.

Plaxis. (2019a). *PLAXIS Material Models Manual* (No. V20). Delft.

Plaxis. (2019b). *PLAXIS Reference Manual* (No. V20). Delft.

Plaxis. (2019c). *PLAXIS Scientific Manual* (No. V20). Delft.

Portugal Quevedo, V. (2019). *Seismic Liquefaction Analysis of a Critical Facility with PM4Sand in Plaxis* (Master's thesis). TU Delft. Delft, the Netherlands.

Potts, D. M., & Zdravković, L. (2001). *Finite Element Analysis in Geotechnical Engineering: Volume two - Application*. London: Telford.

Randolph, M., & Gourvenec, S. (2011). *Offshore Geotechnical Engineering*. London: Taylor & Francis.

Rijksoverheid. (2019). *Climate Agreement*. Ministry of Economic Affairs and Climate Policy. The Hague.

Rijkswaterstaat. (2016). *Achtergrondrapport Ontwerpinstrumentarium 2014*. Rijkswaterstaat.

Rijkswaterstaat. (2017). *Wettelijk Beoordelingsinstrumentarium 2017*. Rijkswaterstaat.

Robertson, P. (2010). Evaluation of Flow Liquefaction and Liquefied Strength Using the Cone Penetration Test. *Journal of Geotechnical and Geo-Environmental Engineering*, *136*(6), 842–853.

Schanz, T., Vermeer, P., & Bonnier, P. (1999). The Hardening Soil model: Formulation and Verification. *Beyond 2000 in Computational Geotechnics (R.B.J. Brinkgreve, ed)*, 281–296.

Seed, H. (1983). Earthquake Resistant Design of Earth Dams. *Proceedings of Symposium on Seismic Design of Embankments and Caverns*, 41–64.

Seed, H., & Idriss, I. (1970). *Soil Moduli and Damping Factors for Dynamic Response Analyses* (Report No. EERC 70-10). Earthquake Engineering Resource Centrum, University of California. Berkeley, CA.

Seed, H., & Rahman, M. (1978). Wave-Induced Pore Pressure in Relation to Ocean Floor Stability of Cohesionless Soils. *Marine Geotechnology*, *3*(2), 123–150.

Seed, H., Wong, R., Idriss, I., & Tokimatsu, K. (1986). Moduli and Damping Factors for Dynamic Analyses of Cohesionless Soils. *Journal of Geotechnical Engineering*, *112*(11), 1016–32.

Seymour, S. (2018). *Numerical Modelling of Onshore Wind Turbine Gravity Foundations Susceptible to Cyclic Soil Degradation* (Master's thesis). University of Cape Town. South-Africa.

Sociaal-Economische Raad. (2013). *Energieakkoord voor Duurzame Groei*. Sociaal-Economische Raad.

STOWA. (2018). *Handreiking Windturbines en Waterkeringen: Techniek* (No. 53). Stichting Toegepast Onderzoek Waterbeheer. Amersfoort: STOWA.

Taiebat, H. (1999). *Three dimensional liquefaction analysis of offshore foundations* (Doctoral dissertation). The University of Sydney.

Tasiopoulou, P., Giannakou, A., Chacko, J., & de Wit, S. (2019). Liquefaction Triggering and Post-Liquefaction Deformation of Laminated Deposits. *Soil Dynamics and Earthquake Engineering*, *124*, 330–344.

Tatsuoka, F., Toki, S., Miura, S., Kato, H., Okamoto, M., Yamada, S., Yasuda, S., & Tanizawa, F. (1986). Some Factors Affecting Cyclic Undrained Triaxial Strength of Sand. *Soils and Foundations*, *26*(3), 99–116.

Terzaghi, K. Et al. (1925). *Erdbaumechanik auf bodenphysikalischer Grundlage*. F. Deuticke.

Toloza, P. (2018). *Liquefaction Modelling using the PM4Sand Constitutive Model in Plaxis 2D* (Master's thesis). TU Delft. Delft, the Netherlands.

Tsegaye, A., Molenkamp, F., Brinkgreve, R., Bonnier, P., de Jager, R., & Galavi, V. (2009). Modelling Liquefaction Behavior of Sands by means of Hypoplastic Model, In *Numerical methods in geotechnical engineering (numge)*.

Tziolas, A. (2019). *Evaluation of the PM4Sand Constitutive Model for the Prediction of Earthquake-Induced Static Liquefaction in Hydraulic Fills* (Master's thesis). TU Delft. Delft, the Netherlands.

Union of Water Authorities, & Rijkswaterstaat. (2011). *Green Deal Energie* (GD195). Unie van Waterschappen - het Rijk.

van der Tempel, J. (2006). *Design of support structures for offshore wind turbines* (Doctoral dissertation). TU Delft.

Vasquez-Herrera, A., & Dobry, R. (1988). *The behavior of undrained contractive sand and its effect on seismic liquefaction flow failures of earth structures* [Report to U.S. Army Corps of Engineers]. Renssalaer Polytecnic Institute. Report to U.S. Army Corps of Engineers.

Verruijt, A. (2013). *Theory and Problems of Poroelasticity*. Delft, the Netherlands: Delft University of Technology.

Vucetic, M., & Dobry, R. (1991). Effect of Soil Plasticity on Cyclic Response. *Journal of Geotechnical Engineering*, *117*(1), 89–107.

Wichtmann, T., Niemunis, A., & Triantafyllidis, T. (2004). Strain accumulation in sand due to drained uniaxial cyclic loading. *Cyclic Behaviour of Soils and Liquefaction Phenomena*, 233–246.

Wichtmann, T., & Triantafyllidis, T. (2012). Behaviour of Granular Soils Under Environmentally Induced Cyclic Loads, In *Mechanical behavior of soils under environmentally induced cyclic loads*, Springer.

Wijngaarden, M. v. (2017). *Gravity Based Foundations for Offshore Wind Turbines* (Master's thesis). TU Delft. Delft, the Netherlands.

Winde, H. (2015). *Finite Element Modelling for Earthquake Loads on Dykes* (Master's thesis). TU Delft. Delft, the Netherlands.

Wu, J., Kammaerer, A., Riemer, M., Seed, R., & Pestana, J. (2004). Laboratory Study of Liquefaction Triggering Criteria, In *Proceedings of 13th world conference on earthquake engineering*.

Youd, T., Idriss, I., Andrus, R., Arango, I., Castro, G., Christian, J., Dobry, R., Finn, W., Harder Jr., L., Hynes, M., Ishihara, K., Koester, J., Liao, S., Marcuson III, W., Martin, G., Mitchell, J., Moriwaki, Y., Power, M., Robertson, P., … Stokoe II, K. (October 2001). Liquefaction Resistance of Soils: Summary Report from the 1996 NCEER and 1998 NCEER/NSF Workshops on Evaluation of Liquefaction Resistance of Soils. *Journal of Geotechnical and Geoenvironmental Engineering*, *127*(10).

Sources

Andresen, L. (2015). Finite Element Analyses in design of Foundations and Anchors for Offshore Structures [Online Webinar. Accessed on 05-02-2020 via: https://www.nafems.org/].

Arcadis. (2019). *Windpark Oostpolderdijk - Cyclische Verweking*. Arcadis Nederland B.V.

Ashlock, J., & Schaefer, V. (2011). Foundation for wind turbines [Lecture Notes].

Brinkgreve, R. (2019). Behaviour of Soils and Rocks CIE4361 [Online Syllabus; accessed 29-12-2019].

de Bruin, H., van Meurs, G., & van der Meij, R. (2017). *Ontwerpuitgangspunten Hoogwateropgave Dijkverbetering Eemshaven-Delfzijl* (Design tool 1220173-005, 1220173-005-GEO-0025-ydh). Deltares.

Langtangen, H., & Linge, S. (2016). Finite Difference Computing with PDEs - A Modern Software Approach [Accessed on 15-05-2020 via: https://hplgit.github.io/fdm-book/doc/pub/book/pdf/fdm-book-4print.pdf].

Neyt, P. (1865). Verhandelingen van het Koninklijk Instituut van Ingenieurs, 1865-1866 [Accessed on 26-08-2020 via http://lib.tudelft.nl/books/].

van der Weijden, G. (2015). *General specification Lagerwey L100-2.5MW Wind Turbine Generator* (SD116ENR4). Lagerwey.

Vereniging Hollandsche Molen. (2020). Veel gestelde vragen [Accessed on 18-09-2020].

Windcollectief Wieringermeer B.V. (Various). Documents for Environmental Permit Windpark Cluster Poldermolen [Accessed on 27-05-2020 via: https://www.rvo.nl/].

A

Literature Review

Appendix A contains the relevant theoretical background information of the topic introduced in chapter 2.

A.1. Wind Turbines

The first wind mills were probably developed in China around the year 200. By the 11^{th} century, wind mills were constructed in the Netherlands as well. There used to be around 10.000 windmills, whereof approximately 1200 still remain today (Vereniging Hollandsche Molen, 2020). Windmills have been crucial to the Netherlands for centuries and have gained a lot in efficiency to extract power from the wind, especially in the 20^{th} century. Historically, windmills have been used to transform kinetic wind energy into mechanical power for grain crushing or pumping water.

Figure A.1: Examples of old and new wind power: David (4.5 MW wind turbine, at that time (2017) largest in the Netherlands) and Goliath (old wind mill from 1897) at the Eemshaven.

Today, wind turbines are used to generate electricity from kinetic wind energy. Kinetic wind energy is converted into mechanical energy as wind flow incites rotation of the blades of the wind turbine. Subsequently, the mechanical energy is converted into electrical energy by a generator and delivered into the electricity grid. Modern wind turbines are made up of slender structures with turbines rotating about horizontal or vertical axis and are equipped with one, two, three or multiple blades. This results in all of the grid connected wind turbines to be of the propeller-type on a horizontal axis on top of a tower (HAWT).

As described in section 1, a 2.5 mega-watt (MW) HAWT-type of turbine with 3 rotor blades will be constructed at the location of the case study in Groningen. Accordingly, this thesis considers a 2.5 MW turbine with 3 rotor blades inflicting similar loads.

A.1.1. Loading Situations

An onshore wind turbine is mainly loaded by wind and mechanical loads. Seismic influences are neglected for this thesis. Wind loads are mainly influenced by the wind speed. Mechanical loads are generated by rotating structural elements of the wind turbine, like the blades and nacelle. The slender geometry of the structure results in a dynamically sensitive structure. Rotations of the blades will generate inertia load in addition to gravitational forces (Arany et al., 2015). DNV/Risø (2002) makes the distinction between the following loads:

1. Inertia and gravity loads: are mass dependent loads. Inertia forces are generated through rotations, vibration or seismic activity (not considered in this thesis). Gravitational loads are due to the dead weight of the structure.

2. Aerodynamic loads: are loads generated due to interaction of the blades, rotor and nacelle with the air. Aerodynamic loads can be either static, from a stationary wind flow, or dynamic, during storms.

3. Functional loads: are loads as a result of transient operational conditions, like braking loads, yawing loads, loads due to the engagement to the generator or control system initiated loads.

4. Other loads: induced by vortex shedding, damping and vibration when stalled.

These loads are transferred to the wind turbines foundation and are cyclic in nature. Cyclic loads contain load reversals and have a periodic nature. The above mentioned loads, including the excitation force, are commonly summarized as design loads for foundations as follows and graphically presented in Figure A.2:

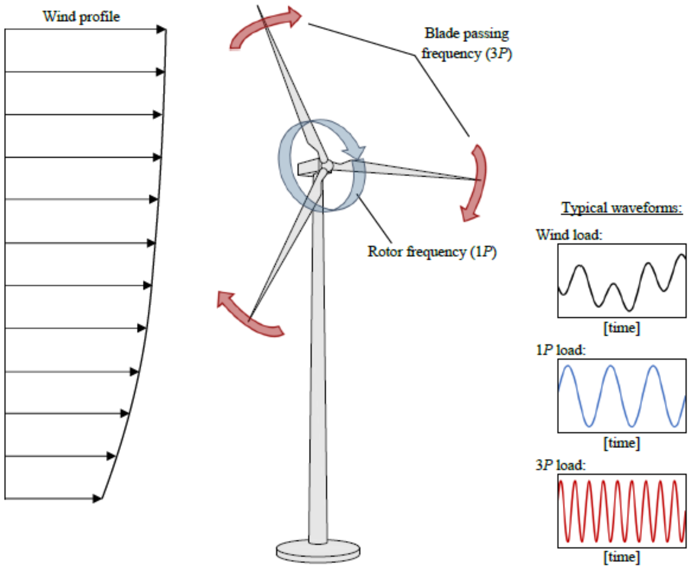

Figure A.2: Typical cyclic loads on an onshore wind turbine. After Seymour, 2018

All of these loads can be summarized in three categories, making a distinction between external en internal loads. The loads are dependent on various aspects of the wind spectrum, like wind speed and direction. The loads are generally represented using a frequency band between the lowest and highest revolutions per minute (rpm) rather than a single frequency.

1. External load: an onshore wind turbine is only loaded by wind and its turbulence. Figure A.2 gives an approximation of an average wind profile while in reality wind is highly irregular phenomena.

2. 1P loading: due to revolutions of the rotor system. This load can be induced due to rotor imbalances, wind shear and tower shadow. Modern turbines have a characteristic range within the frequency spectrum where this forcing frequency is located.

3. 3P loading: due to the passing of the blades, also called 2P when the wind turbine has 2 blades instead of 3. An internal load is generated when the blade passes in front of the tower tower and there is a temporary loss of wind load on the turbine tower (called blade shadowing effect).

Wind turbines are designed in order to avoid loading frequencies as they could result in resonance and instabilities. The first natural frequency of the tower, hub and rotor system should not coincide with the 1P or 3P ranges. A natural frequency below the 1P range results in a very soft structure (indicated by soft-soft). A natural frequency between the 1P and 3P ranges results in a soft structure (indicated by soft-stiff) and a natural frequency above the 3P range results in a stiff structure (stiff-stiff). The natural frequency of the wind turbine is dependent on the stiffness of the support structure as well as the surrounding soil.

Figure A.3 illustrates the source of two different soil-structure interaction situations associated with an onshore wind turbine on a shallow foundation, a fatigue type of problem and a resonance type of problem. Figure A.3c shows a resonance type of problem where low amplitude vibrations are acting on the structure. The 1P and 3P ranges combined with the stiffness properties of the wind turbine, foundation and soil are important information in order to prevent resonance of the structure. However, large amplitude cyclic loads can lead to a fatigue-type of problem, as illustrated by Figure A.3b. Arany et al. (2015) shows that the 1P and 3P loading has little impact (>1%) on the fore-aft (forwards, afterwards) bending moment of an offshore wind turbine, but the low frequency fore-aft bending will result in cyclic shearing of the soil. The loading frequency of the onshore wind turbine from the case study is between 0.3-0.4 Hz. Wichtmann and Triantafyllidis (2012) indicates that dynamic problems can be modelled as quasi-static problem when the loading frequency is low, e.g. $f \leq 5$ Hz. Andresen (2015) states that environmental (wind and wave) loads on offshore wind turbines are around $f = 0.2 - 0.08$ Hz and inertia effects are negligible in the soil domain.

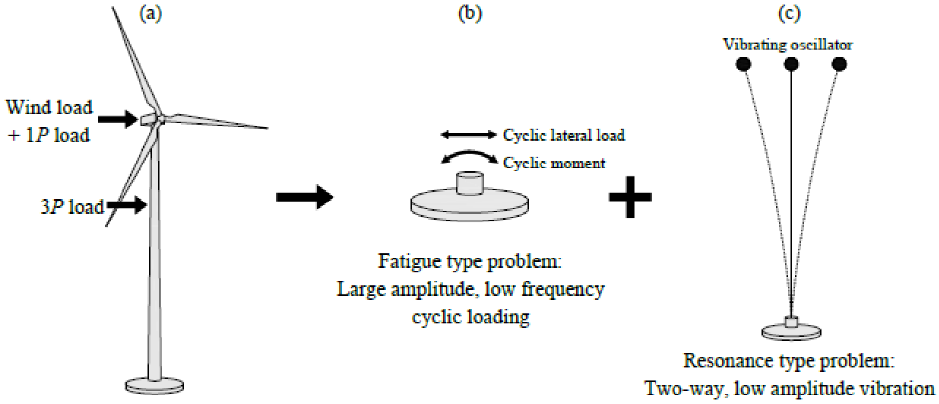
(a)
(b)
(c)
Wind load + 1P load
3P load
Cyclic lateral load
Cyclic moment
Fatigue type problem: Large amplitude, low frequency cyclic loading
Vibrating oscillator
Resonance type problem: Two-way, low amplitude vibration

Figure A.3: Loading scenarios associated with onshore wind turbines. After Seymour (2018)

A.1.2. Foundation

Onshore wind turbines are supported by shallow or deep foundations, dependent on the geotechnical conditions. The foundation is the connection to the soil and transfers the wind and mechanical loads from the turbine to load bearing layers. A shallow foundation has a larger width (W) compared to the embedment depth (D). Gravity based foundations (GBF) or caisson type of structures can be classified as a shallow foundation but are not considered in this thesis. Shallow foundations usually consist of a gravity base slab, either at the surface or buried into the soil (Figure A.4). Gravity based foundations rely on its self-weight and soil overburden to provide stability. A circular or polygonal footing is able to transfer loads from multiple directions from the super-structure into the soil. A gravity-based foundation (GBF) can be a convenient and cost-effective solution because of the relatively simple installation method. The reinforced concrete footing can be cast either prefab or in-situ.

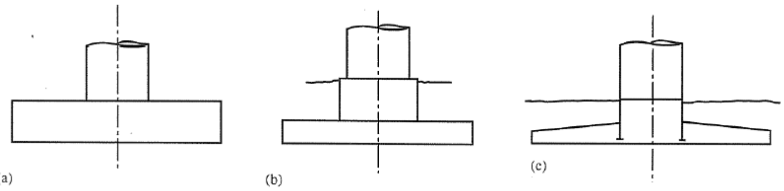

Figure A.4: Shallow Foundations: a. Plain Slab, b. Stub and Pedestal, c. Tapered Slab and Stub. Adapted from Ashlock and Schaefer (2011)

A deep foundation can be required to transfer the loads into deeper soil layers when the bearing capacity of a soil is insufficient to support a shallow foundation or when deformations become too large. Deep foundations can have a smaller width compared to the embedment depth (e.g. pile length). Deep foundations mostly consist of piles, either multiple piles or mono piles, to transfer loads into the soil through axial and lateral pile resistance. Smaller piles used in pile groups usually consist of concrete, while monopiles can be made from either concrete or steel. The resistance is generated by end bearing capacity and wall shear friction and group effect, respectively. Multiple piles are often grouped in a circular configuration to support a turbine tower (Figure A.5). Piles can be installed using by hammering, vibration or drilling. A preferred method is chosen depending on the local soil conditions and sensitivity of surroundings to construction influences. Hammering and vibratory installation of piles are often associated with vibrations within the surroundings of the construction site. Drilling results in less influences on the surroundings but is associated with a smaller bearing capacity of the piles.

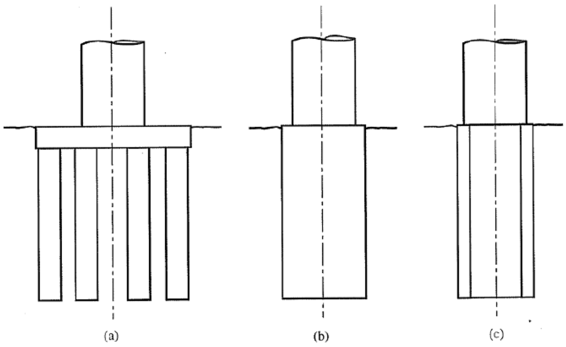

Figure A.5: Deep Foundations: a. Pile group with Cap, b. Solid Monopile, c. Hollow Monopile. After Ashlock and Schaefer (2011)

A.2. Dike Design

A dike or an embankment can be defined as a man-made water retaining soil body situated on the border of land and water. The Netherlands has a system which separates the water defence system of dikes into primary and regionally dikes. Primary dikes are situated next to the big rivers in the Netherlands, as well as the North Sea, Wadden Sea and inner lakes of the Netherlands. The maintainer of primary dikes is obligated by law, the Dutch Water act, to report on the general state of the hydrological conditions of the primary flood defences every 12 years (Waterwet 2014). Several guidelines are available to assess the safety of the dikes, like the Voorschrift Toetsen op Veiligheid (VTV2006, (Ministerie van Verkeer en Waterstaat, 2007)) and the WBI 2017 (Rijkswaterstaat, 2017). According to VTV2006, a dike design is based on hydraulic conditions with a certain defined norm frequency, in combination with design values for the geotechnical and loading parameters. In the WBI, the flooding risk is leading in the dike design. As an example, figure A.6 shows the failure mechanisms related that are considered in dike design. As this thesis is focused on liquefaction and not on dike design, no further elaboration on these mechanisms will presented.

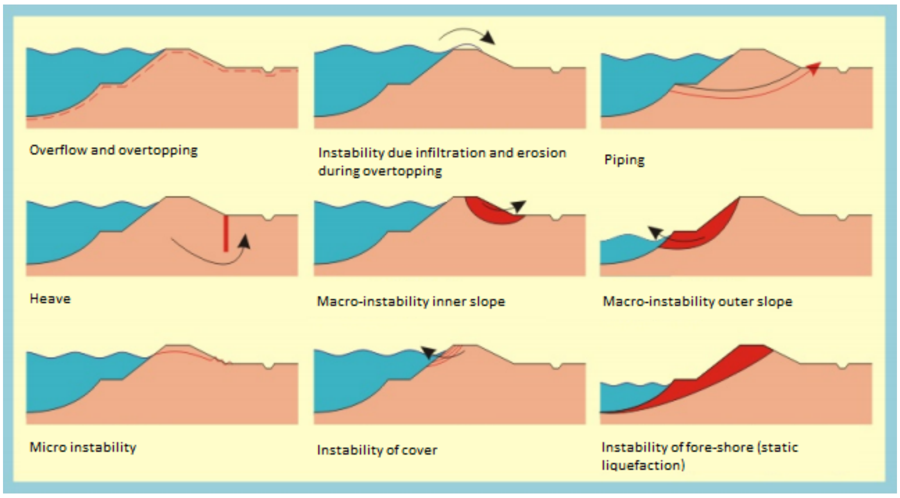
Overflow and overtopping
Instability due infiltration and erosion during overtopping
Piping
Heave
Macro-instability inner slope
Macro-instability outer slope
Micro instability
Instability of cover
Instability of fore-shore (static liquefaction)

Figure A.6: Failure mechanisms of a dike. After Ministerie van Verkeer en Waterstaat (2007)

In terms of dike safety, wind turbines and their foundations are considered 'non-water retaining' objects (Dutch: 'niet-waterkerend' object). An 'non-water retaining' object is an object present in the flood defense system but does not contribute to the water retaining function of the system which is its primary function (Bizzarri and de Looff, 2000). Ministerie van Verkeer en Waterstaat (2007) categorises the turbine foundation as a type IV construction with respect to the water safety: a construction without any water retaining functions, but object potentially has a negative influence on the flood defense if it fails. The main principle of safety remains that the non-water retaining object is not allowed to influence the dike in any negative way. A detailed analysis on the influence of the non-water retaining object on the embankment is required when the influence zone of a non-water retaining object crosses the influence zone of the embankment.

Shallow and deep foundations can have specific impacts on the dike safety and can include: settlements, inward stability, outward stability, piping, static liquefaction and cyclic liquefaction. Figure A.7 gives a visual representation of the poitential failure mechanisms. The main expected consequence of the placement of a wind turbine on a shallow foundation is the addition of external loads on the soil body and potential (differential) settlements and increased effective stresses leading to a reduction of crest height or cracks in the soil body. The placement of a wind turbine using a deep foundation can include the disruption of the soil body and impounding of the ground water level around the deep foundation as well as additional loading. Piles can create preferential paths for piping wells if the piles puncture sealing soil layers.

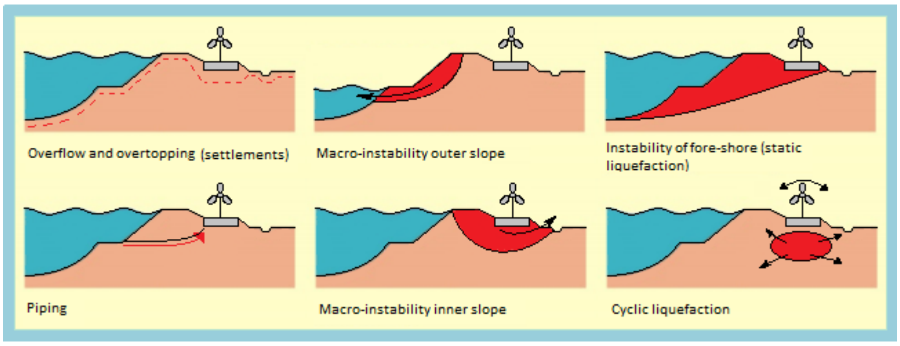
Overflow and overtopping (settlements)
Macro-instability outer slope
Instability of fore-shore (static liquefaction)
Piping
Macro-instability inner slope
Cyclic liquefaction

Figure A.7: Failure mechanisms of a dike including a shallow foundation. Adapted from Ministerie van Verkeer en Waterstaat (2007)

A.3. Behaviour of Soils Under Cyclic Loading

The behaviour of soil is dependent on the initial stress state and on the imposed stresses due to loading. It is possible to represent the stress path of a single soil element using the p'-q stress state space. The p'-q stress space is a tool to visualize the stress path of a soil element where $p' = \frac{\sigma_1' + \sigma_3'}{2}$ and $q = \frac{\sigma_1 - \sigma_3}{2}$. The difference of soil behaviour compared to other engineering material can be generalized by four characteristics and are described in the following subsections.

A.3.1. Volumetric Behaviour

The first aspect is the volumetric behaviour of the soil and is dependent on the density of the soil specimen and the different responses during loading. A general distinction between 2 states is made: a loose and dense state. A loose soil contracts and decreases in volume when sheared (Figure A.8) while a dense soil dilates and increases in volume (Figure A.9). These are known as dilatancy and contractancy. In 1936, Casagrande concluded that during shearing loose and dense sands contracted and dilated to the same stress dependent void ratio (volume of pores divided by volume of solids in a unit soil volume), respectively. This was termed the critical state. The critical state was defined by Roscoe et al. (1958) as "the state at which a soil continues to deform at constant stress and constant void ratio". The critical void ratio becomes smaller as the mean effective stress level increases.

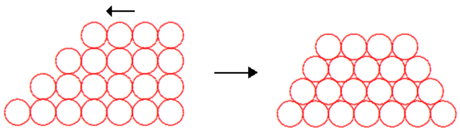

Figure A.8: Contractive behaviour

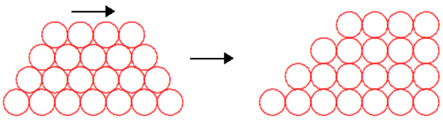

Figure A.9: Dilative behaviour

A widely used theoretical framework that takes the density into account as a state variable is known as critical state soil mechanics (Schofield and Wroth (1968)). This theory is based on theoretical elasto-plasticity while taking volume changes into account during loading and unloading. The critical state is defined as an asymptotic state in which shearing of the soil can continue without further change in effective stress or density (ref. @@). Several researchers (see for example Jefferies and Been (2006) for further information) have deduced the critical state line from shearing experiments and defined it in terms of void ratio and effective pressures:

$$e_c = \Gamma - \lambda ln(p_c') \tag{A.1}$$

In here, Γ is the offset of the critical state line in and λ is the slope of the critical state line (Jefferies and Been, 2006).

The void ratio is defined as the ratio between the pore volume and the volume of the solid particles (CROW (2004)). The state parameter ψ is defined as the difference between the current void ratio, e, to the critical state void ratio, e_c:

$$\Psi = e - e_c \tag{A.2}$$

A positive state parameter will indicate a loose/contractive soil, while a negative state parameter will indicate a dense/dilative soil (Figure A.10).

The actual void ratio indicates whether the material exhibits contractive or dilative behaviour. The critical void ratio, ec, is reached when the void ratio does not change anymore when the soil is sheared indefinitely. A state further away from the critical state results in a faster response in volumetric change.

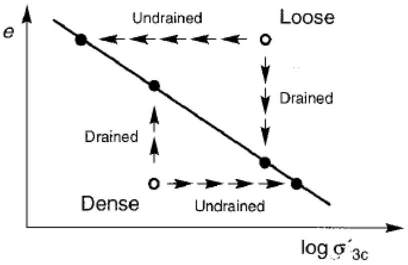

Figure A.10: Critical state and state parameter concepts from Kramer (1996). Definition of the CSL depends on the author and parameters should be consistent with their corresponding definition.

A.3.2. Multi-Phase Material

The second aspect of behaviour specific for soils is due to the multi-phase composition of solid particles and water. The drainage response of the pore fluid inside the soil specimen has influence on the soil behaviour assuming the soil is fully saturated with water. The drainage conditions of a soil specimen have two extreme scenarios: drained or undrained. During drained conditions, pore water can freely move through the pores of the soil grain skeleton. This results in zero excess pore pressures due to the pore fluid when the specimen is loaded as the fluid can move freely. During undrained conditions, the pore fluid is unable to move freely through the pores due to the speed of loading or because of drainage conditions such as a low permeability. Drainage conditions are dependent on the porosity of soil and the intrinsic viscosity of the fluid (water in this case) and are generally described by the hydraulic conductivity of the soil. Water is assumed to be incompressible relative to the soil skeleton and loading it results in excessive pore pressure. Terzaghi's effective stress principle states that the stresses are transmitted through the contact areas of the grains, or inter-granular stresses. The effective stress can be calculated through:

$$\sigma' = \sigma - p_w \tag{A.3}$$

where σ is the total stress and p_w is the water pressure.

Drained conditions allow a soil to compact as the pore water is able to move freely as illustrated by figure A.8. Undrained conditions prevent a soil from compacting and excess pore pressures can be generated. This results in a reduction of effective stresses. Drained conditions also allow a soil to dilate as illustrated by figure A.9. During undrained conditions, the soil particles are prevented from dilating and increasing in volume. Negative excess pore pressures can lead to an apparent and temporary tensile strength of the soil. Positive and negative excess pore pressures consolidate or dissipate over time, more information can be found in section A.6.

A.3.3. Stress Dependent Stiffness

General strain levels considered in engineering and thus in conventional soil testing are mostly within the large and residual strain regions. In dynamic and cyclic situations soil strains are mostly in the region between (very) small to large strains. Diaz-Rodriguez and Lopez-Molina (2009) defined the following regions for soil dynamics (Figure A.11):

1. Very-small strain ($\gamma < \gamma_{tl}$, where γ is the shear strain and subscript tl indicates the linear threshold). Shear strains up to $\frac{G}{G_{max}} = 0.99$ are assumed to behave at a constant linear shear stiffness. G and G_{max} indicate the shear strength and maximum shear strength, respectively. No generation of pore pressures takes place.

2. Small strain ($\gamma_{tl} < \gamma < \gamma_{tv}$, subscript tv indicates the volumetric cyclic threshold). Shear strains between very-small strains up to approximately $0.6 > \frac{G}{G_{max}} > 0.85$ represent the region between fully recoverable behaviour and minor degradation. The soil is already behaving according to a non-linear stress-strain relation but no generation of pore pressure or volume change yet.

3. Medium strain ($\gamma_{tv} < \gamma < \gamma_{td}$, where subscript td indicates the degradation strain threshold). Below the degradation strain threshold (γ_{td}), soil failure does not occur and a hysteretic equi-

librium with almost elastic pore pressure response was observed. Typical observed strains are $0.5\% < \gamma < 2\%$.

4. Large and residual strain ($\gamma > \gamma_{td}$). After reaching the degradation strain threshold de-structuring of the soil fabric and high energy losses are observed. At $\gamma \geq 10\%$, the flow threshold(γ_{tf}) is reached where visco-plastic behaviour is observed and a steady state phase is reached.

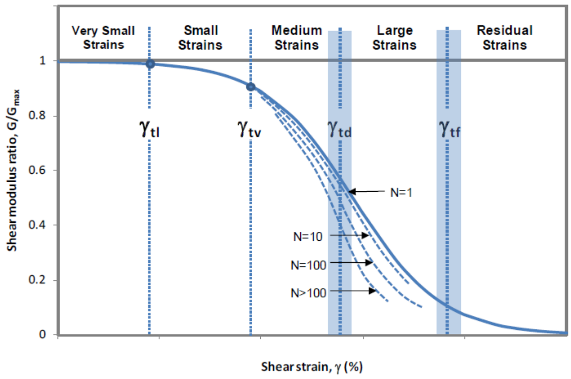

Figure A.11: Shear Modulus Reduction Curve with Strain Thresholds, from Diaz-Rodriguez and Lopez-Molina (2009)

A.3.4. Plastic Behaviour

Seed and Idriss (1970) concluded that the shear modulus, G, and damping ratio, ξ, are dependent on the strain magnitude, even for strains in the small strain region. The damping ratio is proportional to the area of the hysteresis loop and increases with decreasing shear stiffness (Figure A.12). A larger area of the hysteresis loop results in a larger amount of damping as well as more shear straining. Considering cyclic shear loading by loading-unloading a sample results in energy dissipation, or hysteresis, proportional to the strain magnitude. The hysteresis loop of the specimen for evolving shear strain is represented in Figure A.13. The shear modulus of the soil is expressed as the secant modulus of the two extreme points of the hysteresis loop. The soil reacts relatively stiff to the initial loading cycle, whereas the stiffness reduces with an increasing strain.

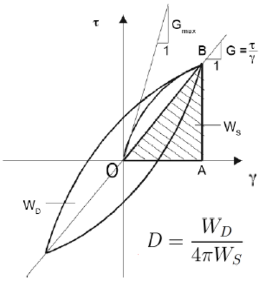

Figure A.12: Strain-stress hysteresis loop

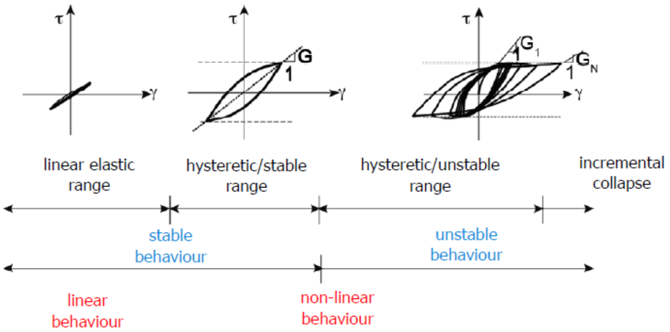

Figure A.13: Response to cyclic loading

The hysteretic behaviour of the soil can be stable or unstable. Stable behaviour occurs within the domain of (very) small strains and is characterized by a constant shear modulus during successive cycles. Unstable behaviour occurs within the domain of large strains as shear stresses increase. The development of the shear modulus and damping ratio is often expressed using the backbone curve. The backbone curve describes extreme locations of the stress-strain development of the soil during (re-)loading in the $\gamma - \tau$ space (shear strain - shear stress, shown in figure A.14). A simple example of a back-bone curve can be described using a hyperbola or the Ramberg-Osgood model (non-linear model describing stress-strain behaviour). The development of the hysteresis loop proceeds along the path defined by the back-bone curve according to the (extended) Masing rules (Kramer (1996)).

The (extended) Masing rules describe how the hysteresis loop develops with respect to cyclic loading. The hysteresis loop develops differently during initial loading, unloading and reloading. The generally, extended Masing rules are as follows and are visualized in Figure A.14:

1. The stress strain curve follows the (backbone curve) during initial loading.
2. If stress reversal occurs, the stress-strain curve reverses in the same shape.
3. If unloading or reloading intersects the initial backbone curve, the initial backbone curve will be followed.
4. If unloading or reloading intersects an unloading or reloading cycles of the previous cycle, the strain-strain curve follows the previous cycle.

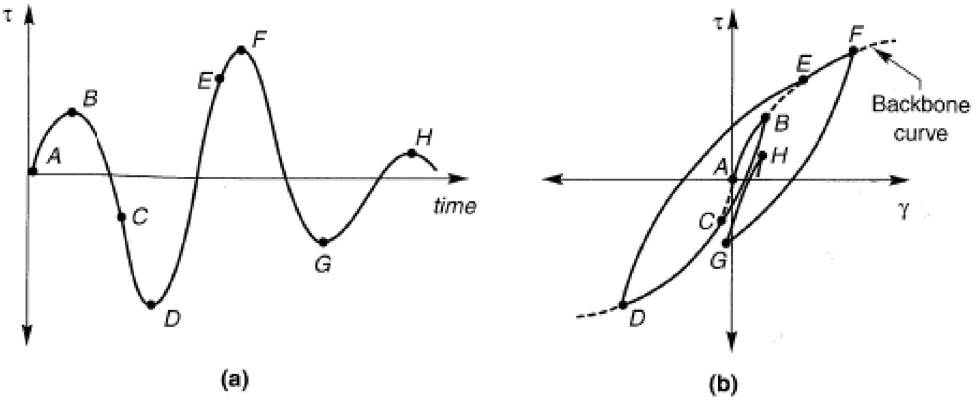

Figure A.14: Visualisation of Extended Masing Rules. (a) shows the variation of shear stress with time while (b) shows the corresponding stress-strain response, including the backbone curve. After Kramer(1996)

Cyclic loading results often in degradation of the soil structure. Densification of granular soils occurs during drained cyclic loading. The sign and magnitude of volumetric straining is dependent on the state of the soil as well as the intensity of the loading. During undrained loading, volumetric strain accumulation of the soil-water matrix is prevented by the incompressible water and pore pressures are accumulated in a similar manner. This results in a reduction of effective stresses, increase in strains and finally into a loss of shear strength or stiffness.

A.3.5. Cyclic Loading Scenarios

Figure A.15 shows four examples in which soil can be loaded. In reality, the frequency and amplitude of environmental loads are irregular of nature. Laboratory tests were here conducted using a constant amplitude and loading frequency. The uppper two examples are loaded in a so-called two-way manner. The principle stress directions in the sample are reversed completely during a full loading cycle as the stress state crosses the origin (zero stress). A test is symmetric or unbiased when the two-way loading is around an average shear stress of zero (top left). The bottom left sample is loaded in a pure one-way matter where the average shear stress is equal to the shear stress amplitude. The upper and lower right samples are loaded in a biased manner where the cyclic shear stresses are not equal but bigger than zero. The bottom two examples are loaded in a one-way manner where the principle stress directions are not reversed, not crossing the zero stress condition. In general, two-way cyclic loading results in larger stress accumulation (drained conditions) or excess pore pressure accumulation (undrained conditions) as the sample needs to resist both triaxial compression and extension stresses in a short time.

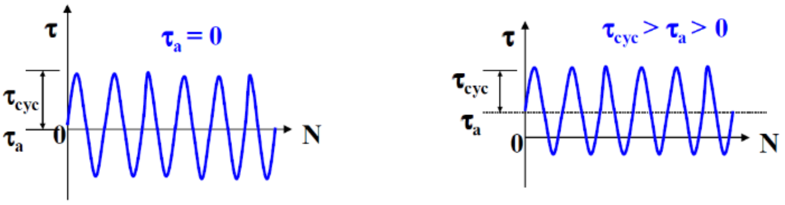

2-way cyclic loading (Symmetric)

Biased 2-way cyclic loading (Asymmetric)

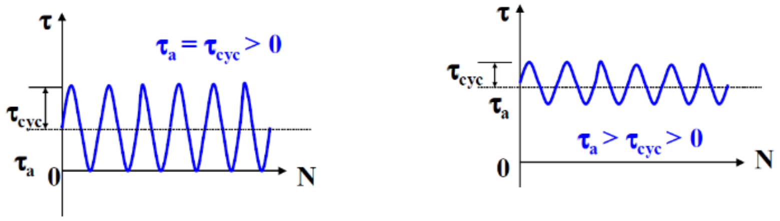

Pure 1-way cyclic loading (Asymmetric)

Biased 1-way cyclic loading (Asymmetric)

Figure A.15: Cyclic loading scenarios including unbiased loading. After Randolph and Gourvenec (2011)

A.4. Liquefaction

Liquefaction can be defined as ”the transformation of a granular material from a solid to a liquefied state as a consequence of increased pore-water pressure and reduced effective stress” by Youd et al. (October 2001). One can distinguish between static liquefaction and cyclic liquefaction. Both type are discussed in the next pages.

A.4.1. Flow/Static Liquefaction

Flow failures or static liquefaction occurs at shores and dams since ages. Failures recognised as flow failures are observed as early as 1864 in Zeeland, the Netherlands (Neyt (1865)). The following figure shows an example of the impact of a flow failure in the same region in 1966. Flow failures are sudden of nature and develop over a large distance over a short amount of time. Flow failures are assosiated with

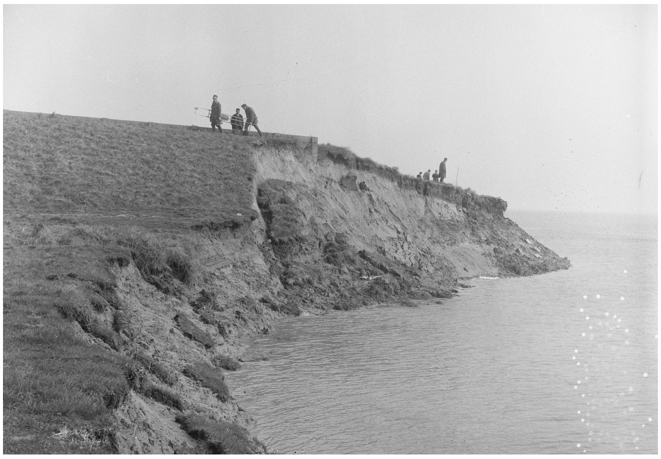

Figure A.16: Flow failure near Kats in Zeeland, the Netherlands in 1966. From https://www.nationaalarchief.nl/

Flow liquefaction, or static liquefaction, is characterized by a brittle failure mechanism during undrained loading conditions and often spreads over a wide area. Typical loading conditions that result in flow liquefaction are ebb, static loads and deepening of the foreshore. It can be responsible for a great amount of human and economic losses due to the sudden loss of strength of the material. Static shear stresses drive the static liquefaction when triggered. It is associated with sand specimen that have a contractive state (Ψ > 0).

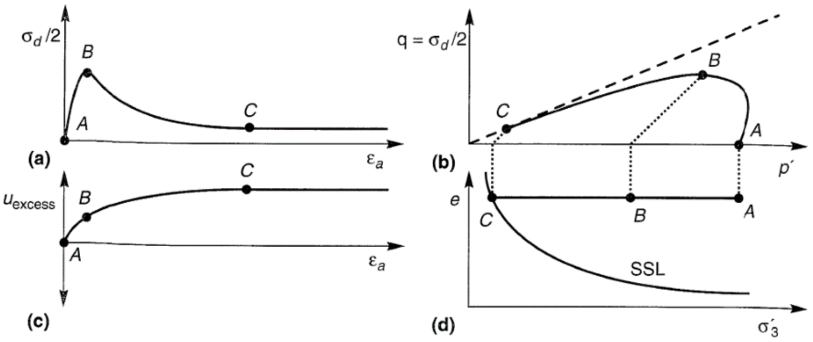

Figure A.17: Response of isotropically consolidated specimen of loose, saturated sand: (a) stress-strain curve; (b) effective stress path; (c) excess pore pressure; (d) effective confining pressure, after Kramer (1996).

Figure A.17 shows a typical stress path development for a loose sand sample. Prior to the application of the static load, the sample is in drained equilibrium (A). Positive pore pressures are being generated immediately after loading (A-B). The sample becomes unstable at this point, where pore pressures and shear strains are rapidly accumulated in a short time span. Flow liquefaction is irreversibly initiated at this point. Point C indicates the steady state of deformation and the specimen has failed. The SSL line is an equivalent to the critical state line as introduced in Section A.3.

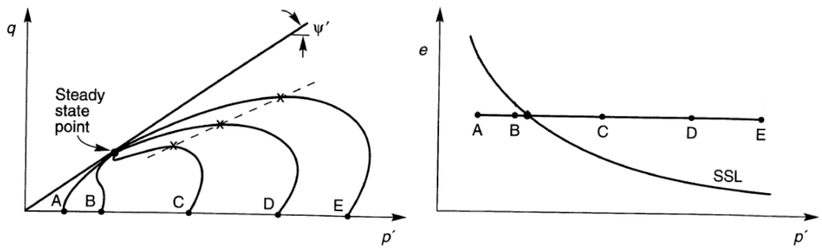

Figure A.18: Response of 5 isotropically consolidated specimen of loose, saturated sand with different state parameters. Adapted from Kramer (1996)

Figure A.18 shows the effect of different void ratio's but with different state parameters for multiple samples. Samples A and B exhibit dilative behavior associated with a negative state parameter upon shearing, while samples C – D exhibit contractive behavior. All the sample strain towards the steady state point. Kramer (1996) has found that the peak of the stress paths in de effective stress space can be connected by a straight line and can define the flow liquefaction surface (FLS). This surface marks the boundary between stable and unstable states of undrained shearing. Flow liquefaction is triggered when the FLS is crossed, whether due to monotonic or cyclic loading. In Kramer (1996) it is suggested that a conservative assumption for the FLS can be approximated as 2/3 of the slope of the drained failure envelope. The FLS applies for both monotonic (A-B-C) and cyclic (A-D-C) loading.

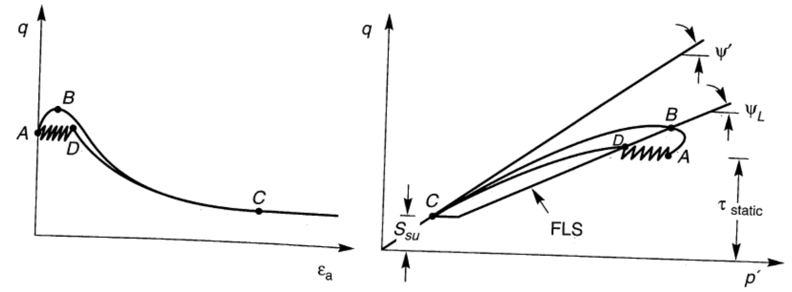

Figure A.19: Flow liquefaction stress path for monotonic (A-B-C) and cyclic (A-D-C), after Kramer (1996).

Figure A.19 displays the development of the effective stress path during undrained conditions for both cases. The cyclic loading causes the development of excess pore pressures and plastic strains to be mobilized, until the stress path hits the FLS (D). Hereafter, flow liquefaction is induced, and the shear strains will develop rapidly. However, flow liquefaction can only be initiated by monotonic and cyclic loading when the initial conditions are in the region above point C on the right graph in Figure A.19. The initial stress condition has to be greater than the steady state point.

A.4.2. Cyclic Liquefaction

Cyclic liquefaction is caused by the repetitive loading of the soil. Essential to the initiation of liquefaction (the same applies to static liquefaction) is the change in pore pressures which result in the change of effective stresses in the soil. Cyclic liquefaction is often associated with earthquake loads and their consequences as shown in figure A.20. However, cyclic loads can also consist of traffic, industrial sources or wind and wave loads.

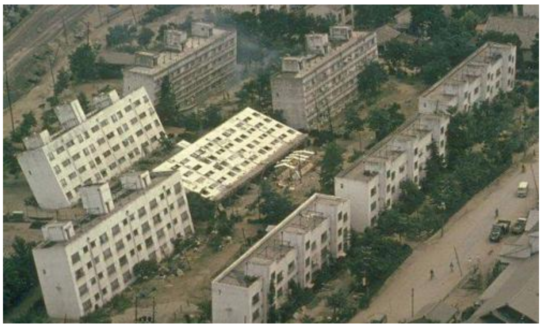

Figure A.20: Rigid body rotation of several residential buildings as a result of liquefaction due the 1964 Niigata Earthquake.

The excess pore water pressures are generated as a result of the tendency of granular soils to compact when subjected to cyclic shear deformations but volumetric straining is prevented due to undrained conditions. As a result, the soil can reach the failure state which allows for the occurrence of large deformations. The latter is termed cyclic mobility. Cyclic mobility can develop when static shear stresses are smaller than the steady-state shear strength, indicated by the area below point C of Figure A.19b.

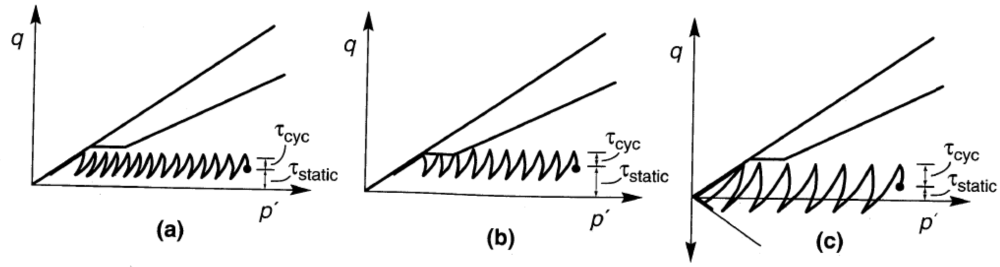

Figure A.21: Three different cyclic loading scenario's, after Kramer (1996).

Cyclic loading results in the development of excess pore pressures and the accumulation of plastic strains. It affects both loose and dense sands at effective confining pressures varying from very low to very high. Three different loading scenarios can result in cyclic mobility:

1. No stress reversal and no exceedance of the steady-state strength (Figure A.21a). The stress path will move towards the failure surface, but cannot cross it. The stress path will continue to move up and down, resulting in both contractive and dilative behavior. This reduces the stiffness of the soil significantly and allows for excessive strains to accumulate.

2. No stress reversal but temporary exceedance of the steady-state strength (Figure A.21b). The stress path again moves to the failure surface. When it hits the FLS, momentarily instability occurs and strains develop. When the stress drops below the steady state strength the accumulation of strains stops.

3. Stress reversal but no exceedance of the steady-state strength (Figure A.21c). The shear stress direction varies between compressional and extensional loading. The rate of pore pressure generation increases with the degree of stress reversal. The stress path oscillates around the compression and extension regions failure envelope in both stress directions. Significant amounts of permanent strains accumulate during this final process, even though flow liquefaction does not occur.

The resistance of soils to liquefaction is often characterized using cyclic strength curves, or liquefaction curves. The liquefaction curve relates the density, cyclic shear stress amplitude and number of cycles until cyclic liquefaction. The liquefaction curve is normalized using the initial effective stress (σ'_{v0}) of the soil. This results in the Cyclic Shear Ratio (CSR, equation A.4 (Kramer, 1996), (Randolph and Gourvenec, 2011). A soil loaded by a high CSR requires less cycles until liquefaction compared to a soil loaded by a low CSR. $\Delta\tau_{cyc}$ is the single amplitude of the shear stresses of a full load cycle. It can be determined by calculating the average of the shear stress during the maximum and minimum shear load of a full cycle.

$$CSR = \frac{\Delta\tau_{cyc}}{\sigma'_{v0}} = \frac{(\tau_{max} - \tau_{min})/2}{\sigma'_{v0}} \tag{A.4}$$

The cyclic liquefaction curves can be produced by laboratory tests, such as the cyclic direct simple shear test (CDSS), cyclic triaxial test (CTX) or cyclic torsional test, and originates from the cyclic stress approach (the cyclic stress approach will be outlined section A.7). Loading situations are different for each test and thus the CSR are not equivalent to each other. For each test, the CSR can be defined differently, e.g.: $CSR_{DSS} = \tau_{cyc}/\sigma'_{v0}$ or $CSR_{TX} = \sigma_{dc}/2\sigma'_3$, where σ_{dc} is the maximum cyclic shear stress and $2\sigma'_3$ is the confining pressure. The cyclic direct simple shear and triaxial tests are often related using the following relationship:

$$CSR_{CDSS} = c_r CSR_{CTX} \tag{A.5}$$

where c_r is a correction factor related to the at-rest earth pressure coefficient, K0. Liquefaction curves are used in both Earthquake and Offshore Engineering, where liquefaction curves capture the behavior of soil in response to cyclic loading. Cyclic tests for earthquake applications are generally performed around the 1 Hz (Kramer, 1996) and do not account for inertial effects. In offshore engineering, the typical loading frequency is between 0.05-0.1 Hz to represent typical frequencies of wave loads (Randolph and Gourvenec, 2011). Lee and Focht (1975) and Tatsuoka et al. (1986), offshore and earthquake engineering respectively, both indicate that a loading frequency $\leq$ 1 Hz has only minor effect on the cyclic strength.

A.5. Constitutive Soil Models

Constitutive models are mathematical tools to simulate the stress-strain behavior of soils. Constitutive models can be formulated in terms of total effective stresses and strains, incremental effective stresses, and strains and in terms of rates. Also, material models can be formulated in terms of total stresses and strains instead of effective stresses and strains. Below we consider effective stress type constitutive models.

The quality of a Finite Element Analysis (FEA) is largely dependent on the quality and capabilities of the constitutive models. 2D and 3D constitutive models are more versatile in their capabilities of modeling the soil response, but no model is truly able to represent the full behavior of a soil. Below we outline the following constitutive models:

1. Hooke's Law or Linear-Elasticity
2. Mohr-Coulomb model
3. Hardening Soil Small strain
4. PM4Sand
5. UBC3D-PLM
6. Hypoplastic model

A.5.1. Hooke's Law

Hooke's law, or linear-elastic model (**Verruijt2001** (**Verruijt2001**)) assumes a linear relationship between the stress and strain increments which are fully recoverable when unloaded (Equation A.6). Hooke's law does not incorporate plastic yielding of the soil nor failure. As long as the soil response can be characterized with a (nearly) linear stiffness, linear-elastic model provides a good estimation of the soil behavior. In dynamic situations this can be the case. However, as soil begins to move towards the plastic region it is known that soil behavior is nonlinear and thus oversimplifies actual soil behavior.

$$\begin{Bmatrix} \sigma_{xx} \\ \sigma_{yy} \\ \sigma_{zz} \end{Bmatrix} = \frac{E}{(1+\nu)(1-2\nu)} \begin{bmatrix} 1-\nu & \nu & \nu \\ \nu & 1-\nu & \nu \\ \nu & \nu & 1-\nu \end{bmatrix} \begin{Bmatrix} \epsilon_{xx} \\ \epsilon_{yy} \\ \epsilon_{zz} \end{Bmatrix} \tag{A.6}$$

A.5.2. Mohr-Coulomb Model

The Mohr-Coulomb(MC) model combines the Mohr-Coulomb failure criterion with Hooke's law into a linear elastic perfectly-plastic stress-strain relationship. The MC model is straightforward and in many cases it provides a sufficiently good representation of soil behaviour. Also, the failure behavior during drained conditions is good and dilatancy can be included by adapting the dilatancy angle. However, there are several disadvantages of the model: the stiffness is constant, resulting in stress-independency of the stiffness and no distinction between primary and unloading/reloading. In undrained conditions, stress paths are not modelled realistically, and the shear strength can be overestimated. Finally, the MC model is not based on the critical state concept (Brinkgreve, 2019).

A.5.3. HSsmall Model

The Hardening Soil model with small-strain stiffness (HSsmall) is a modification on the Hardening Soil (HS) model. The HS model is an advanced soil model which is based on the MC model but takes the stress-dependency of the stiffness moduli into account. This results in an increase of stiffness with an increase of effective pressure. Also, the initial conditions of the soil can be taken into account. The HSsmall takes the higher small strain stiffness at small strains into account (degradation curve). The HSsmall model leads to hysteretic material damping during stress reversals. However, HSsmall model does not take softening into account during cyclic loading. Neither are plastic volumetric strain accumulation or pore pressure accumulation incorporated as the HSss only models one hysteresis loop (Brinkgreve, 2019).

A.5.4. PM4Sand Model

Plasticity Model for Sand (PM4Sand) follows the basis framework of the stress-ratio controlled, critical state compatible, bounding surface plasticity model for sand by Dafalias and Manzari (2004). Boulanger and Ziotopoulou (2017) modified and implemented the model in order to approximate engineering design relationships. The model is developed for earthquake applications enabling to reasonably approximate empirical relationships in practice and to be calibrated within reasonable engineering effort. Version 3.1 of the model (Boulanger and Ziotopoulou, 2017) includes the following features and revisions:

1. Dependency of dilatany and plastic modulus on fabric and fabric history;
2. Modifications to the initial back-stress ratio tracking logic;
3. Modifications for improved modeling of post-liquefaction reconsolidation strains;
4. Addition of a minor cohesion term to reduce potential hour-glassing and improve behavior near the free-surface.

Basic stress and strain terms are used in the model for plain-strain applications. The prime symbol, indicating effective stress, is dropped as all stresses are effective. The stresses are indicated by σ, principal effective stresses σ_1, σ_2 and σ_3, mean effective stress p, deviatoric stress tensor **s** and deviatoric stress ratio tensor **r**. The relationships can be summarized as follows:

$$\sigma = \begin{pmatrix} \sigma_{xx} & \sigma_{xy} \\ \sigma_{yx} & \sigma_{yy} \end{pmatrix} \tag{A.7}$$

$$p = \frac{\sigma_{xx} + \sigma_{yy}}{2} \tag{A.8}$$

$$\mathbf{s} = \sigma - p\mathbf{I} = \begin{pmatrix} s_{xx} & s_{xy} \\ s_{yx} & s_{yy} \end{pmatrix} = \begin{pmatrix} \sigma_{xx} - p & \sigma_{xy} \\ \sigma_{yx} & \sigma_{yy} - p \end{pmatrix} \tag{A.9}$$

$$\mathbf{r} = \frac{\mathbf{s}}{p} = \begin{pmatrix} r_{xx} & r_{xy} \\ r_{yx} & r_{yy} \end{pmatrix} = \begin{pmatrix} \frac{\sigma_{xx}-p}{p} & \frac{\sigma_{xy}}{p} \\ \frac{\sigma_{yx}}{p} & \frac{\sigma_{yy}-p}{p} \end{pmatrix} \tag{A.10}$$

The strains are represented by tensor ϵ and divided into a volumetric, ϵ_v, and deviatoric component **e**. In incremental form, both the volumetric and deviatoric strains are decomposed into an elastic, $d\mathbf{e}^{el}$ and $d\epsilon_v^{el}$ and a plastic component, $d\mathbf{e}^{pl}$ and $d\epsilon_v^{pl}$. The relationships can be summarised as follows:

$$\epsilon_v = \epsilon_{xx} + \epsilon_{yy} \tag{A.11}$$

$$\mathbf{e} = \epsilon - \frac{\epsilon_v}{3}\mathbf{I} = \begin{pmatrix} \epsilon_{xx} - \frac{\epsilon_v}{3} & \epsilon_{xy} \\ \epsilon_{yx} & \epsilon_{yy} - \frac{\epsilon_v}{3} \end{pmatrix} \tag{A.12}$$

$$d\mathbf{e} = d\mathbf{e}^{el} + d\mathbf{e}^{pl} \tag{A.13}$$

$$d\epsilon_v = d\epsilon_v^{el} + d\epsilon_v^{pl} \tag{A.14}$$

The following power relationship is used to approximate the critical state line:

$$e_{cs} = e_0 - \lambda(\frac{p_{cs}}{p_A})^m \tag{A.15}$$

where p_{cs} is the mean stress at critical state, e_{cs} is the critical void ratio and e_0, λ and m are fitting parameters. The state of the sand is determined using the relative state parameter . The relative state parameter normalized by the difference between the maximum void ratio and minimum void ratio in order to define the relative density (Konrad 1988). Bolton's (1986) dilatancy relationship is used to define the empirical CS-line:

$$\xi_R = D_{R,cs} - D_R \tag{A.16}$$

$$D_{R,cs} = \frac{R}{Q - ln(100\frac{p}{p_A})} \tag{A.17}$$

where $D_{R,cs}$ is the relative density at the critical state for the current mean effective stress, Q and R are empiric parameters of approximately 10 and 1.0, respectively. Figure A.22 illustrates the effect of various values for Q and R.

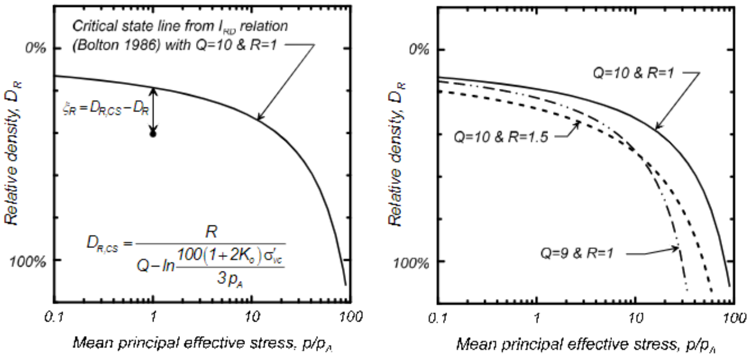

Figure A.22: Relative state parameter definition and the effects of varying Q and R

PM4Sand incorporates bounding, dilatancy and critical surfaces following Dafalias and Manzari (2004). The model is simplified by removing the Lode angle dependency (same friction angles for compression and extention) in order to relate the bounding, M^b, and dilatancy, M^d, ratios to the critical stress ratio, M, using simpler expressions. The bounding surface allows a more flexible way to determine plastic strains (with respect to the conventional plasticity concept present in for example the MC model). The dilatancy surface corresponds with the phase transformation line equivalent to the unstable point B in figure A.17. The critical surface corresponds with the critical state line as presented in section A.3. The yield surface indicates the region wherein elastic strains occur and is usually small to simulate highly non-linear behaviour of the soil. The yield surface moves as the stress path evolves during the loading whereas the other surfaces are fixed depending on the material parameters.

$$M^b = M \cdot exp(n^b \xi_R) \tag{A.18}$$

$$M^d = M \cdot exp(-n^d \xi_R) \tag{A.19}$$

$$M = 2 \cdot \sin \phi_{cv} \tag{A.20}$$

where n^b and n^d are parameters determining M^b and M^d, respectively, and phi_{cv} is the constant volume or critical state effective friction angle. The surfaces of M^b and M^d move together until they coincide with the critical state surface at critical state (Figure A.23). The bounding stress ratio controls the relationship between peak friction angle and the relative state. Differences between loose-of-critical and dense-of-critical result in different peak friction angles as well as n^b and n^d for the same sand. The yield surface and back-stress ratio tensor, α are simplified due to removing any Lode angle dependency.

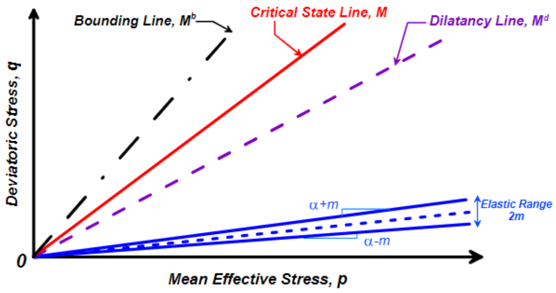

Figure A.23: Yield, critical, dilatancy and bounding lines in q-p space. Position of the dilatancy and bounding lines correspond with a dense-of-critical state of stress

The yield surface is defined as a cone in stress space:

$$f = [(\mathbf{s} - p\alpha) : (\mathbf{s} - p\alpha)]^{\frac{1}{2}} - \sqrt{\frac{1}{2}}pm = 0 \tag{A.21}$$

The back-stress ratio tensor defines the center of the yield space and m defines the radius of the cone in terms of stress ratio. Similar back-stress ratios are defined for the bounding and dilatancy surfaces:

$$\alpha^b = \sqrt{\frac{1}{2}}[M^b - m]\mathbf{n} \tag{A.22}$$

$$\alpha^d = \sqrt{\frac{1}{2}}[M^d - m]\mathbf{n} \tag{A.23}$$

where the tensor **n** is the normal to the yield surface (Figure A.24). The bounding surface formulation tracks the initial back-stress ratio, α_{in}, and uses it to calculate the plastic modulus K_p. A reversal in loading direction is identified following traditional bounding surface practice. A fabric-dilatancy tensor, **z**, is introduced to account for the effects of prior straining on the soil fabric. The soil fabric indicates the geometrical arrangement of particles and pore spaces. **z** evolves in response to plastic deviatoric strains that occur during dilation:

$$d\mathbf{z} = -\frac{c_z}{1 + \langle \frac{z_{cum}}{2z_{cum}} - 1 \rangle} \frac{\langle -d\epsilon_v^{pl} \rangle}{D} (z_{max}\mathbf{n} + \mathbf{z}) \tag{A.24}$$

The model requires three primary input parameters: relative density, D_R, which influences the peak (un)drained strength and rate of strain accumulation during cyclic loading, G_o which is the shear modulus to be calibrated by estimated or measured in-situ shear wave velocity and h_{po} which is the contraction rate parameter used to calibrate the estimated in-situ cyclic resistance ratio after other properties have been set.

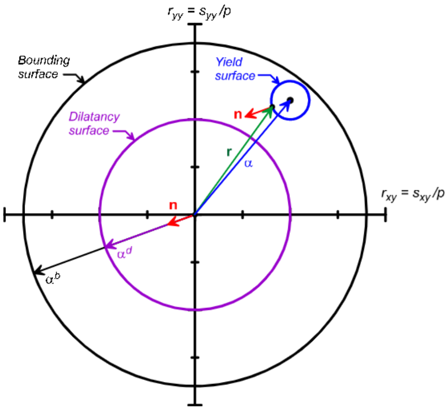

Figure A.24: Yield, critical, dilatancy and bounding surfaces in $r_{yy} - r_{xy}$ stress ratio plane with the yield surface, normal tensor, dilatancy back-stress ratio and bounding back-stress ratio.

The following conclusion are summarized as stated in previous research by various authors about the PM4Sand model:

- (Toloza, 2018): PM4Sand is limited to a 2D plain-strain formulation preventing the application to a 3D geometry. A correction is applied to take into account 3D effects but could lead to overestimation of displacements. The model has limited ability to modify the slope of the liquefaction curves in order to match experimental data. The introduction of static shear stresses does not result in weaker liquefaction curves with no proper understanding of the effect. Finally, initial and loading conditions have a large impact on the response of the soil. It is recommended to create multiple calibrated parameter sets to represent various conditions.

- (Tziolas, 2019): PM4Sand overpredicts the CRR at small number of cycles and underpredicts the CRR at large number of cycles. There is a dependence of the CRR on the overburden stress level according to the K_σ behavior of the model. A relative large generation of excess pore pressures during the first two cycles in the experimental tests is noticed while the model does not generate these pressures.
- (Portugal Quevedo, 2019): PM4Sand is not able to simulate different initial and loading conditions using one parameter set. Loose sands are simulated adequately while for dense sands not. Large dilation components are not represented well in the model. Often, the peak pore pressure magnitudes and initial pore pressure generation are underestimated.

A.5.5. UBC3D-PLM Model

UBC3D-Plaxis Liquefaction Model (UBC3D-PLM) is an advanced model to simulate liquefaction behavior based on the UBCSAND model but generalized for 3D applications. UBC3D-PLM is based on plasticity theory and uses two yield surfaces rather than one: the Mohr-Coulomb yield condition as well as a hyperbolic strain hardening rule, based on the Duncan-Chang (**DuncanChang1970** (**DuncanChang1970**)) approach with modifications. The Mohr-Coulomb yield functions are applied using the full 3D representation. The critical yield surface is given by:

$$f_m = \frac{\sigma'_{max} - \sigma'_{min}}{2} - (\frac{\sigma'_{max} + \sigma'_{min}}{2} + c' \cot \phi'_p) \sin \phi_{mob} \tag{A.25}$$

Elastic behaviour within the yield surface is governed by a non-linear rule, controlled by the stress dependent elastic bulk and shear modulus. Plastic straining is based on the principal of strain hardening. The hardening rule relates the plastic straining to the mobilisation of shear strength ($sin\phi_{mob}$):

$$\sin \phi_{mob} = \frac{\sigma'_1 - \sigma'_3}{\sigma'_1 + \sigma'_3} = \frac{t_{mob}}{s'} \tag{A.26}$$

where t_{mob} is the mobilized shear strength and s is the mean effective stress. The hardening rule is reformulated in the UBC3D-PLM as:

$$d \sin \phi_{mob} = 1.5 K_G^p (\frac{p}{p_A})^{np} \frac{p_A}{p_m} (1 - \frac{\sin \phi_{mob}}{\sin \phi_{peak}} R_f)^2 d\lambda \tag{A.27}$$

where K_G^p is the plastic shear modulus number, *np* is the plastic shear modulus exponent, ϕ_{mob} is the mobilized friction angle, ϕ_{peak} is the peak friction angle, R_f is the failure ratio n_f/n_{ult} and $d\lambda$ is the plastic strain increment multiplier. The plastic potential function consists of a non-associated flow rule based on the Drucker-Prager plastic potential function. The flow rule based on Rowe's stress dilatancy theory as used in the original UBCSAND model and is based on three observations, e.g.: there is an unique stress ratio defined by the constant volume friction angle ϕ_{cv}, dependent on the position relative of the stress ratio to $\sin \phi_{cv}$ results in contractive or dilative behaviour and the amount of deformation is dependent on the difference between the current stress ratio and stress ratio at $\sin \phi_{cv}$ (Figure A.25). The flow rule is:

$$d\epsilon_v^p = \sin \psi_m d\gamma^p \tag{A.28}$$

$$\sin \psi_m = \sin \phi_m - \sin \phi_{cv} \tag{A.29}$$

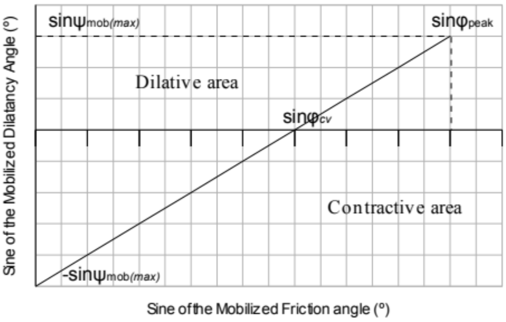
sinψmob(max)
sinφpeak
Dilative area
sinφcv
Contractive area
-sinψmob(max)
Sine of the Mobilized Dilatancy Angle (°)
Sine ofthe Mobilized Friction angle (°)

Figure A.25: Graphical representation of the modified Rowe's flow rule

A secondary yield surface is introduced in order to make a distinction between primary and secondary loading. Where the primary yield surface is based on an isotropic hardening rule, the secondary yield surface is based on a kinematic hardening rule. A stress reversal based rule is used to count loading to unloading cycles. The mobilised friction angle can be demobilised during unloading. Figure A.26 gives a graphical representation of the position of the primary and secondary yield surfaces relative to the failure surface. The (de)mobilisation of the friction angle is possible due to the kinematic hardening rule and results in additional straining or pore pressure generation even if the stress ratio of the primary yield function is not reached.

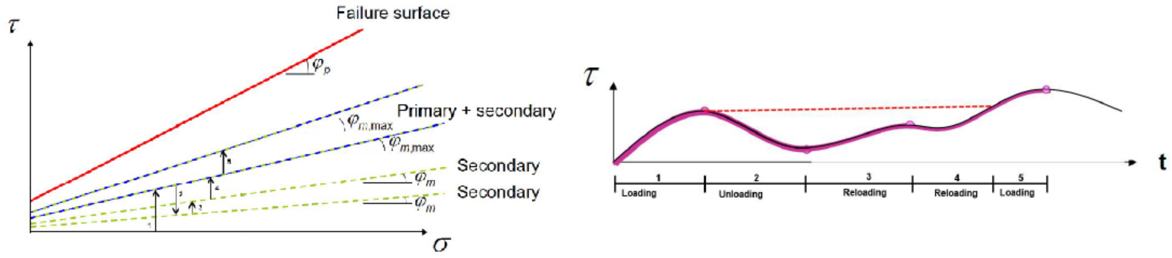

Figure A.26: Graphical representation of the yield and failure surfaces of UBC3D-PLM, from Winde (2015)

Pore pressure generation during undrained loading is treated implicitly by UBC3D-PLM. Increments of pore water pressure are determined using:

$$dp_w = \frac{K_w}{n} d\epsilon_v \tag{A.30}$$

The following conclusion are summarized as stated in previous research by various authors about the UBC3D-PLM model:

- (Brinkgreve, 2019): UBC3D-PLM is not critical state compatible and does not include compaction hardening. Cyclic loading and liquefaction behaviour are not always realistic during dynamic calculations. Also, the model overestimates the damping of the soil.

- (Makra, 2013): UBC3D-PLM generally predicts the onset of liquefaction well, while an over-prediction of the excess pore pressure during the beginning of the earthquake is observed. The model does not predict displacements adequate resulting in both under- and over-estimations during excitation and post-liquefaction. The effect of lateral earth pressure and static shear stresses is not well captured by the model. However, the research shows that with proper calibration using appropriate loading conditions the accuracy can be improved.

- (Winde, 2015): UBC3D-PLM models the horizontal accelerations relatively accurate, but over-damps near the surface. Pore pressures are generated too early during excitation and the maximum value is slightly overestimated. Post-liquefaction displacements are generally excessive, resulting in unreliable deformations.

- (Elsacker, 2016): UBC3D-PLM is reasonably able to match experimental data after calibration. Adjustment of plastic stiffness parameters are most efficient in the calibration process to match experimental data. Initial shear stresses cause the model to underestimate the liquefaction potential.

A.5.6. Hypoplastic Model

Hypo-plasticity distinguishes itself by a direct tensorial relation between the stress and strain rate instead of the distinction between elastic and plastic strains. The hypoplastic model (Von Wolffersdorff version) is a critical state model and is stiffness, strength void ratio dependent. The critical state concept allows for 'interpolation' between two known states of the soil. Stress dilatancy theory captures the shear volume coupling. The model uses the Matsuoka-Nakai failure criteria rather than the MC failure criteria and includes a small-strain stiffness formulation (intergranular strains). Cyclic undrained behaviour is captured reasonably well with incorporation of the intergranular strain formulation (Tsegaye et al., 2009). However, many of the parameter do not have a clear physical meaning and are difficult to determine (Brinkgreve, 2019).

A.6. Consolidation

Consolidation can be described as the coupled response of deformation and groundwater flow of a saturated soil due to a change of stress conditions. Changed stress conditions can occur because of external loading, (re-)distribution of pore pressures, change in geometry, degradation of stiffness or chemical/biological activity. The time required to reach the final steady state pore pressure (fully consolidates situation) is dependent on the characteristics of a geotechnical system relative to the speed of external changes (see next section). Volume changes due to external changes are prevented by the (relatively) incompressible pore water fluid resulting in an undrained soil response and generation of excess pore pressures. The external load is initially fully carried by the pore fluid but gets transferred to the soil skeleton when the excess water pressure dissipates due to consolidation. The flow of water and thus the rate of dissipation of excess pore pressures is, amongst others, controlled by the hydraulic conductivity and the stiffness of the soil.

A.6.1. Terzaghi's 1D Formulation

The simplest consolidation problem is a one-dimensional situation. This classic problem was formulated by Terzaghi et al. (1925) and studied and discussed often, like in Verruijt (2013). Terzaghi's 1D consolidation problem is constrained by a circular ring, only allowing for deformation in the vertical direction. The top of the sample is drained while the bottom is impermeable. The sample is loaded constantly in the vertical direction (Figure A.27).

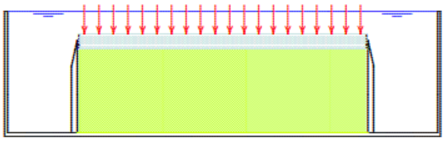

Figure A.27: Terzaghi's problem representing an oedometer test, after Verruijt (2013)

Terzaghi's 1D consolidation theory makes several assumptions: the soil is homogeneous and saturated, the soil particles cannot be crushed, the fluid is incompressible, only small strains are valid, Darcy's law applies for all hydraulic gradients and the coefficients of permeability and compressibility remain constant. Terzaghi's classic 1D formulation starts from the mass conservation equation for porous media by taking into account the mentioned assumptions:

$$\frac{\partial u}{\partial t} = c_v \frac{\partial^2 u}{\partial z^2} \tag{A.31}$$

with

$$c_v = \frac{k}{\gamma_f m_v} \tag{A.32}$$

where c_v is the consolidation coefficient, k is the hydraulic conductivity, γ_f is the unit weight of the pore fluid and $m_v = 1/E_{oed}$ is the confined compressibility of the soil. Initial and boundary conditions of the system have to be known in order to be able to solve the problem. Conte and Troncone (2006) studied an extension for time-dependent loads to the classic 1D formulation under the same assumptions as Terzaghi except for the assumptions of pore fluid incompressibility, instantaneous loading and no change in vertical stress over time:

$$c_v \frac{\partial^2 u}{\partial z^2} = \frac{1}{\eta}\frac{\partial u}{\partial t} - \frac{d\sigma}{dt} \tag{A.33}$$

Here η is a parameter accounting for the soil and pore fluid compressibility and $d\sigma/dt$ introduces a time dependent total vertical stress. A Fourier series was used to describe the time dependent loading and can consist of cyclic loading, a single load or a gradual load applied over time.

A.6.2. Biot's Consolidation Formulation

Biot (1956) presented a general solution for 2D situation as an extension to Terzaghi's classic 1D problem. Biot's consolidation theory assumes Darcy's law for fluid flow and elastic soil behavior. Plaxis implemented these solutions for a finite element method including an extension to 3D situations (Plaxis, 2019c). The implementation starts from the incremental equilibrium equation where the total stresses are consisting of body forces, surface tractions and residual forces. The total stress is divided into effective stresses and pore water pressures according to the effective stress principle. This results in the following system of equations using a weak formulation:

$$\underline{\underline{K}}\,d\underline{v} + \underline{\underline{L}}\,d\underline{p}_n = d\underline{f}_n \tag{A.34}$$

where $\underline{\underline{K}}$ is the stiffness matrix, $\underline{\underline{L}}$ the coupling matrix and $d\underline{p}_n$ is the incremental pore pressure vector. The continuity equation is used to formulate the flow problem. The following weak formulation is used:

$$-\underline{\underline{H}}\,d\underline{p}_n + \underline{\underline{L}}^T \frac{d\underline{v}}{dt} - \underline{\underline{S}}\frac{d\underline{p}_n}{dt} = \underline{q}_n \tag{A.35}$$

where $\underline{\underline{H}}$ describes the permeability behavior, $\underline{\underline{S}}$ the compressibility of the pore fluid and $\underline{q}_n$ is a prescribed outflow vector at the boundary. By combining the equations the following discrete coupled system of equations is formed:

$$\begin{bmatrix} \underline{\underline{K}} & \underline{\underline{L}} \\ \underline{\underline{L}}^T & -\underline{\underline{S}} \end{bmatrix} \begin{bmatrix} \frac{d\underline{v}}{dt} \\ \frac{d\underline{p}_n}{dt} \end{bmatrix} = \begin{bmatrix} 0 & 0 \\ 0 & \underline{\underline{H}} \end{bmatrix} \begin{bmatrix} \underline{v} \\ \underline{p}_n \end{bmatrix} + \begin{bmatrix} \frac{d\underline{f}_n}{dt} \\ \underline{q}_n \end{bmatrix} \tag{A.36}$$

The presented formulation assumes linear-elastic soil behavior. An incremental form is used to describe the consolidation behavior when a non-linear soil model is used.

A.7. Various Approaches to Liquefaction Modelling

This Section describes various approaches to model liquefaction. The following approaches are considered:

- Reference engineering methodology. The reference engineering methodology mentioned in chapter 1 is a product of various theories and experimental results published in literature from where a possible workaround is deduced.
- Earthquake engineering. Earthquake engineering relies heavily on empirical relationships to describe earthquake loads and soil characteristics. Alternatively, effective stress analysis can be performed but is subject to many uncertainties.
- Offshore engineering. Offshore engineering uses (semi-)analytical model to describe the hydrological and geotechnical behaviour of the problem. Therefore, it is limited to specific situations. An agreement between earthquake and offshore engineering is the use of liquefaction curves to describe the behaviour of the soil specimen subjected to a cyclic load.

A.7.1. Reference Engineering Practice

The main assumption of this method is a direct relation between densification and excess pore pressure generation. The liquefaction susceptibility is assessed using empirical relationships (Robertson, 2010) and critical state soil mechanics (Jefferies and Been, 2006). These theories are used to determine contractive or dilative behavior of the soil layers based on CPT tests.

If a soil layer is susceptible to liquefaction, it needs to be determined whether liquefaction is triggered or not. Several research papers ((Kusumawardani et al., 2015), (Vasquez-Herrera and Dobry, 1988) and (Wichtmann et al., 2004)) indicate that liquefaction is possible even at very small shear strain amplitudes at very high numbers of loading cycles. Wichtmann et al. (2012) performed cyclic tests using a high variety of test conditions, including very small shear strain amplitudes of $0.5 \cdot 10^{-4}$ (Figure A.28). From Figures A.28 and A.29 it can be seen that a small change in shear strain amplitude can have a large influence on the strain accumulation. Using Figures A.28 and A.29 the following is deducted:

1. Densification is possible at very small cyclic shear strain amplitudes at plane-strain conditions if loaded for $10^4 - 10^5$ cycles.

2. Even at a shear strain amplitude of $0.5 \cdot 10^{-4}$ there is a possibility of a strain accumulation of 0.03%.

3. At an effective stress of 100 kPa the strain accumulation is approximately 50% larger compared to 200 kPa (Figure A.29).

4. The expected strain accumulation for a shallow layer at very small strain amplitudes at a high number of cycles can be $1.5 \cdot 0.03 = 0.045\%$.

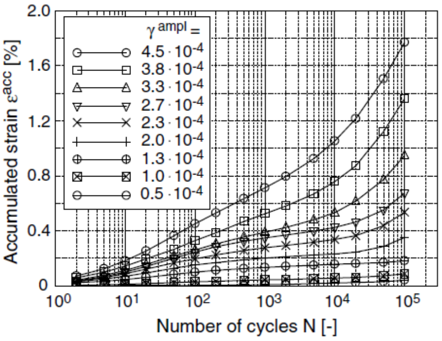

Figure A.28: Strain accumulation as a function of number of cycles. After Wichtmann et al. (2004)

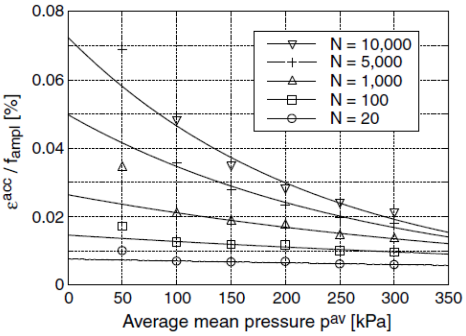

Figure A.29: Strain accumulation divided by the amplitude function. After Wichtmann et al. (2004)

During storm conditions, it is assumed that no consolidation takes place and excess pore water pressures are generated until full liquefaction is reached. It is assumed that during storm conditions the ULS signal is constantly dominant while various loading amplitudes will occur. The value of the shear strain amplitude is used as a threshold value at which densification is still possible.

In order to determine the cyclic strear strains, Plaxis 2D was used. The liquefiable soil layer was modeled using the HSss model (Section A.5). The parts of the soil layer which have a cyclic shear strain amplitude above the threshold value are assumed to fully liquefy.

If the criteria of liquefaction are met, the principle of normalized shear strength is used. The residual liquefied undrained shear strength is related to initial vertical stress. Robertson (2010) is used to determine the residual liquefied undrained shear strength. This paper back-analysed the residual liquefied undrained shear strength for several liquefaction cases. A phi-c reduction is performed using Plaxis to evaluate the effect on the dike in terms of stability and mechanisms.

A.7.2. Offshore Engineering

Pore pressure development as a result of wave action is probable within the oceanic environment, especially in the nearshore region. Structures, such as pipelines and anchors, founded on the seabed can become unstable by the decrease of effective stresses due to increasing pore pressures. The following section contains a model which is used to describe the progressive built-up of pore pressures in oceanic environments. The loading frequency as well as the drainage conditions of the soil are comparable with the situations discussed in this thesis. However, the shear loads subjected to the soil are different.

Seed and Rahman (1978) created a method to determine a progressive built-up of pore pressures as a result of wave action using linear wave theory. The original paper uses Terzaghi's classic 1D consolidation equation (equation A.31) to describe the pore pressure distribution. An extension is created to account for pore pressure generation. The net pore pressure Δu changes over an interval of time Δt by an arbitrary pore pressure generation function Ψ. The total dissipated pore pressure then will be $\Psi\Delta t - \Delta u$. It is assumed that there is no influx of water and the dissipation of pore pressures corresponds to the change in effective bulk stress $d\sigma'_d$:

$$d\sigma'_d = -(\Psi\Delta t - \Delta u)$$

$$d\sigma'_d = \Delta u - \Psi\Delta t \tag{A.37}$$

Assuming a linear-elastic stress-strain relationship gives:

$$\Delta\epsilon = m_v(\Delta u - \Psi\Delta t) \tag{A.38}$$

where m_v is the compressibility coefficient and ϵ is strain. Applying $\Delta t \rightarrow 0$ gives:

$$\frac{\Delta\epsilon}{\Delta t} = m_v(\frac{\Delta u}{\Delta t} - \Psi) \tag{A.39}$$

$$\frac{\partial\epsilon}{\partial t} = m_v(\frac{\partial u}{\partial t} - \Psi) \tag{A.40}$$

Combining this with the vertical consolidation equation results in:

$$\frac{k_z}{\gamma_w}\frac{\partial^2 u}{\partial z^2} = m_v(\frac{\partial u}{\partial t} - \Psi) \tag{A.41}$$

where k_z is the vertical permeability and γ_w is the unit weight of water. The (until now) arbitrary function Ψ describes the undrained-pore pressure generation and can be written as:

$$\Psi = \frac{\partial u_g}{\partial t} = \frac{\partial u_g}{\partial N} \cdot \frac{\partial N}{\partial t} \tag{A.42}$$

$\frac{\partial N}{\partial t}$ describes the amount of cycles at time t. The paper uses the following formulation to describe the relationship between the generated pore pressure u_g and number of cycles N:

$$\frac{u_g}{\sigma'_{v0}} = \frac{2}{\pi}\arcsin\left(\frac{N}{N_l}^{1/2\theta}\right) \tag{A.43}$$

where σ'_{v0} is the initial vertical stress, θ is an empirical constant ($\theta = 0.7$ is often resonable for the average sand) and N_l is the number of cycles until liquefaction. Differentiating the last equation with respect to N results in:

$$\frac{\partial u_g}{\partial N} = \frac{\sigma'_{v0}}{\theta\pi N_l} \cdot \frac{1}{\sin(\pi/2r_u)^{2\theta-1}\cos(\pi/2r_u)} \tag{A.44}$$

Wijngaarden (2017) adapted equation A.41 allowing for dissipation in the vertical and radial directions:

$$\frac{\partial}{r\partial r}\left(r\frac{k_r}{\gamma_w}\frac{\partial u}{\partial r}\right) + \frac{\partial}{\partial z}\left(\frac{k_z}{\gamma_w}\frac{\partial u}{\partial z}\right) = m_v(\frac{\partial u}{\partial t} - \frac{\partial u_g}{\partial t}) \tag{A.45}$$

Rahman created an empirical relationship based on liquefaction curves to determine the number of cycles to full liquefaction, N_l:

$$\frac{\Delta\tau/\sigma'_{v0}}{I_d} = aN_l^{-b} \tag{A.46}$$

where I_d is the relative density and a and b are fitting constants. I_d can be determined experimentally, whereas a and b are fitting constants which are applied on the results of CDSS or CTX tests.

A.7.3. Earthquake Engineering

Cyclic Stress Approach: Boulanger and Idriss (2014)
The cyclic stress approach is a semi-empirical method that is based on the comparison of the (earthquake)-induced loading, expressed in terms of cyclic shear stresses, to the liquefaction resistance, also expressed in terms of cyclic shear stresses. This is based on the assumption that excess pore pressures are fundamentally related to cyclic shear stresses. The initiation of liquefaction is expected where the imposed loading surpasses the resistance of the soil (Figure A.30). This can be expressed as a factor of safety against liquefaction, FS_L:

$$FS_L = \frac{CRR}{CSR} \tag{A.47}$$

Where CSR is the cyclic stress ratio, CRR is the cyclic resistance ratio and $FL_L < 1$ indicates the initiation of liquefaction.

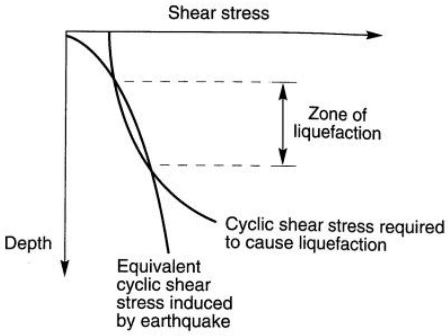
Shear stress
Zone of liquefaction
Cyclic shear stress required to cause liquefaction
Depth
Equivalent cyclic shear stress induced by earthquake

Figure A.30: Graphical method to identify zones of liquefaction. After Kramer (1996)

The CPT-based and SPT-based liquefaction triggering procedures for cohesionless soils (Boulanger and Idriss, 2014) is a well known framework based on a stress-based approach. The CRR of the soil is correlated with in-situ parameters such as CPT penetration resistance and SPT blow count. The CSR, induced by earthquake loading, is given by:

$$CSR_{M,\sigma_v'} = 0.65\frac{\tau_{max}}{\sigma_v'} \tag{A.48}$$

where τ_{max} is the maximum earthquake induced shear stress, σ_v' is the vertical effective stress and the subscripts indicate the moment magnitude (M) and in-situ vertical effective stress. The maximum shear stress can be determined using dynamic response analyses or alternatively by the Seed-Idriss Simplified Liquefaction Procedure given by:

$$CSR_{M,\sigma_v'} = 0.65\frac{\sigma_v}{\sigma_v'}\frac{a_{max}}{g}r_d \tag{A.49}$$

where σ_v is the vertical total stress at depth z, a_{max}/g is the maximum horizontal acceleration at the ground surface and r_d is the shear stress reduction factor accounting for the dynamic response of the soil profile. The CRR is correlated to standardized, energy-corrected N_{60} values and corrected cone tip resistance values q_c. These values are corrected for overburden stress effects by:

$$q_{c1N} = C_N q_{cN} = C_n\frac{q_c}{P_a} \tag{A.50}$$

$$(N_1)_{60} = C_N N_{60} \tag{A.51}$$

where C_N is the overburden correction factor, P_a is the atmospheric pressure, $q_{cN} = q_c/P_a$ and q_{c1N} and $(N_1)_{60}$ are the penetration resistances at an overburden stress of 1 atm. The penetration resistance values can also be expressed in terms of an equivalent clean-sand value: q_{c1Ncs} or $(N_1)_{60cs}$ using:

$$q_{c1Ncs} = q_{c1N} + \Delta q_{c1N} \tag{A.52}$$

$$(N_1)_{60cs} = (N_1)_{60} + \Delta(N_1)_{60} \tag{A.53}$$

where Δq_{c1N} and $\Delta(N_1)_{60}$ are functions of the fines content (FC). These adjustment to transform the soil penetration resistance values to equivalent clean sand can be expressed as:

$$\Delta q_{c1N} = \left(11.9 + \frac{q_{c1N}}{14.6}\right)\exp\left(1.63 - \frac{9.7}{FC+2} - \left(\frac{15.7}{FC+2}\right)^2\right) \tag{A.54}$$

$$\Delta(N_1)_{60} = \exp\left(1.63 - \frac{9.7}{FC+0.01} - \left(\frac{15.7}{FC+0.01}\right)^2\right) \tag{A.55}$$

where FC is the fines content in percentage. The CRR can now be expressed by only the soil penetration resistance values of q_{c1Ncs} or $(N_1)_{60cs}$ for a normalized situation of a M = 7.5 and σ'_v= 1 atm:

$$CRR_{M=7.5,\sigma'_v=1atm} = \exp\left(\frac{q_{c1Ncs}}{113} + \left(\frac{q_{c1Ncs}}{1000}\right)^2 - \left(\frac{q_{c1Ncs}}{140}\right)^3 + \left(\frac{q_{c1Ncs}}{137}\right)^4 - 2.80\right) \tag{A.56}$$

$$CRR_{M=7.5,\sigma'_v=1atm} = \exp\left(\frac{(N_1)_{60cs}}{14.1} + \left(\frac{(N_1)_{60cs}}{126}\right)^2 - \left(\frac{(N_1)_{60cs}}{23.6}\right)^3 + \left(\frac{(N_1)_{60cs}}{25.4}\right)^4 - 2.80\right) \tag{A.57}$$

The CRR for a given magnitude is dependent on three other factors as the relationships are valid for a standardized situation for M = 7.5 and σ'_v = 1 atm: the magnitude scaling factor or MSF (duration of the shaking), effective overburden stress (K_σ) and presents of sustained static shear stresses (K_α). The CRR for a certain M and σ'_v can be determined by adjusting the calculated value of $CRR_{M=7.5,\sigma'_v}$ using:

$$CRR_{M,\sigma'_v} = CRR_{m=7.5,\sigma'_v} \cdot K_\sigma \cdot K_\alpha \cdot MSF \tag{A.58}$$

The four relationships describing the dynamic behaviour, penetration resistance and soil characteristics are:

1. Overburden correction factor, C_N
   The overburden correction factor C_N can be expressed as:

$$C_N = \left(\frac{P_a}{\sigma'_v}\right)^m \leq 1.7 \tag{A.59}$$

$$m = 1.338 - 0.249(q_{c1Ncs})^{0.264} \tag{A.60}$$

$$m = 0.784 - 0.0768\sqrt{(N_1)_{60cs}} \tag{A.61}$$

2. Overburden correction factor, K_σ
   The overburden correction factor K_σ can be expressed as:

$$K_\sigma = 1 - C_\sigma ln\left(\frac{\sigma'_v}{P_a}\right) \leq 1.1 \tag{A.62}$$

$$C_\sigma = \frac{1}{37.3 - 8.27(q_{c1Ncs})^{0.264}} \leq 0.3 \tag{A.63}$$

$$C_\sigma = \frac{1}{18.9 - 2.55\sqrt{(N_1)_{60cs}}} \leq 0.3 \tag{A.64}$$

3. Static shear stress correction factor, K_α
   The static shear stress correction factor K_α can be expressed as:

$$K_\alpha = a + b\exp\left(\frac{-\xi_R}{c}\right) \tag{A.65}$$

$$a = 1267 + 636\alpha^2 - 634\exp(\alpha) - 632\exp(-\alpha) \tag{A.66}$$

$$b = \exp(-1.11 + 12.3\alpha^2 + 1.31\ln(\alpha + 0.0001)) \tag{A.67}$$

$$c = 0.138 + 0.126\alpha + 2.52\alpha^3 \tag{A.68}$$

$$\alpha = \frac{\tau_s}{\sigma'_{vc}} \tag{A.69}$$

$$\xi_R = \frac{1}{Q - \ln\left(\frac{100(1+3K_0)\sigma'_{vc}}{3P_a}\right)} - (0.479(q_{c1N})^{0.263} - 1.063) \tag{A.70}$$

$$\xi_R = \frac{1}{Q - \ln\left(\frac{100(1+3K_0)\sigma'_{vc}}{3P_a}\right)} - \sqrt{\frac{(N_1)_{60}}{46}} \tag{A.71}$$

where K_0 is the at-rest earth pressure. The relationships are valid within the following limits: $\alpha \leq 0.35$ and $-0.6 \leq \xi_R \leq 0.1$.

4. Magnitude scaling factor, MSF
   The magnitude scaling factor (MSF) accounts for duration effects of the earthquake loading, i.e. number and amplitude of loading cycles. The MSF can be expressed as:

$$MSF = 6.9\exp\left(\frac{-M}{4}\right) - 0.058 \leq 1.8 \tag{A.72}$$

where M is the moment magnitude.

Cyclic Strain Approach

The cyclic strain approach is a semi-empirical method and based on experimental evidence that densification of dry sand can be controlled by cyclic strains and the existence of the critical state density. Densification of dry sand is directly related to the generation of excess pore pressures in saturated sand. The cyclic strain approach is analogous to the cyclic stress approach (Figure A.30). While the (earthquake-)imposed strains are more difficult to determine, the test procedure to determine the liquefaction resistance from element tests using strain boundaries rather than stress boundaries is easier. The determination of the liquefaction resistance based on cyclic stresses is dependent on a higher amount of factors compared to the cyclic strain based determination procedures. These factors include density, soil fabric, strain history, over-consolidation ratio (OCR) and length of time under sustained pressure. These also have influence on τ_{cyc} and G, resulting in even smaller influence on the ratio $\gamma_{cyc} = \tau_{cyc}/G$.

Effective Stress Analysis

Effective stress analyses prove to be challenging and is highly dependent on the capability of the constitutive model to accurately model the stress-strain behavior. Effective stress methods have been implemented the Finite Element Method (FEM) and Finite Difference Method (FDM). Simple models, like Hooke's law, simplify soil behavior but can be very useful for situations within the small strain boundaries. Simple models are generally fast and computationally less demanding, and can provide an accurate estimation dependent on the situation. Advanced constitutive models, like PM4Sand and UBC3D-PLM, are capable of describing the soil behavior more accurately but also have limitations as described in Section A.5. Advanced constitutive models often required parameters which are only obtainable using complicated and expensive tests, such as cyclic triaxial test, cyclic direct simple shear test or resonant column test.

A.8. Summary on the Literature Review

Regarding the wind turbine (Section A.1): this thesis is restricted to a 2.5 MW wind turbine on a shallow foundation. The foundation is cyclically loaded due to variable wind loads, which results in a fatigue type of problem where large amplitudes in the load and a low frequency is expected. The wind turbine is expected to have a loading frequency between 0.3-0.4 Hz. Literature suggests that low frequency problem (e.g. $f \leq 5\ Hz$) can be modelled as quasi-static(Wichtmann et al., 2004). It is also mentioned that wind and wave loads on offshore foundations have negligible effects in the soil domain (Andresen, 2015). Further research is required upon this subject.

Regarding the design of the dike (Section A.2): a shallow foundation on a dike is considered for this thesis. Excess pore pressures and additional settlements are expected consequences of the installation and commissioning of a shallow foundation. Important failure mechanisms that are influenced by these phenomena are stability of the outer and inner slope and settlements of the crest. These failure mechanisms are considered in the analysis to determine the influence of cyclic loading on the liquefiable soil layer.

Regarding the (modelling of) soil behaviour (Section A.3): cyclic soil behaviour is considered highly complex, and constitutive models are not capable do capture all features of liquefaction behaviour in a single model. The Mohr-Coulomb and Hardening Soil Small Strain models are capable of modelling cyclic loading, but do not account for accumulation of pore pressures or volumetric strains. PM4Sand and UBC3D-PLM are capable of accounting for pore pressure and volumetric strain accumulation. However, these models are difficult to calibrate and have various parameters of which the meaning is not clear. Both of the models give a better prediction of the soil response when calibrated to the appropriate loading conditions, but have shortcomings on the calculation of both the displacements and pore pressures.

Regarding the consolidation behaviour (Section A.6): Consolidation behaviour can be taken into account using analytic or numerical models do describe the pore pressure development over time. Fully undrained conditions may overestimate pore pressures as the cyclic loads have a relatively low frequency to earthquakes. Terzaghi's consolidation theory can be used for relatively simple situation with simple geometries whereas Biot's formulation is used in finite element analysis program Plaxis.

Regarding the various approaches of liquefaction modelling (Section A.7): Earthquake and offshore engineering both deal with cyclic loading. The driving force for the liquefaction analysis is expressed as the cyclic stress ratio as an result of a change in shear stresses. The resisting forces are expressed as the cyclic resistance ratio defined by experimental liquefaction curves. Earthquake engineering depends more on an empiric approach to determine the cyclic stress ratio as it is difficult to predict where earthquakes will occur and only a small amount of information is available. Linear or non-linear models can be used to predict the site response as a result of an earthquake but these methods are uncertain. Seed and Rahman (1978) determine the shear stresses in the soil are a result of linear wave theory, which is based on analytic solutions. The soil behavior is modelled as a linear elastic material. A difference between the two disciplines is the handling of drainage conditions. Earthquake loading takes place in a matter of seconds, whereas wave action as a result of a storm takes places over hours. The first is therefore determined using undrained conditions whereas the offshore application uses Terzaghi's consolidation theory to determine the partial drainage condition during the wave action. Important features that need to be included into the further analysis are the determination of the cyclic stress ratio as a result of the shallow foundation. Also, the process of pore pressure redistribution needs to be integrated into the model as the cyclic loading conditions are slow and fully undrained conditions may overestimate the pore pressures.

B

Starting Points Additional Information

This appendix contains additional information on the starting points used in th the soil-structure interaction and consolidation

B.1. Material Parameter Set for Plaxis 2D

The following tables contain the input parameters used for the soil models.

Table B.1: Linear Elastic parameters

Material	Concrete	Unit
Drainage type	Non-Porous	
γ_{unsat}	24.0	kN/m^3
E	20.0E6	kN/m^2
ν	0.3	-

Table B.2: Mohr-Coulomb parameters

Material	Clay	Sand	Clay Deep	Unit
Drainage	Undrained (A)	Undrained (A)	Undrained (A)	
γ_{unsat}	17	17	19	kN/m^3
γ_{sat}	17	19	19	kN/m^3
E’	2000	55000	4000	kN/m^2
ν'	0.3	0.2	0.3	-
c'_{ref}	5.0	0.0	5	kN/m^2
ϕ'	17.5	24.6	17.5	°
ψ	0.0	0.0	0.0	°
$e_{initial}$	0.7	0.75	0.7	-

Table B.3: Hardening Soil Small Strain parameters

Material	Clay	Sand	Clay Deep	Unit
Drainage	Undrained (A)	Undrained (A)	Undrained (A)	
γ_{unsat}	17	17	19	kN/m^3
γ_{sat}	17	19	19	kN/m^3
E_{50}^{ref}	10.8E3	25E3	9E3	kN/m^2
E_{oed}^{ref}	11.4E3	25E3	9E3	kN/m^2
E_{ur}^{ref}	32.4E3	75E3	27E3	kN/m^2
power (m)	1.0	0.5	.7	-
c'_{ref}	5.0	0.0	5.0	kN/m^2
ϕ'	17.5	24.6	17.5	°
ψ	0.0	0.0	0.0	°
$e_{initial}$	0.7	0.75	0.7	-
$\gamma_{0.7}$	0.11E-3	0.161E-3	0.169E-3	-
G_0^{ref}	150E3	98.0E3	115E3	kN/m^2

Table B.4: Elastic Plate parameters

Material	Plate	Unit
Type	Elastic	
Isotropic	Yes	
EA_1	90.0E6	kN/m
EI	45.0E6	kNm^2/m
d	2.449	m
w	0.0	kN/m/m
ν	0.15	-

B.2. Natural Frequencies

This Section contains the analysis of the natural frequencies of the soil and the wind turbine for the purpose of supporting the dynamic analysis in Chapter 4. An estimation of the natural frequency of the soil can be approximated using a linear transfer function. A linear transfer function is a mathematical method to calculate the response of a single-degree-of-freedom system (SDOF) to an excitation. Shearing and damping characteristics can be included when a Kelvin-Voigt type of solid is adopted to model the soil behaviour. Kramer (1996) presents the following formula for the frequency-dependent amplification factor for a forced vibration:

$$|F_w(f)| = \frac{1}{\sqrt{\cos^2 fH/v_s + (\xi(fH/v_s))^2}} \tag{B.1}$$

where F_w is the amplification factor, f is the frequency, H is the height of the soil layer in m, $v_s = \sqrt{G/\rho}$ is the shear wave velocity in m/s and ξ is the damping ratio. G is the shear modulus and ρ is the density of the material. The n-th natural frequency can be found using the following equation:

$$f_n = \frac{v_s}{H}(\frac{\pi}{2} + n\pi) \quad with,\ n\ =\ 0, 1, 2, ..., \infty \tag{B.2}$$

The fundamental frequency or natural frequency of the soil layer can be found applying n = 0. Significant amplification can be expected when the load has a frequency that is sufficiently close to the natural frequency of the soil determined by Equation B.1. Figure B.1 shows the influence of the shear wave velocity and damping characteristics on the amplification factor of the whole soil body (up to -20 m below surface level). The weighted average of the full profile is used to determine the natural frequency. The weighted average of the shear wave velocity is determined for the Mohr-Coulomb material set (Section 3.3) using shear modulus G and is indicated by MC. The weighted average for the Hardening Soil Small

Strain material set (Section 3.3) is determined using the unloading/reloading shear modulus (G_{ur}) and is indicated by HSss. An increase of shear modulus results in an increase of shear wave velocity and shifts the natural frequency of the layer towards a higher frequency spectrum. A decrease of shear modulus results in a decrease of shear wave velocity resulting in a shift towards a lower frequency spectrum. A second order amplification peak is observed around 7.2 Hz for the MC set.

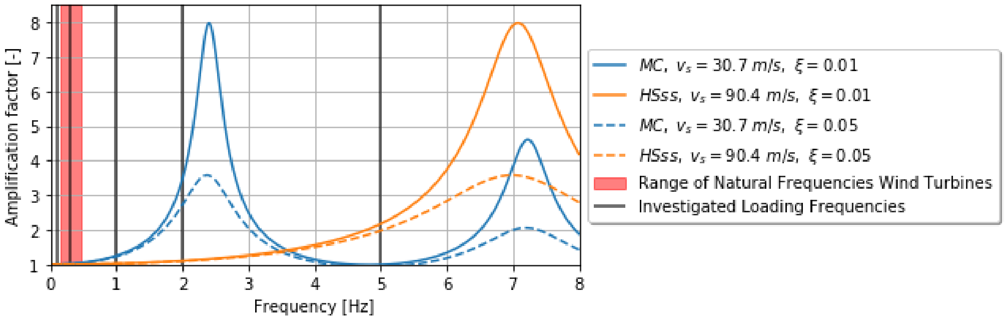

Figure B.1: Influence of the shear wave velocity and damping on the amplification factor of a linear elastic soil layer (Equation B.1)

The dynamic characteristics of the wind turbine can be modelled using discrete elements like masses and springs. The structure can be represented using either a SDOF system or a multiple-degrees-of-freedom (nDOF) schematization. 1P and 3P characteristics are not taken into account in this analysis. A reversed pendulum with a mass on top, fixed to a rigid base is a possibility to schematise a wind turbine. Figure B.2 shows the representation where the stiffness and damping properties of the beam correspond with the SDOF characteristics. The dynamics of the SDOF system are described by the following equation of motion (Clough and Penzien, 2003):

$$m\ddot{x}(t) + c\dot{x}(t) + kx(t) = f(t), \quad with\ x(0) = x_0\ and\ \dot{x}(0) = v_0 \tag{B.3}$$

Where m is the mass of the wind turbine, c is the damping ratio of the tower corresponding to horizontal motion, k is the equivalent horizontal flexural stiffness of the tower and f(t) is an external force representing the wind load on the rotor. x_0 and $\dot{x}_0$ represent the initial conditions of the system.

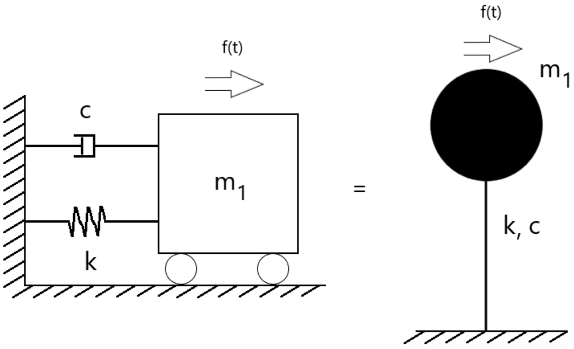

Figure B.2: SDOF representation of a wind turbine, where m is the mass, c the damping ratio, k the stiffness and f(t) is a time dependent external force

The mass m_1 consists of the mass of the top structure (gondola and rotor) and 22.7% of the mass of the turbine tower according to van der Tempel (2006): $m = m_{top} + 0.227 m_{tower}$. The stiffness parameter is determined using the area moment of inertia, I, for a cylinder in longitudinal direction and the Young's modulus, E:

$$I = \frac{1}{8}\pi r_{tower}^3 t_{wall} \tag{B.4}$$

$$k = \frac{3EI}{L_{tower}^3} \tag{B.5}$$

where r_{tower} is the inner radius of the tower, L_{tower} is the length of the tower and t_{wall} is the wall thickness of the tower. The free response of the system is found using f(t) = 0 and damping is disregarded resulting in c = 0. The solution to equation B.3 results in the natural frequency of the SDOF system and the results using this equation are presented in Table B.7:

$$f_n = \frac{1}{2\pi}\sqrt{\frac{k}{m}} \tag{B.6}$$

A more accurate representation is a two-degrees-of-freedom (2DOF) schematization where the mass of the foundation and soil beneath the turbine is connected to a stationary point using springs and dashpots. Figure B.3 depicts the 2DOF system using 2 masses connected by springs and dashpots as defined by equation B.7. The influence of the rotational and lateral springs on the lower mass are included using an equivalent stiffness, k_{eq}. The equations of motion for the 2DOF system are (Clough and Penzien, 2003):

$$\begin{bmatrix} m_1 & 0 \\ 0 & m_2 \end{bmatrix}\begin{bmatrix} \ddot{x}_1(t) \\ \ddot{x}_2(t) \end{bmatrix} + \begin{bmatrix} c_{eq}+c_1 & -c_1 \\ -c_1 & c_1 \end{bmatrix}\begin{bmatrix} \dot{x}_1(t) \\ \dot{x}_2(t) \end{bmatrix} + \begin{bmatrix} k_{eq}+k_1 & -k_1 \\ -k_1 & k_1 \end{bmatrix}\begin{bmatrix} x_1(t) \\ x_2(t) \end{bmatrix} = \begin{bmatrix} f_1(t) \\ f_2(t) \end{bmatrix} \tag{B.7}$$

where m_1 represents the gondola, rotor and 22.7% of the mass of the turbine tower, m_2 represents the mass of the foundation and remaining 77.3% of the mass of the turbine tower, k_{eq}, k_1 are the equivalent stiffness simulating the rotational and lateral stiffness of the foundation. The free response of the system is determined by setting the external forces equal to zero. The damping coefficients is assumed to have little impact and thus set to zero. The nontrivial solution of the eigenvalue problem is obtained by setting the determinant to zero:

$$m_1 m_2 \omega^4 - (k_{eq} m_2 + m_2(k_{eq} + k_1))\omega^2 + k_{eq} k_1 = 0 \tag{B.8}$$

where ω is the angular velocity leading to the natural frequency. The mass of the foundation is determined as:

$$m_{found} = \gamma_{found} H_{found} \pi r_{found}^2 \tag{B.9}$$

where γ is the unit weight of the foundation, H_{found} is the thickness and r_{found} the radius of the foundation. The rotational and lateral spring stiffness characteristics are defined using API (1993) and the equivalent stiffness is defined using Harland and Vugts (1996):

$$k_r = \frac{8 G r_{found}^3}{3(1-\nu)} \tag{B.10}$$

$$k_l = \frac{32(1-\nu) G r_{found}}{7-8\nu} \tag{B.11}$$

$$k_{eq} = \frac{k_r k_l L_{turbine}^2}{k_r + k_l L_{turbine}^2} \tag{B.12}$$

where G is the shear modulus of the soil, r_{found} is the radius of the foundation, ν is the Poisson ratio of the soil, $L_{turbine}$ is the turbine length.

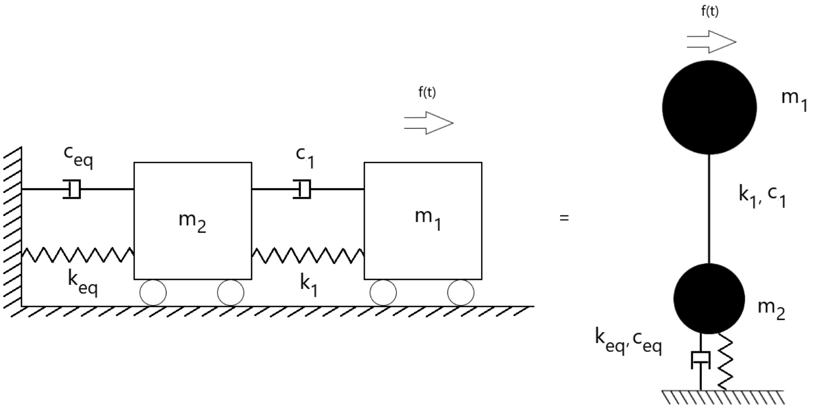

Figure B.3: 2DOF representation of a wind turbine. Additional mass m_2 represents the foundation and the 77.3% of the tower. The foundation is connected to the soil using lumped parameters k and c to describe the stiffness and damping characteristics, respectively.

Tables B.5 and B.6 show the input for the natural frequency analysis. The range of turbines vary from small to very large. Turbine #2 has the same properties as the 2.5 MW wind turbine that is modelled in the reference case.

Table B.5: Input analysis natural frequency

G [MPa]	ν [-]	γ_{found} $[kg/m^3]$	E [kN/m^2]
20.0	0.3	24.0	2.1E8

Table B.6: Input analysis natural frequency

Turbine #	r_{tower} [m]	t_{wall} [m]	L_{tower} [m]	m_{top} [ton	r_{found} [m]	H_{found} [m]
1	2.0	0.1	65	80	4	1.0
2	3.0	0.125	98	107	12.5	1.5
3	4.0	0.15	150	450	7.5	2.0
4	6.0	0.2	250	600	10	3.0

Table B.7 shows the results of the natural frequency analysis of a wind turbine as SDOF and 2DOF schematizations using discrete elements. The range of frequencies is plotted in figure B.1 as a red bar to compare the natural frequencies of the turbine with respect to the soil. Figure B.1 also shows the loading frequencies that are defined in Section 3.4 and investigated in the frequency analysis of Chapter 4. Turbine #2 has a similar natural frequency compared to the loading signal as presented in Section 3.4 concluding that the orders of magnitude of the used input are correct. Three additional cases are analyzed using information of wind turbine producers ((Windcollectief Wieringermeer B.V., Various), (van der Weijden, 2015). This results in a smaller, lighter turbine (#1) and two larger, heavier turbines (#3 and #4). In Table B.7 it is observed that the natural frequency of the turbine decreases with increasing mass and stiffness for both the SDOF and 2DOF schematizations. The natural frequency of the wind turbine shifts further apart from the natural frequency of the soil as the wind turbines are increasing in size. However, a larger size implies bigger loads induced by the wind turbine onto the soil. In addition, it is observed that the impact of the second mass in the 2DOF schematization has a larger impact on the natural frequency for the heavier turbines compared to the lighter turbines. The addition of the relatively heavy mass on the bottom of the system results in a stiffer response of the system. The distribution of the masses along the length of the turbine gives a more realistic estimation of the natural frequency.

Table B.7: Results natural frequencies for a SDOF and 2DOF schematization

Turbine #	m_1 [ton]	m_2 [ton]	k_1 [kN/m]	k_{eq} [kN/m]	$f_{n,SDOF}$ [Hz]	$f_{n,2DOF}$ [Hz]
1	105.5	1291.8	720.7	4861.8	0.4160	0.4473
2	195.3	17965.9	887.1	146939.3	0.3392	0.4582
3	691.3	9290.3	703.7	32080.1	0.1606	0.3003
4	1330.1	25063.7	1336.0	76041.8	0.1595	0.2808

C

Results Analysis SSI

C.1. Results Frequency Analysis

The cyclic stress ratio is also determined using two different profiles where the liquefiable soil layer is located between -5 m and -10.5 m below the surface and between -10 m and -15.5 m below the surface. The influence of the depth of the liquefiable soil layer on the magnitude of the CSR is determined. Figures C.1 to C.4 show the results where the liquefiable soil layer is located between -5 m and -10.5 m below surface level. The soil behaviour is simulated using the Mohr-Coulomb soil model and the calculation method is mentioned in the accompanying subscript.

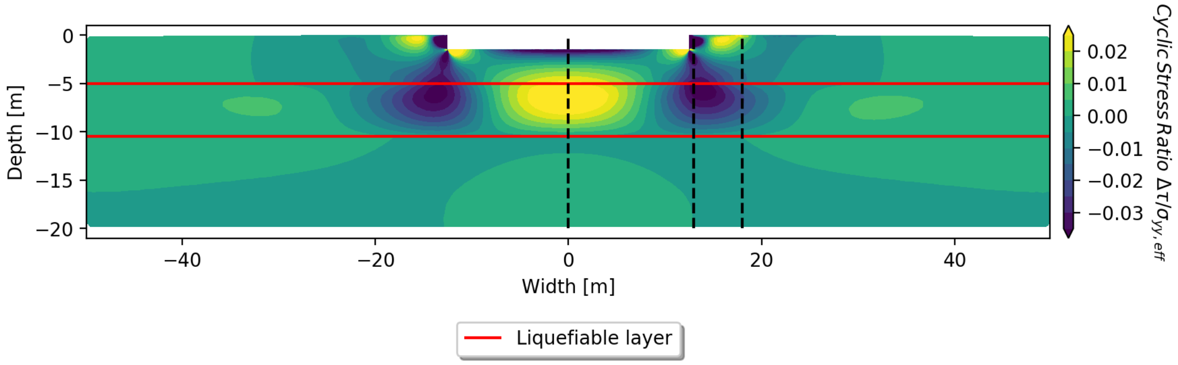

Figure C.1: CSR contour plot, MC, quasi-static

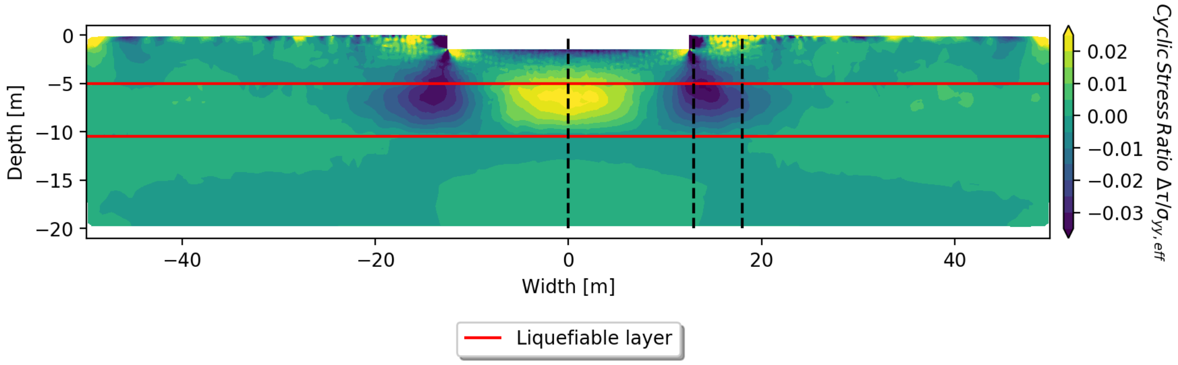

Figure C.2: CSR contour plot, MC, dynamic, load frequency of 0.3 Hz

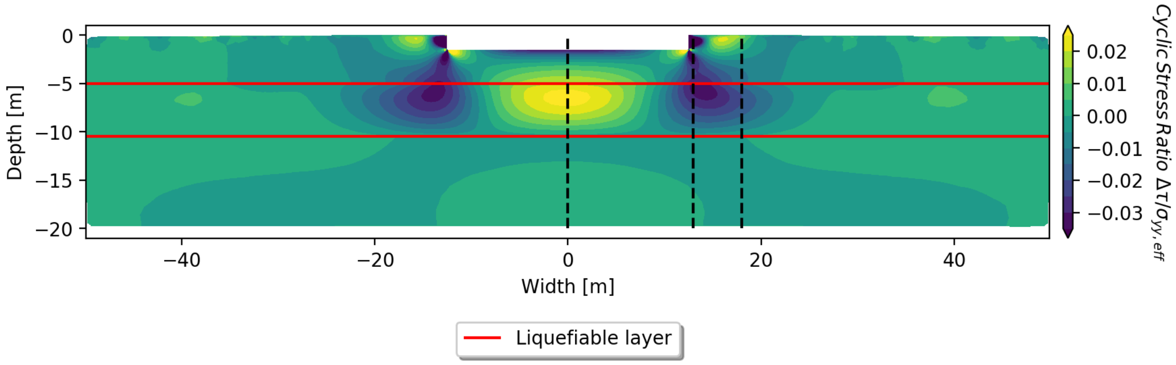

Figure C.3: CSR contour plot, MC, dynamic with 2% Rayleigh damping, load frequency of 0.3 Hz

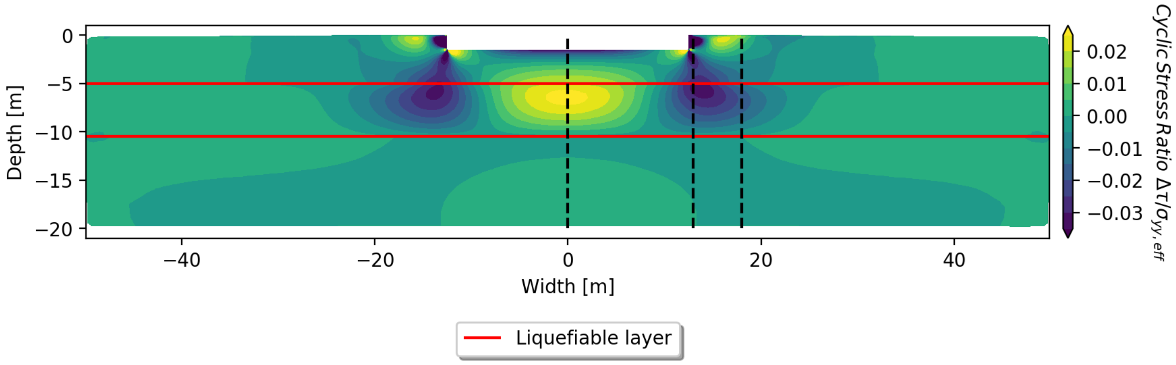

Figure C.4: CSR contour plot, MC, dynamic with 5% Rayleigh damping, load frequency of 0.3 Hz

Figures C.5 to C.8 show the results where the liquefiable soil layer is located between -5 m and -10.5 m below surface level. The soil behaviour is simulated using the Hardening Soil Small Strain soil model and the calculation method is mentioned in the accompanying subscript.

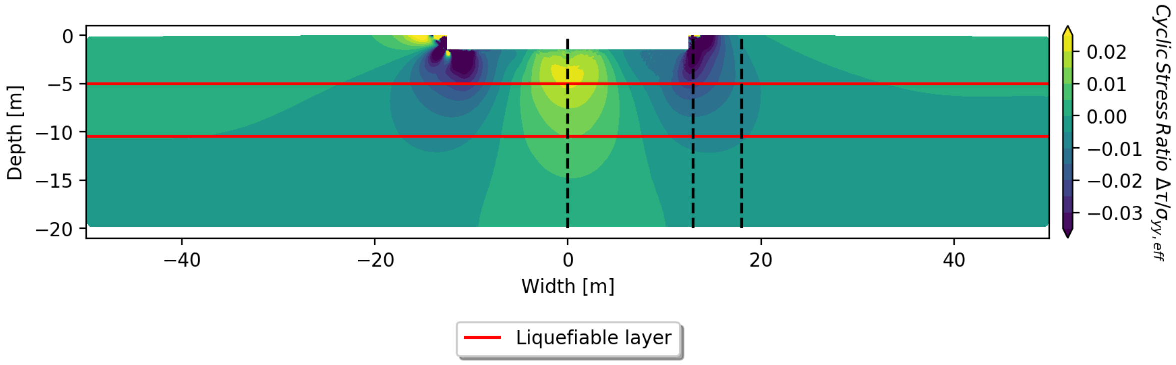

Figure C.5: CSR contour plot, HSss, quasi-static

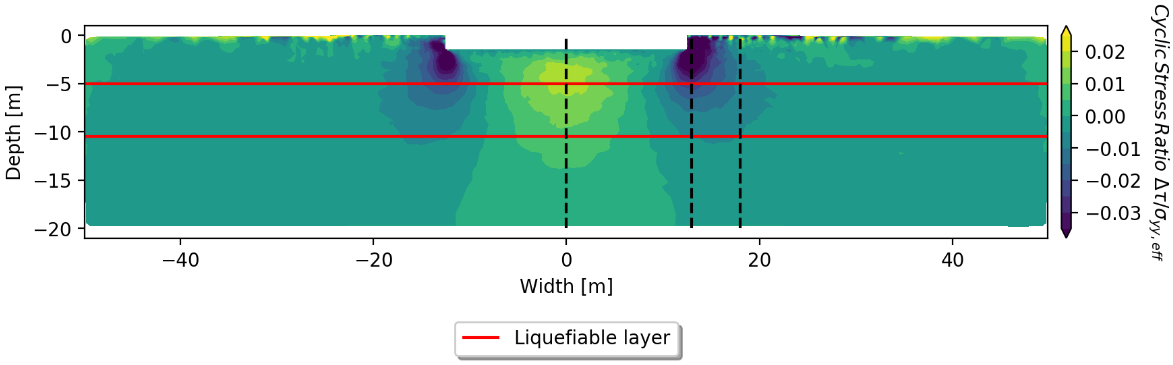

Figure C.6: CSR contour plot, HSss, dynamic, load frequency of 0.3 Hz

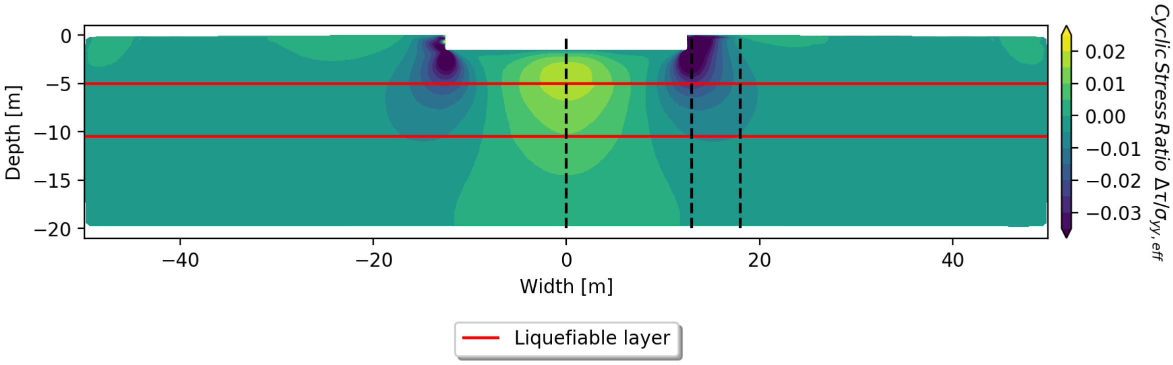

Figure C.7: CSR contour plot, HSss, dynamic with 2% Rayleigh damping, load frequency of 0.3 Hz

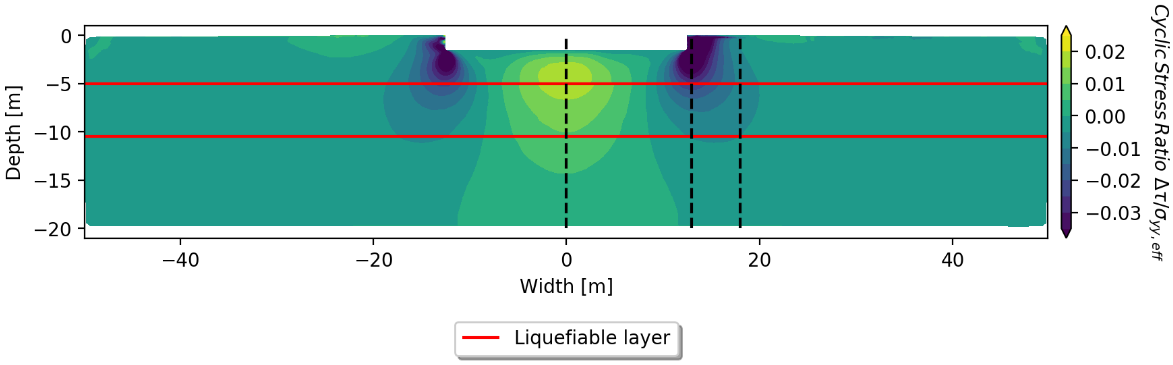

Figure C.8: CSR contour plot, HSss, dynamic with 5% Rayleigh damping, load frequency of 0.3 Hz

Figures C.9 to C.12 show the results where the liquefiable soil layer is located between -7.5 m and -13 m below surface level. The soil behaviour is simulated using the Mohr-Coulomb soil model and the calculation method is mentioned in the accompanying subscript.

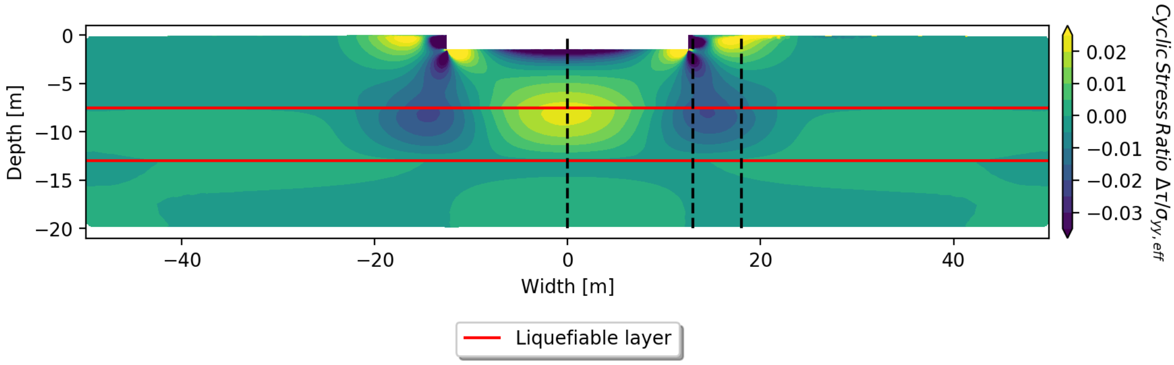

Figure C.9: CSR contour plot, MC, quasi-static

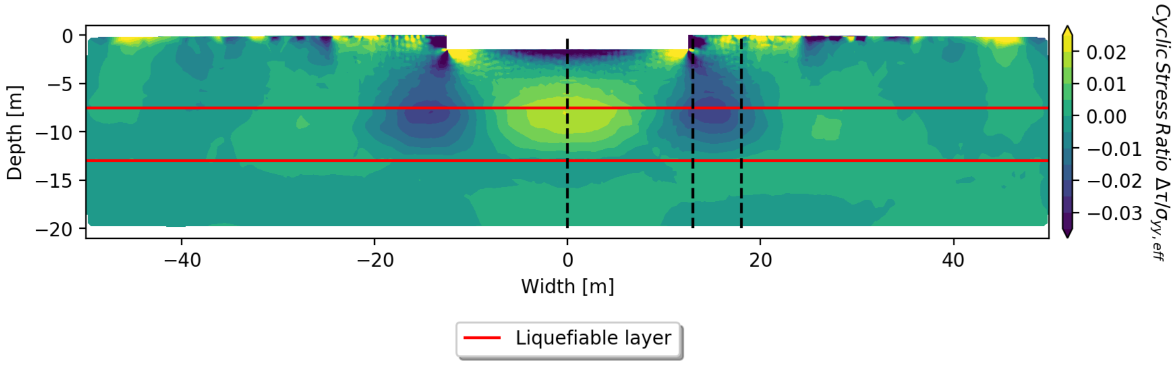

Figure C.10: CSR contour plot, MC, dynamic, load frequency of 0.3 Hz

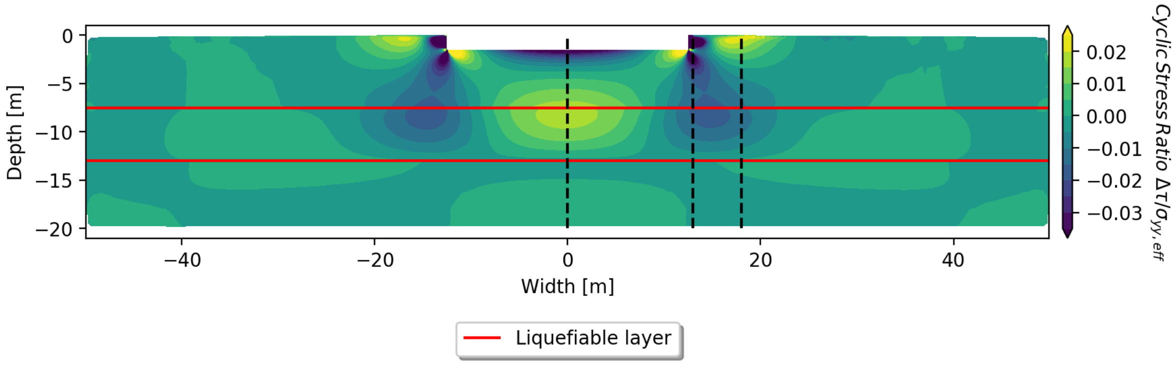

Figure C.11: CSR contour plot, MC, dynamic with 2% Rayleigh damping, load frequency of 0.3 Hz

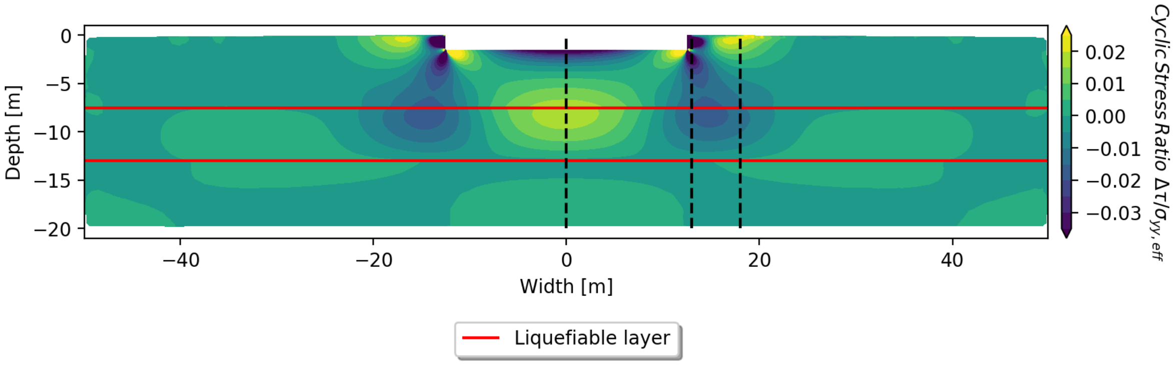

Figure C.12: CSR contour plot, MC, dynamic with 5% Rayleigh damping, load frequency of 0.3 Hz

Figures C.13 to C.16 show the results where the liquefiable soil layer is located between -7.5 m and -13 m below surface level. The soil behaviour is simulated using the Hardening Soil Small Strain soil model and the calculation method is mentioned in the accompanying subscript.

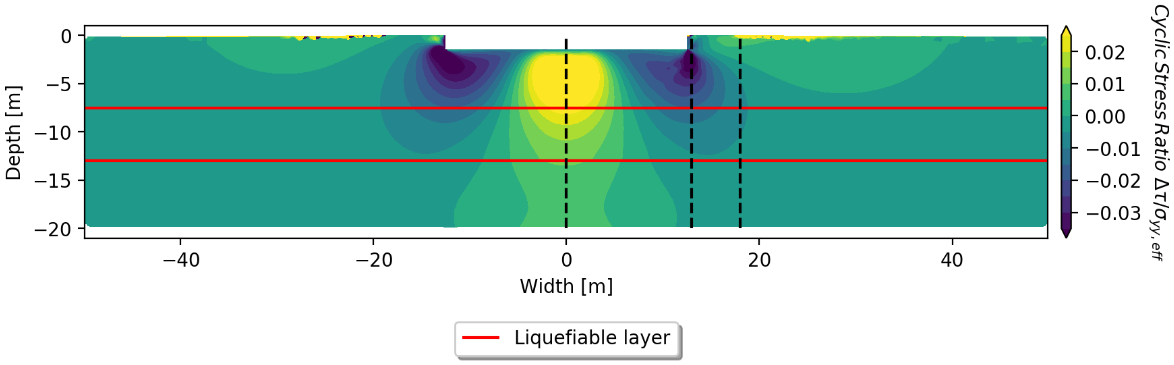

Figure C.13: CSR contour plot, HSss, quasi-static

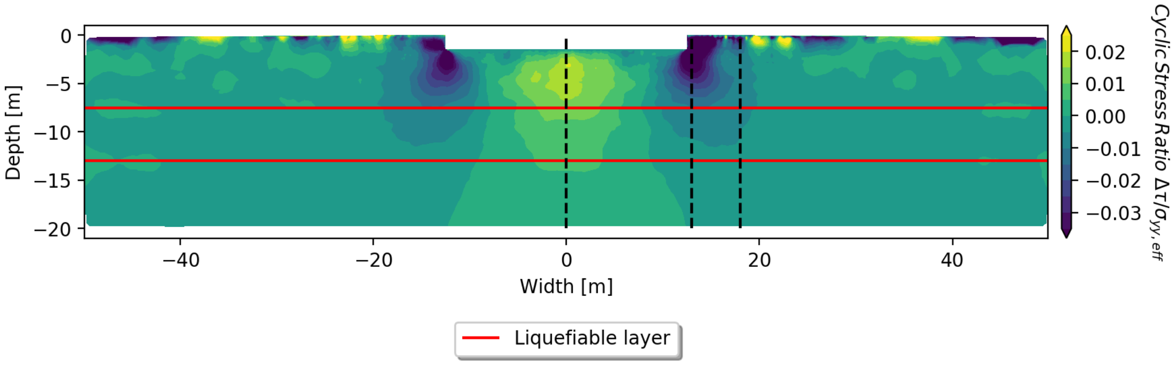

Figure C.14: CSR contour plot, HSss, dynamic, load frequency of 0.3 Hz

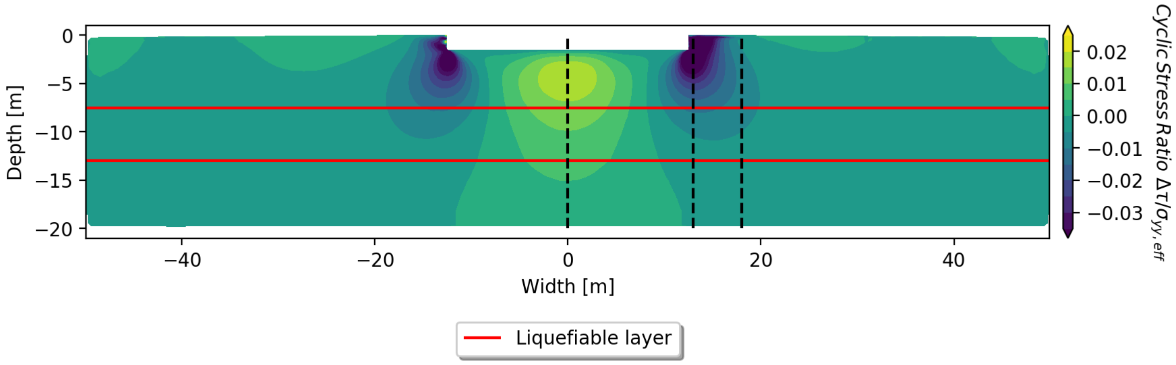

Figure C.15: CSR contour plot, HSss, dynamic with 2% Rayleigh damping, load frequency of 0.3 Hz

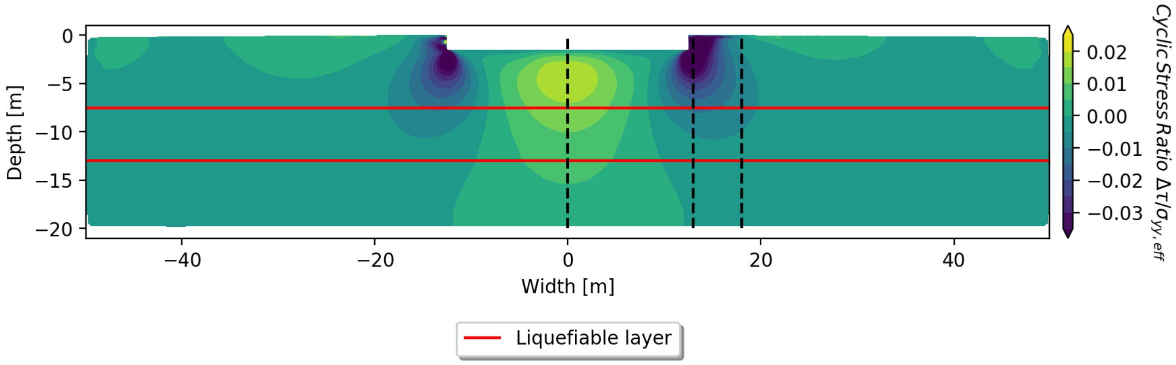

Figure C.16: CSR contour plot, HSss, dynamic with 5% Rayleigh damping, load frequency of 0.3 Hz

Figures C.17 to C.20 show the results where the liquefiable soil layer is located between -10 m and -15.5 m below surface level. The soil behaviour is simulated using the Mohr-Coulomb soil model and the calculation method is mentioned in the accompanying subscript.

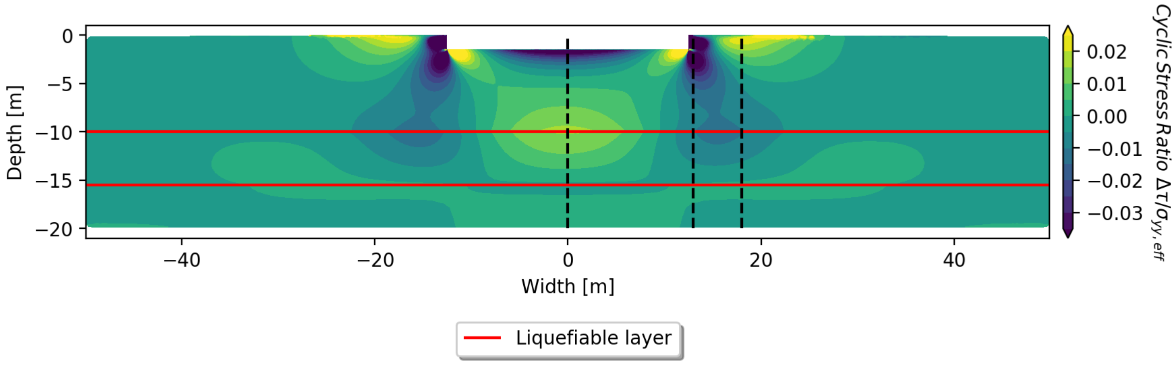

Figure C.17: CSR contour plot, MC, quasi-static

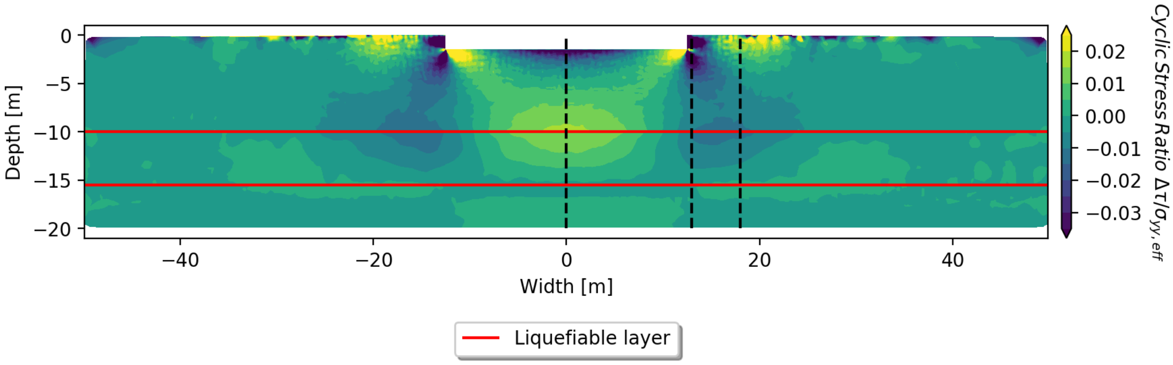

Figure C.18: CSR contour plot, MC, dynamic, load frequency of 0.3 Hz

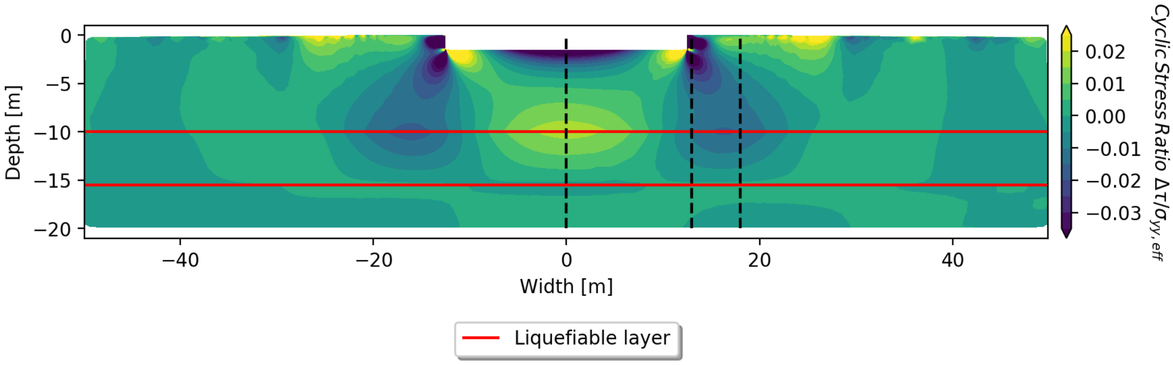

Figure C.19: CSR contour plot, MC, dynamic with 2% Rayleigh damping, load frequency of 0.3 Hz

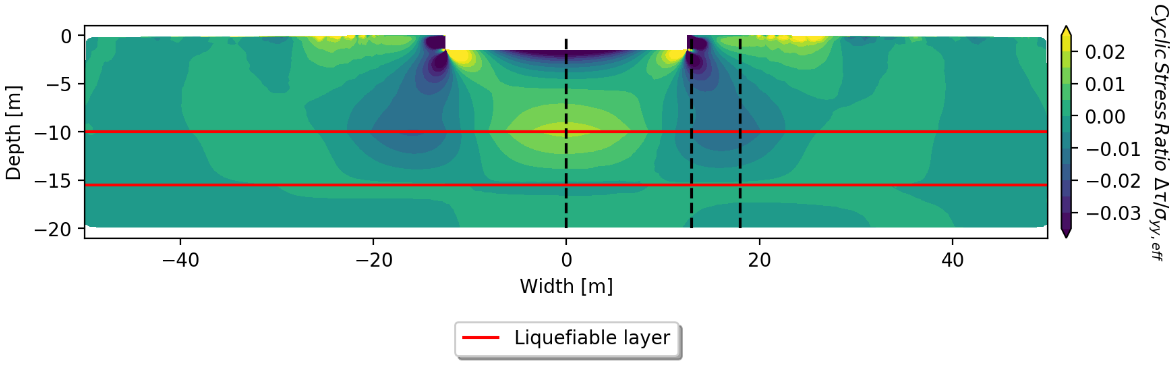

Figure C.20: CSR contour plot, MC, dynamic with 5% Rayleigh damping, load frequency of 0.3 Hz

Figures C.21 to C.24 show the results where the liquefiable soil layer is located between -10 m and -15.5 m below surface level. The soil behaviour is simulated using the Hardening Soil Small Strain soil model and the calculation method is mentioned in the accompanying subscript.

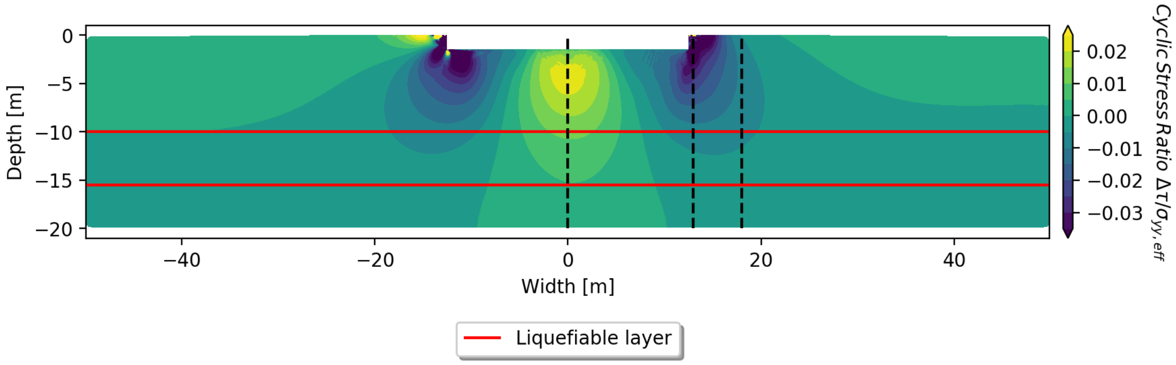

Figure C.21: CSR contour plot, HSss, quasi-static

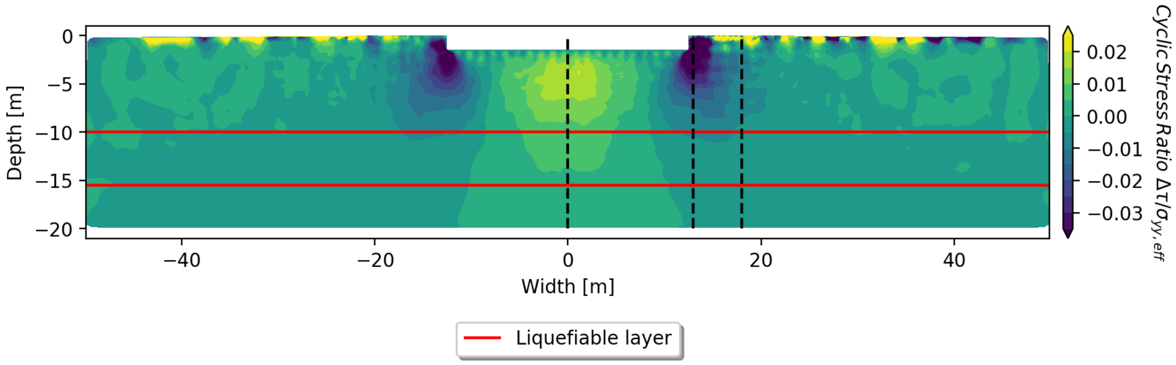

Figure C.22: CSR contour plot, HSss, dynamic, load frequency of 0.3 Hz

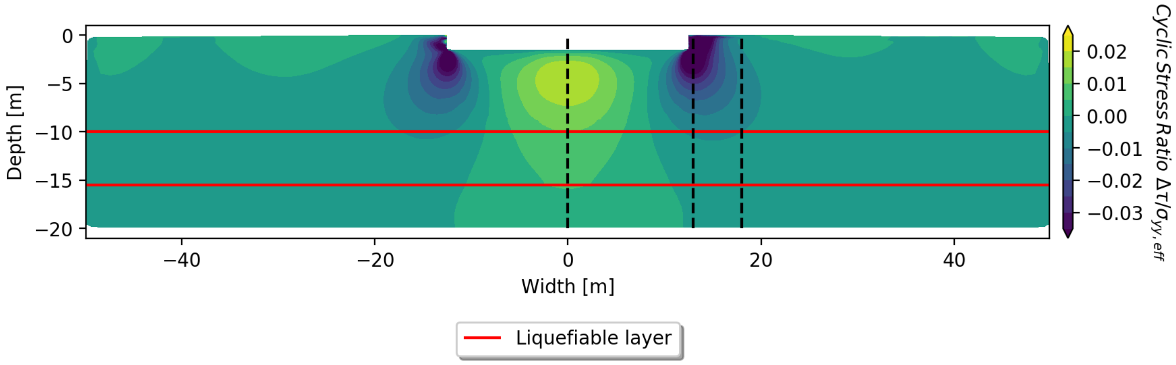

Figure C.23: CSR contour plot, HSss, dynamic with 2% Rayleigh damping, load frequency of 0.3 Hz

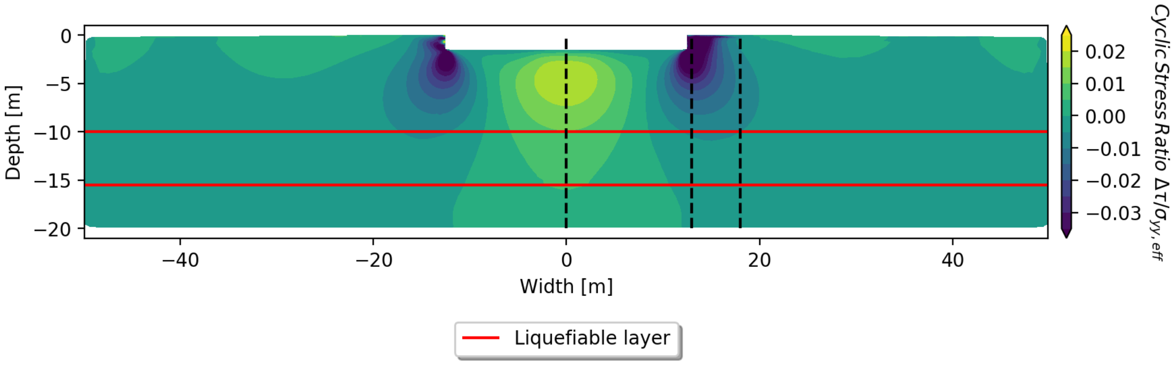

Figure C.24: CSR contour plot, HSss, dynamic with 5% Rayleigh damping, load frequency of 0.3 Hz

Dynamic Frequency Analysis

Figures C.30 to C.34 give the results of the CSR determination for various loading frequencies. The frequencies vary from 0.1 Hz to 5.0 Hz. The dynamic calculations are performed such that at least 2 full cycles are captured. The plots show the result of the CSR using the maximum and minimum shear stress. The Mohr-Coulomb material model is used for all the layers and no Rayleigh damping is applied.

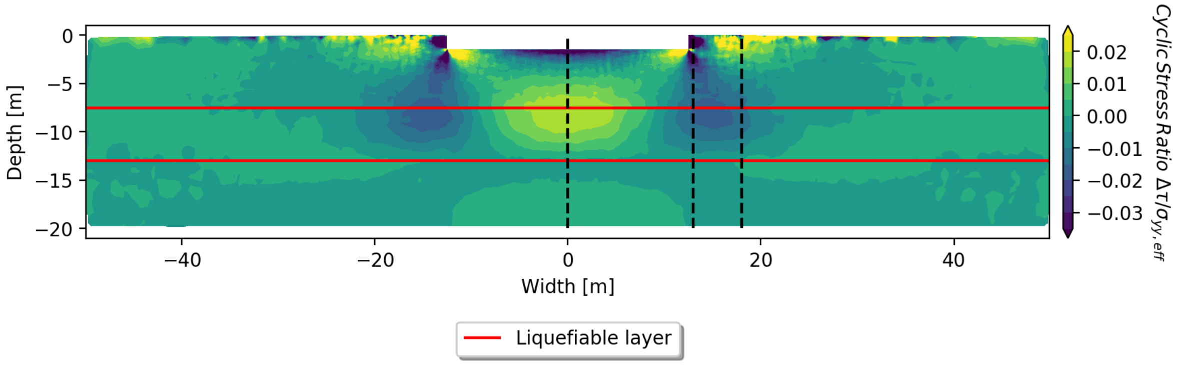

Figure C.25: CSR contour plot, MC, dynamic, load frequency of 0.1 Hz

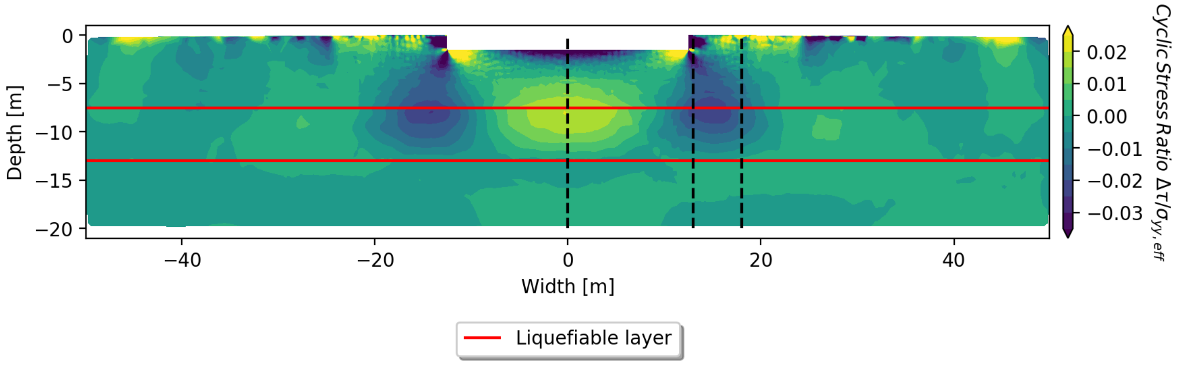

Figure C.26: CSR contour plot, MC, dynamic, load frequency of 0.3 Hz

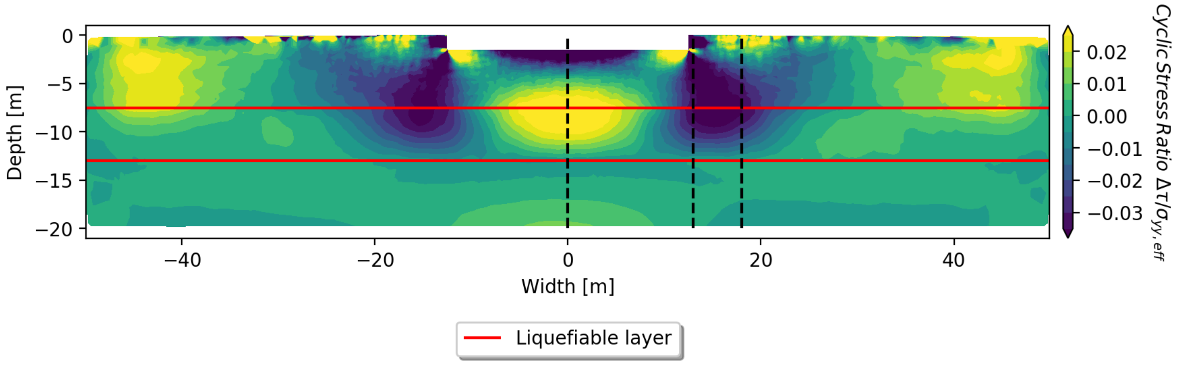

Figure C.27: CSR contour plot, MC, dynamic, load frequency of 1.0 Hz

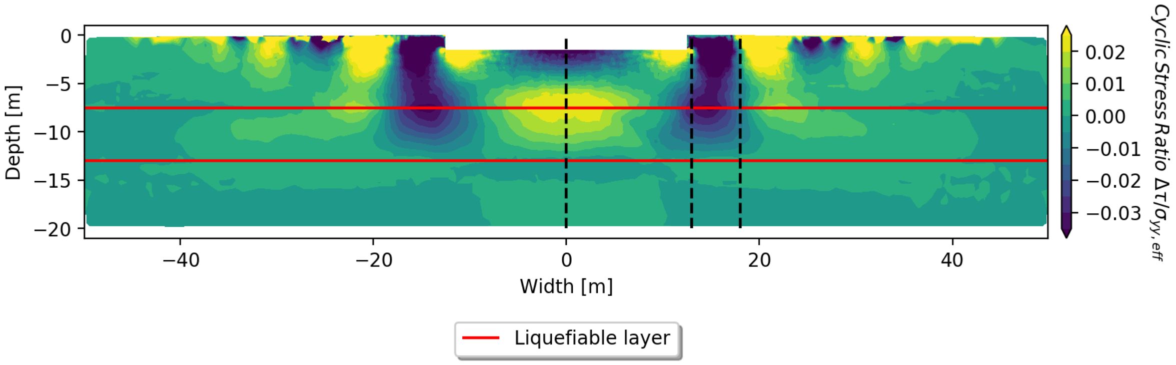

Figure C.28: CSR contour plot, MC, dynamic, load frequency of 2.0 Hz

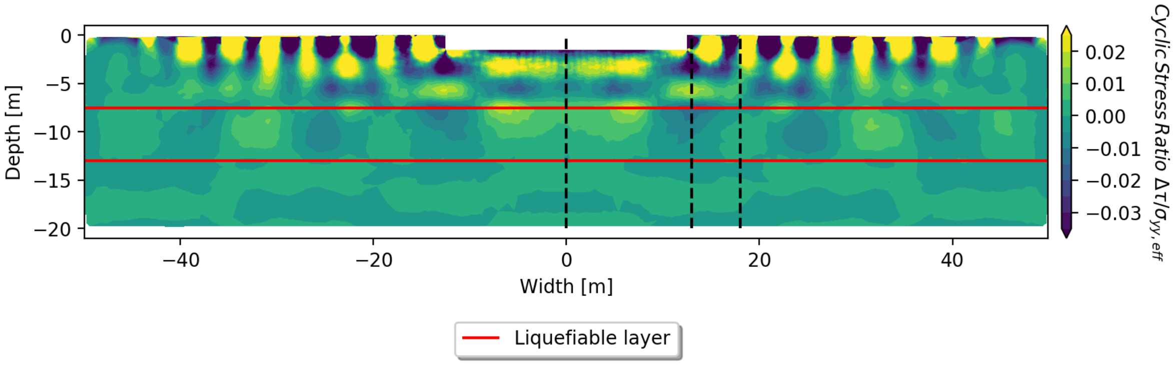

Figure C.29: CSR contour plot, MC, dynamic, load frequency of 5.0 Hz

Figures C.30 to C.34 give the results of the CSR determination for various loading frequencies. The frequencies vary from 0.1 Hz to 5.0 Hz. The dynamic calculations are performed such that at least 2 full cycles are captured. The plots show the result of the CSR using the maximum and minimum shear stress. The Hardening Soil Small Strain material model is used for all the layers and no Rayleigh damping is applied.

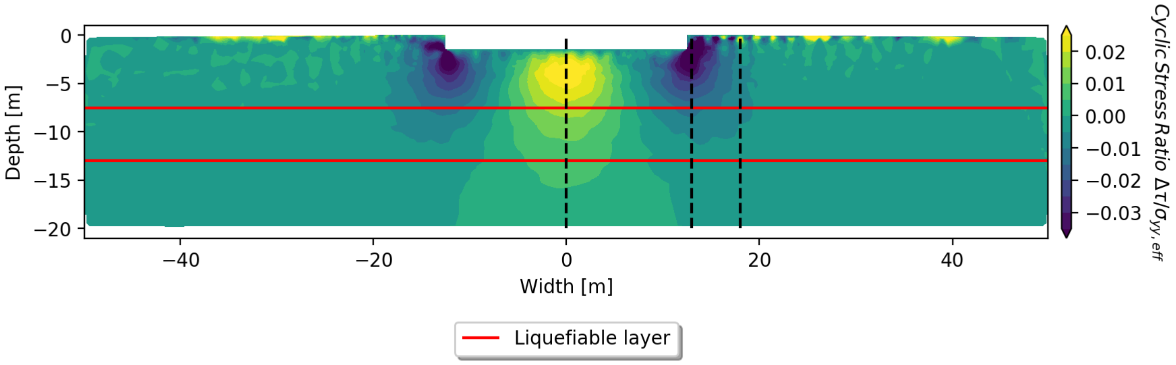

Figure C.30: CSR contour plot, HSss, dynamic, load frequency of 0.1 Hz

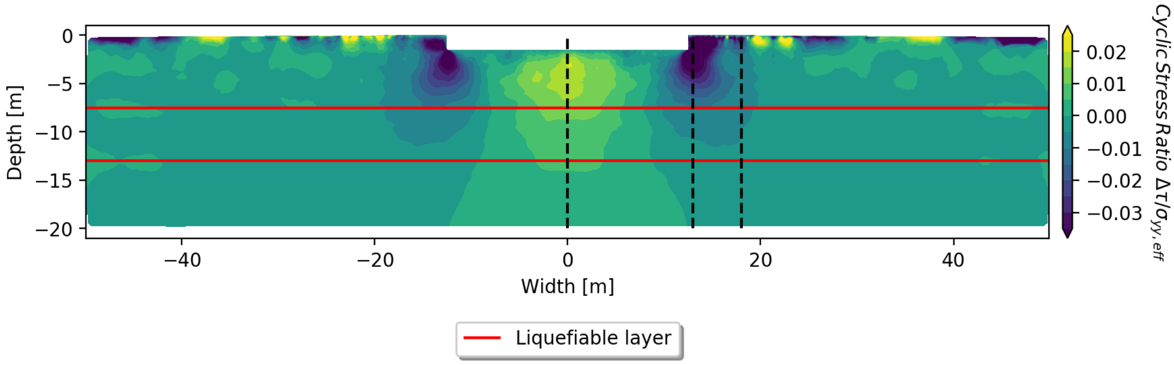

Figure C.31: CSR contour plot, HSss, dynamic, load frequency of 0.3 Hz

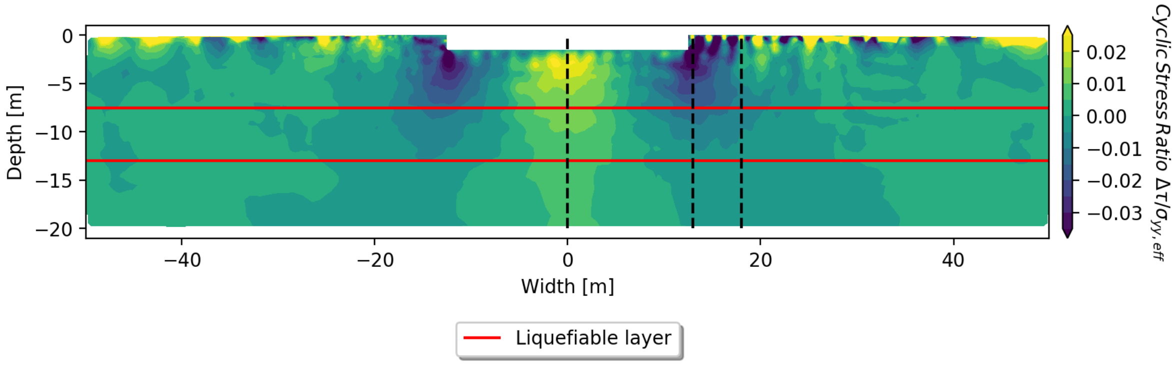

Figure C.32: CSR contour plot, HSss, dynamic, load frequency of 1.0 Hz

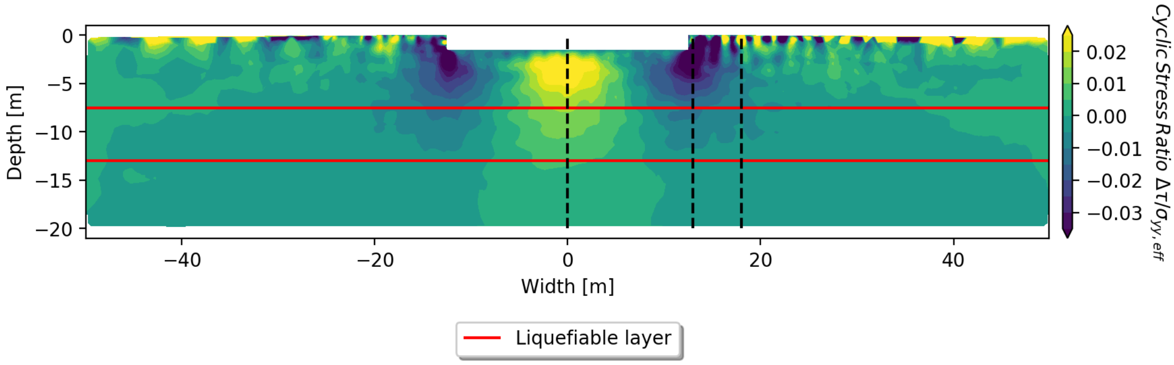

Figure C.33: CSR contour plot, HSss, dynamic, load frequency of 2.0 Hz

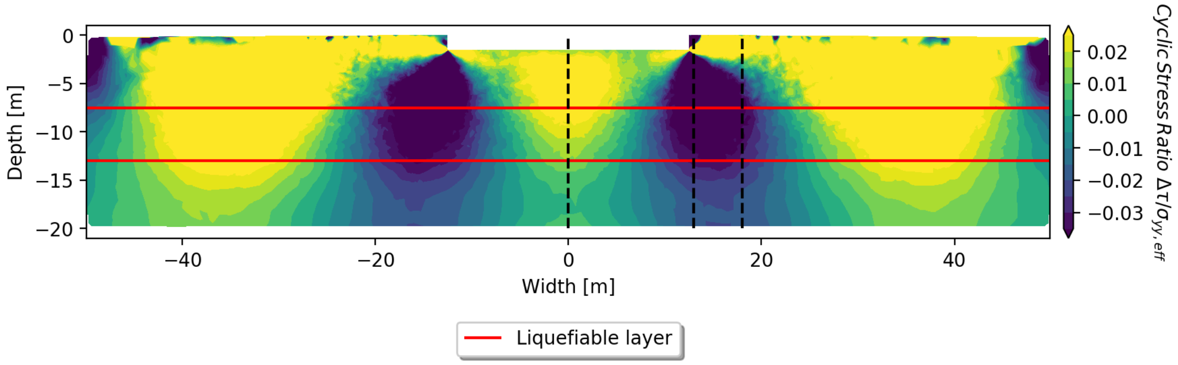

Figure C.34: CSR contour plot, HSss, dynamic, load frequency of 5.0 Hz

Frequency Analysis - dynamic with 2% Rayleigh damping

Figures C.35 to C.39 give the results of the CSR determination for various loading frequencies. The frequencies vary from 0.1 Hz to 5.0 Hz. The dynamic calculations are performed such that at least 2 full cycles are captured. The plots show the result of the CSR using the maximum and minimum shear stress. The Mohr-Coulomb material model is used for all the layers and 2% Rayleigh damping is applied.

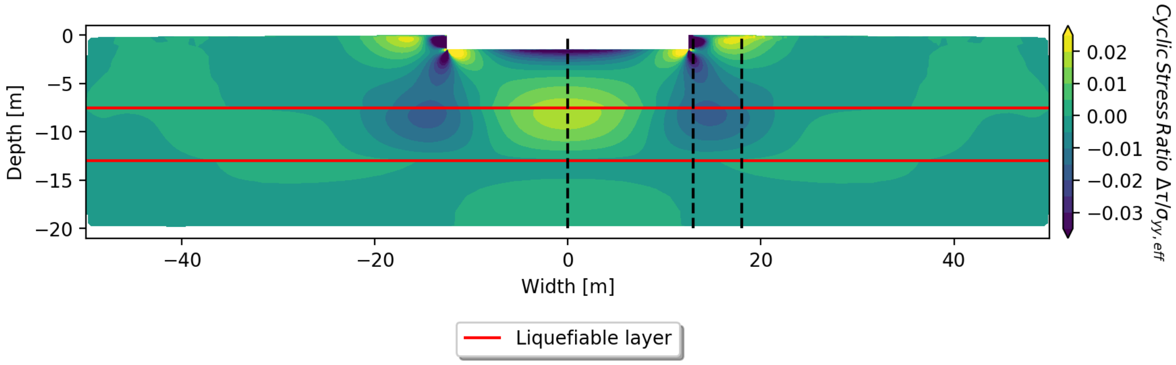

Figure C.35: CSR contour plot, MC, dynamic with 2% Rayleigh damping, load frequency of 0.1 Hz

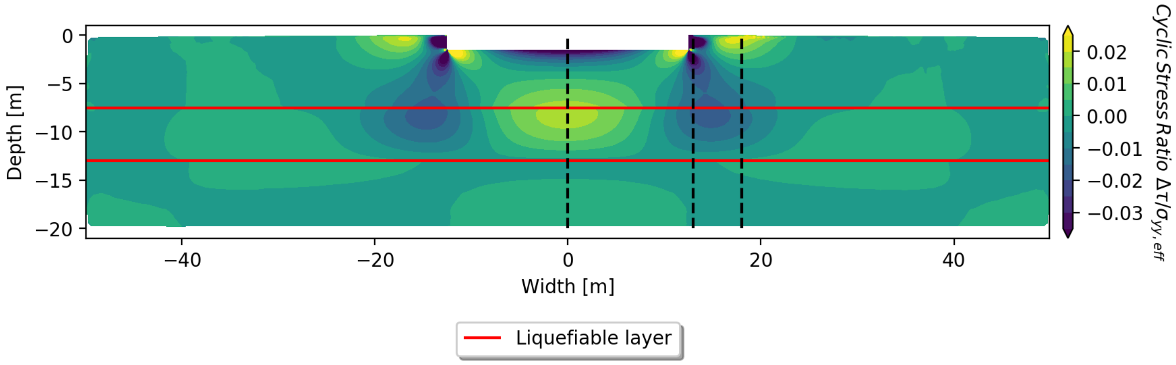

Figure C.36: CSR contour plot, MC, dynamic with 2% Rayleigh damping, load frequency of 0.3 Hz

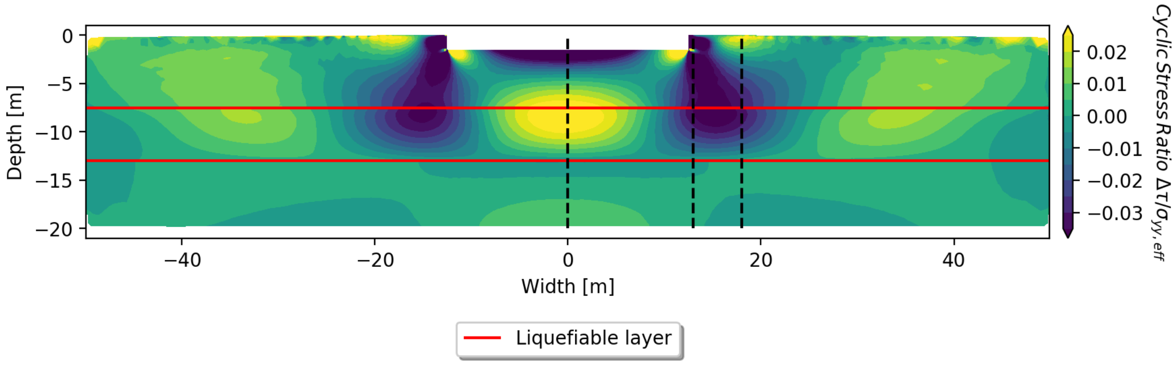

Figure C.37: CSR contour plot, MC, dynamic with 2% Rayleigh damping, load frequency of 1.0 Hz

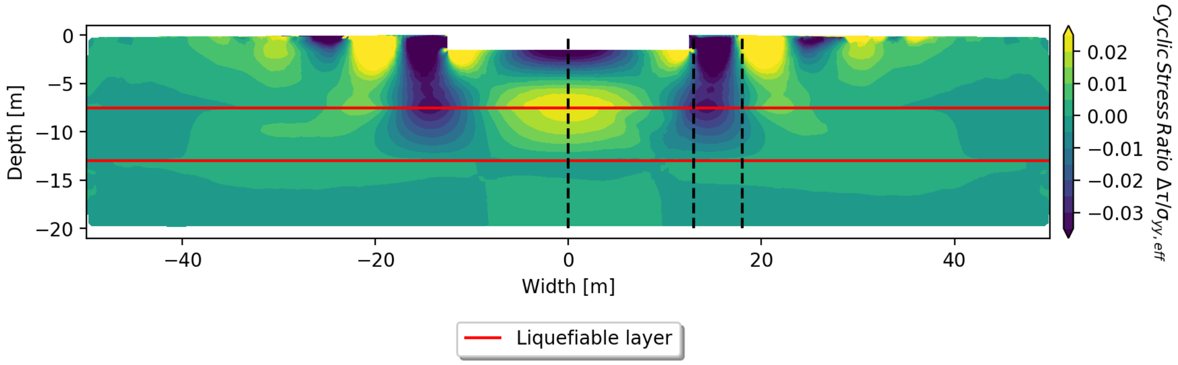

Figure C.38: CSR contour plot, MC, dynamic with 2% Rayleigh damping, load frequency of 2.0 Hz

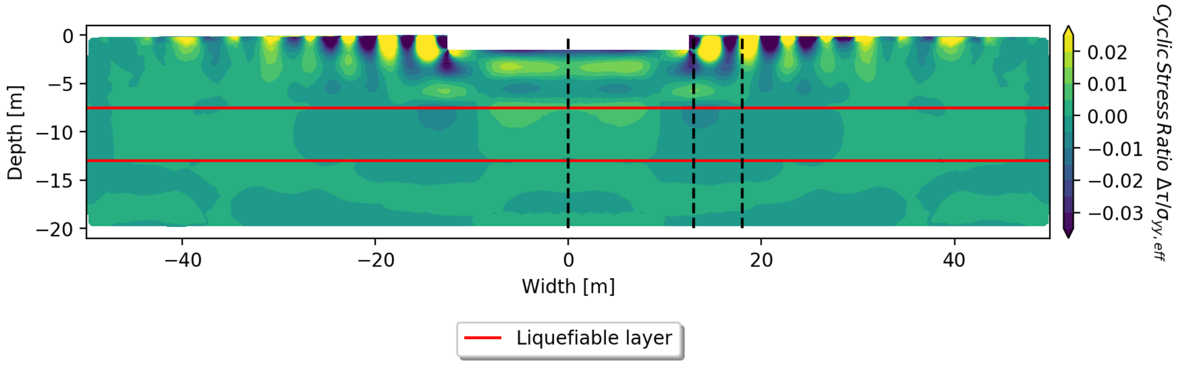

Figure C.39: CSR contour plot, MC, dynamic with 2% Rayleigh damping, load frequency of 5.0 Hz

Figures C.40 to C.44 give the results of the CSR determination for various loading frequencies. The frequencies vary from 0.1 Hz to 5.0 Hz. The dynamic calculations are performed such that at least 2 full cycles are captured. The plots show the result of the CSR using the maximum and minimum shear stress. The Hardening Soil Small Strain material model is used for all the layers and 2% Rayleigh damping is applied.

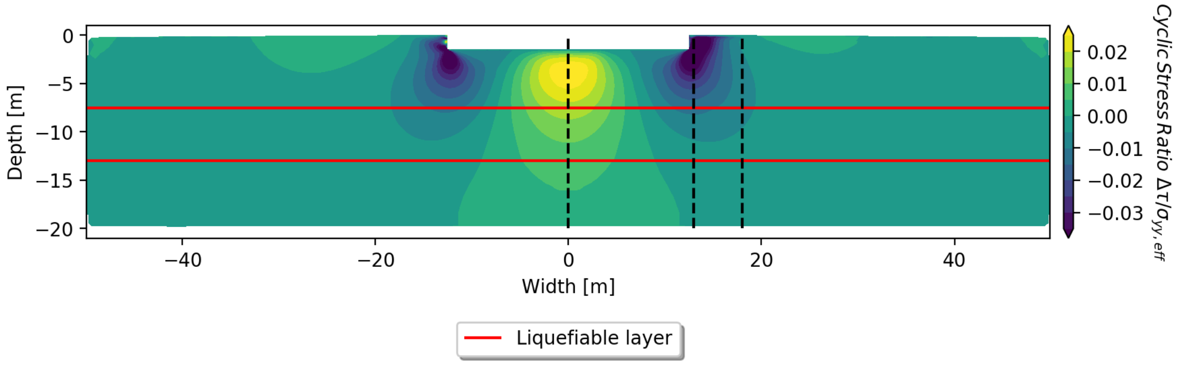

Figure C.40: CSR contour plot, HSss, dynamic with 2% Rayleigh damping, load frequency of 0.1 Hz

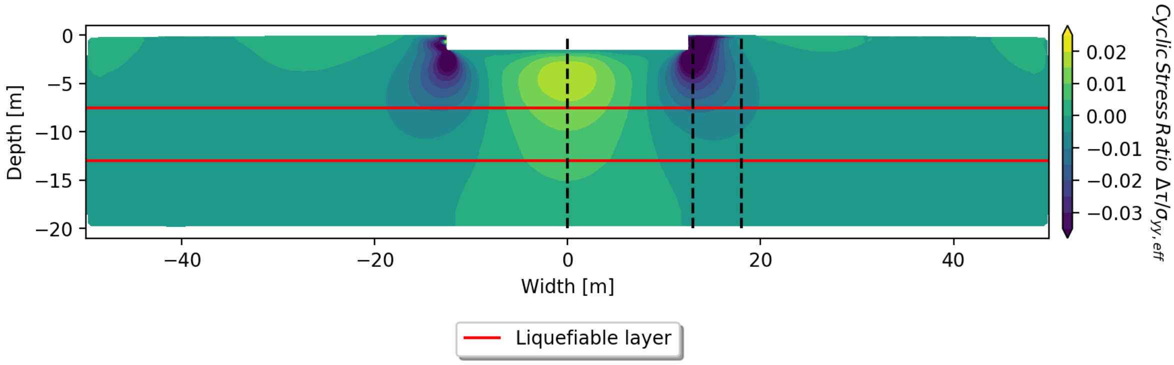

Figure C.41: CSR contour plot, HSss, dynamic with 2% Rayleigh damping, load frequency of 0.3 Hz

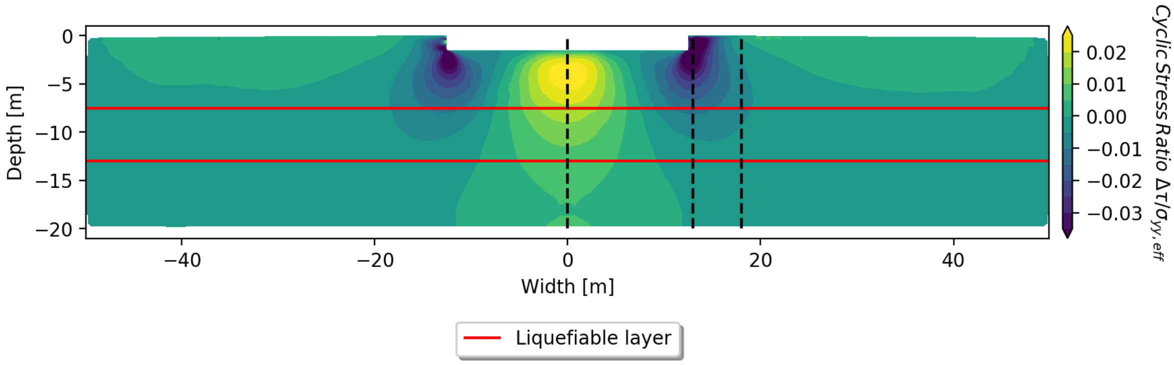

Figure C.42: CSR contour plot, HSss, dynamic with 2% Rayleigh damping, load frequency of 1.0 Hz

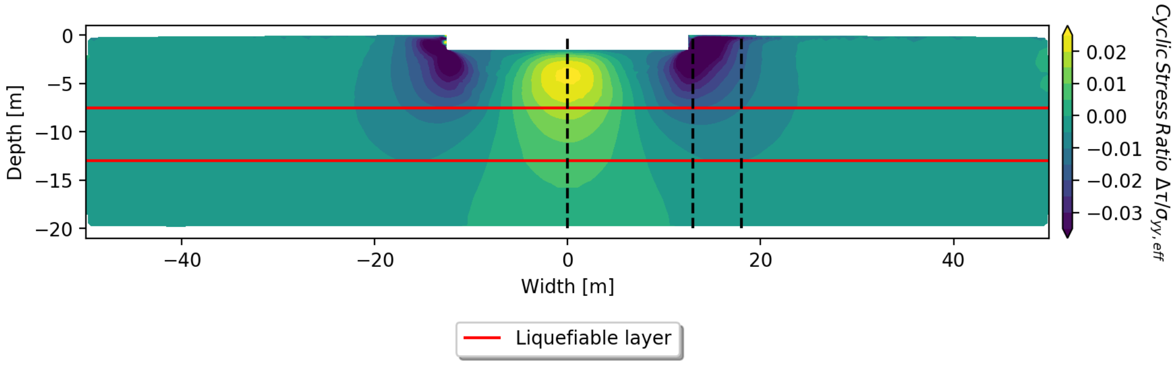

Figure C.43: CSR contour plot, HSss, dynamic with 2% Rayleigh damping, load frequency of 2.0 Hz

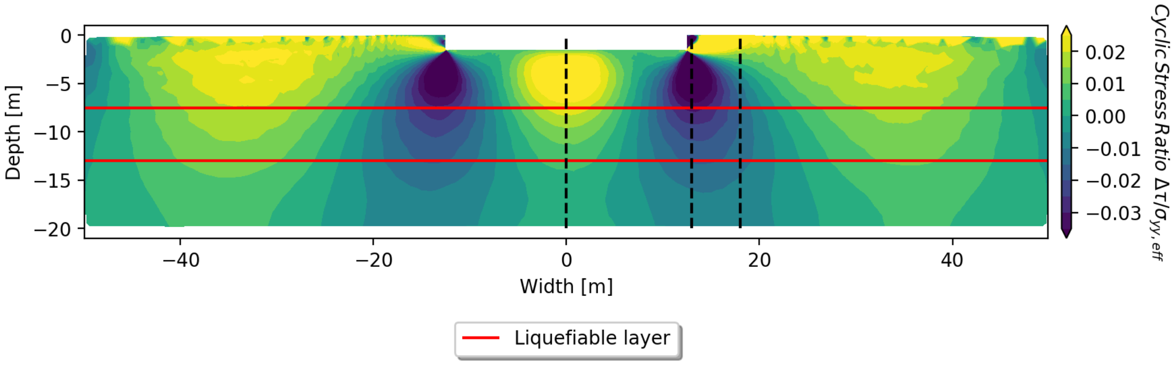

Figure C.44: CSR contour plot, HSss, dynamic with 2% Rayleigh damping, load frequency of 5.0 Hz

Frequency Analysis - dynamic with 5% Rayleigh damping

Figures C.45 to C.49 give the results of the CSR determination for various loading frequencies. The frequencies vary from 0.1 Hz to 5.0 Hz. The dynamic calculations are performed such that at least 2 full cycles are captured. The plots show the result of the CSR using the maximum and minimum shear stress. The Mohr-Coulomb material model is used for all the layers and 5% Rayleigh damping is applied.

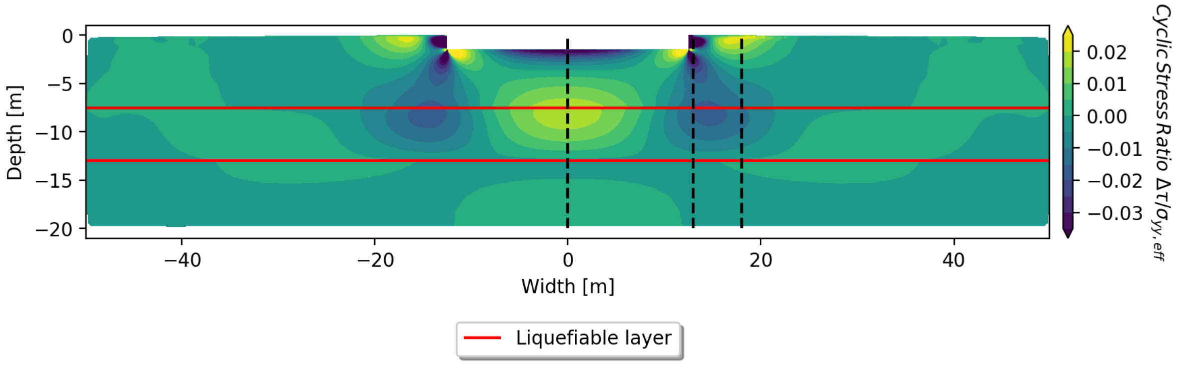

Figure C.45: CSR contour plot, MC, dynamic with 5% Rayleigh damping, load frequency of 0.1 Hz

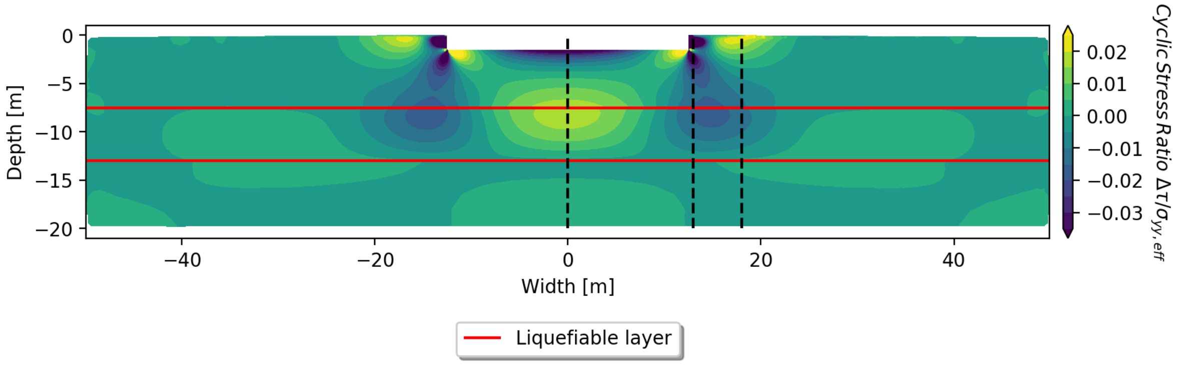

Figure C.46: CSR contour plot, MC, dynamic with 5% Rayleigh damping, load frequency of 0.3 Hz

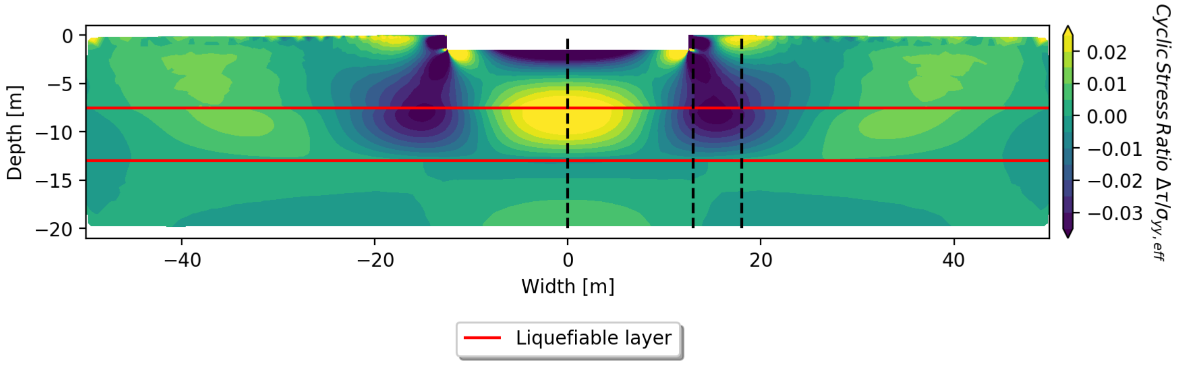

Figure C.47: CSR contour plot, MC, dynamic with 5% Rayleigh damping, load frequency of 1.0 Hz

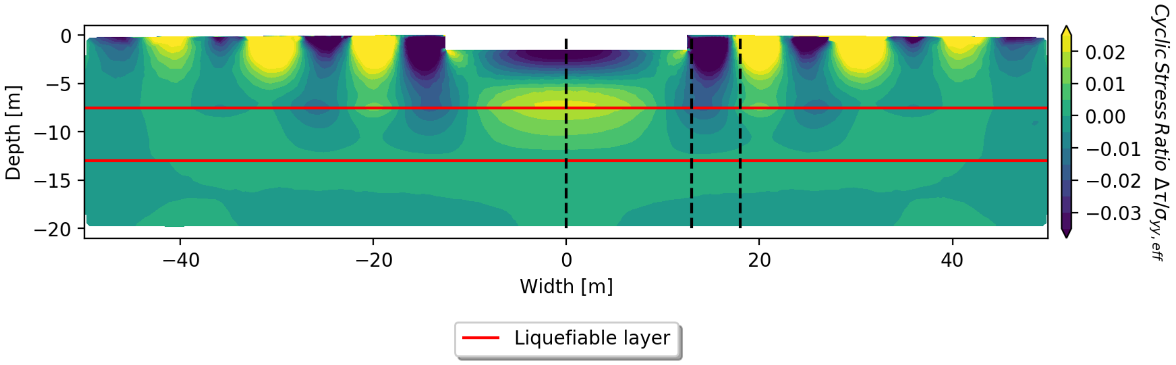

Figure C.48: CSR contour plot, MC, dynamic with 5% Rayleigh damping, load frequency of 2.0 Hz

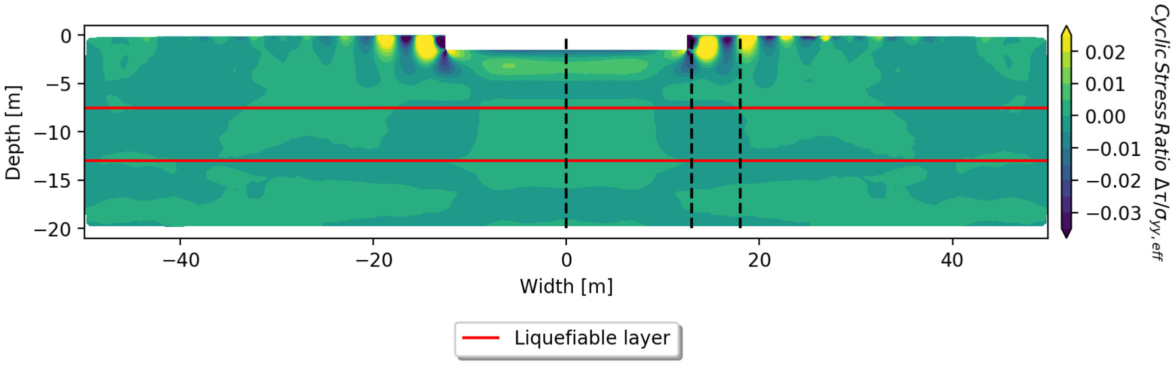

Figure C.49: CSR contour plot, MC, dynamic with 5% Rayleigh damping, load frequency of 5.0 Hz

Figures C.50 to C.54 give the results of the CSR determination for various loading frequencies. The frequencies vary from 0.1 Hz to 5.0 Hz. The dynamic calculations are performed such that at least 2 full cycles are captured. The plots show the result of the CSR using the maximum and minimum shear stress. The Hardening Soil Small Strain material model is used for all the layers and 5% Rayleigh damping is applied.

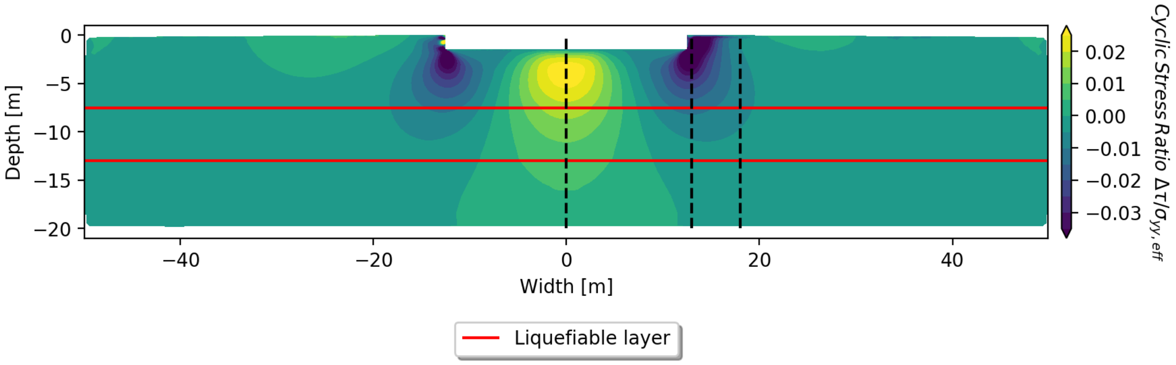

Figure C.50: CSR contour plot, HSss, dynamic with 5% Rayleigh damping, load frequency of 0.1 Hz

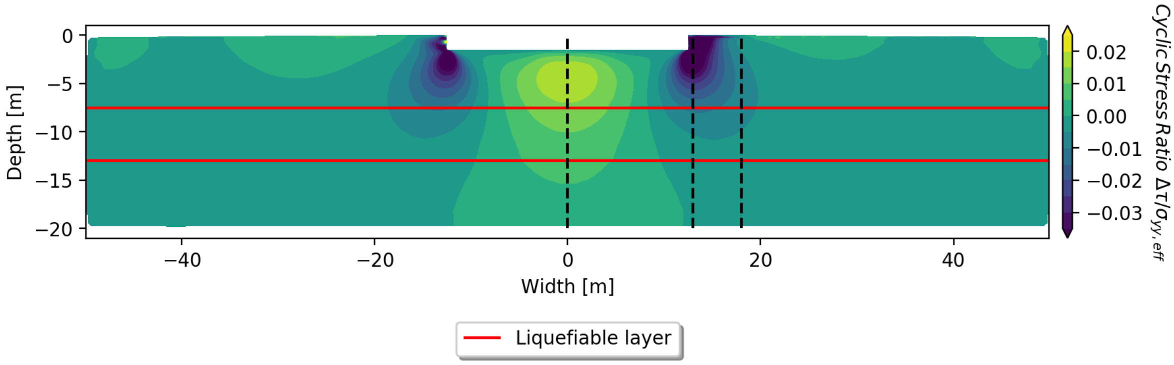

Figure C.51: CSR contour plot, HSss, dynamic with 5% Rayleigh damping, load frequency of 0.3 Hz

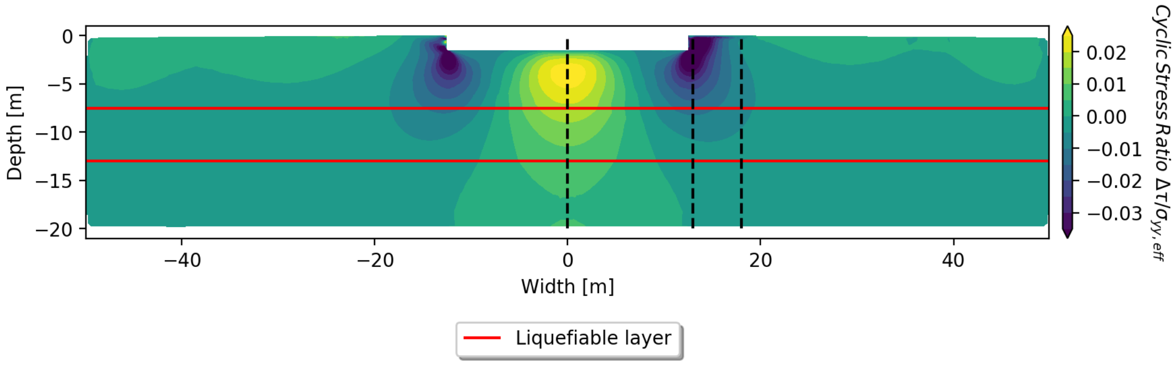

Figure C.52: CSR contour plot, HSss, dynamic with 5% Rayleigh damping, load frequency of 1.0 Hz

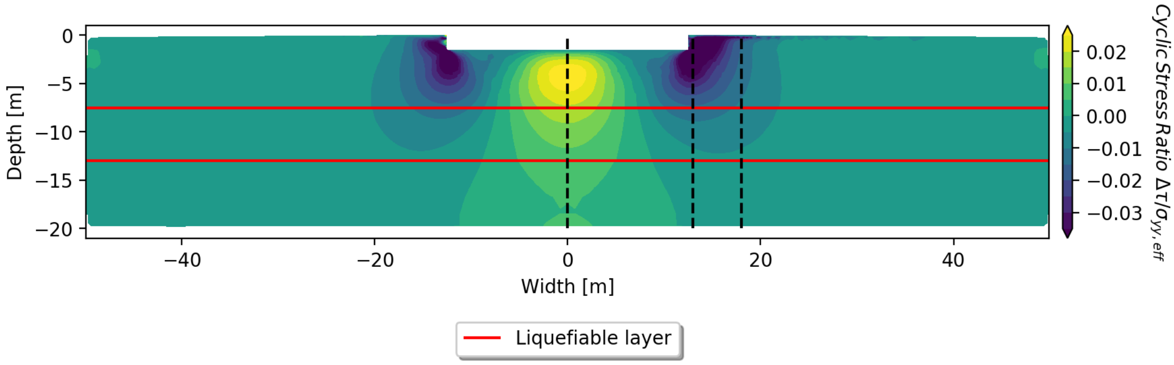

Figure C.53: CSR contour plot, HSss, dynamic with 5% Rayleigh damping, load frequency of 2.0 Hz

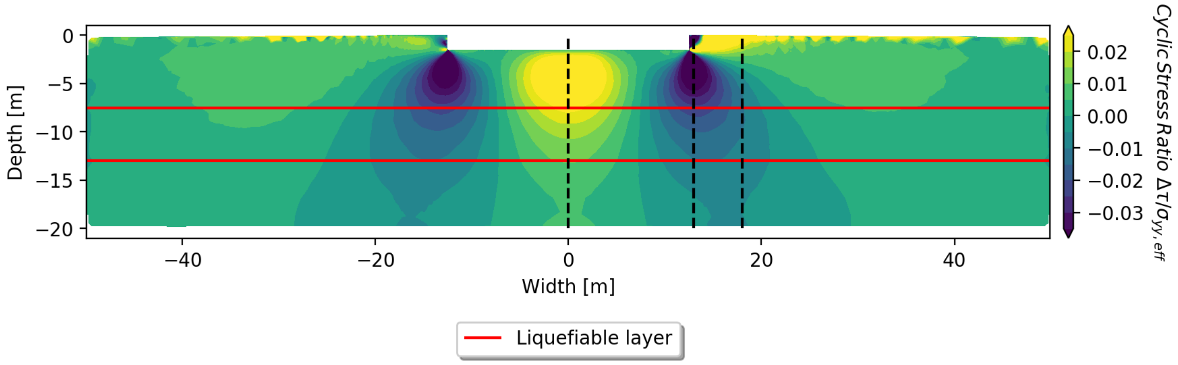

Figure C.54: CSR contour plot, HSss, dynamic with 5% Rayleigh damping, load frequency of 5.0 Hz

C.2. Results Sensitivity Analysis

Figure C.55: CSR profile at x = 37 m, varying G_0

Figure C.56: CSR profile at x = 37 m, varying ϕ

Figure C.57: CSR profile at x = 50 m, varying G_0

Figure C.58: CSR profile at x = 50 m, varying ϕ

Figure C.59: CSR profile at x = 55 m, varying G_0

Figure C.60: CSR profile at x = 55 m, varying ϕ

D

Verification Python Code

D.1. Verification Case 1: 1D Radial Consolidation

The first reference case used to verify the code is first described analytically by de Leeuw De Leeuw (1965). De Leeuw's problem consists of a cylindrical sample between two stiff and impermeable plates with a diameter of 2a. The sample is loaded by a uniform radial pressure q at the radial boundary. The sample contains a drainage boundary at the radial outside. De Leeuw (1965) gives the analytic solution for this problem and is depicted in Figure D.1.

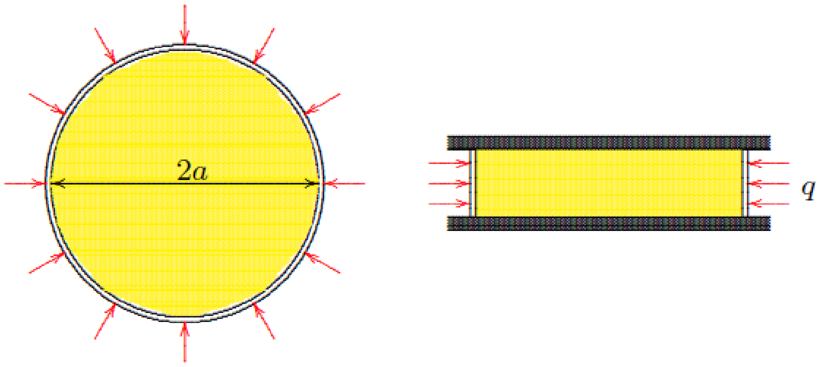

Figure D.1: De Leeuw's problem, from Verruijt (2013)

Verruijt (2013) presents a more general solution to De Leeuw's problem by considering the particle and fluid compressibility. However, incompressible pore fluid and particles are assumed. The analytic solution for radial consolidation is given by:

$$\frac{u}{u_0} = \sum_{j=1}^{\infty} \frac{J_0(\xi_j) - J_0(\xi_j r/a)}{(1 - m\xi_j^2 - 1/4m)j_0(\xi_j)} exp(-\xi_j^2 c_v t/a^2) \tag{D.1}$$

$$m = \frac{1}{2}(1 - \nu)/(1 - 2\nu) \tag{D.2}$$

where u is the excess pore pressure, u_0 is the initial pore pressure, m is an additional parameter only applicable for incompressible fluid and particles, ν is the Poisson's ratio, c_v is the consolidation coefficient, t is the time and a is the radius of the sample. ξ_j is the j^{th} root of the function: $J_1(\xi_j) - 2m\xi_j J_0(\xi_j) = 0$ where $J_0(x)$ and $J_1(x)$ are the Bessel functions of the first kind of the zeroth and first order, respectively.

The finite difference model as described in Section 5.2 is used to create matching the boundary conditions of the analytic solution presented in Figure 5.6. The pore pressure generation term, $\partial u_g/\partial t$, is disregarded for this calculation. A grid of 20x20 square elements is used and a permeable boundary is implemented at the right side of the model. The top and bottom of the model contains impermeable boundaries as indicated by Figure D.2. At time t = 0, the sample is uniformly loaded with a load equal to q. Load q is fully transformed to the initial excess pore pressure u_0. Figure D.3 shows the nondimensionalized pore pressure development in the sample. From this figure it is stated that the FDM gives a slight overestimation of the pore pressures but generally matches the analytic solution. Figures D.4 to D.6 show agreement of the results between the analytic solution, Plaxis results and Python code results.

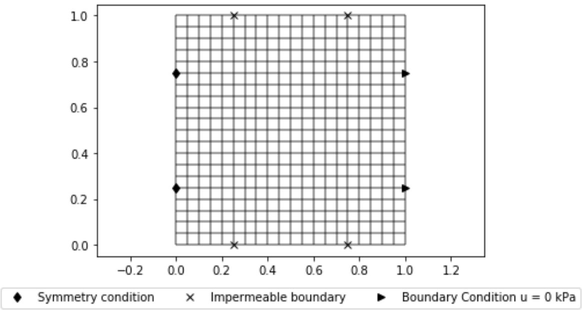

Figure D.2: Grid and boundary conditions to model De Leeuw's problem using the FDM

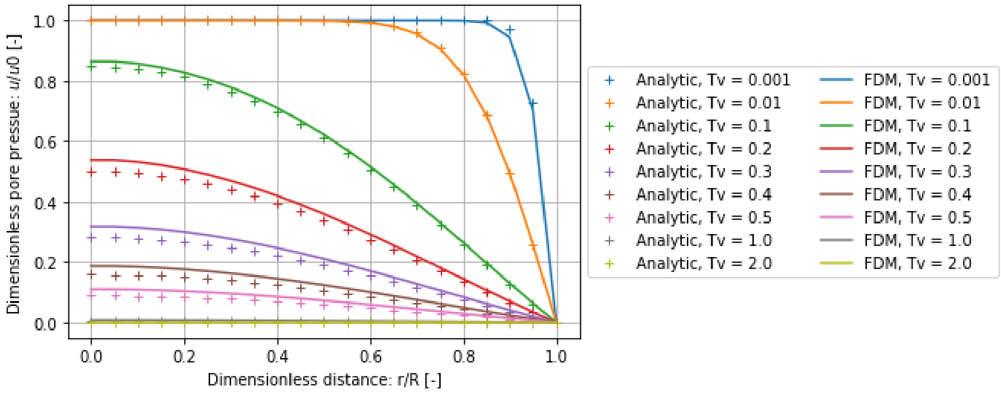

Figure D.3: Pore pressure development at z = 1/2 of the height of the soil sample, $T_v = c_r t/a^2$

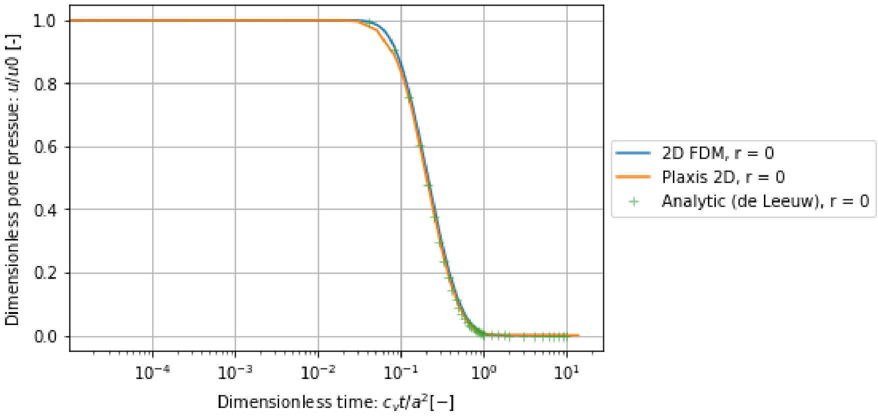

Figure D.4: Pore pressure development at the center of the sample, r = 0. $c_r = 0.001\ m^2/d$, E_{oed} = 20.000 kPa, k_r = $5.0 \cdot 10^{-7}$ m/d

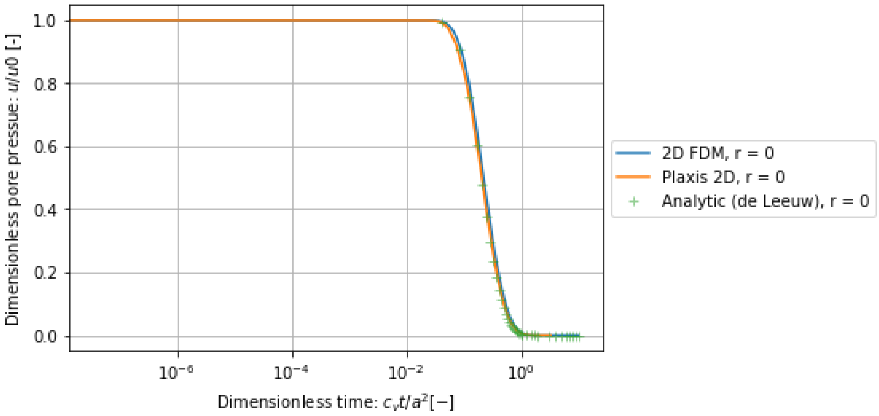

Figure D.5: Pore pressure development at the center of the sample, r = 0. $c_r = 100\ m^2/d$, E_{oed} = 20.000 kPa, k_r = 0.05 m/d

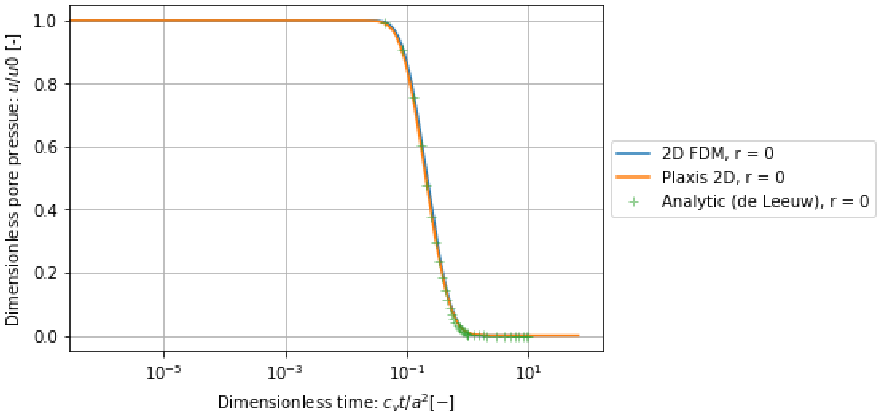

Figure D.6: Pore pressure development at the center of the sample, r = 0. $c_r = 2000\ m^2/d$, E_{oed} = 20.000 kPa, k_r = 1 m/d

D.2. Verification Case 2: 2D Radial Consolidation

The second verification case is used to verify the capability of the model to solve 2D radial consolidation. The results of the code are compared with a numeric solution determined by Plaxis 2D as no analytic solution is available for this type of problem. The problem contains a cylindrical layer between impermeable boundaries, see figure D.7.

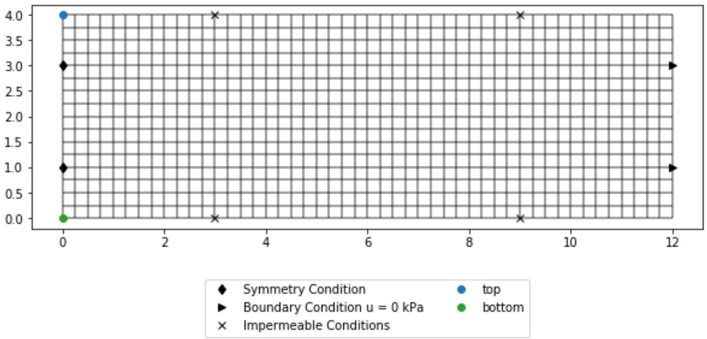
4.0
3.5
3.0
2.5
2.0
1.5
1.0
0.5
0.0
0
2
4
6
8
10
12
Symmetry Condition
Boundary Condition u = 0 kPa
Impermeable Conditions
top
bottom

Figure D.7: Boundary conditions verification case 2

Excess pore pressures are applied in the left upper corner of the layer. Consolidation in radial and vertical direction are both affected during the process as the problem is not axisymmetric anymore.

The verification case is used for several different consolidation coefficients, varying between 0.001 to 2000 m^2/d.

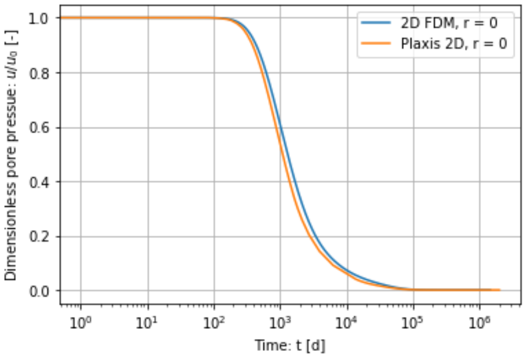

Figure D.8: Pore pressure development at the center of the sample, r = 0 m, z = 4 m. $c_r = c_v = 0.001\ m^2/d$, $E_{oed} = 20.000$ kPa, $k_r, k_v = 5.0 \cdot 10^{-7}$

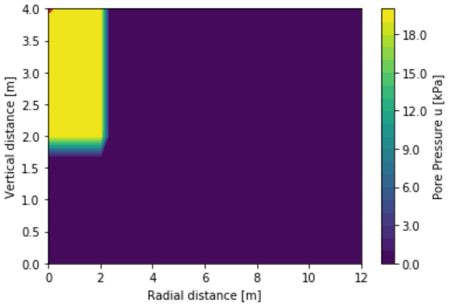

Figure D.9: Contour plot excess pore pressures at t = 0 d

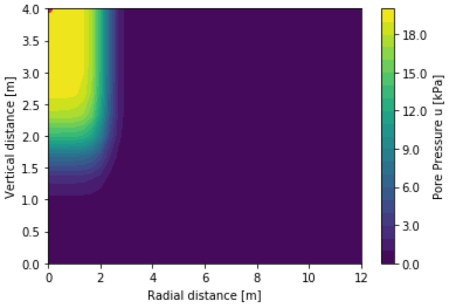

Figure D.10: Contour plot excess pore pressures at t = 100 d

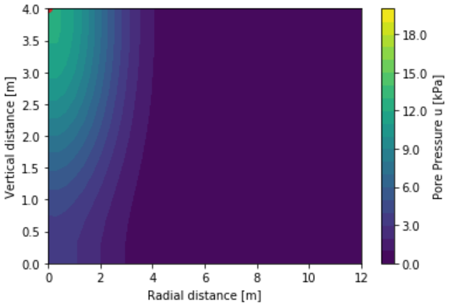

Figure D.11: Contour plot excess pore pressures at t = 1000 d

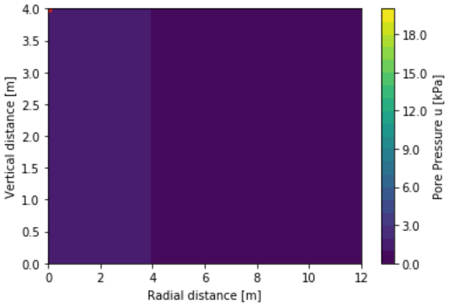

Figure D.12: Contour plot excess pore pressures at t = 10000 d

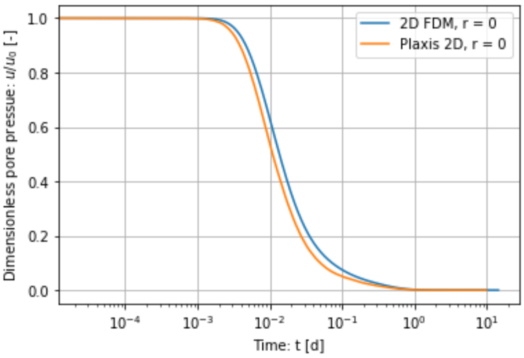

Figure D.13: Pore pressure development at the center of the sample, r = 0 m, z = 4 m. $c_r = c_v = 100\ m^2/d$, $E_{oed} = 20.000$ kPa, k_r, k_v = 0.05 m/d

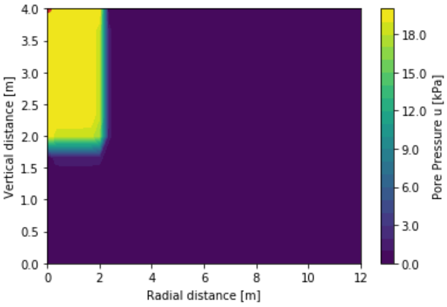

Figure D.14: Contour plot excess pore pressures at t = 0 d

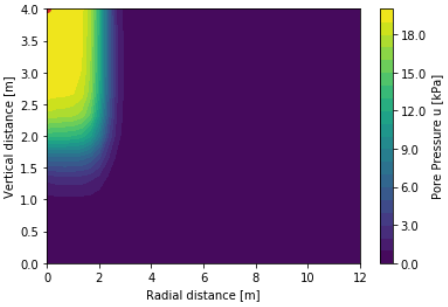

Figure D.15: Contour plot excess pore pressures at t = 0.001 d

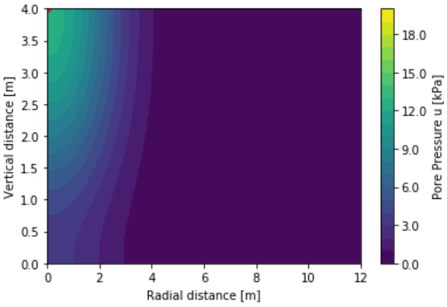

Figure D.16: Contour plot excess pore pressures at t = 0.01 d

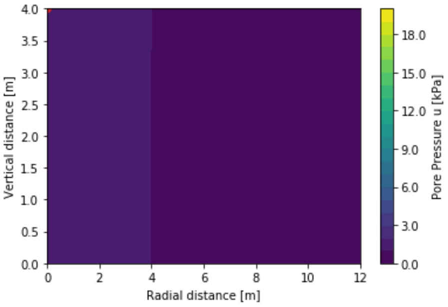

Figure D.17: Contour plot excess pore pressures at t = 0.1 d

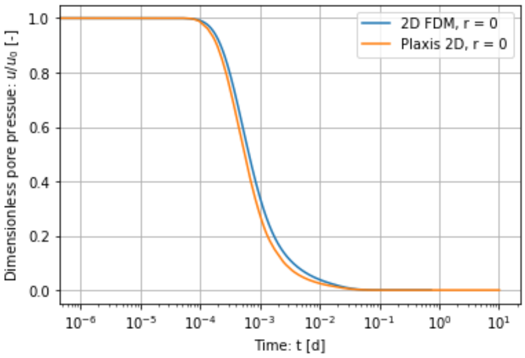

Figure D.18: Pore pressure development at the center of the sample, r = 0 m, z = 4 m. $c_r = c_v = 2000\ m^2/d$, E_{oed} = 20.000 kPa, k_r, k_v = 1 m/d

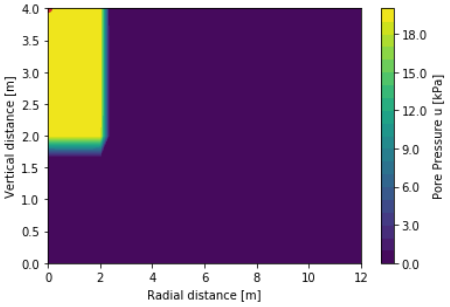

Figure D.19: Contour plot excess pore pressures at t = 0 d

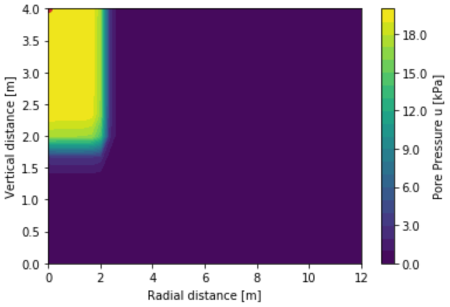

Figure D.20: Contour plot excess pore pressures at t = 0.00001 d

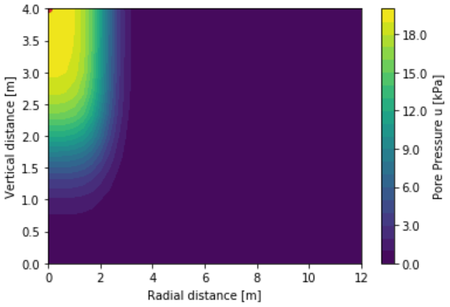

Figure D.21: Contour plot excess pore pressures at t = 0.0001 d

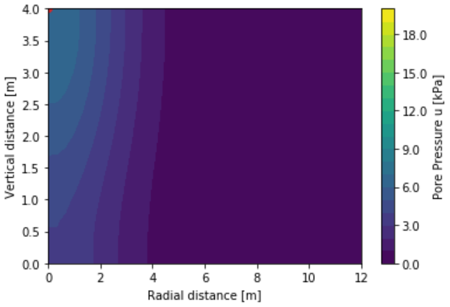

Figure D.22: Contour plot excess pore pressures at t = 0.001 d

D.3. Verification Case 3: 2D Radial Consolidation

The third verification case is used to verify the capability of the model to solve 2D radial consolidation. The results of the code are compared with a numeric solution determined by Plaxis 2D as no analytic solution is available for this type of problem. The problem contains a cylindrical layer where only the top boundary is impermeable, see figure D.23.

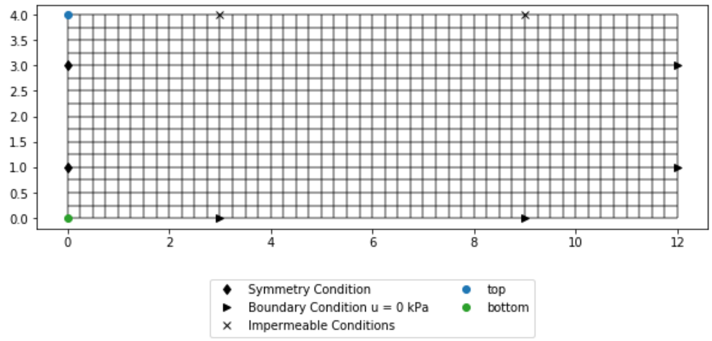
4.0
3.5
3.0
2.5
2.0
1.5
1.0
0.5
0.0
0
2
4
6
8
10
12
◆ Symmetry Condition
▶ Boundary Condition u = 0 kPa
× Impermeable Conditions
● top
● bottom

Figure D.23: Boundary conditions verification case 3

Excess pore pressures are applied in the left upper corner of the layer. Consolidation in radial and vertical direction are both affected during the process as the problem is not axisymmetric anymore. The verification case is used for several different consolidation coefficients, varying between 0.001 to 2000 m^2/d.

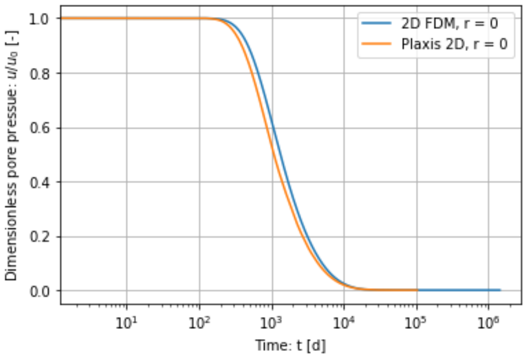

Figure D.24: Pore pressure development at the center of the sample, r = 0 m, z = 4 m. $c_r = c_v = 0.001\ m^2/d$, $E_{oed} = 20.000$ kPa, $k_r, k_v = 5.0 \cdot 10^{-7}$

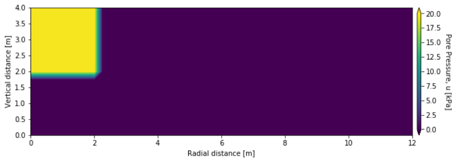

Figure D.25: Contour plot excess pore pressures at t = 0 d

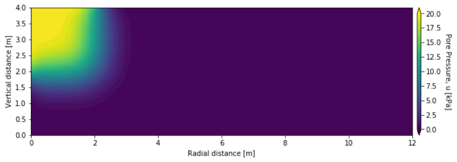

Figure D.26: Contour plot excess pore pressures at t = 100 d

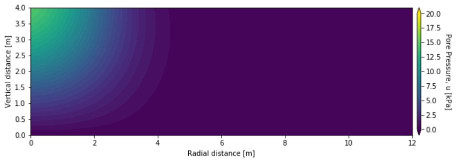

Figure D.27: Contour plot excess pore pressures at t = 1000 d

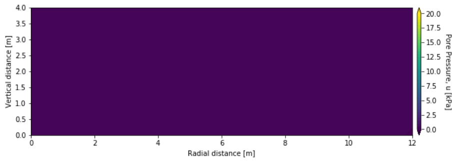

Figure D.28: Contour plot excess pore pressures at t = 10000 d

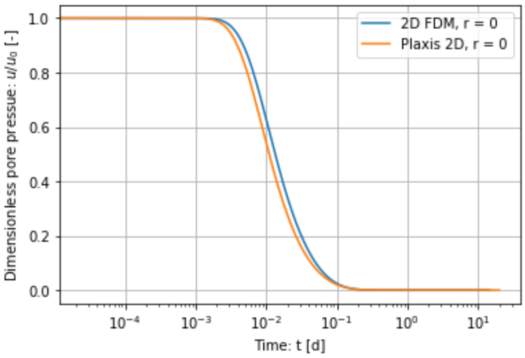

Figure D.29: Pore pressure development at the center of the sample, r = 0 m, z = 4 m. $c_r = c_v = 100\ m^2/d$, $E_{oed} = 20.000$ kPa, k_r, k_v = 0.05 m/d

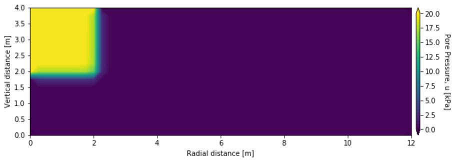

Figure D.30: Contour plot excess pore pressures at t = 0 d

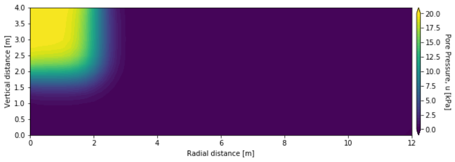

Figure D.31: Contour plot excess pore pressures at t = 0.001 d

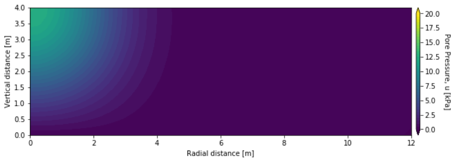

Figure D.32: Contour plot excess pore pressures at t = 0.01 d

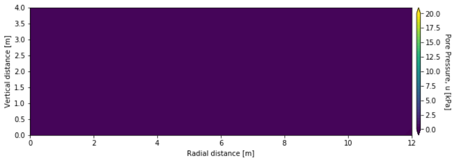

Figure D.33: Contour plot excess pore pressures at t = 0.1 d

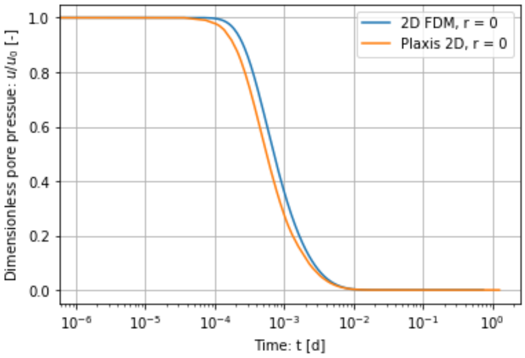

Figure D.34: Pore pressure development at the center of the sample, r = 0 m, z = 4 m. $c_r = c_v = 2000\ m^2/d$, $E_{oed} = 20.000$ kPa, k_r, k_v = 1 m/d

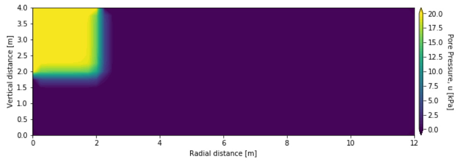

Figure D.35: Contour plot excess pore pressures at t = 0 d

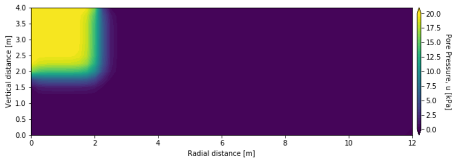

Figure D.36: Contour plot excess pore pressures at t = 0.00001 d

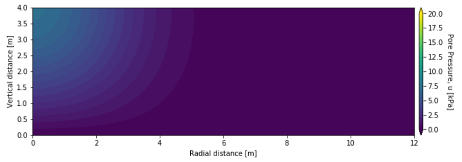

Figure D.37: Contour plot excess pore pressures at t = 0.0001 d

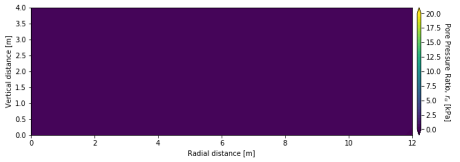

Figure D.38: Contour plot excess pore pressures at t = 0.001 d

D.4. Verification Case 4: Simulation of a CDSS test

The fourth verification case is used to verify the capability of the model to simulate pore pressure generation based on experimental data. The results of the code are compared with a data set consisting of CDSS tests loaded by various cyclic stress ratios. The data set is part of the Liquefaction Experiments and Analysis Projects (LEAP, (Manzari, 2018)). The sample is consolidated to an initial vertical effective stress of 100 kPa and has a relative density of 71.5%. The liquefaction strength curve is fitted using 11 individual tests where liquefaction is defined at a double amplitude shear strain of 7.5%. The density of the sample is implicitly included by the CSR curve and is assumed to be constant for the sample. Figure D.39 shows that the model gives a good estimation of the fitted CSR curve. In figures D.40 to D.49 it is observed that varying the fit parameter θ does not influence the number of cycles required to reach initial liquefaction. However, it can be noticed that the pore pressure development with respect to the number of cycles does change with various θ values. Seed and Rahman (1978) suggests a value of $\theta = 0.7$ to model the pore pressure development in general sands, but for the specific sample a value of 2.0 gives a better fit.

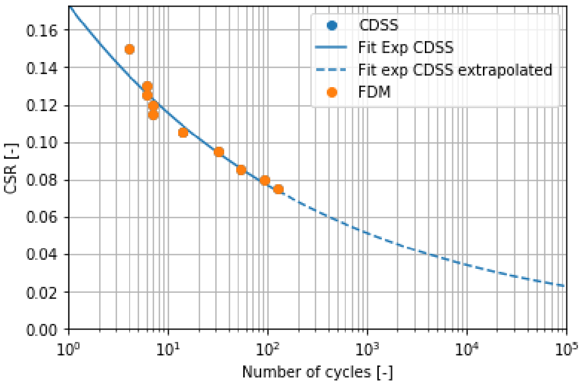

Figure D.39: Result of CSR curve for experimental and numerical tests

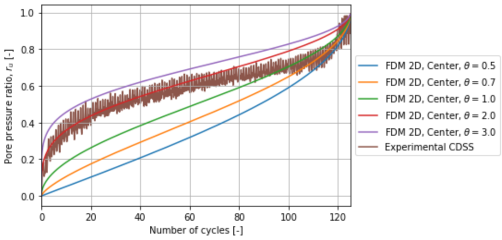

Figure D.40: Pore pressure development for experimental and numerical test, CSR = 0.075

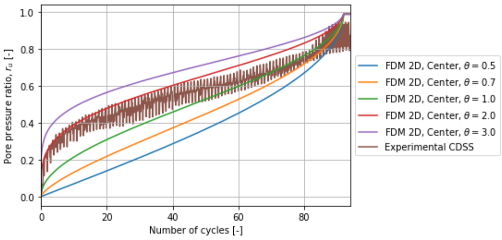

Figure D.41: Pore pressure development for experimental and numerical test, CSR = 0.08

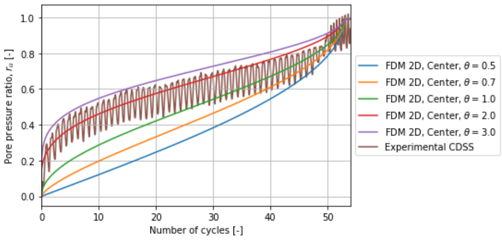

Figure D.42: Pore pressure development for experimental and numerical test, CSR = 0.085

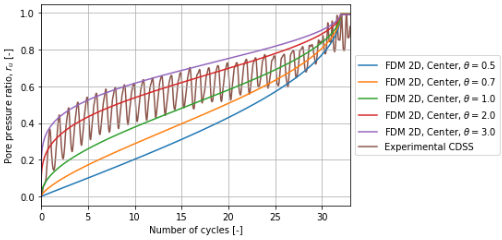

Figure D.43: Pore pressure development for experimental and numerical test, CSR = 0.095

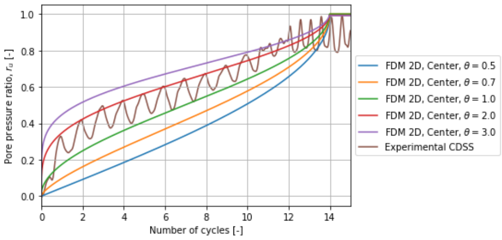

Figure D.44: Pore pressure development for experimental and numerical test, CSR = 0.105

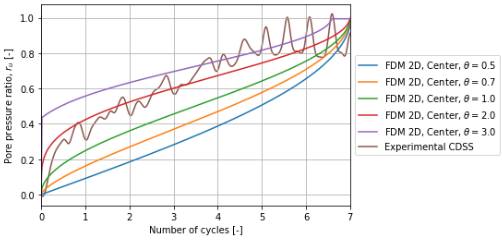

Figure D.45: Pore pressure development for experimental and numerical test, CSR = 0.115

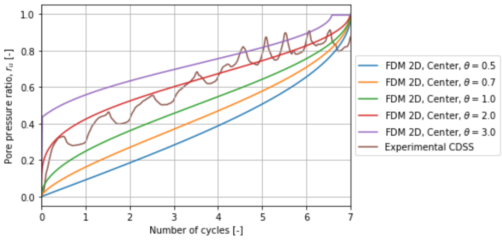

Figure D.46: Pore pressure development for experimental and numerical test, CSR = 0.12

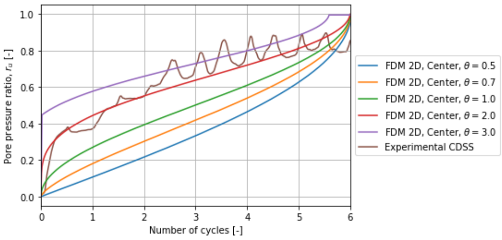

Figure D.47: Pore pressure development for experimental and numerical test, CSR = 0.125

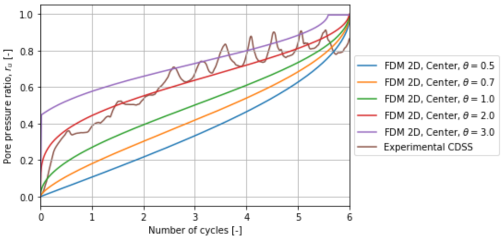

Figure D.48: Pore pressure development for experimental and numerical test, CSR = 0.13

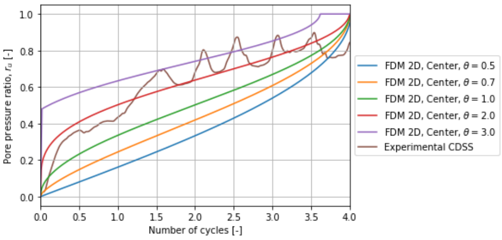

Figure D.49: Pore pressure development for experimental and numerical test, CSR = 0.15

E

Additional Information Case Study Oostpolderdijk

This appendix contains additional information for the Oostpolderdijk case study.

E.1. CPT Oostpolderdijk inner berm

[redacted]

Figure E.1: CPT at project location

E.2. Geotechnical Parameters

Table E.1: Material parameters OPD - 1

[redacted]	[redacted]	[redacted]	[redacted]	[redacted]	[redacted]	[redacted]	[redacted]
[redacted]	[redacted]	[redacted]	[redacted]	[redacted]	[redacted]	[redacted]	
[redacted]	[redacted]	[redacted]	[redacted]	[redacted]	[redacted]	[redacted]	
[redacted]	[redacted]	[redacted]	[redacted]	[redacted]	[redacted]	[redacted]	[redacted]
[redacted]	[redacted]	[redacted]	[redacted]	[redacted]	[redacted]	[redacted]	[redacted]
[redacted]	[redacted]	[redacted]	[redacted]	[redacted]	[redacted]	[redacted]	[redacted]
[redacted]	[redacted]	[redacted]	[redacted]	[redacted]	[redacted]	[redacted]	[redacted]
[redacted]	[redacted]	[redacted]	[redacted]	[redacted]	[redacted]	[redacted]	[redacted]
[redacted]	[redacted]	[redacted]	[redacted]	[redacted]	[redacted]	[redacted]	
[redacted]	[redacted]		[redacted]	[redacted]	[redacted]	[redacted]	
[redacted]	[redacted]		[redacted]	[redacted]	[redacted]	[redacted]	
[redacted]	[redacted]		[redacted]	[redacted]	[redacted]	[redacted]	
[redacted]	[redacted]	[redacted]	[redacted]	[redacted]	[redacted]	[redacted]	[redacted]
[redacted]	[redacted]	[redacted]	[redacted]	[redacted]	[redacted]	[redacted]	[redacted]
[redacted]	[redacted]	[redacted]	[redacted]	[redacted]	[redacted]	[redacted]	[redacted]
[redacted]	[redacted]	[redacted]	[redacted]	[redacted]	[redacted]	[redacted]	
[redacted]	[redacted]	[redacted]	[redacted]	[redacted]	[redacted]	[redacted]	
[redacted]	[redacted]	[redacted]	[redacted]	[redacted]	[redacted]	[redacted]	[redacted]

Table E.2: Material parameters OPD - 2

[redacted]	[redacted]	[redacted]	[redacted]	[redacted]	[redacted]
[redacted]	[redacted]	[redacted]	[redacted]	[redacted]	
[redacted]	[redacted]	[redacted]	[redacted]	[redacted]	
[redacted]	[redacted]	[redacted]	[redacted]	[redacted]	[redacted]
[redacted]	[redacted]	[redacted]	[redacted]	[redacted]	[redacted]
[redacted]	[redacted]	[redacted]	[redacted]	[redacted]	[redacted]
[redacted]	[redacted]	[redacted]	[redacted]	[redacted]	[redacted]
[redacted]	[redacted]	[redacted]	[redacted]	[redacted]	[redacted]
[redacted]	[redacted]	[redacted]	[redacted]	[redacted]	[redacted]
[redacted]	[redacted]	[redacted]	[redacted]	[redacted]	[redacted]
[redacted]	[redacted]	[redacted]	[redacted]	[redacted]	[redacted]
[redacted]	[redacted]	[redacted]	[redacted]	[redacted]	[redacted]
[redacted]	[redacted]	[redacted]	[redacted]	[redacted]	[redacted]
[redacted]	[redacted]	[redacted]	[redacted]	[redacted]	[redacted]
[redacted]	[redacted]	[redacted]	[redacted]	[redacted]	[redacted]

Table E.3: Material parameters OPD - 3

[redacted]	[redacted]	[redacted]	[redacted]	[redacted]	[redacted]
[redacted]	[redacted]	[redacted]	[redacted]	[redacted]	
[redacted]	[redacted]	[redacted]	[redacted]	[redacted]	
[redacted]	[redacted]	[redacted]	[redacted]	[redacted]	[redacted]
[redacted]	[redacted]	[redacted]	[redacted]	[redacted]	[redacted]
[redacted]	[redacted]	[redacted]	[redacted]	[redacted]	[redacted]
[redacted]	[redacted]	[redacted]	[redacted]	[redacted]	[redacted]
[redacted]	[redacted]	[redacted]	[redacted]	[redacted]	[redacted]
[redacted]	[redacted]	[redacted]	[redacted]	[redacted]	[redacted]
[redacted]	[redacted]	[redacted]	[redacted]	[redacted]	[redacted]
[redacted]	[redacted]	[redacted]	[redacted]	[redacted]	[redacted]
[redacted]	[redacted]	[redacted]	[redacted]	[redacted]	[redacted]
[redacted]	[redacted]	[redacted]	[redacted]	[redacted]	[redacted]
[redacted]	[redacted]	[redacted]	[redacted]	[redacted]	[redacted]
[redacted]	[redacted]	[redacted]	[redacted]	[redacted]	[redacted]
[redacted]	[redacted]	[redacted]	[redacted]	[redacted]	[redacted]
[redacted]	[redacted]	[redacted]	[redacted]	[redacted]	[redacted]

The following correlations are used to determine the soil parameters of the Hardening Soil small strain parameters.

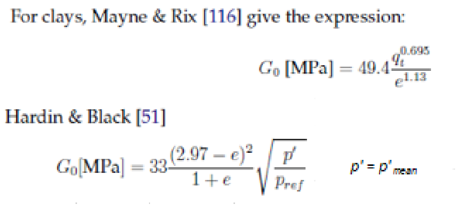

For clays, Mayne & Rix [116] give the expression:

$$G_0\,[\mathrm{MPa}] = 49.4\frac{q_t^{0.695}}{e^{1.13}}$$

Hardin & Black [51]

$$G_0[\mathrm{MPa}] = 33\frac{(2.97-e)^2}{1+e}\sqrt{\frac{p'}{p_{ref}}} \qquad p' = p'_{mean}$$

Figure E.2: Correlation Benz (2007)

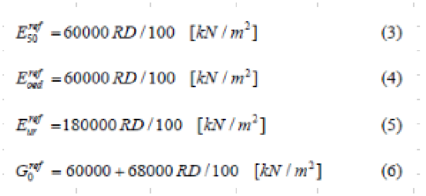

$$E_{50}^{ref} = 60000\,RD/100 \quad [kN/m^2] \qquad (3)$$

$$E_{oed}^{ref} = 60000\,RD/100 \quad [kN/m^2] \qquad (4)$$

$$E_{ur}^{ref} = 180000\,RD/100 \quad [kN/m^2] \qquad (5)$$

$$G_0^{ref} = 60000 + 68000\,RD/100 \quad [kN/m^2] \qquad (6)$$

Figure E.3: Correlation Brinkgreve et al. (2010)

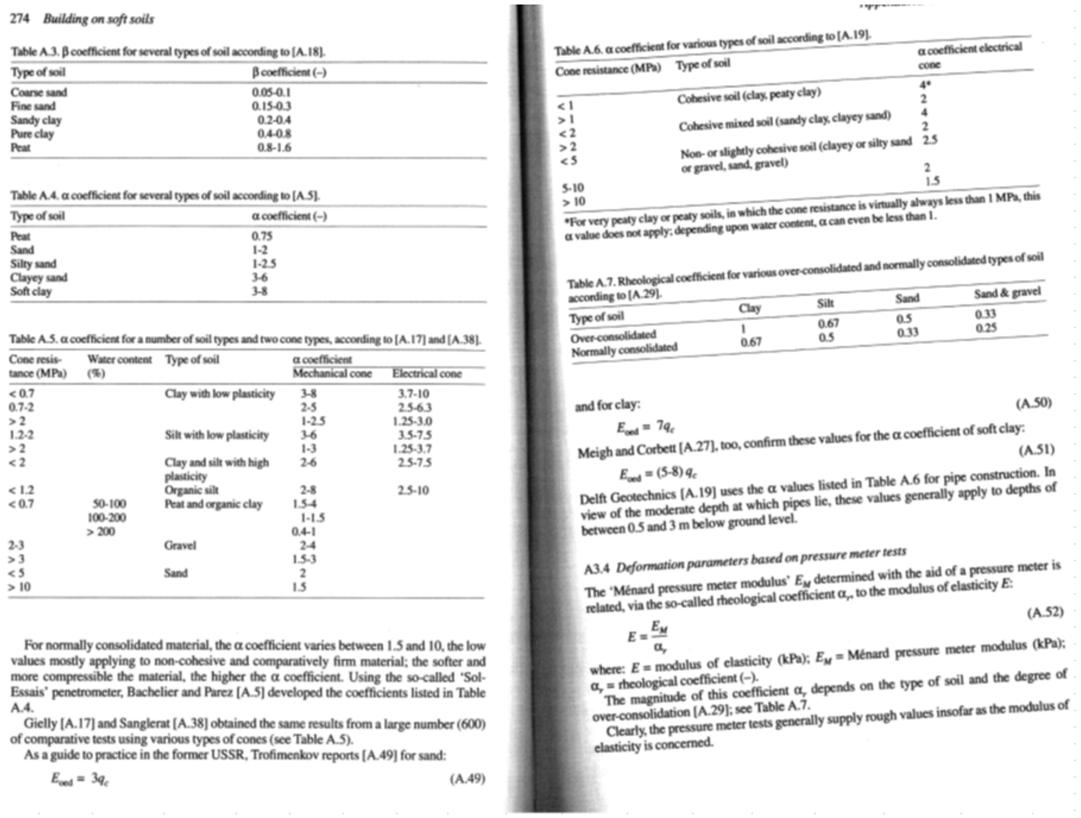

274 *Building on soft soils*

Table A.3. β coefficient for several types of soil according to [A.18].

Type of soil	β coefficient (–)
Coarse sand	0.05-0.1
Fine sand	0.15-0.3
Sandy clay	0.2-0.4
Pure clay	0.4-0.8
Peat	0.8-1.6

Table A.4. α coefficient for several types of soil according to [A.5].

Type of soil	α coefficient (–)
Peat	0.75
Sand	1-2
Silty sand	1-2.5
Clayey sand	3-6
Soft clay	3-8

Table A.5. α coefficient for a number of soil types and two cone types, according to [A.17] and [A.38].

Cone resistance (MPa)	Water content (%)	Type of soil	α coefficient	
			Mechanical cone	Electrical cone
< 0.7		Clay with low plasticity	3-8	3.7-10
0.7-2			2-5	2.5-6.3
> 2			1-2.5	1.25-3.0
1.2-2		Silt with low plasticity	3-6	3.5-7.5
> 2			1-3	1.25-3.7
< 2		Clay and silt with high plasticity	2-6	2.5-7.5
< 1.2		Organic silt	2-8	2.5-10
< 0.7	50-100	Peat and organic clay	1.5-4	
	100-200		1-1.5	
	> 200		0.4-1	
2-3		Gravel	2-4	
> 3			1.5-3	
< 5		Sand	2	
> 10			1.5	

For normally consolidated material, the α coefficient varies between 1.5 and 10, the low values mostly applying to non-cohesive and comparatively firm material; the softer and more compressible the material, the higher the α coefficient. Using the so-called 'Sol-Essais' penetrometer, Bachelier and Parez [A.5] developed the coefficients listed in Table A.4.

Giélly [A.17] and Sanglerat [A.38] obtained the same results from a large number (600) of comparative tests using various types of cones (see Table A.5).

As a guide to practice in the former USSR, Trofimenkov reports [A.49] for sand:

$$E_{oed} = 3q_c \tag{A.49}$$

Table A.6. α coefficient for various types of soil according to [A.19].

Cone resistance (MPa)	Type of soil	α coefficient electrical cone
< 1	Cohesive soil (clay, peaty clay)	4*
> 1		2
< 2	Cohesive mixed soil (sandy clay, clayey sand)	4
> 2		2
< 5	Non- or slightly cohesive soil (clayey or silty sand or gravel, sand, gravel)	2.5
5-10		2
> 10		1.5

*For very peaty clay or peaty soils, in which the cone resistance is virtually always less than 1 MPa, this α value does not apply; depending upon water content, α can even be less than 1.

Table A.7. Rheological coefficient for various over-consolidated and normally consolidated types of soil according to [A.29].

Type of soil	Clay	Silt	Sand	Sand & gravel
Over-consolidated	1	0.67	0.5	0.33
Normally consolidated	0.67	0.5	0.33	0.25

and for clay:

$$E_{oed} = 7q_c \tag{A.50}$$

Meigh and Corbett [A.27], too, confirm these values for the α coefficient of soft clay:

$$E_{oed} = (5\text{-}8)\,q_c \tag{A.51}$$

Delft Geotechnics [A.19] uses the α values listed in Table A.6 for pipe construction. In view of the moderate depth at which pipes lie, these values generally apply to depths of between 0.5 and 3 m below ground level.

A3.4 *Deformation parameters based on pressure meter tests*

The 'Ménard pressure meter modulus' E_M determined with the aid of a pressure meter is related, via the so-called rheological coefficient α_r, to the modulus of elasticity E:

$$E = \frac{E_M}{\alpha_r} \tag{A.52}$$

where: E = modulus of elasticity (kPa); E_M = Ménard pressure meter modulus (kPa); α_r = rheological coefficient (–).

The magnitude of this coefficient α_r depends on the type of soil and the degree of over-consolidation [A.29]; see Table A.7.

Clearly, the pressure meter tests generally supply rough values insofar as the modulus of elasticity is concerned.

Figure E.4: Correlation CUR162

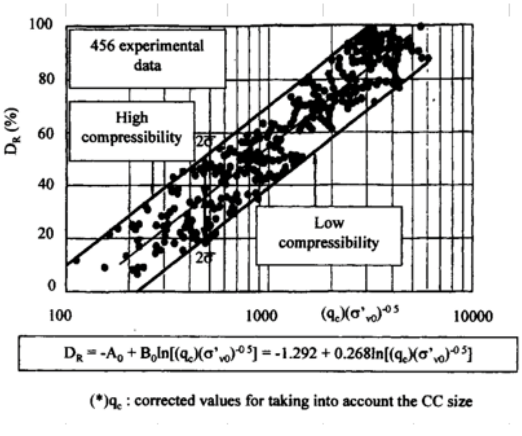

$D_R = -A_0 + B_0 \ln[(q_c)(\sigma'_{v0})^{-0.5}] = -1.292 + 0.268 \ln[(q_c)(\sigma'_{v0})^{-0.5}]$

(*)q_c : corrected values for taking into account the CC size

Figure E.5: Correlation Jamiolkowski et al. (2001)

$$R_e = \frac{1}{2.91} \cdot \ln\left(\frac{q_c}{61 \cdot {\sigma_v}^{0.71}}\right)$$

Figure E.6: Correlation Lunne and Christoffersen (1983)

$$E_{50} = E_{50}^{ref}\left(\frac{c\cos\varphi - \sigma'_3\sin\varphi}{c\cos\varphi + p^{ref}\sin\varphi}\right)^m$$

$$E_{oed} = E_{oed}^{ref}\left(\frac{c\cos\varphi - \frac{\sigma_3}{K_0^{nc}}\sin\varphi}{c\cos\varphi + p^{ref}\sin\varphi}\right)^m$$

$$E_{ur} = E_{ur}^{ref}\left(\frac{c\cos\varphi - \sigma'_3\sin\varphi}{c\cos\varphi + p^{ref}\sin\varphi}\right)^m$$

$$\gamma_{0.7} \approx \frac{1}{9G_0}[2c'(1+\cos(2\varphi')) - \sigma'_1(1+K_0)\sin(2\varphi')]$$

$$G_0 = G_0^{ref}\left(\frac{c\cos\varphi - \sigma'_3\sin\varphi}{c\cos\varphi + p^{ref}\sin\varphi}\right)^m$$

Figure E.7: Correlation Plaxis (2019b)

E.3. Construction Phases

The following construction phases are used during the calculations.

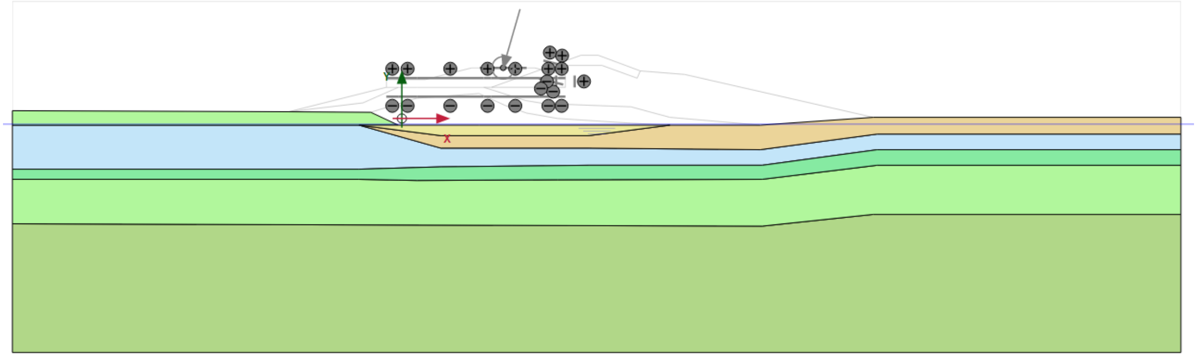

Figure E.8: Case study phase 1: initial conditions

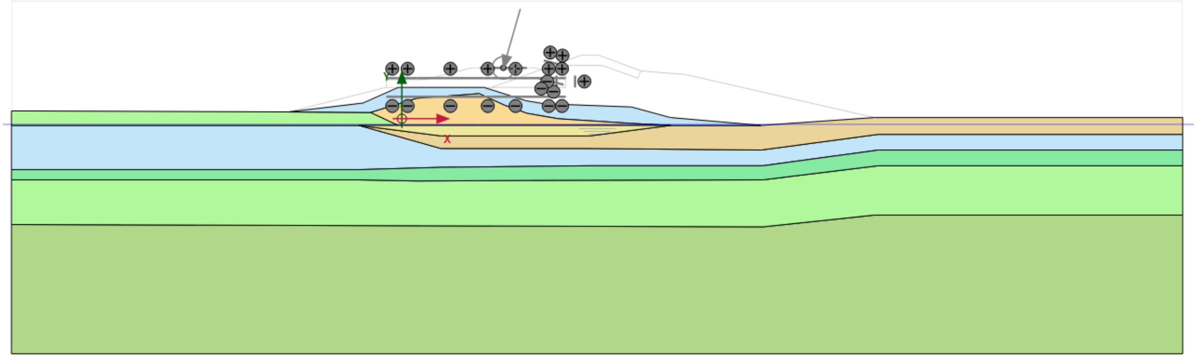

Figure E.9: Case study phase 2: old dike

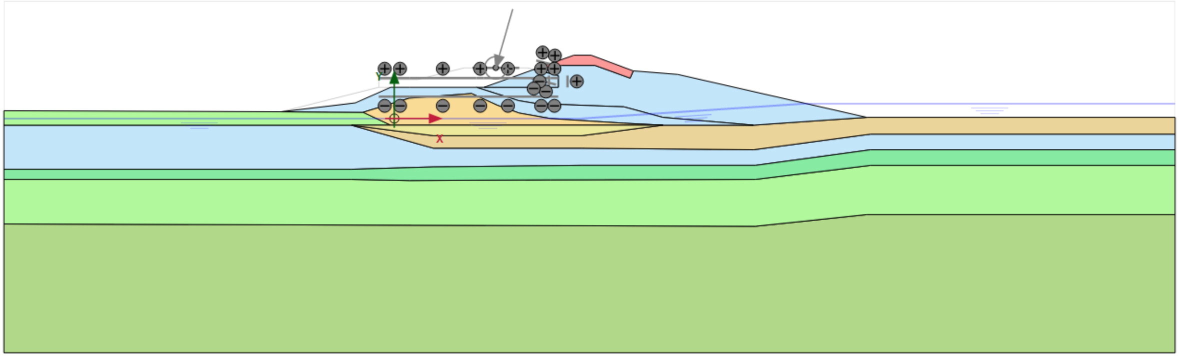

Figure E.10: Case study phase 3: new dike 1977

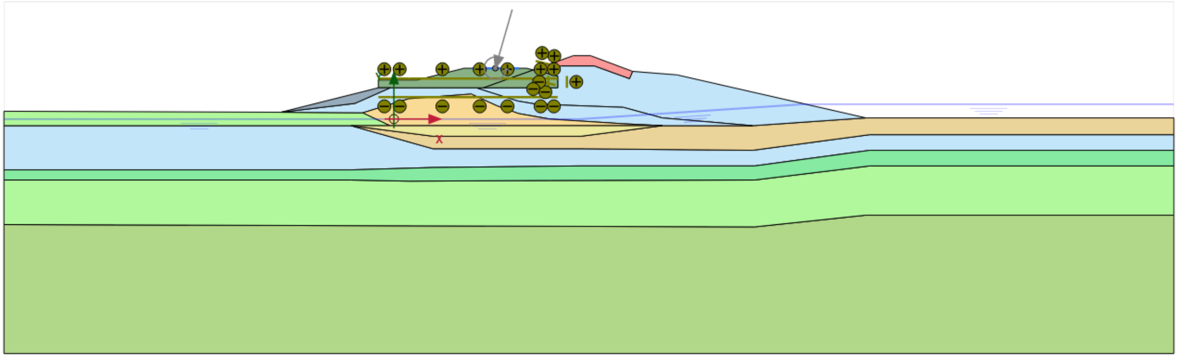

Figure E.11: Case study phase 4: current situation

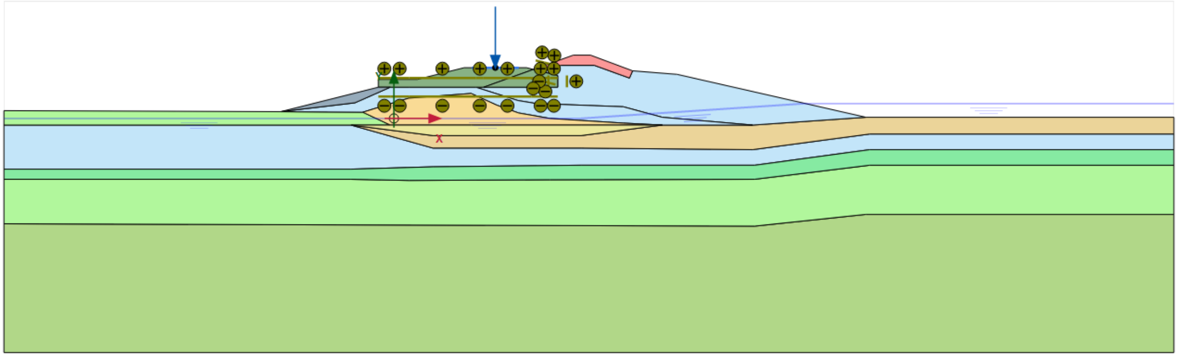

Figure E.12: Case study phase 5: installation turbine

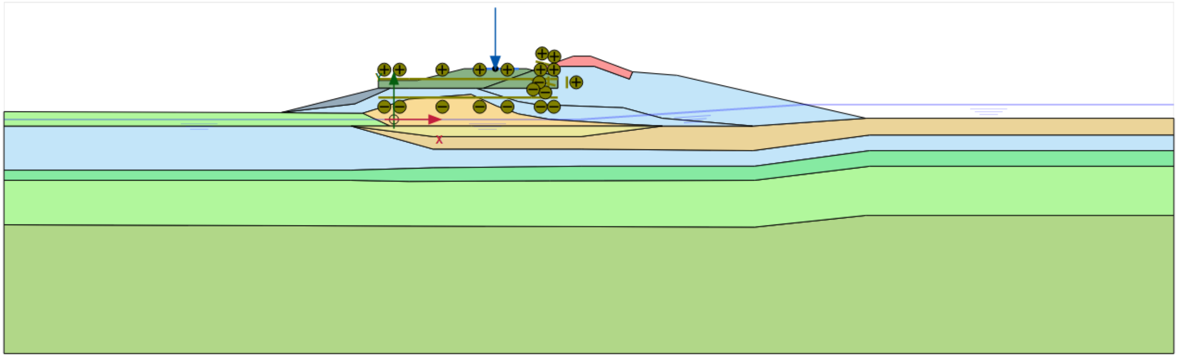

Figure E.13: Case study phase 6: consolidation

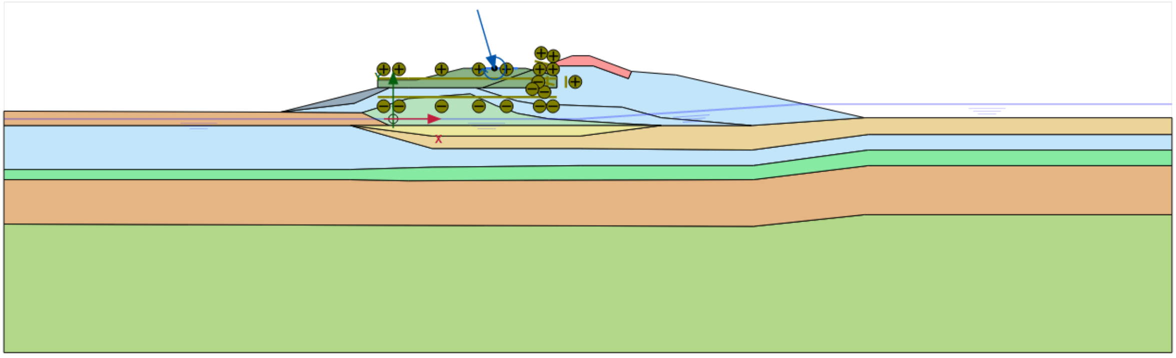

Figure E.14: Case study phase 7: user phase, average forces

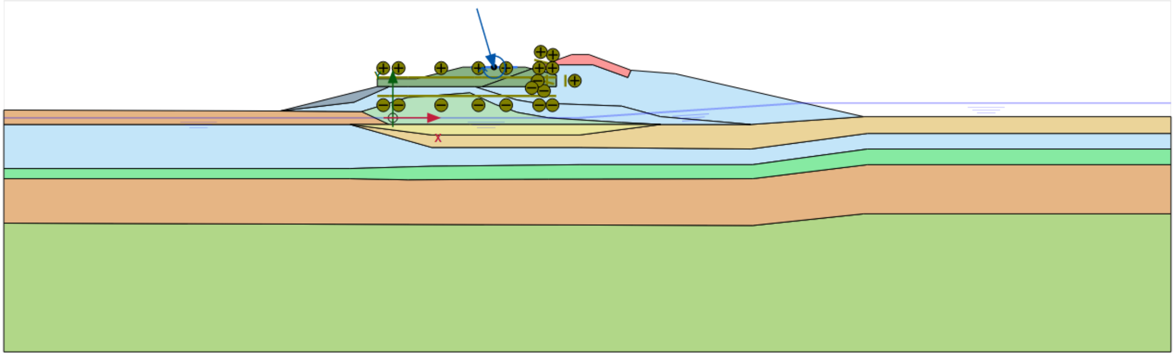

Figure E.15: Case study phase 8: user phase, largest loads

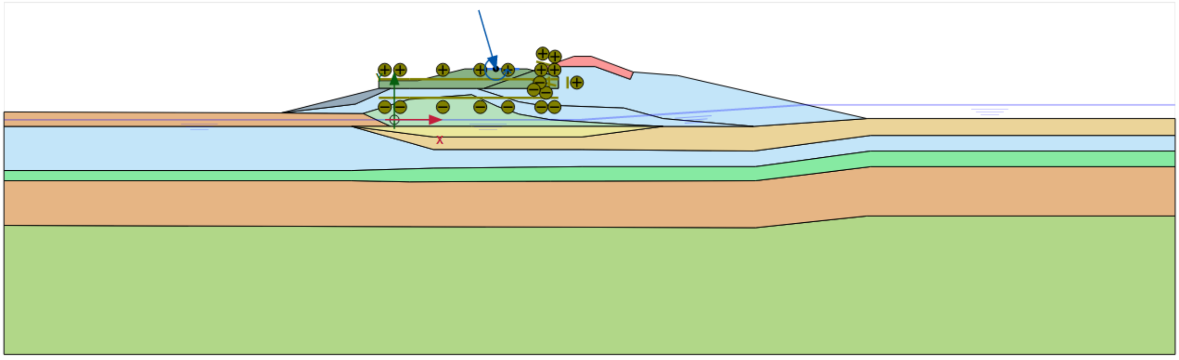

Figure E.16: Case study phase 8: user phase, smallest loads